Alma Mater Studiorum - Università di Bologna

DOTTORATO DI RICERCA IN

CHIMICA

Ciclo 35

Settore Concorsuale: 03/A2 - MODELLI E METODOLOGIE PER LE SCIENZE CHIMICHE

Settore Scientifico Disciplinare: CHIM/02 - CHIMICA FISICA

MODELLING THE INFLUENCE OF DIRADICAL CHARACTER AND AGGREGATION ON CONJUGATED MOLECULAR MATERIALS

Presentata da: Yasi Dai

Coordinatore Dottorato

Luca Prodi

Supervisore

Fabrizia Negri

Co-supervisore

Massimo Marcaccio

Esame finale anno 2023

Glossary of Acronyms

A: acceptor

ALDA: adiabatic local density approximation

AOB: atomic orbital basis

AOS: active orbital space

AP: Adiabatic Potential

BS: broken symmetry

CASSCF (or CAS): Complete active space self-consistent field

CI: configuration interaction

CR: charge resonance

CS: closed shell

CSF(s): configuration state function(s)

CT: charge transfer

de: doubly excited

D^+: donor

De: delocalized excitation

DE: double-exciton state

DFT: density functional theory

DFT/MRCI: DFT multireference configuration interaction

DMO(s): delocalized molecular orbital(s)

ECC: effective conjugation coordinate

FE: Frenkel

FMO(s): frontier molecular orbitals

FO: fragment orbital

FOD: fractional orbital density

FT: finite-temperature

GGA: Gradient Corrected Approximation

GS: ground state

H: highest occupied molecular orbital

H_{dia}: Hamiltonian in the diabatic basis

HF: Hartree-Fock

HOMO: highest occupied molecular orbital

HR: Huang-Rhys

HT: Herzberg–Teller

ICT: Internal Charge Transfer

KMC: Kinetic Monte Carlo

KS: Kohn-Sham

L: lowest unoccupied molecular orbital

LCD: liquid crystal display

LDA: Local Density Approximation

LE(s): localized excitation(s) / locally excited

LMO(s): monomer localized molecular orbital(s)

LR: linear response

LRC: long-range corrected

LSDA: Local Spin Density Approximation

LUMO: lowest unoccupied molecular orbital

mH: model Hamiltonian

MCSCF: multiconfigurational self-consistent field

MD: molecular dynamics

MIOS: minimal orbital space

MLJ: Marcus-Levich-Jortner

MM: molecular mechanics

MO(s): molecular orbital(s)

MOB: monomer orbital basis

MRPT: multireference perturbation theory

MSD: mean square displacement

NLO: non-linear optical

OFET: organic field-effect transistor

OLED: organic light-emitting diode

OPD: organic photodetector

OS: open shell

OSC: organic solar cell

p-QDM: *para*-quinodimethane

PAH(s): polycyclic aromatic hydrocarbon(s)

PES: Potential energy surface

PT: perturbation theory

QC: quantum-chemical

QM: quantum-mechanics

sa: spin-adapted

SA: symmetry-adapted

SC: Slater-Condon

SCXRD: Single Crystal X-ray Diffraction

SE: singly excited state dominated by H$\rightarrow$L excitation

SF: spin flip

SIE: Self-Interaction error

SOMO: singly occupied molecular orbital

SP: sudden polarization

SUMO: singly unoccupied molecular orbital

TCNQ: tetracyanoquinodimethane

TDA: Tamm-Dancoff Approximation

TD-DFT: Time dependent DFT

TOF: time of flight

TRC: triplet reference configuration

TS: totalsymmetric

UDFT: unrestricted DFT

V: intermolecular electronic coupling

XRD: X-ray diffraction

2e-2o: 2 electrons in 2 orbitals

Table of contents

Chapter 4: Charge transport in conjugated molecular materials 71

Chapter 5: Exciton states in molecular aggregates 96

Abstract

Molecular materials are made by the assembly of specifically designed molecules to obtain bulk structures with desired solid-state properties, enabling the development of materials with tunable chemical and physical properties. These properties result from the interplay of intra-molecular constituents and weak intermolecular interactions. Thus, small changes in individual molecular and electronic structure can substantially change the properties of the material in bulk.

The purpose of this dissertation is, thus, to discuss and to contribute to the structure-property relationships governing the electronic, optical and charge transport properties of organic molecular materials through theoretical and computational studies. In particular, the main focus is on the interplay of intra-molecular properties and inter-molecular interactions in organic molecular materials.

In my three-years of research activity, I have focused on three major areas: 1) the investigation of isolated-molecule properties for the class of conjugated chromophores displaying diradical character which are building blocks for promising functional materials; 2) the determination of intra- and intermolecular parameters governing charge transport in molecular materials and, 3) the development and application of diabatization procedures for the analysis of exciton states in molecular aggregates.

The properties of diradicaloids are extensively studied both regarding their ground state (diradical character, aromatic vs quinoidal structures, spin dynamics, *etc.*) and the low-lying singlet excited states including the elusive double-exciton state.

The efficiency of charge transport, for specific classes of organic semiconductors (including diradicaloids), is investigated by combining the effects of intra-molecular reorganization energy, inter-molecular electronic coupling and crystal packing.

Finally, protocols aimed at unravelling the nature of exciton states are introduced and applied to different molecular aggregates. The role of intermolecular interactions and charge transfer contributions in determining the exciton state character and in modulating the H- to J-aggregation is also highlighted.

Chapter 1: Introduction

Molecular materials are made by the assembly of specifically designed molecules to obtain bulk structures with desired solid-state properties, enabling the development of materials with tunable chemical and physical properties. These properties result from the interplay of intra-molecular constituents and weak intermolecular interactions. Thus, small changes in individual molecular and electronic structure can substantially change the properties of the material in bulk.

Broadly speaking, my thesis is centered on organic molecular materials which are soft solids with a 3D distribution of organic molecules exhibiting weak intermolecular forces. Their cohesion is essentially mediated by *Van der Waals,* electrostatic, hydrogen bonding and $\pi-\pi$ interactions. The molecules involved in the formation of such materials may be of a purely organic nature (*e.g.*, metal free) or based on hybrid organic–inorganic combinations (*e.g.*, organo-metallic with transition metals). Organic molecular solids have attracted much interest in the past two decades in diverse disciplines ranging from the medical sciences to the semiconductor industry. Due to the huge range of possible molecular constituents, molecular solids can show an exceptional variety of properties.

Restricting further the vast area of organic molecular materials, this thesis is focused on those made of conjugated, metal free molecules displaying semiconducting properties[1,2].

Thanks to the combined role of intra- and inter-molecular properties, these materials offer several advantages[1,3–5]. To mention just a few:

- **Tunability:** organic semiconductors are obtained from organic synthesis which allow different modifications on the molecular structure ultimately leading to tunable photophysical properties.
- **Lightness:** molecules are based on light elements such as C and H which allow a low molecular weight.
- **Flexibility:** organic molecules are deposited as thin film on the substrate. This is one of the most fascinating properties allowing applications in *e.g.* curved displays.
- **Low-cost:** compared to inorganic semiconductors, the cost of raw materials for organic semiconductors is lower. Additionally, the latter also exhibit a lower price

in production as they can be processed at lower temperature and deposited from solution using low-cost coating procedures.

Incorporation of functionalities by molecular design is undoubtedly the most appealing potential offered by molecular materials. This capability is reflected in the remarkable growth of organic light-emitting diodes (OLED)[6,7] in displays that are gradually replacing old type displays based on liquid crystal (LCD). Other than OLED, organic materials cover important roles also in solar cells (*organic solar cell,* OSC)[8,9], in transistors (*organic field-effect transistor,* OFET)[5,10,11], in batteries (*organic battery*), in photodetectors (*organic photodetector*, OPD)[12,13], *etc.* In these devices conjugated molecules are involved in charge generation (either electrons or holes) and charge transfer processes. Although charge transport can be rationalized in terms of two major mechanisms, band-like or hopping, depending on the relative magnitude of intermolecular electron interactions[14–17], the latter is generally a suitable model at room temperature, owing to the weak intermolecular forces that characterize most organic semiconductors. The magnitude of charge mobility is also strongly influenced by a combination on intra-molecular parameters and inter-molecular organization [18–20].

The suitable reciprocal orientation of molecules in an organic material not only impacts the charge conduction but also determines relevant optical phenomena due to excitonic effects such as the formation of J- or H-aggregates[21,22]. The term 'exciton' is referred to an **excited state** of condensed matter, which can transport energy without bearing a net charge. It is generally regarded as a bound state of an electron e^- and a hole h^+, kept together by Coulomb forces. Excitons can be generated *via* photoexcitation or by charge recombination (*i.e.* charges are generated electrically). In molecular materials there are essentially two types of excitons depending on their radius and energies:

- **Frenkel exciton:** the excitation is localized on a single molecule and thus, the exciton radius is small.
- **Charge transfer (CT) exciton:** here the excitation is accompanied by an electron transfer from one molecule to the nearest. The exciton radius here is larger than that of Frenkel excitons.

The importance of CT excitons has been outlined in several photophysical processes such as: singlet fission [23–29], formation of excimers[30–32], exciton-dissociation, charge-separation and charge-recombination processes in organic photovoltaics[33,34]. Intermolecular interactions, which strongly depend on the packing arrangement, play a key role in determining the photo-induced processes in aggregates of organic chromophores and the control of chromophore's assembly has become a challenging target in supramolecular chemistry[35–44]. A parallel effort in conceptual comprehension of the underlying fundamental physics of photoinduced processes has led to deep advancements in understanding the influence of interchromophoric arrangements on the optical properties of aggregates[21,22,45], and in modelling the photo-induced relaxation processes leading to excimer formation[46–48]. Determining the CT character of exciton states predicted from calculations is, therefore, an essential task. Several approaches have been proposed to expand computed adiabatic states in terms of diabatic bases[49,50,59–62,51–58] although most applications have been limited to small aggregates or to restricted orbital spaces. Extending such approaches to enable applicability to molecular aggregates of increasing complexity is highly desirable.

To take advantage of the easily tunable optical and charge transport properties of organic molecular materials, it is necessary to obtain a comprehensive and detailed knowledge not only on inter-molecular, but also on intra-molecular properties. In this regard, tuning of molecular orbitals through extension of the π-conjugated system, incorporation of specific molecular moieties as well as derivatization with electron-withdrawing or electron-donating groups, impacts the electronic gap and consequently, both charge transport and optical properties of the organic material can be tailored by suitably modifying structural features of the molecule.

A class of organic molecules that have recently attracted considerable interest, for their potential applications in optoelectronics, is conjugated diradicaloids[63–65]. These systems are generally characterized by small HOMO (*highest occupied molecular orbital,* H) / LUMO (*lowest unoccupied molecular orbital,* L) gap which is tunable with conjugation length and suitable substituents. Such small HOMO/LUMO gap favors ambipolar conduction of charges, double and reversible redox potentials, narrow singlet-triplet gaps, absorption in the near-infrared region, large two-photon absorption and distinctive optical properties influenced by the presence of a low-lying double-exciton (DE) state[66,67]. Consequently, conjugated diradicaloids have been proposed as candidates for a variety of applications in materials science, such as ambipolar OFET[68,69], singlet fission[23,70–76] in organic photovoltaics, near infrared photodetector, nonlinear optical materials [77] and spintronics[78] thanks to the presence of thermally convertible spin states[63–65,79–81]. Several enlightening studies have been reported since the early 70's [82–86] including reviews[63] and books[64] providing a comprehensive overview of diradicaloids from chemical-physical properties to material applications. The pioneering works of Salem[84], Michl [85] and more recently by Hoffmann[86], have contributed in a fundamental way to the comprehension of their electronic structure, which can be rationalized in terms of a simple two-electrons in two-orbitals (2e-2o) model [76,84–86].

On the other hand, the recent advances in synthetic strategies and the enormous effort in designing new stable diradicaloids, often featuring extended conjugated moieties, have provided a large amount of experimental data including singlet/triplet energy gaps, photophysical and optoelectronic properties. This impressive amount of information calls for a rationalization which generally cannot be achieved based on simple models. Thus, the elucidation of optoelectronic and spintronic properties is crucial for advanced applications but challenging from the computational point of view, due to the open-shell nature, spin polarization and strong sensitivity to electron correlation of conjugated diradicals[83][87].

At present, several theoretical and computational studies have sensibly contributed to shed light on the parameters governing the performance of different organic molecular materials and on the structural and electronic properties of their constituent molecular systems, demonstrating the fundamental role of modelling for both the rationalization of experimentally observed behaviors and the design of new materials with suitable properties.

From this perspective, the purpose of this dissertation is to contribute, through theoretical and computational studies, to the understanding of the structure-property relationships governing the electronic, optical and charge transport properties of organic molecular materials by focusing on the combined influence of intra-molecular properties and inter-molecular interactions. The aim is to contribute to both the rationalization of experimentally observed behaviors and the improvement in the design of new organic functional materials by

understanding their constituent properties.

In line with the interplay of intra-molecular properties and inter-molecular interactions, in my three-years of research activity I have focused on three major areas: <u>1) the investigation of isolated-molecule properties for the class of conjugated chromophores displaying diradical character which are building blocks for promising functional materials</u>; 2) <u>the determination of intra- and intermolecular parameters governing charge transport in molecular materials and</u>, 3) <u>the development and application of diabatization procedures for the analysis of exciton states in molecular aggregates.</u>

This work encompassed the use of accurate models for the prediction of photophysical properties using state-of-the-art electronic structure methods ranging from density functional theory (DFT), time dependent density functional theory (TD-DFT) but also DFT/multireference configuration interactions (DFT/MRCI) and complete active space self-consistent field (CASSCF). Quantum-chemical methods were also used to determine the intra-molecular parameters relevant for charge transport and inter-molecular electronic couplings governing charge transfer rate constants and required to simulate charge mobilities. In addition, I have contributed to the development of analysis tools to disentangle the nature of exciton states in molecular aggregates.

The final aim was to develop optimized protocols and novel strategies to 1) characterize the emerging class of conjugated organic molecules displaying diradical character and 2) uncover the effects of molecular organization in condensed phases on optoelectronic properties.

How to read this work

Apart from this introductory chapter, this dissertation consists of five additional chapters, organized as follows. Most of the computational work is based on quantum-chemical calculations and the description of the standard approaches for ground and excited electronic states is summarized in Chapter 2.

As discussed above, the thesis covered three specific areas of investigations and the corresponding results are collected in the following three Chapters. Since specific models and methods were required in each case, the corresponding methodological approaches are introduced at the beginning of each Chapter. More precisely, in Chapter 3 methods specifically suited to investigate ground and excited states of diradicaloids are introduced. In Chapter 4 a brief introduction is given on the approaches used to calculate the required intra- and inter-molecular parameters, and on the protocols employed to model charge transport in molecular materials. In Chapter 5 we provide a general introduction to diabatization approaches and details on the *in-house* developed diabatization procedure used to analyze exciton states of molecular aggregates.

Apart from the specific methodological introduction, Chapter 3 to Chapter 5 are centered on applications and results.

Chapter 3 deals with the investigation of conjugated organic molecules displaying diradical character focusing on their potential applications in optoelectronics and spintronics. To this end a collection of properties are investigated computationally encompassing the thermally induced

spin-mobility in an azobenzene derivative featuring diradical character, the identification of specific resonance Raman active modes in a series of quinoidal oligothiophenes, the influence of the distinctive low-lying DE state on optical absorption features including a benchmarking of the most reliable computational approaches and, finally, an interpretation of the luminescence properties of a Thiele derivative. All these studies have been published in the following papers[88–91], except for the last which has been submitted for publication.

1. Shen, Y.; Xue, G.; **Dai, Y.;** Quintero, S.M.; Chen, H.; Wang, D.; Miao, F.; Negri, F.; Zheng, Y.; Casado, J., "Normal & reversed spin mobility in a diradical by electron-vibration coupling", *Nat. Commun.* **2021**, *12,* 6262, doi:10.1038/s41467-021-26368-8.

2. **Dai, Y.;** Bonometti, L.; Zafra, J.L.; Takimiya, K.; Casado, J.; Negri, F. "Raman Activities of Cyano-Ester Quinoidal Oligothiophenes Reveal Their Diradical Character and the Proximity of the Low-Lying Double Exciton State", *Chemistry,* **2022**, *4*, 329–344, doi:10.3390/chemistry4020025.

3. Canola, S.; **Dai, Y**.; Negri, F., "The Low Lying Double-Exciton State of Conjugated Diradicals: Assessment of TDUDFT and Spin-Flip TDDFT Predictions", *Computation,* **2019,** *7*, 68. doi:10.3390/computation7040068.

4. Negri, F.; Canola, S.; **Dai, Y**. "Spectroscopy of Open-Shell Singlet Ground-State Diradicaloids: A Computational Perspective. In *Diradicaloids",* Wu, J., Ed.; Jenny Stanford Publishing: New York, 2022; pp. 145–179 ISBN 978-981-4968-08-9.

5. Punzi, A.; **Dai, Y.;** Dibenedetto, C.N.; Mesto, E.; Schingaro, E.; Striccoli, M.; Negri, F.; Farinola, G.M.; Blasi, D., submitted.

Chapter 4 focusses on applications to charge transport in molecular semiconductors. In this regard, diradicaloids are interesting owing to their potential ambipolar properties. Prompted by this, I have investigated the impact of diradical character on intra-molecular reorganization energies for the family of difluorenoheterole diradicaloids[69] and extended the study to a library of diradicaloid molecules either exhibiting similar molecular building blocks (fluorene) or more generally featuring varying diradical character. The combined effect of intra-molecular properties and inter-molecular interactions on charge transport efficiency have been investigated for two naphtho-dithiophene di-imide (NDTI) derivatives[92] featuring different fluoroalkylation. Most of the results reported in this Chapter have been published in the following papers:

6. Mori, S.; Moles Quintero, S.; Tabaka, N.; Kishi, R.; González Núñez, R.; Harbuzaru, A.; Ponce, R.; Marin Beloqui, J.; Suzuki, S.; Kitamura, C.; Gómez, C.; **Dai, Y**.; Negri, F.; Nakano, M.; Kato, S.; Casado, J. "Medium Diradical Character, Small Hole and Electron Reorganization Energies and Ambipolar Transistors in Difluorenoheteroles", *Angew. Chemie Int. Ed.* **2022**, *202206680.* doi:10.1002/anie.202206680.

7. Ricci, G.; Canola, S.; **Dai**, Y.; Fazzi, D.; Negri, F. "Impact of fluoroalkylation on the n-type charge transport of two naphthodithiophene diimide derivatives", *Molecules,* **2021**, *26*, doi:10.3390/molecules26144119.

The effects of inter-molecular interactions on the exciton states of molecular aggregates are considered in Chapter 5. Here, I have applied a general procedure to analyze the adiabatic exciton states derived from TD-DFT calculations to triplet and singlet exciton states of perylene

di-imide (PDI) aggregates [93,94] and I have contributed to the extension of the protocol for larger orbital spaces and aggregate dimension. These extensions have been applied to the study of oligoacene aggregates[95] and used to parametrize a model Hamiltonian, motivated by the need of cost-effective approaches to afford the study of larger aggregates.

8. Canola, S.; Bagnara, G.; **Dai, Y.**; Ricci, G.; Calzolari, A.; Negri, F., "Addressing the Frenkel and charge transfer character of exciton states with a model Hamiltonian based on dimer calculations: application to large aggregates of perylene bisimide", *J. Chem. Phys.* **2021**, *154*,124101. doi: 10.1063/5.0045913

9. **Dai, Y.**; Zubiria-Ulacia, M.; Casanova, D.; Negri, F. "Impact of Charge-Resonance Excitations on CT-Mediated J-Type Aggregation in Singlet and Triplet Exciton States of Perylene Di-Imide Aggregates: A TDDFT Investigation", *Computation,* **2022**, *10*, 18, doi:10.3390/computation10020018.

10. **Dai, Y.**; Calzolari, A.; Zubiria-Ulacia, M.; Casanova, D.; Negri, F. "Intermolecular Interactions and Charge Resonance Contributions to Triplet and Singlet Exciton States of Oligoacene Aggregates", *Molecules,* **2023**, *28*, doi:10.3390/molecules28010119

Finally, the concluding Chapter 6 summarizes the most relevant outcomes of this work.

Additional work published during my PhD

Below, for completeness, I include a list of publications to which I contributed and that were published during my PhD although these are not included as part of my dissertation.

1. Bassan, E.; **Dai, Y.**; Fazzi, D.; Gualandi, A.; Cozzi, P.G.; Negri, F.; Ceroni, P., "Effect of the iodine atom position on the phosphorescence of BODIPY derivatives: a combined computational and experimental study", *Photochem. Photobiol. Sci.,* **2022**, doi:10.1007/s43630-021-00152-5.

2. Bassan, E.; Calogero, F.; **Dai, Y.**; Dellai, A.; Franceschinis, A.; Pinosa, E.; Negri, F.; Gualandi, A.; Ceroni, P.; Cozzi, P.G. "Meso-2-MethoxyNaphthalenyl-BODIPY as Efficient Organic Dye for Metallaphotoredox Catalysis", *ChemCatChem,* **2023**, e202201380, doi:10.1002/cctc.202201380.

3. Mesto, D.; **Dai, Y.**; Dibenedetto, C.N.; Punzi, A.; Krajčovič, J.; Striccoli, M.; Negri, F.; Blasi, D. "Tuning the Electro-Optical Properties of Mixed-Halide Trityl Radicals Bearing para-Brominated Positions through Halogen Substitution", *European J. Org. Chem.,* **2023**, *26*, e202201030, doi:10.1002/ejoc.202201030

Chapter 2: Computational Methods

In this Chapter, I introduce a fundamental description of Quantum-Chemical methods suitable to study structural and electronic properties of ground and excited states of molecular systems. These include DFT in its restricted and unrestricted formulation and TD-DFT for excited states. This introduction also covers methods suitable when static correlation is relevant, such as Complete Active Space Self Consistent Field (CASSCF) or when multiple excitations and not only single excitations are necessary to correctly describe excited states, such as spin-flip TD-DFT and DFT/multireference configuration interaction (DFT/MRCI).

2.1 Restricted and Unrestricted Density Functional Theory

Density Functional Theory (DFT)[96] is a *Single-Reference mono-determinantal quantum mechanical* method useful for the study of the **ground electronic state**. DFT is based on Hohenberg and Kohn's **Existence** and **Variational** theorems which stated that "*properties at the ground state of a many-electron system are uniquely determined by electron density. This density exists, it is unique and it obeys the variational principle*". Therefore, energy of molecular system, functional of the electron density, can be expressed as follow:

$$E_{DFT}[\rho] = T[\rho] + E_{ne}[\rho] + J[\rho] + E_{xc}[\rho] \tag{2.1}$$

where ρ is the electron density; T is the kinetic energy; E_{ne} stands for the attractive coulombic energy between electrons and nuclei; J is the repulsive coulombic energy between electrons and finally E_{xc} is the exchange-correlation energy.

The novelty of such method is to take advantage of a non-interacting system of electrons, as proposed by Kohn and Sham in 1965[97]. The over-all ground state density of such system

has the same density of the real system where electrons interact. Advantage of such approach is to express the Hamiltonian as sum of one-electron operators and the corresponding eigenvalue could be obtained as simple sum of one-electron eigenvalues[96].

Similar to the Hartree-Fock (HF) method, also the Kohn-Sham (KS) procedure consists in solving iteratively the eigenvalue equation:

$$h_i^{KS} \chi_i = \varepsilon_i \chi_i \tag{2.2}$$

where χ_i is the KS orbital for *i*-th electron built from the density; ε_i is the energy associated to orbital χ_i. h_i^{KS} is the one-electron KS operator for a non-interacting system of electrons which is expressed as follow:

$$h_i^{KS} = -\frac{1}{2}\nabla_i^2 - \sum_k^{nuclei} \frac{Z_k}{|r_i - r_k|} + \int \frac{\rho(r')}{|r_i - r'|} dr' + V_{xc} \tag{2.3}$$

where $-\frac{1}{2}\nabla_i^2$ expresses the monoelectronic kinetic energy; $-\sum_k^{nuclei} \frac{Z_k}{|r_i - r_k|}$ is the attractive coulombic energy between the electron and nuclei; $\int \frac{\rho(r')}{|r_i - r'|} dr'$ is the repulsive coulombic energy between the electron and others; V_{xc} is called as *functional derivative* and it is the operator for which the expectation value of the KS Slater determinant is E_{xc}.

DFT is a *formally exact* method: an exact electron density leads to exact energy. This definition requires the exact exchange-correlation functional ($E_{xc}[\rho]$ in Eq. 2.1). Unfortunately, the correct form of the exchange-correlation operator (V_{xc} in Eq. 2.3) is unknown. As a consequence, DFT's relevant equations must be solved approximately. Nevertheless, by including E_{xc}, DFT's quality in describing ground state of molecules is very satisfying.

Many exchange-correlation functionals have been developed and they can be divided into four main families:

1. **Local Density Approximation** (LDA) where exchange and correlation functionals depend on the 'local' value of ρ; LDA exchange functionals can be extended to the spin-polarized regime to treat systems including spin-polarization. Such functionals are also known as Local Spin Density Approximation (LSDA).

2. **Gradient Corrected Approximation** (GGA) which also includes the gradient of the density. A typical GGA exchange-correlation functional is BLYP. An improvement for GGA functionals is to consider also the second derivative of the density. Such functionals are named meta-GGA which are more accurate than GGA and their cost are similar. One typical example is M06-2X.

3. **Hybrid functionals** (also known as Adiabatic Connection Methods) which consider E_{xc} as a linear combination of the HF exchange and DFT exchange-correlation:

$$E_{xc} = (1-a)E_{xc}^{DFT} + aE_x^{HF} \tag{2.4}$$

a determines the contribution of HF exchange and DFT exchange-correlation: when $a = 0.5$ we have the so-called *half-and-half* (H&H) method. Typical functional of this family is the well-known B3LYP.

These three families of functionals do not include dispersion energy and they suffer from Self-Interaction error (SIE). These problems can be corrected by Long-Range corrected functionals.

4. **Long-Range corrected functionals (LRC)** which are an upgrade of the hybrid and GGA functionals. They separate electron-electron interactions into short-range and long-range with different dependency. Dispersive interactions are also included. Examples of functional from this family are CAM-B3LYP and ωB97X-D.

One weak point of DFT is its **single reference nature**, which can be translated into the **neglect of static correlation**, a term that rises from interaction between degenerate or quasi-degenerate configurations. Due to this absence, the wavefunction resulting from a restricted DFT (RDFT) calculation may be inappropriate in describing multiconfigurational systems such as diradicaloids.

A cost-effective alternative to RDFT that can include, to a certain extent, static correlation is to employ **Unrestricted DFT (UDFT) method**, analogously as using UHF instead of RHF for the study of H_2 dissociation. The unrestricted approach is based on the **release of a constraint,** that is to say paired α and β electrons must have the same spatial wavefunction. By doing so, α and β electrons are not forced to stay in the same space region of an orbital. As a consequence, two sets of orbitals, one for α electrons and the other for β electrons, are computed separately. The UDFT approach is suitable to describe open-shell species such as radical cations, radical anions and diradicals.

2.2 Time-dependent Restricted Density Functional Theory

Time-Dependent DFT (TD-DFT)[98] is the approach used to investigate excited states within DFT method. TD-DFT is based on the Runge-Gross Theorem[99], which is the time-dependent analogue of the first Hohenberg-Kohn theorem. It states that there exists an exact time-dependent electron density $\rho(r, t)$ which determines time-dependent potential $v(r, t)$, which consequently determines the time-dependent wavefunction $\Psi[\rho](r, t)$. The time-dependent KS equation (Eq 2.5), then, can be solved assuming a non-interacting system whose electron density $\rho_s(r, t)$ corresponds to $\rho(r, t)$ of the real interacting system. The non-interacting system is described by a single Slater determinant built up with single-electron orbitals $\phi_i(r, t)$.

$$i \frac{\partial}{\partial t} \phi_i(r,t) = \left(-\frac{1}{2} \nabla_i^2 + v(r,t) + \int \frac{\rho(r_{j,t})}{r_{ij}} dr_j + K_{XC}(r,t) \right) \phi_i(r,t) \qquad (2.5)$$

$K_{XC}(r, t)$ is known as Kernel and it includes exchange and correlation effects.

The first approximation made to solve the time-dependent KS equation is the so-called "adiabatic local density approximation" (ALDA). It assumes that the density varies slowly with

the time and consequently the original non-local time-dependent Kernel can be replaced with a time-independent local one. ALDA allows to use standard ground state exchange-correlation potentials in TD-DFT.

To obtain excitation energies and oscillator strengths, one can take the linear response (LR) of the time-dependent KS equation. This leads to the scheme of LR-TD-DFT.

Under small time-dependent perturbations (*e.g.*, electric field), the density $\rho(r, t)$ changes accordingly. $\rho(r, t)$ can be expanded in a series:

$$\rho(r, t) = \rho_0(r) + \rho_1(r, t) + \rho_2(r, t) + \cdots \qquad (2.6)$$

where $\rho_0(r)$ is the zero-th order density and it corresponds to the unperturbed ground state (GS); $\rho_n(r, t)$ is the *n*-th order density response. If the perturbation is small, we can safely consider the linear (first order) density response. Usually, one is more interested in the frequency-dependent response. This implies a Fourier's transformation of $\rho_1(r, t)$ to the frequency region. The Fourier-transformed linear response function of the density shows poles at the exact excitation energies of the system. Eigenfunctions of the time-dependent KS equation are then obtained through Casida's equation[100]:

$$\begin{bmatrix} A & B \\ B^* & A^* \end{bmatrix} \begin{bmatrix} X \\ Y \end{bmatrix} = \omega \begin{bmatrix} 1 & 0 \\ 0 & -1 \end{bmatrix} \begin{bmatrix} X \\ Y \end{bmatrix} \qquad (2.7)$$

A and **B** are matrices containing excitations and de-excitations, respectively; **X** and **Y** are coefficients for excitation and de-excitation, respectively. By simply assuming the off-diagonal matrices **B** and **B*** to zero, one arrives to the so-called Tamm-Dancoff approximation (TDA)[101].

TD-DFT is known to describe, with good accuracy, the excitation energies of low-lying excited states (typical error is within $0.1 - 0.5$ eV). One drawback of TD-DFT is to include only **one electron excitations**, while multiple excitations are not considered. Therefore, only states dominated by single electron excitations can be described. The other well-known drawback of TD-DFT regards states with charge-transfer character. In this case, the use of a LRC functional (e.g., CAM-B3LYP or ωB97X-D) can improve the description quality.

2.3 Spin Flip TD-DFT (SF-TDDFT)

The Spin flip (SF) approach was proposed by Krylov[102,103] in the early 2000s and implemented to TD-DFT method within the TDA by Shao, Head-Gordon and Krylov some years later[104]. In general, the SF approach, although based on a single reference configuration, is able to recover the lack of static correlation (*for instance: in diradicaloids*) thanks to the inclusion of some doubly excited configurations.

The starting point of the spin flip approach is a high- spin $\alpha\alpha$ triplet reference configuration (TRC) as can be seen in the center of Figure 2.1. By spin-flipping, *i.e.*, α→β one electron excitation and de-excitation, both excited and ground state configurations can be generated. Notably, there is a tight connection between the configurations included in the SF approach and the 2e-2o model introduced much earlier to describe diradicals. (More details on the 2e-2o

model will be given in Section 3.1.2).
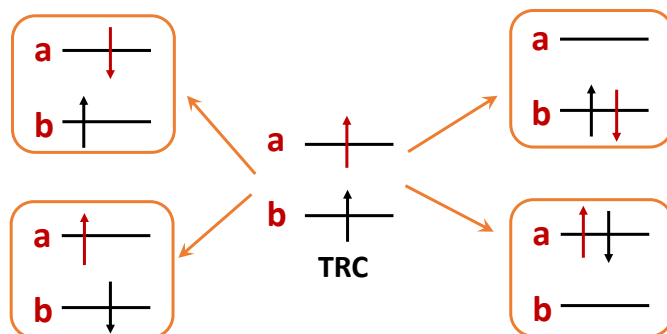
Figure 2.1. General scheme of configurations generated from spin-flipping starting from the high spin triplet reference configuration (TRC) in a 2e-2o space.

Figure 2.1 shows configurations generated in a 2e-2o scheme. Of course, by using a complete orbital and electron set, more excited configurations can be obtained. The four configurations listed in Figure 2.1 form a spin-complete set, thus only states dominated by these four configurations are spin-pure, other states will suffer from some degrees of spin contamination. From these four configurations the four states corresponding to the 2e-2o model (see Section 3.1.2) can be obtained, as listed by Krylov in her work [105].

From the combination of two right-hand side configurations of Figure 2.1, one obtains the ground and the DE states, whereas from the combination of the two left-hand side configurations, a pair of excited states, respectively with singlet and triplet spin multiplicities, is obtained.

SF-TDDFT calculations were carried out in this work within the collinear approximation. In this case, only Hartree-Fock exchange contributes to single electron spin-flipping excitations. According to Rinkevicius *et al.*[106]*,* TDA combined with the collinear approximation leads to underestimation of excited states dominated by the H→L excitation.

2.4 DFT multi-reference Configuration Interaction (DFT/MRCI)

DFT multi-reference configuration interaction (DFT/MRCI) was first proposed by Grimme and Waletzke in 1999[107]. The general idea behind this work is the combination of DFT and CI in order to take into account the dynamical electron correlation from DFT and to treat non-dynamical (static-correlation) effects with CI methods. Being a method that combines both dynamic and static electron correlation, DFT/MRCI is a powerful tool for the characterization of diradicaloids' excited states. The theory behind this method is well-explained in the two works of Grimme[107] and Marian [108], the latter further improved the original code and is the holder of the software. Here, I give only a brief introduction of this method.

DFT/MRCI adopts a semi-empirical Hamiltonian which is parameterized in combination with the BHLYP functional. The methodological idea behind DFT/MRCI is to employ DFT orbitals for constructing configuration state functions (CSFs) and to dress the MRCI matrix elements by appropriate portions of Coulomb and exchange-like integrals. In Grimme's original

work[107], different parameter sets were employed for singlet and triplet state calculations. More recently, a spin-invariant parameterization has been introduced by Marian's group[108]. The new parametrization incorporates less empiricism compared to the original formulation while preserving its computational efficiency. In this work, DFT/MRCI calculations are carried out using both sets of parameters hereafter labelled as original[107] and R2018[108].

The method has been shown to perform well in extended π-systems such as polyenes and polyacenes[109] where different doubly excited configurations are present in low-lying excited states and the DE state is one of them. The method is therefore suitable to describe both singly excited and DE states of singlet ground state diradicaloids.

One limitation of DFT/MRCI is related to the dimension of the basis functions: the upper limit of current version of DFT/MRCI is 1200 basis functions excluding frozen orbitals. Indicatively, the current program can handle up to molecules with ca. 116 atoms whose DFT molecular orbitals (MOs) are calculated with a small basis-set (*e.g.,* def2-SV(P)).

2.5 Complete active space self-consistent field (CASSCF) method

A solution to include static correlation is to use multiconfigurational self-consistent field (MCSCF) methods[96]. This name is given because the coefficients of molecular orbitals are optimized simultaneously with those of a combination of configurations. The wavefunction is written as linear combination of the ground and excited configurations:

$$\Psi^{MCSCF} = a_1 \Phi_{GS} + \sum_S a_2 \Phi_S + \sum_D a_3 \Phi_D + \cdots \qquad (2.8)$$

where Φ_{GS} represents the CSF of the GS and it usually corresponds to the ground configuration obtained with HF; Φ_S and Φ_D are CSFs formed as linear combination of singly excited and doubly excited Slater determinants generated from the ground (HF) one, respectively. Of course, higher order (triple, quadruple …) excited CSFs can be included in the MCSCF wavefunction. a_1, a_2 and a_3 (generally a_n) are general combination coefficients of each CSF. The resolution of Schrödinger's equation using a MCSCF wavefunction, as that for HF method, follows a variational principle and consists in an iterative procedure. During this procedure, both the combination coefficients (which account for the weight of each CSF) and molecular orbitals (MOs, which build up the CSFs) are optimized. Hence, MCSCF procedure can handle both multiple configurations and eventually the multi-determinantal character of a single configuration. Due to this particularity, it is almost impossible to think to include all electrons and all MOs of the system. In general, a very practical way to perform a MCSCF calculation is to select an active space, which is usually defined as *(m,n)* where *m* stands for the number of electrons and *n* the number of MOs (either occupied and virtual). When all possible arrangement of the selected *m* electrons in *n* MOs are considered in the MCSCF expansion, we have chosen a '**complete active space**' and this approach is known as **CASSCF** or simply **CAS**.

The choice of the active space is really tricky and crucial for a CASSCF calculation. Usually, it is a good practice to always inspect the occupation numbers of the active orbitals. A

general rule of thumb is to include, in the CAS space, all orbitals with occupation numbers between 1.98 and 0.02[96]. MO energies are no longer a selection rule since an 'active' orbital may have different occupation numbers in any given determinant, therefore MCSCF orbitals do not have unique eigenvalue associated with them.

CASSCF is a very robust method, but it still lacks dynamical correlation which is essential for the determination of a correct energy. A typical procedure to include dynamical correlation is to use multireference perturbation theory (MRPT) which uses the MCSCF (in this particular case CASSCF) wavefunction as the unperturbed wavefunction $\Psi^{(0)}$. Most multireference methods are limited to the second order perturbation and in this regard, the most popular methods are CASPT2[110,111] and NEVPT2 (*n*-electron valence state second order PT)[112–114]. These two methods mainly differ from the choice of the *zero*-th order Hamiltonian, as well as the definition of the perturbers and their corresponding energies[115]. While CASPT2 adopts the monoelectronic Møller-Plesset *zero*-th order Hamiltonian and excitation operators as perturbers, NEVPT2 adopts Dyall's Hamiltonian, which is bielectronic, and the perturbers are defined as state specific *n*-electron valence state[112].

2.6 Computational software used in this work

The majority of DFT-based quantum-chemical calculations were carried out with the Gaussian 16 package[116]. DFT/MRCI calculations were carried out both with the ORCA 4.0.1.2 [117], ORCA 5.0.1 packages[118] and the DFT/MRCI program [108]. CASSCF/NEVPT2 calculations were performed with ORCA 5.0.1 package[118]. Finally, SF-TDDFT calculations were accomplished with the GAMESS package[119].

Chapter 3: Conjugated Diradicals for applications in optoelectronics

This chapter encompasses the computational investigations carried out on several conjugated chromophores displaying diradical character.

Understanding the electronic structure of these peculiar molecular systems may be challenging because of their open shell character. Thus, the chapter starts with an introduction on their distinctive electronic structure based on a simple model including two electrons in two orbitals. This introduction helps understanding the nature of the lowest electronic states and the optical properties that depend on them. Specifically, a distinctive lowest lying double-exciton (DE) state is identified and shown to play a relevant role in the photo-physics of conjugated diradicals.

In the second part of this chapter, I summarize the results of several investigations concerning diradicaloids.

Section 3.2 describes an investigation on a series of quinoidal oligothiophenes of increasing conjugation length and diradical character[88]. The objective here is two-fold. On one hand we want to provide an interpretation of Raman and resonance Raman spectra measured by the group of Prof. Casado in Málaga, Spain. On the other hand, we wish to benchmark the most suitable functional/functionals by exploiting structure-property relationships: on one side the dependence of computed vibrational frequencies and intensities on geometry and, on the other side, the undeniable dependence of computed geometries on the chosen functional.

In Section 3.3, I supported computationally the experimental evidence of spin mobility in a π-conjugated diradical derivative of azobenzene[89] and investigated the connections between structural flexibility and spin delocalization and dynamics in the flexible backbone driven by thermal activation.

Conjugated diradicals are characterized by distinctive photophysical properties, among which a low-lying excited state dominated by a doubly excited configuration. A reliable prediction of the excited states and excitation energies is challenging because of correlation effects and in these cases multi-reference methods that ensure the appropriate level of electron correlation would be desirable. However, such high level approaches cannot be applied to large conjugated systems. In Section 3.4, I therefore discuss cost-effective DFT-based computational approaches that can capture, with suitable accuracy, the excitation energies of these low-lying electronic states[90,91].

Finally, another uncommon but very intriguing consequence of the proximity of the DE state is the possibility of mixing with the singly-excited (SE) state which can lead to the emission from the DE state. In this context, in Section 3.5 I discuss the unusual luminescence properties of a Thiele derivative, interpreted through quantum-chemical calculations indicating that its fluorescence arises from the low-lying dark DE zwitterionic state, typically found at low excitation energies in diradicaloids. Such state acquires dipole moment and intensity by state mixing *via* twisting around the strongly elongated exocyclic CC bonds of the excited *p*-quinodimethane (*p*-QDM) core.

During my PhD, I had the chance to study most of these phenomena thanks to collaborations with experimental groups from the Universities of Málaga (Spain) and Bari (Italy).

3.1 Electronic structure and specific computational approaches for conjugated diradicals

3.1.1 Localized and delocalized diradicals

According to the IUPAC definition, the word "diradical" refers to molecular species having two unpaired electrons, in which at least two electronic states with different multiplicities (an electron paired singlet state or an electron unpaired triplet state) can be identified[120]. A "diradicaloid", instead, means "diradical-like" and it is referred to "species in which two radical centers interact significantly"[121]. A diradicaloid is, thus, a system in-between pure open-shell diradical and pure closed-shell molecules[86].

According to Abe's scheme[63], diradical molecules can be divided into two major classes (see also Figure 2 of Ref. [63]): **localized** and **delocalized**. The latter, then, can be divided into Kekulé, non Kekulé and antiaromatic molecules. Different classes of diradicals have different properties, which, in turn, influence the possible applications of these molecules. The most interesting class of diradicals for optoelectronic applications is represented by "**Kekulé-type**" **delocalized diradicals.** The prototype of this class of molecule is *para*-quinodimethane (*p*-QDM) as shown in figure below. In fact, polycyclic aromatic hydrocarbons (PAHs) including at least one benzene ring could be seen as *p*-QDM derivatives.
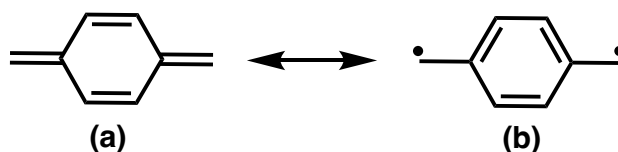
Figure 3.1. Chemical structure of *p*-QDM and its resonance form.

They are characterized by several resonance forms, one of which is closed-shell **quinoidal** (Figure 3.1(a)) and at least one open-shell **aromatic** (Figure 3.1(b)). The presence of one or multiple aromatic rings in diradical resonance formulas implies that most Kekulé-type molecules exhibit a stable open-shell ground electronic state owing to the recovery of aromaticity, in accordance with Clar's sextet rule [122].

A problem, from the experimental point of view, is the stabilization of diradical molecules using synthetic strategies which, in turn, prevents their characterizations. Open-shell species (not including O_2) are generally known to be reactive. Nevertheless, thanks to new synthetic strategies in recent years, for instance *cross-conjugation*[123,124], a large number of conjugated chromophores with open-shell singlet ground state have been rationally designed and synthesized[125–129]. All these chromophores display varying diradical character, and some examples include quinoidal oligothiophenes[130–132], tetracyano quinodimethane derivatives of phenylene-vinylenes[133], diphenalenyl compounds[134], several different flavors of PAHs[135–140], heteroacenes[141–144], indeno-derivatives[123,128,145–147], rylene ribbons[148,149], and their tetracyano derivatives[150,151]. The major interest on this class of molecules, as already mentioned, is related to their potential use in optoelectronics and spintronics thanks to their distinctive properties.

In the following, I will introduce some fundamental concepts concerning the electronic structure of diradicals, first by referring to the 2e-2o model applied to the dissociation of the H_2 molecule and then by adapting the derivation to a general homosymmetric diradical molecule.

3.1.2 Two-electrons in two-orbitals model to describe a diradical

A simple way to imagine diradical is to have two unpaired electrons located in two degenerate or nearly degenerate orbitals (2e-2o). One could take the stretched hydrogen molecule (H_2) as an example (Figure 3.2). In the dissociation limit, the two MOs that host two unpaired electrons coincide with the *s* orbitals of each H. Each electron behaves independently and we have a perfect diradical. When the interaction comes to play, for instance increasing of the overlap integral (S_{AB}), as well as enlarging of the energy gap between two orbitals (ΔE_{AB}), one orbital will be more stabilized than the other leading to a pair of bonding/anti-bonding MOs.
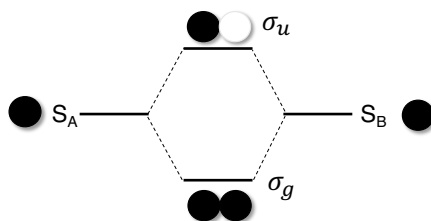
Figure 3.2. Molecular orbital diagram of hydrogen molecule.

On the other hand, the size of interaction could also be measured by the two-electron

exchange integral (K). In fact, the correct description for the lowest states of the 2e-2o system is a triplet-singlet pair (Figure 3.3) whose splitting is related to K.
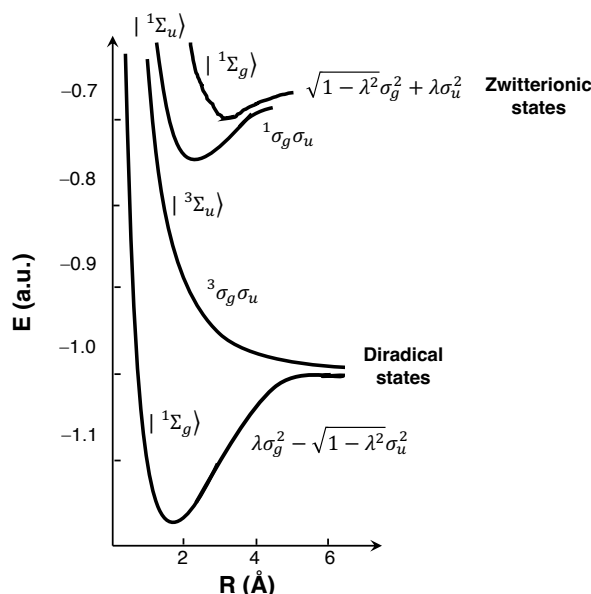
Figure 3.3. Four lowest-lying electronic states of H_2. Adapted from Salem's [84] work.

Taking H_2 as an example (Figures 3.2 and 3.3), the four configurations that can be generated are:
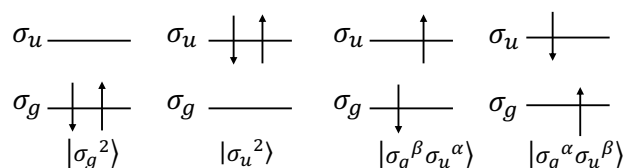
Figure 3.4. The four configurations required for the full configuration interaction for H_2.

The first two configurations in Figure 3.4 have singlet spin and they are the appropriate representations, respectively, of the ground state (GS) and the doubly excited state of H_2 in the equilibrium region, where S_{AB} is still strong. We can write the GS wavefunction, regardless of normalization factor, and expand it in terms of atomic orbitals as follow:

$$\Psi_{GS} = \left|\sigma_g^2\right\rangle = [S_A(1)S_B(2) + S_B(1)S_A(2)] + [S_A(1)S_A(2) + S_B(1)S_B(2)] \tag{3.1}$$

The black-colored term in Eq. 3.1 describes a **covalent contribution** to the GS wavefunction: two electrons are equally distributed into two different orbitals; while the red-colored term shows the **ionic contribution** and it is responsible for the quick energy rise of GS when the overlap S_{AB} decreases [84]. This effect can be seen, for instance, from the dissociation curve of H_2 using RHF wavefunction[152].

The erroneous trend can be corrected by combining $\left|\sigma_g^2\right\rangle$ and $\left|\sigma_u^2\right\rangle$ with negative sign. In fact, $\left|\sigma_u^2\right\rangle$ can be expressed, in terms of atomic orbitals and regardless of normalization factor, as:

$$\left|\sigma_u^2\right\rangle = -[S_A(1)S_B(2) + S_B(1)S_A(2)] + [S_A(1)S_A(2) + S_B(1)S_B(2)] \tag{3.2}$$

The corrected wavefunction for the GS, is:

$$\Psi_{GS} = \lambda \, |\sigma_g{}^2\rangle - \sqrt{1-\lambda^2} \, |\sigma_u{}^2\rangle \tag{3.3}$$

It should be noticed that after the mixing, a small amount of ionic contribution still remains leaving the nature of the wavefunction as **covalent + (ionic)**.

Analogously, the correct wavefunction of the doubly excited (*de*) state should be the other combination of the aforementioned configurations:

$$\Psi_{de} = \sqrt{1-\lambda^2} \, |\sigma_g{}^2\rangle + \lambda |\sigma_u{}^2\rangle \tag{3.4}$$

The positive combination, contrarily, enhances the ionic contribution conferring a dominant ionic character to the doubly excited state. The overall nature of this state is then **ionic + (covalent).**

Finally, the combination of the remaining two configurations in Figure 3.4 gives rise to one triplet and one singlet with, respectively, covalent and ionic character:

$$\Psi_T = \frac{1}{\sqrt{2}}(|\sigma_g{}^\alpha \sigma_u{}^\beta\rangle + |\sigma_g{}^\beta \sigma_u{}^\alpha\rangle) \tag{3.5}$$

$$\Psi_S = \frac{1}{\sqrt{2}}(|\sigma_g{}^\alpha \sigma_u{}^\beta\rangle - |\sigma_g{}^\beta \sigma_u{}^\alpha\rangle) \tag{3.6}$$

These derivations can be extrapolated to any diradical and therefore, a common feature for diradicals, is thus, to have a singlet-triplet low-lying pair of diradical states with *covalent* nature and a pair of *zwitterionic* singlet states with ionic or dominantly ionic character (Figure 3.3).

Thus, Eq. 3.3 to 3.6 can be adapted to a general homosymmetric diradical by replacing σ_g with HOMO (H) and σ_u with LUMO (L).

Because most synthetized conjugated diradicals have a singlet ground state, we neglect, for now, the triplet state in the 2e-2o model. The wavefunctions of diradicaloids can be written:

$$\Psi_{GS} = \lambda \, |\text{H}^2\rangle - \sqrt{1-\lambda^2} \, |L^2\rangle \tag{3.7}$$

$$\Psi_{DE} = \sqrt{1-\lambda^2} \, |\text{H}^2\rangle + \lambda |L^2\rangle \tag{3.8}$$

$$\Psi_{SE} = \frac{1}{\sqrt{2}}(|H^\alpha L^\beta\rangle - |H^\beta L^\alpha\rangle) = \frac{1}{2}(|H\bar{L}\rangle + |L\bar{H}\rangle) \tag{3.9}$$

The GS is dominated by $|H^2\rangle$ corrected with $|L^2\rangle$. The last configuration implies that for a correct description of this state, a multiconfigurational method is needed. Regarding the two singlet excited states, one is dominated by H→L one electron excitation configuration and it is strongly allowed (or **bright**) spectroscopically. This state will be called as SE state hereafter. The second one is dominated by [H,H] → [L,L] doubly excited configuration, hereafter named as the "**double-exciton state**" (DE). For centrosymmetric molecules, this state is one-photon forbidden and two-photon allowed. On one hand, as long as the DE state is really high in energy, it should not bother the one-photon spectroscopic properties of diradicals. Within the simple 2e-2o model, in fact, this state is higher in energy with respect to SE. However, the vicinity of

SE and DE states can already be appreciated from the potential energy curves of H_2 at the dissociation limit, considered as a perfect diradical system (Figure 3.3). Thus, it can be expected that the DE state can become the lowest lying excited state in conjugated diradicals featuring large diradical character. In addition, diradicals of real interest contain more than two electrons and orbitals, and therefore electron correlation can also contribute to lower the DE state. This distinctive property of conjugated diradicals has been shown for the first time[66] in the laboratory where I have done my PhD. More precisely, a combined theoretical and experimental work revealed that for *quinoidal oligothiophenes* exhibiting remarkable diradical characters, the DE state of A_g symmetry becomes the **lowest excited state**[66]. The presence of the low-lying DE state was also well known in polyenes[153] whose diradical character has been recognized[154]. More recently, it has also been proposed to be the lowest singlet excited state in heptacene[155] from MCCEPA level calculations based on a CASSCF(6,6) wavefunction and in a series of different conjugated diradicaloids at TD-UDFT and SF-TDDFT levels[67]. Indeed, organic diradicaloids are usually not fluorescent[86]. Yet, the DE state can be vibronically activated and appears as weak progression on the red side of the main absorption band[66,130,155]. Recently it has been shown that such state can be considered as the "*fingerprint*" of conjugated diradicals[66,67].

3.1.3 Unrestricted Density Functional Theory and diradicals

In Chapter 2 we have introduced the UDFT approach. Generally, for system showing relevant diradical character, the unrestricted wavefunction will lead to a more stable solution at lower energy compared to RDFT and will be characterized by **localized frontier molecular orbitals (FMOs)**, namely H and L (Figure 3.5). It is interesting to observe that, within the same FMO, α and β electrons occupy different spatial space. Indeed, orbital localization leads to symmetry-breaking (BS) of the orbital itself. Therefore, in this work, we generally indicate the equilibrium structure determined from a UDFT calculation as **BS geometry,** although it should be clear that the symmetry of the molecule is maintained and that BS refers simply to the nature of the unrestricted orbitals.

RDFT   **UDFT**

(a)   (b)

L   L (α)   L (β)

H   H (α)   H (β)
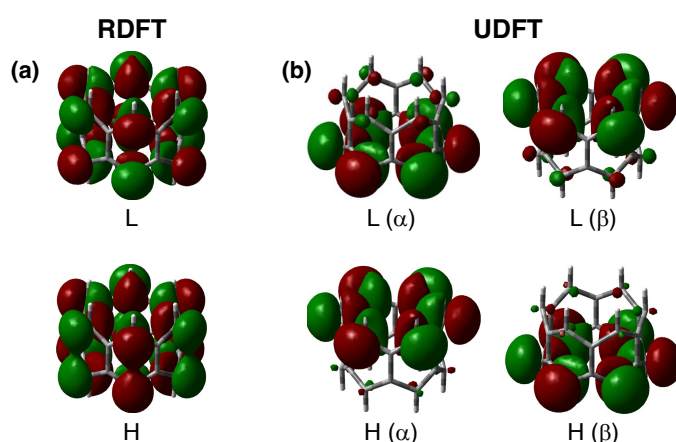
Figure 3.5. Frontier molecular orbitals of [6]-cyclacene computed with (a) RB3LYP/6-31G* and (b) UB3LYP/6-31G* levels of theory.

Note that the unrestricted solution will become lower than the restricted one only when

the diradical character is significant. Thus, a BS solution at lower energy will not be found for molecules displaying small diradical character. Taking H_2 as an example, RHF still describes quite well the equilibrium region, where the molecule is a closed-shell species, or distances not too far away from the equilibrium region, namely where H_2 is still a closed-shell species to a good approximation. With reference to the wavefunctions in Figure 3.3, the need for an unrestricted approach becomes relevant when the GS wavefunction (Eq. 3.3) starts to mix significantly with the doubly excited configuration. Such mixing indicates that a single determinant is insufficient and, if we want to keep a single determinant wavefunction, the only possibility is to relax a constraint such that the wavefunction becomes more flexible and the energy can lower. By relaxing the constraint of same spatial occupation of α and β electrons, the GS wavefunction is more flexible and suitable to describe the two unpaired electrons.

On the contrary, when the only solution is the restricted one, the closed-shell (CS) configuration gives a good representation of the GS wavefunction. In this work, the equilibrium structures determined from a standard restricted DFT calculation will be, therefore, labeled as **CS geometry** or simply CS.

3.1.3.1 The ground state wavefunction of a singlet open-shell from UDFT

Following Yamaguchi's [156] and Nakano's [76] previous works, the BS H and L orbitals can be defined as linear combinations of delocalized CS orbitals and they are related through the rotation angle θ:

$$H_\alpha = \varphi^\alpha_{HOMO} = \cos\theta \cdot H_{CS} + \sin\theta \cdot L_{CS}$$

$$H_\beta = \varphi^\beta_{HOMO} = \cos\theta \cdot H_{CS} - \sin\theta \cdot L_{CS}$$

$$L_\alpha = \varphi^\alpha_{LUMO} = \sin\theta \cdot H_{CS} - \cos\theta \cdot L_{CS} \tag{3.10}$$

$$L_\beta = \varphi^\beta_{LUMO} = \sin\theta \cdot H_{CS} + \cos\theta \cdot L_{CS}$$

θ varies from 0°, when BS and CS orbitals coincide, to 45°, when the BS orbitals are perfect mixing of H_{CS} and L_{CS}, therefore fully localized.

The Slater determinant that corresponds to the unrestricted GS wavefunction is defined as[76,91]:

$$\psi^{U(GS)} = \left| \varphi^\alpha_{HOMO} \varphi^\beta_{HOMO} \right\rangle$$

$$= \frac{1}{\sqrt{2}} \left[\varphi^\alpha_{HOMO}(1) \varphi^\beta_{HOMO}(2) - \varphi^\beta_{HOMO}(1) \varphi^\alpha_{HOMO}(2) \right] \tag{3.11}$$

Substituting Eq. 3.10 into Eq. 3.11, we get:

$$\psi^{U(GS)} = C_{GR} |H_{CS}\bar{H}_{CS}\rangle + C_D |L_{CS}\bar{L}_{CS}\rangle$$

$$+ C_T \frac{1}{\sqrt{2}} (|H_{CS}\bar{L}_{CS}\rangle - |L_{CS}\bar{H}_{CS}\rangle) \tag{3.12}$$

where $C_{GR} = cos^2\theta$, $C_D = -(sin^2\theta)$ and $C_T = -sin\theta cos\theta$ are combination coefficients for the CS GS determinant $|H_{CS}\bar{H}_{CS}\rangle$, the doubly excited determinant $|L_{CS}\bar{L}_{CS}\rangle$ and the combination of two singly excited determinants $\frac{1}{\sqrt{2}}(|H_{CS}\bar{L}_{CS}\rangle - |L_{CS}\bar{H}_{CS}\rangle)$, respectively. The latter owns triplet multiplicity and accounts for ***spin contamination*** to the unrestricted GS wavefunction. In fact, the price to pay for using an unrestricted approach, in diradicals, is spin contamination: the spin part of the wavefunction ceases to be eigenfunction of the spin operator.

3.1.4 Time-Dependent Unrestricted Density Functional Theory and the 2e-2o model

Time-Dependent UDFT (TD-UDFT), in this work, indicates the execution of TD-DFT calculations starting from a spin-paired open-shell reference configuration, obtained at UDFT level and characterized by BS orbitals. In a recent work by the group where I did my PhD, it has been shown that with this approach, the low-lying state of a conjugated diradical characterized by the double excitation (*e.g.,* the DE state) can be reasonably well described when the diradical character is significant[67].

As stated in Section 3.1.2, four configurations and consequently four states can be generated from the 2e-2o space. The DE state emerges as one of the two singlet excited states (Figure 3.6). Following Michl's pioneering work[85] we can consider two limiting cases: a delocalized basis set (a, b) and a localized basis set (A, B). Using the same notation, we can write the four configurations with paired spins for the two sets of orbitals:

In terms of delocalized basis, we have: $a(1)a(2) = a^2$, $b(1)b(2) = b^2$, $a(1)b(2) = ab$ and $b(1)a(2) = ba$; Note that the wavefunctions indicated in Figure 3.6 essentially correspond to Eq. 3.7 - 3.9 when a = H and b = L.

In terms of localized basis: $A(1)A(2) = A^2$, $B(1)B(2) = B^2$, $A(1)B(2) = AB$ and $B(1)A(2) = BA$.
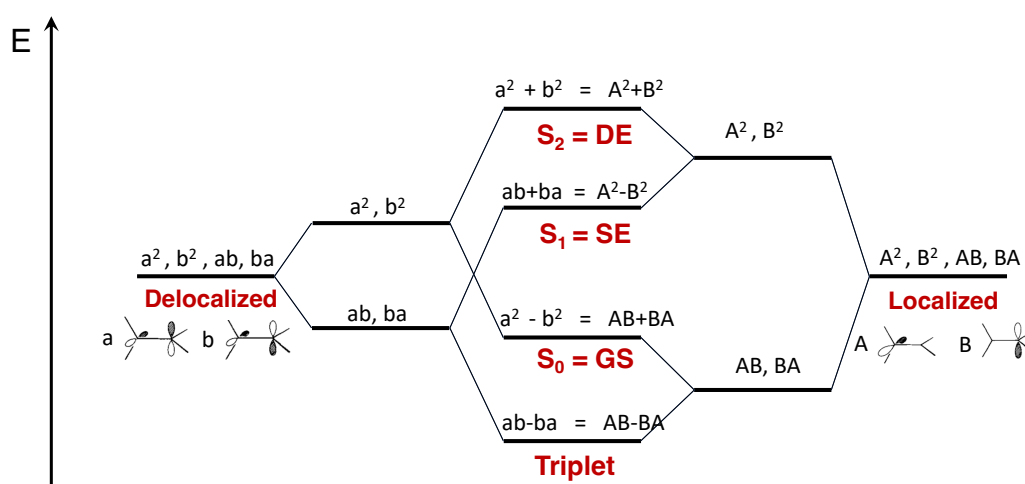
Figure 3.6. Schematic representation of the four electronic states generated from the 2e-2o model. Configurations and consequently wavefunctions are expressed both in terms of delocalized (left) and localized (right) orbital basis.

Configuration interaction (CI) leads to the formation of one triplet state and three singlet states as already noted in Section 3.1.2. Ignoring the triplet state, the spatial wavefunctions of

the three singlet states, for perfect homosymmetric diradicals, are expressed as in Ref. [85]. These equations correspond essentially to Eq.3.7 - 3.9, the difference being related to the fact that the following are derived for a perfect diradical and not for a diradicaloid:

$$S_0 = \psi_0 = b^2 - a^2 = AB + BA$$
$$S_1 = \psi_1 = ab + ba = A^2 - B^2 \quad (3.13)$$
$$S_2 = \psi_2 = a^2 + b^2 = A^2 + B^2$$

Michl showed that ψ_2 is always the doubly-excited state whether localized (A & B) or delocalized (a & b) orbitals are used. Within the 2e-2o model, ψ_2 is always above ψ_1, the singly-excited state espressed as $ab + ba$ in the delocalized basis.

Section 3.1.3 mentioned that one consequence of adopting UDFT is the localization of electronic densities in two FMOs. Interesting to note that H_α is similar to L_β and $H\beta$ is similar to L_α (Figure 3.5). Indeed, from the closed-shell viewpoint, an orbital can host two electrons with different spins, this means that a pair of localized orbitals with the same space region is able to hold either α electron or β electron. Since two orbitals from the same precursor must be localized in two different space regions, $H\alpha$ needs to be similar to $L\beta$ and $H\beta$ similar to $L\alpha$. As we showed in the previous section, such similarity becomes exact only for a perfect diradical (or $\theta = 45°$ in Eq. 3.10 in Section 3.1.3.1).

Following the assignment of Michl and noting that we can label H_α as B and H_β as A, L_α must be A and L_β is B for strong diradical character and orbital localization. The four configurations in terms of localized FMOs are shown in Figure 3.7.
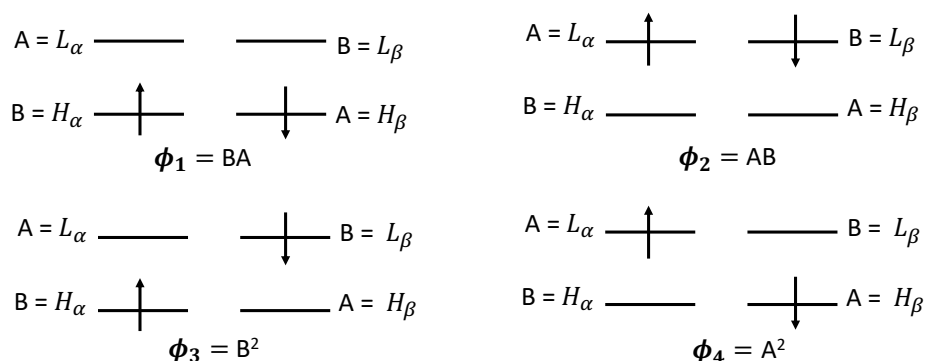
Figure 3.7. Four configurations generated in the 2e-2o model in terms of localized orbitals.

Note that now, the two doubly-excited configurations (A^2 and B^2) can be generated from a **one-electron excitation** from the ground configuration expressed in terms of localized orbitals (ϕ_1): A^2 can be expressed as $H_\alpha \rightarrow L_\alpha$ and B^2 as $H_\beta \rightarrow L_\beta$. Therefore, from a TD-UDFT calculation, that is a TD-DFT calculations based on the unrestricted BS ground configuration, the DE state ($A^2 + B^2$) can be extracted[67] as the positive combination of $H_\alpha \rightarrow L_\alpha$ and $H_\beta \rightarrow L_\beta$. Also, the SE state can be obtained from TD-UDFT calculation: it is the negative combination of the aforementioned two excitations.

3.1.4.1 Applicability of TD-UDFT to the DE state

Now, we shall derive the expression for the DE state in the TD-UDFT approach and recognize the limits of this approach[91].

In terms of Slater determinants (see also Figure 3.7), the wavefunction of the DE state in TD-UDFT can be expressed as:

$$\psi^{DE} = \frac{1}{\sqrt{2}}\left\{\left|\varphi^{\alpha}_{LUMO}\varphi^{\beta}_{HOMO}\right\rangle + \left|\varphi^{\alpha}_{HOMO}\varphi^{\beta}_{LUMO}\right\rangle\right\}$$

$$= \frac{1}{2}\left[\varphi^{\alpha}_{LUMO}(1)\varphi^{\beta}_{HOMO}(2) - \varphi^{\beta}_{HOMO}(1)\varphi^{\alpha}_{LUMO}(2)\right] \qquad (3.14)$$

$$+ \frac{1}{2}\left[\varphi^{\alpha}_{HOMO}(1)\varphi^{\beta}_{LUMO}(2) - \varphi^{\beta}_{LUMO}(1)\varphi^{\alpha}_{HOMO}(2)\right]$$

Substituting Eq.3.10 into 3.14 we get:

$$\psi^{DE} = D_{GR}|H_{CS}\bar{H}_{CS}\rangle + D_D|L_{CS}\bar{L}_{CS}\rangle$$

$$+ D_T \frac{1}{\sqrt{2}}(|H_{CS}\bar{L}_{CS}\rangle - |L_{CS}\bar{H}_{CS}\rangle) \qquad (3.15)$$

D_{GR} and D_D are combination coefficients for the ground and doubly excited configurations, respectively. They have the same value: $\frac{\sin(2\theta)}{\sqrt{2}}$. $D_T = \cos(2\theta)$ accounts for the contribution of triplet spin to the DE state. Hence, the DE state in the TD-UDFT approach, as well as the GS in UDFT, suffers from some degrees of spin contamination which could be a relevant issue. Generally, when spin contamination is large, the wavefunction is less reliable. The magnitude of spin contamination in the DE wavefunction can be appreciated by plotting the contribution of the triplet spin component (*i.e.* $D_T{}^2$) as function of θ.
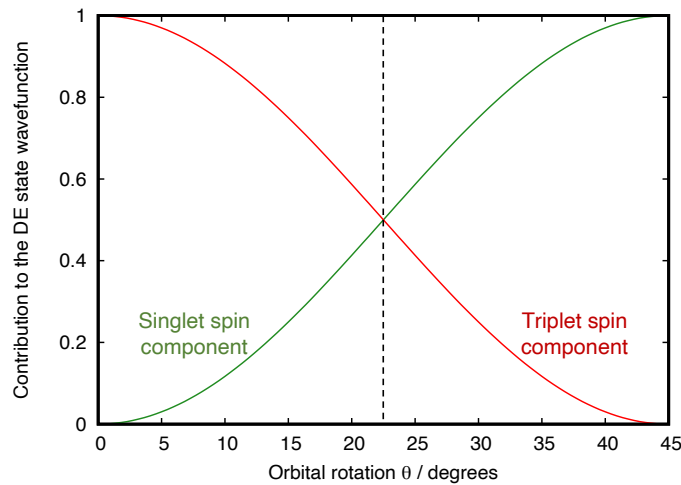
Figure 3.8. Contribution of the singlet spin (considered as $D_{GR}{}^2 + D_D{}^2$) and triplet spin components to the DE state wavefunction as function of the rotation angle θ.

At 0°, $D_T{}^2 = 1$, the state is a pure triplet state. From *ca.* 5° to *ca.* 22.5° (black dashed line in Figure 3.8), the triplet spin component dominates. In this region, the DE state wavefunction

is strongly spin contaminated and the TD-UDFT description is incorrect. At 22.5°, we have an equal contribution of the triplet spin component and the singlet one, which becomes dominant when $\theta > 22.5°$. In this region, the triplet spin component tends to decrease with increasing θ value. When $\theta = 45°$ (fully localized BS orbitals), the DE state is a pure singlet spin state. Therefore, TD-UDFT is applicable when θ is in-between 22.5° and 45°, when BS orbitals are well-localized[91]. We will see, in the following, that the diradical character can be expressed as function of θ. Thus, the DE state can be predicted by TD-UDFT with good quality for molecules showing appreciable diradical character. For molecules exhibiting small diradical character, TD-UDFT's results can be unreliable due to the dominant triplet contribution.

Other drawback of TD-UDFT is that the doubly excited and the ground Slater determinants have equal contributions to the DE state (Eq. 3.15) independently from the value of θ. This might be relevant in some molecules where *e.g.,* the *real* contributions of the doubly excited and the ground determinant are very different.

3.1.5 Descriptors of diradical character

In this work, the diradical character of diradicaloids is evaluated mainly through two descriptors: the y_0 parameter and the N_{FOD} value.

The y_0 parameter, in the spin-unrestricted single-determinant formalism, can be determined in the spin-projection scheme (*i.e.* eliminating the triplet contribution in Eq. 3.12 keeping the ratio C_{GR}/C_D) as [76,156]:

$$y_0^{PUnrestricted} = 1 - \frac{2T_0}{1 + T_0^2} \tag{3.16}$$

where T_0 is calculated as:

$$T_0 = \frac{n_{HONO} - n_{LUNO}}{2} \tag{3.17}$$

n is the occupation number of the frontier natural orbitals.

y_0 is a number between 0 (indicating a pure closed-shell system) and 1 (a pure diradical). In this work, Eq 3.16 and 3.17 are employed to determine both y_0^{PUHF} and $y_0^{PUB3LYP}$.

y_0 is directly related to θ, the rotation angle between CS and BS MOs. Indeed, in the spin-projected scheme[76], y_0 can be defined as $2\left(C_D/\sqrt{1 - C_T^2}\right)^2$ and by expressing C_D and C_T in terms of θ one obtains:

$$y_0 = 2(\sin^4 \theta)/(1 - 2(\sin^2 \theta)(\cos^2 \theta)) \tag{3.18}$$

θ can be readily obtained from the BS frontier orbitals expressed as linear combination of the CS frontier orbitals (Eq. 3.10) and can be used as a diradical character indicator. Indeed, the larger is θ, the larger is the diradical character y_0 (Figure 3.9).
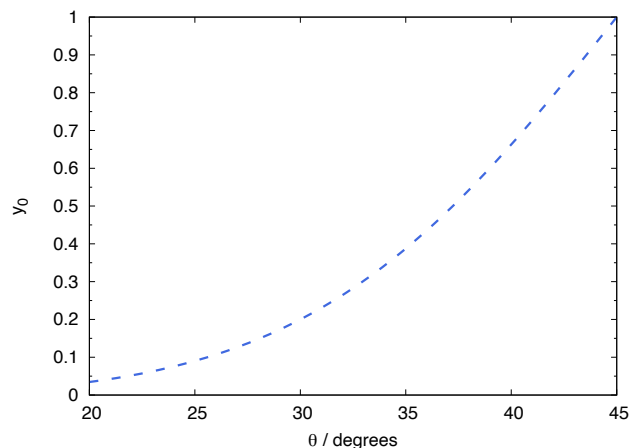
Figure 3.9. Relation between diradical parameter y_0 and the rotation angle θ.

On the other hand, the N_{FOD} descriptor is a number based on fractional orbital density (FOD). It was proposed by Grimme and Hansen[157] in 2015. The key point of their assumption is the fractional orbital density function (ρ^{FOD}):

$$\rho^{FOD}(r) = \sum_i^N (\delta_1 - \delta_2 f_i)|\varphi_i(r)|^2 \tag{3.19}$$

where δ_1 and δ_2 are two constants and they are set in the way that only fractional occupied orbitals are taken into account; φ_i are molecular spin orbitals, and f_i are the fractional orbital numbers ($0 \leq f_i \leq 1$) determined by the Fermi-Dirac distribution:

$$f_i = \frac{1}{e^{(\varepsilon_i - \varepsilon_F)/KT_{el}} + 1} \tag{3.20}$$

ρ^{FOD} is strictly linked to the temperature. In fact, finite-temperature (FT) DFT approach is necessary to compute it. By integrating ρ^{FOD} over all space, N_{FOD} can be obtained. As mentioned in Ref. [157], N_{FOD} considers the so-called "hot electrons" (correlated electrons) and acts like a measure of the static electron correlation. A later work by Bauer *et al.*[158] demonstrated a linear relationship between N_{FOD} and y_0.

N_{FOD} is computed with the ORCA 4.0.1.2 package[117] with the default setting (TPSS/def2-TZVP level with T_{el}=5000K).

3.2 Raman and resonance Raman spectra of Cyano-Ester quinoidal oligothiophenes

Raman spectroscopy is a powerful tool to experimentally characterize conjugated molecules. Indeed, Raman spectroscopy, combined with results from computational studies, has been the technique of choice to study molecular and electronic structures of π-conjugated molecules[131,132,159–166]. In particular, in the case of quinoidal oligomers, Raman spectroscopy proved to be an important source of information from which insight on the molecular structure can be obtained. To mention just one example, the most-intense Raman band in oligothiophenes is due to a collective mode dominated by the so-called *effective conjugation coordinate* (ECC), which involves the out-of-phase stretching between adjacent C-C and C=C bonds along the conjugation core[166–168]. This mode corresponds also to the out-of-phase C-C/C=C vibration responsible for the Franck-Condon activity in the electronic spectra of oligothiophenes[169].

Modes dominated by the ECC coordinate are sensitive to geometry change. In fact, it has been shown that the evolution of the most intense Raman band recorded for a series of quinoidal oligothiophenes, with increasing oligomer length, drastically differs from that recorded for a series of aromatic oligothiophenes. While for the latter, the frequency of the mode dominated by ECC coordinate downshifts with increasing oligomer length; in the quinoidal oligothiophene series, it downshifts from dimer to tetramer[131] with tetramer behaving as an inflection point after which the active frequency upshifts as a result of the aromatization of the ground electronic state.

From the computational point of view, the determination of a suitable ground state geometry, representative of the real molecular structure, is of prior importance. Generally, ground state structural information of conjugated diradicals, with small to moderate diradical character, derived by Raman investigations are well supported by computed Raman spectra simulated at the ground state equilibrium structures[131,132,161–163,170]. The correct prediction of Raman intensities for conjugated diradicals, especially for large diradical character, is not, however, a trivial problem. The reason is that the quality of computed Raman activities is tightly connected with the quality of computed equilibrium structures since small geometry deviations will imply remarkable differences in computed vibrational frequencies and Raman activities[132].

Within the single-reference DFT method, CS geometries are not suitable for molecules showing remarkable diradical characters since a more stable BS structure can be found and provides a more realistic description of diradical molecules. However, the predicted BS geometries not always provide satisfactory results because large diradical characters usually demand for multireference highly correlated wavefunctions owing to the need to include static correlation[132,171]. Single-reference methods such as UDFT may lead to an unbalanced prediction of the open-shell structure, a result that may be influenced also by the functional chosen. Thus, simulating Raman spectra for diradicaloids is not easy using single-reference methods due to the lack of electron correlation. However, a recent work [170] showed that with an *educated* structure, obtained by displacing the geometry along the predicted BS-CS geometry change, experimental Raman spectra can be correctly reproduced by DFT/UDFT approaches for long rylenes. Thus, at DFT level, in order to predict the evolution of Raman

spectra for increasing diradical character, an assessment of the quality of RDFT/UDFT computed geometries is required for conjugated diradicaloids. Furthermore, ad hoc adjustments of predicted geometries might be required to compensate for the missing of static electron correlation at DFT level.

In this work, the assessment of the quality of simulated Raman spectra computed for a library of different geometries obtained for each of the three oligothiophenes **EsQ2**, **EsQ3** and **EsQ4** (Figure 3.10) is given by comparing computed and observed Raman spectra.

In addition, we also investigate resonance Raman spectra. When the laser light is in resonance or pre-resonance with one or more specific **electronic transitions**[172–174], intensities of some Raman bands can be enhanced. Singlet diradicaloids own two low-lying singlet excited states: the SE state, dominated by the strongly allowed H → L single excitation and the dark DE state, dominated by the H,H → L,L double excitation[67,82,90,91,132,171]. Due to the presence of these two states, Raman intensities may be modulated not only by resonance with the SE state, but also by the proximity of the less active DE state.

3.2.1 Cyano-ester quinoidal oligothiophenes studied in this work

Quinoidal oligothiophene is a well-known class of diradicaloids. Molecules belonging to this class display increasing diradical character with the extension of the conjugated core. They have been extensively investigated experimentally, owing to their potential applications in the field of organic optoelectronics as *e.g.* electron-conducting or ambipolar materials. In this regard, it has been shown that the family of tetracyanoquinodimethane (TCNQ) quinoidal oligothiophenes is endowed with remarkable amphoteric redox behavior[130,159,175–182].

In this study, we considered a series of cyano-ester quinoidal oligothiophenes (Figure 3.10a) bearing cyano (-CN) and ester (-COOC$_8$H$_{17}$) substituents as terminal groups[183]. The three oligomers are labeled as **EsQ2**, **EsQ3** and **EsQ4** because of the ester (Es) substituents and quinoidal (Q) structure. The numbers in molecule names indicate the number of thiophene units.
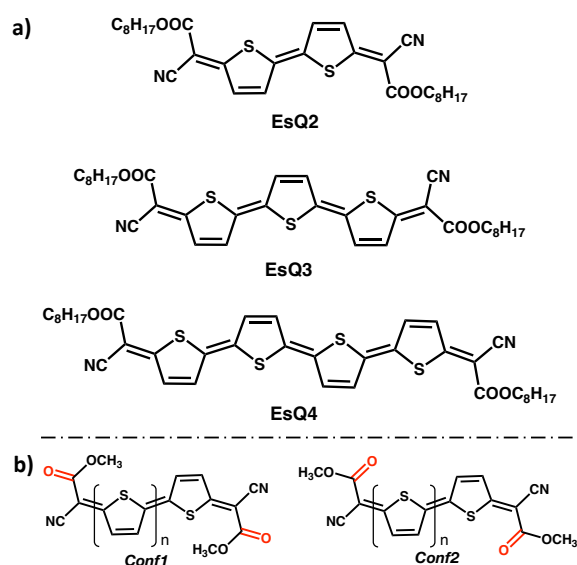
Figure 3.10. Cyano-ester oligothiophenes investigated in this work. a). Chemical structures of **EsQ2**, **EsQ3** and **EsQ4**; b) two conformers considered. Figures reused from Ref. [88].

The three oligomers were characterized by UV-Vis-NIR absorption and Raman spectroscopy measurements at different excitation wavelengths. For the calculations, model systems of the real molecules, in which long alkyl chains of the ester groups are replaced by methyl groups, are considered (Figure 3.10b). As mentioned in previous section, the most active vibrations in oligothiophenes involve the conjugated skeleton. The simplification made will leave untouched the molecular moiety and the π–electronic structure responsible for Raman activity. Meanwhile, the number of Raman active vibrational frequencies to be computed is reduced significantly.

The terminal ester groups are flexible, thus for a more precise interpretation of Raman spectra it is necessary to consider possible conformers. There are two in our case: *Conf1* and *Conf2* (Figure 3.10b) characterized by different orientations of the ester groups with respect to the nearby thiophene ring. The remarkably larger stabilization of *Conf 2* can be traced back to the stronger through space electrostatic interaction between sulfur and the carbonyl oxygen. Hereafter, we will therefore consider only *Conf 2*.

3.2.2 Computational details

To generate the library of geometries, we used DFT and HF methods in conjunction with the 6-31G* basis set. CAM-B3LYP and B3LYP functionals were selected owing to their different bond-length alternation predictions in conjugated hydrocarbons. Whenever possible, also the BS geometries were obtained with the corresponding unrestricted approach. The optimized geometries are identified, with the CS-/BS- prefix followed by the level of theory.

For **EsQ2**, only four geometries were obtained: CS-HF, CS-B3LYP, CS-CAM-B3LYP and BS-UHF; for **EsQ3**, CS-HF, CS-B3LYP, CS-CAM-B3LYP, BS-UCAM-B3LYP and BS-UHF geometries were available; while for **EsQ4**, also the BS-UB3LYP geometry was available reaching a total of six geometries. For each of the geometry considered, diradical character both in terms of y_0 and N_{FOD} was obtained. y_0 was determined at PUHF/6-31G* level, while N_{FOD} was calculated at TPSS/def2-TZVP level with $T_{el} = 5000$ K.

The nature of the stationary points was assessed by computing vibrational frequencies.

On the other hand, to investigate possible resonance effect with the SE and DE states, we firstly determined their energy locations at DFT/MRCI level considering CS-B3LYP geometries for **EsQ2** and **EsQ3** and BS-UB3LYP geometry for **EsQ4**. To simulate resonance Raman spectra, we considered the CS-B3LYP geometry for **EsQ2** and **EsQ3**; while for **EsQ4**, the BS-UCAM-B3LYP geometry was chosen. Additionally, to model resonance Raman spectra, the equilibrium structure of the SE state was obtained at TD-B3LYP level for **EsQ2** together with **EsQ3** and at TD-CAM-B3LYP level for **EsQ4**. Hereafter, the optimized SE state geometries are simply labeled with the level of theory used to determine them. The geometry of the DE state cannot be obtained by TD-DFT calculations owing to its multi-exciton nature[132,171]. Nevertheless, it has been shown that the BS-CS geometry change overlaps with the ECC coordinate and with both the ground to optically active state geometry change and the ground to DE geometry change[132,170,171]. Thus, we can safely assume that Raman modes enhanced by resonance with the DE state are expected to be similar to those enhanced by resonance effect with the SE state.

Raman spectra were, then, computed both considering the GS and SE optimized geometries at B3LYP/6-31G* level. Vibrational frequencies were scaled by 0.97 according to previous studies[132,170] where a very close match with experimental vibrational frequencies and intensities was demonstrated. The geometry change was projected onto ground state vibrational normal coordinates to evaluate B_k (Section 3.2.2.1) and the corresponding Huang-Rhys (HR) factors S_k (Section 3.2.2.1) were obtained.

3.2.2.1 Resonance Raman Activities and Huang-Rhys factors

Considering a Raman transition between two vibronic states: $|i\rangle$ and $|f\rangle$, indicating, respectively, the initial and final states, Raman intensity is proportional to the square of the transition polarizability $\alpha_{f,i}^{\rho,\sigma}$ with ρ and σ standing for cartesian coordinates x, y and z[184]. Generally, Raman spectroscopy detects information regarding the ground state. The electronic states for $|i\rangle$ and $|f\rangle$ are the same and can be indicated as $|g\rangle$ (the ground state, GS). Additionally, Raman spectroscopy involves a virtual intermediate state indicated as $|p\rangle$ here. By assuming the Born-Oppenheimer approximation, the electronic part and the vibrational part of the three vibronic states can be separated into : $|i\rangle = |g\rangle|m\rangle$, $|f\rangle = |g\rangle|n\rangle$ and $|p\rangle = |e\rangle|v\rangle$, with $|m\rangle$, $|n\rangle$ and $|v\rangle$ indicating vibrational states. It can be shown that the transition polarizability can be written as:

$$\alpha_{f,i}^{\rho,\sigma} = \frac{1}{\hbar} \sum_{e,v} \left[\frac{\langle m|[\mu_{g,e}]^\rho|v\rangle\langle v|[\mu_{e,g}]^\sigma|n\rangle}{\omega_{ev} - \omega_{gn} - \omega_{laser} + i\Gamma_{ev}} + \frac{\langle m|[\mu_{g,e}]^\sigma|v\rangle\langle v|[\mu_{e,g}]^\rho|n\rangle}{\omega_{ev} - \omega_{gm} + \omega_{laser} + i\Gamma_{ev}} \right] \tag{3.21}$$

where $i\Gamma_{ev}$ is a damping factor associated to the $|g\rangle \to |e\rangle$ electron transition and $[\mu_{g,e}]^{\rho/\sigma}$ is the electronic transition moment. $\omega_{ev/gn}$ is the frequency associated to the specific vibronic transitions and ω_{laser} is the frequency of the laser light.

It is shown, in Ref. [172,184,185] that, as long as the Born-Oppenheimer approximation is valid, the vibronic transitions in Eq. 3.21 can be expanded using Taylor's series expansion and the final expression can be grouped in four terms among which the Albrecht's A-term[172] is obtained by truncating the Taylor's expansion to the first term.

$$\alpha_{f,i}^{\rho,\sigma}(\text{A} - \text{term}) = \frac{1}{\hbar} \sum_e [\mu_{g,e}^0]^\rho [\mu_{e,g}^0]^\sigma$$
$$\times \sum_v \left[\frac{\langle m|v\rangle\langle v|n\rangle}{\omega_{ev} - \omega_{gn} - \omega_{laser} + i\Gamma_{ev}} + \frac{\langle m|v\rangle\langle v|n\rangle}{\omega_{ev} - \omega_{gm} + \omega_{laser} + i\Gamma_{ev}} \right] \tag{3.22}$$

This term includes only the Franck-Condon effects[172,184] and accounts for the major source of Raman resonance effect [185–189] for totalsymmetric (TS) modes, *i.e.* the only active Raman modes if we restrict to **fundamental vibrations** (*i.e.* no combination nor overtones).

Under resonance or near resonance condition, the second addend of Eq. 3.21 or Eq. 3.22 can be ignored [172]. Assuming a perfect resonance condition with the 0-0 electronic transition, Eq. 3.22 can be recast in:

$$\alpha_{f,i}^{\rho,\sigma} = \frac{1}{\hbar} \sum_e [\mu_{g,e}^0]^\rho [\mu_{e,g}^0]^\sigma \frac{\frac{B_k}{\sqrt{2}} \exp\left(-\Sigma_p^{TS} \frac{B_p^2}{2}\right)}{\omega_{e0} - \omega_{g0} - \omega_{laser} + i\Gamma_{ev}} \tag{3.23}$$

where B_k is the dimensionless displacement parameter related to the k-th vibration. Assuming the **harmonic approximation**, B_k can be calculated as:

$$B_k = \sqrt{\frac{2\pi\nu_k}{\hbar}} [X_j - X_i] M^{1/2} Q_k(j) \tag{3.24}$$

where $X_{i,j}$ is the *3N* dimensional vector of the equilibrium Cartesian coordinates of the *i, j* electronic state (here *i* is the excited electronic state and *j* is the ground state), M is the *3N* × *3N* diagonal matrix of atomic masses and $Q_k(j)$ is the *3N* dimensional vector describing the *k* normal coordinate of the *j* (ground) state in terms of mass weighted Cartesian coordinates. Hence, B_k takes into account the geometric change upon excitation.

B_k is related to the Huang-Rhys (HR) factor S_k [172,190,191] through:

$$S_k = \frac{1}{2} B_k{}^2 \tag{3.25}$$

Therefore, a relationship between the resonance Raman intensity of *k*-th mode and the corresponding HR factor S_k can be drawn consecutively: the intensity of the Raman band is proportional to the square of the associated transition polarizability $\alpha_{f,i}^{\rho,\sigma}$, which is related to the displacement parameter, which in turn, is directly proportional to S_k. Thus, the higher is S_k, the more influenced (enhanced) is the intensity of the related Raman band.

3.2.3 The diradical character for the library of computed geometries and structure-property relationships

y_0^{PUHF} and N_{FOD} values are collected in Tables 3.1 and 3.2, respectively, for each geometry of the three molecules. For a given oligomer, both y_0 and N_{FOD} increase from CS-HF to BS-UHF geometries with intermediate values for CS- and BS-DFT geometries, in agreement with the trend found in other investigations on diradicaloids that will be presented in subsequent sections. y_0 values are functional dependent and they increase when moving from CS to BS geometries. In addition, the trend is influenced by the amount of HF exchange included in the functional used to determine the geometry. Generally, for CS geometries, smaller y_0 is expected for CS-HF geometry, followed sequentially by CS-CAM-B3LYP and CS-B3LYP. For BS geometries, the trend is the opposite. Here, an exception is observed for the BS-UCAM-B3LYP geometry of **EsQ4**, which exhibits the highest y_0^{PUHF} value. The same trend is also followed by N_{FOD} values. Thus, these two diradical descriptors are strictly geometry dependent. The geometry, in turn, is undeniably related to the functional used.

For a fixed geometry, *e.g.*, CS-B3LYP, both y_0^{PUHF} and N_{FOD} increase with the conjugation length (from **EsQ2** to **EsQ4**). This is expected, since the longer is the conjugation chain, the more aromatic should be the corresponding molecule according to Clar's sextet rule[122]. Given the similar trend of the two diradical indexes, we will refer only to y_0^{PUHF} for the remaining

discussion.

Table 3.1. y_0^{PUHF} calculated at different optimized geometries of **EsQ2**, **EsQ3**, and **EsQ4**. Table adapted from Ref. [88].

			y_0^{PUHF}			
Geometry → Molecule ↓	CS-HF	CS-CAM-B3LYP	CS-B3LYP	BS-UB3LYP	BS-UCAM-B3LYP	BS-UHF
EsQ2	0.14	0.21	0.27	/	/	0.39
EsQ3	0.22	0.31	0.41	/	0.50	0.56
EsQ4	0.28	0.42	0.54	0.64	0.73	0.69

Table 3.2. N_{FOD} values of **EsQ2**, **EsQ3** and **EsQ4** at available optimized geometries. Table adapted from Ref. [88].

			N_{FOD}			
Geometry → Molecule ↓	CS-HF	CS-CAM-B3LYP	CS-B3LYP	BS-UB3LYP	BS-UCAM-B3LYP	BS-UHF
EsQ2	0.62	0.72	0.80	/	/	0.93
EsQ3	0.89	1.03	1.15	/	1.25	1.31
EsQ4	1.15	1.34	1.49	1.61	1.69	1.66

Diradical character of quinoidal oligothiophenes is associated with a recovery of aromaticity, the varying y_0^{PUHF} values computed for the same oligomer at different levels of theory ultimately reflect a different CC bond length alternation along the conjugated chain. This can be clearly seen in Figure 3.11 where bond lengths along the conjugation pathway of oligothiophene core of **EsQ4** are presented (the same effect was computed also for the other two molecules[88]). All CS geometries show a more marked CC bond length alternation compared to the corresponding BS geometries, highlighting a more quinoidal structure for the former. Comparing CS geometries, it can be seen that a smaller amount of HF exchange implies a reduced bond-length alternation. At the same time, a more marked bond-length alternation is predicted by functional/method with smaller amount of HF exchange for BS structures. The concomitant effects lead to a reduced CS-BS geometry change. Thus, larger CS-BS bond-length alternation changes are predicted at CAM-B3LYP level and this leads, for **EsQ4**, to the largest recovery of aromaticity predicted by the BS-UCAM-B3LYP geometry.

A tight correlation between CC bond-lengths belonging to the central conjugated core and the computed diradical character can be observed in Figure 3.12a. A very good linear relationship can be found suggesting these bonds as diagnostic of the diradical character. On the contrary, other bond lengths, for instance C=O and C≡N, do not show a diradical character dependent feature (Figure 3.12b). Thus, they cannot be considered as diagnostic.
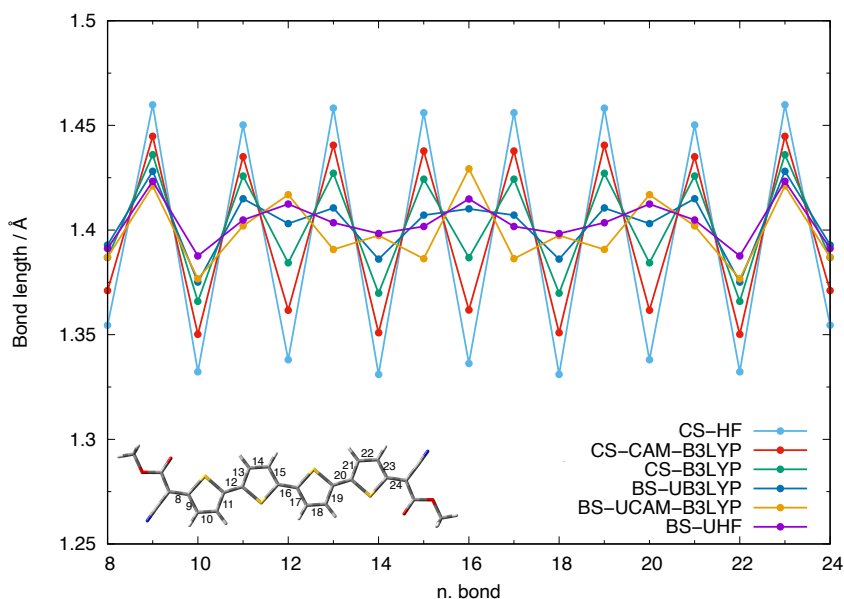
Figure 3.11. Bond lengths of **EsQ4** calculated at CS-HF (cyan), CS-CAM-B3LYP (red), CS-B3LYP (green), BS-UB3LYP (blue), BS-UCAM-B3LYP (orange) and BS-UHF (purple) geometries. Bottom left: bond number definition. Figure adapted from Ref. [88].
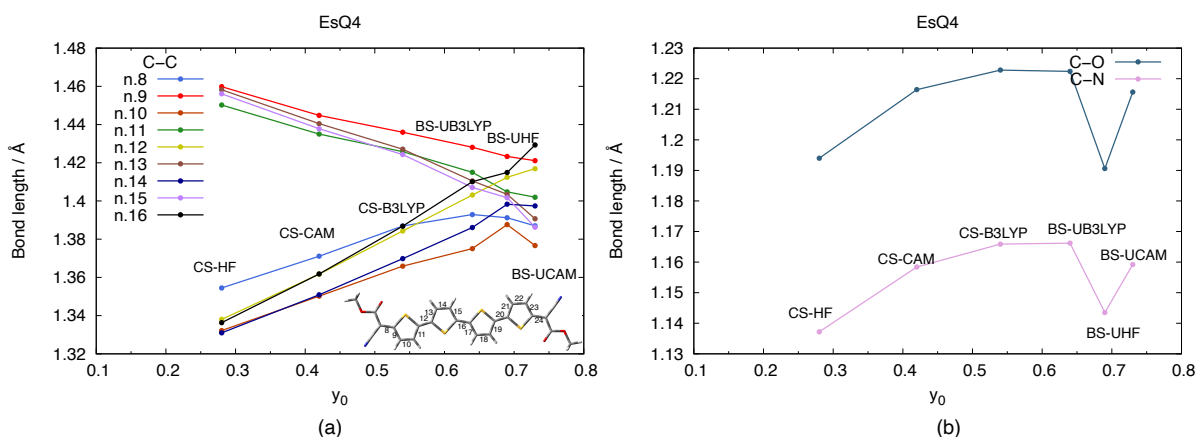
Figure 3.12. (a). Correlation between C-C bond lengths and y_0^{PUHF} of **EsQ4** calculated at different geometries: CS-HF, CS-CAM-B3LYP, CS-B3LYP, BS-UB3LYP, BS-UCAM-B3LYP and BS-UHF. Bottom right: definition of bond number. (b) Correlation between C=O and C≡N bond lengths and y_0^{PUHF} of **EsQ4** calculated at available geometries. Figure adapted from Ref. [88].

3.2.4 Interpretation of experimental absorption spectrum based on computational results

UV-Vis-NIR spectra for the three molecules are recorded experimentally and are shown in Figure 3.13a (black lines). It can be clearly seen that these absorption spectra display additional spectral features on the red side of the main absorption maximum (*e.g.,* absorption at 673 nm for EsQ3 and 851 nm for EsQ4). The same feature has also been observed for some TCNQ derivatives[130,131]. As I mentioned previously, one typical characteristic of the DE state is that, although formally symmetry forbidden for centrosymmetric molecules, it can be vibronically activated and appears as 'shoulder' on the red side of the main absorption band[66,91,171]. The vibronically-activated DE state acquires intensity from the nearby SE state according to the Herzberg–Teller (HT) mechanism of intensity borrowing[192]. On the other hand, owing to conformational flexibility, small deviations from centrosymmetric symmetry may also break

the selection rule and these mechanisms explain why such weak features appear in the spectra.
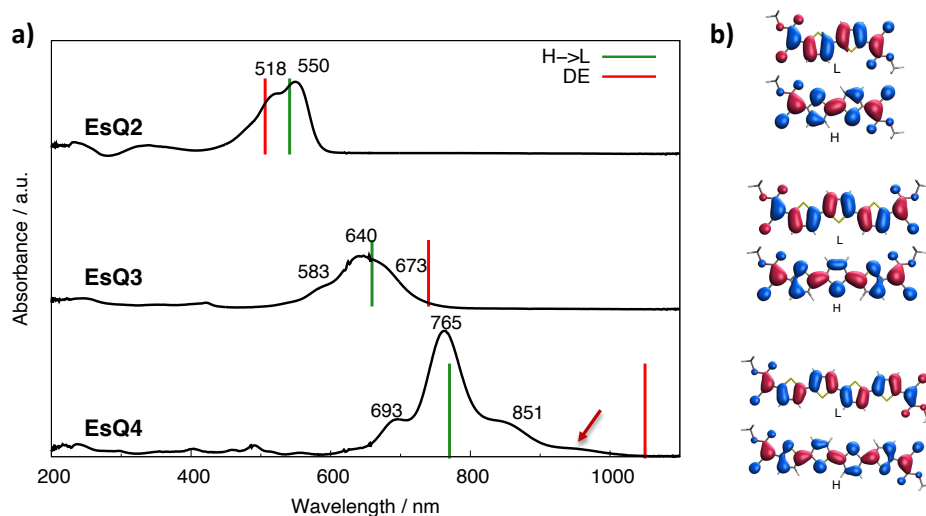
Figure 3.13. a). Experimental UV-Vis-NIR electronic absorption spectra of three cyano-ester oligothiophenes registered in dichloromethane (DCM) (solid black lines and black numbers). Comparison with DFT/MRCI computed excitation energies for the bright SE state (H → L, green bars) and the dark DE state (red bars). b). Frontier molecular orbitals involved in the two transitions of, from top to bottom, **EsQ2**, **EsQ3** and **EsQ4**. Figure a) reused from Ref. [88].

Table 3.3. Computed DFT/MRCI excitation energies of the optically active H→L transition and of the DE state and comparison with observed peaks in absorption spectra of **EsQn** oligomers. Table adapted from Ref. [88].

Molecule ↓	Excited Electronic State	Calc (eV)	Calc (nm)	Exp (nm)
EsQ2	H→L	2.29	541	550
	DE	2.45	506	-
EsQ3	DE	1.67	740	750 *
	H→L	1.88	659	640
EsQ4	DE	1.18	1050	1050 *
	H→L	1.61	770	765

* onset of the absorption spectrum.

DFT/MRCI results are shown as red and green bars for the DE and SE (indicated as H→L in Figure 3.13a and Table 3.3) states, respectively. MOs involved in the excitations are also depicted in Figure 3.13b. DFT/MRCI calculations show clear evidence of a low-lying DE state for all the oligomers investigated. It is the second lowest excited state for **EsQ2** and the lowest excited state for **EsQ3** and **EsQ4** at their ground state geometries (Figure 3.13a, Table 3.3), in agreement with recent analysis of the absorption spectra of related quinoidal oligothiophene trimers[182]. Green bars in Figure 3.13a indicate the bright SE state computed at DFT/MRCI level. The band peaking at 550 nm is clearly due to the transition to the SE state. Whereas there is no clear evidence of such DE state in **EsQ2**. Its transition may be overlapped with the strongly allowed SE state. In contrast, while absorption maxima at 640 nm and 765 nm are assigned to the transition to the SE state respectively for **EsQ3** and **EsQ4**, a clear shoulder at 673 nm of **EsQ3** can be assigned to a vibronically activated transition to the DE state as well as the weak features at 851 and *ca.* 940 nm (indicated by the red arrow) in the spectrum of **EsQ4**. Thus, DFT/MRCI calculations help clarifying when measured Raman spectra may be affected by resonance or pre-resonance not only with the strongly optically active SE state, but also with the more elusive DE state.

3.2.5 Comparison between computed and experimental Raman spectra

It is known that features in the simulated Raman spectra (*e.g.* the ECC mode[132]) are sensitive to geometric parameters, which, as discussed in previous sections, are strictly dependent on the level of theory used. First, we compare, for each oligomer, the Raman intensities computed for each member of the library of ground state structures with the observed off-resonance Raman spectra, to identify the most suitable level of theory for Raman activity prediction.

Experimental Raman spectra were obtained using different excitation wavelengths (Figure 3.14): 1064 nm, 785 nm, 633 nm and 532 nm which may generate resonance or pre-resonance effect due to the location of the SE and DE states in the three molecules considered. Thus, for an appropriate comparison between computed off-resonance Raman intensities and observed spectra, we choose the experimental spectrum less affected by resonance effects.
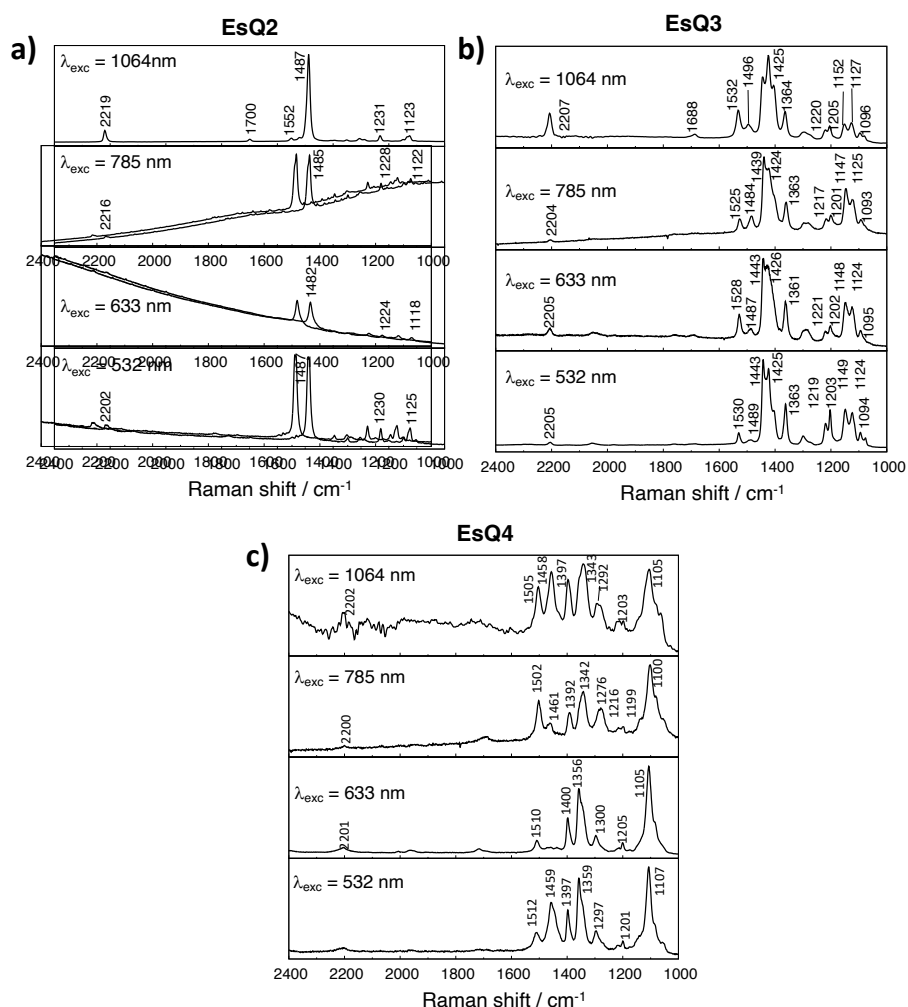
Figure 3.14. Raman spectra of a). **EsQ2**, b) **EsQ3** and c) **EsQ4** measured in the solid state at room temperature with different excitation wavelengths: from top to bottom: 1064 nm; 785 nm; 633 nm; 532 nm. Figure adapted from Ref. [88].

Considering Raman spectra of **EsQ2** for simplicity, it is evident that the spectrum obtained by exciting at 532 nm is in resonance with both the SE and DE states. Therefore, we compare the 1064 nm Raman spectrum (off-resonance) with the computed ones predicted by the library of ground state geometries (Figure 3.15). Similarly to the observed one, all computed spectra

display a dominant active frequency associated with the ECC coordinate (Figure 3.16a). This frequency downshifts with the increasing diradical character associated to the predicted geometry. The best agreement is obtained by the Raman spectrum predicted at the CS-B3LYP geometry: its computed active frequencies are in excellent agreement with the experimental result (Figure 3.17).
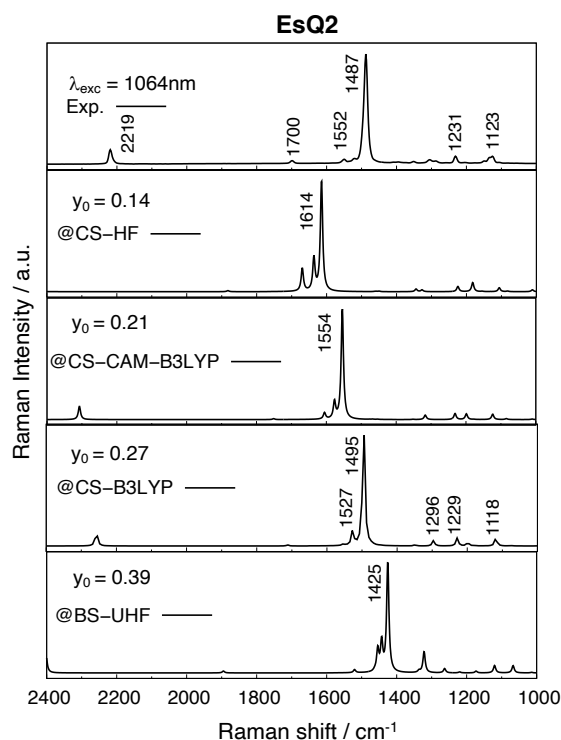
Figure 3.15. Comparison between experimental (top, spectrum measured at 1064 nm) and computed Raman spectra (B3LYP/6-31G* level of theory) for the library of ground state geometries of **EsQ2** characterized by increasing diradical character as indicated in the top left part of each panel. Figure adapted from Ref. [88].

(a) $\tilde{v}_{calc.}(scaled) = 1495\ cm^{-1}$

(b) $\tilde{v}_{calc.}(scaled) = 1447\ cm^{-1}$

(c) $\tilde{v}_{calc.}(scaled) = 1322\ cm^{-1}$
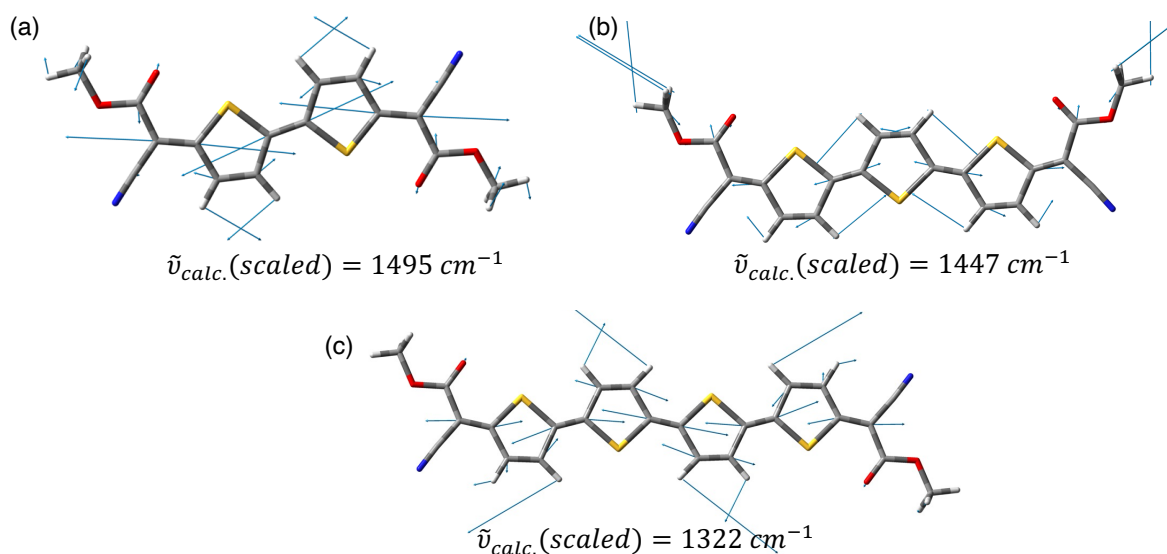
Figure 3.16. Vibrational modes dominated by the ECC coordinate and associated with the most intense bands of (a) **EsQ2** ($\tilde{v}_{Exp}$ =1487 cm⁻¹); (b) **EsQ3** ($\tilde{v}_{Exp}$ =1496 cm⁻¹); (c) **EsQ4** ($\tilde{v}_{Exp}$ =1356 cm⁻¹); The scaled wavenumbers (scale factor = 0.97) calculated at CS-B3LYP geometry (for **EsQ2** and **EsQ3**) and BS-UCAM-B3LYP geometry (for **EsQ4**) are reported below each mode representation. Raman spectra calculated at B3LYP/6-31G* level of theory. Figure adapted from Ref. [88].
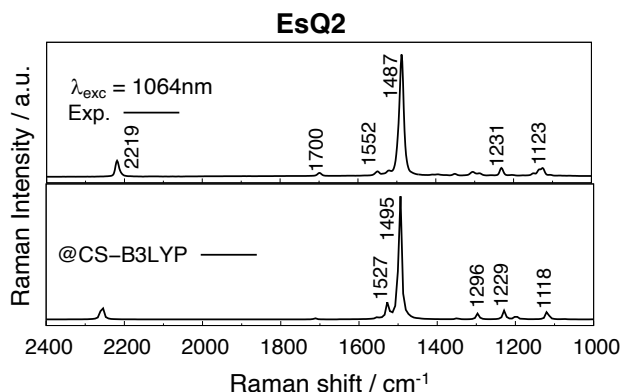
Figure 3.17. Comparison between experimental Raman spectrum obtained by exciting at 1064 nm and computed spectrum calculated at B3LYP/6-31G* level at the CS-B3LYP geometry of **EsQ2**. Computed frequencies are scaled of 0.97. Figure adapted from Ref. [88].

It is now interesting to explore a correlation between diagnostic bond lengths of diradical character (Section 3.2.3) and the vibrational frequency exhibiting ECC character. Figure 3.18 shows the correlation between the unscaled frequency associated to the mode dominated by ECC coordinate and C-C bond lengths diagnostic of diradical character for **EsQ2**. Points at the same row are predicted by the same geometry.

A good linear relationship between these two parameters is observed. The redshift of the vibration dominated by ECC coordinate is accompanied by the elongation of bonds n.8, n.10 and n.12 with the simultaneous shortening of bonds n.9 and n.11. The linear relationship ultimately suggests that the ECC mode can be considered as diagnostic of the diradical character.
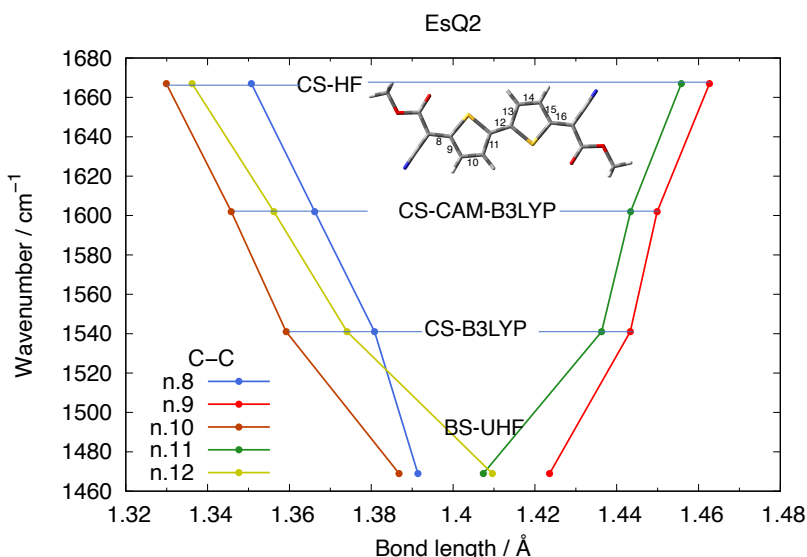
Figure 3.18. Correlation between the unscaled wavenumber of the ECC mode and the lengths of diagnostic bonds for **EsQ2**. Points at the same row indicate that they are calculated at the same geometry.

Now, moving to resonance Raman effect, the spectrum obtained by exciting at 532 nm is in resonance with the SE state and is considered. It can be seen that intensities of vibrational bands, corresponding to 1125 cm^{-1}, 1230 cm^{-1} and 1487 cm^{-1} (Figure 3.14a), show a remarkable enhancement with respect to the corresponding bands in other spectra. HR factors computed for the optically active transition of **EsQ2** (Table 3.4) suggest Raman enhancement for the

vibrations computed at 1118 cm^{-1}, 1229 cm^{-1} and 1495 cm^{-1}, in good agreement with the intensity increase of the corresponding 1125 cm^{-1}, 1230 cm^{-1} and 1487 cm^{-1} bands in the experimental spectrum measured by exciting at 532 nm (Figure 3.14a). Notably, apart from the ECC dominated mode at 1495 cm^{-1}, also the 1229 cm^{-1} frequency mode bears some contribution of out-of-phase adjacent C-C/C=C stretching in the central conjugated core (Figure 3.19). As will be shown below, Raman enhancement due to these modes becomes more relevant for longer oligomers.
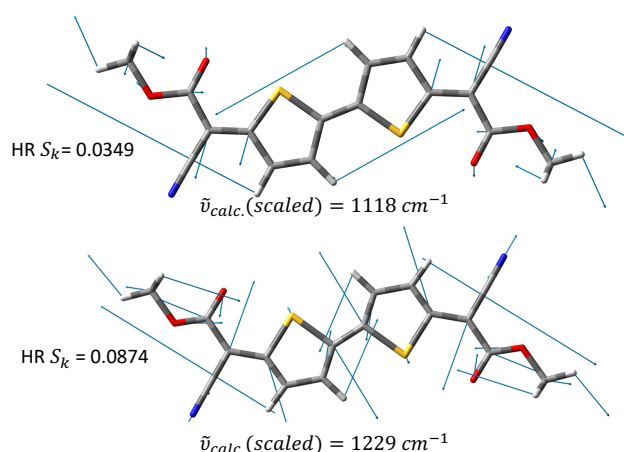
Figure 3.19. Vibrational modes below 1300 cm^{-1} displaying large HR factors and therefore expected to display enhanced Raman activity in resonance with the optically active transition of **EsQ2**. Figure adapted from Ref. [88].

Table 3.4. Computed HR factors for the optically active transition of **EsQ2**, **EsQ3** and **EsQ4**. Frequencies are scaled of 0.97. Table adapted from Ref. [88].

EsQ2		EsQ3		EsQ4	
Frequency/cm^{-1}	HR Factor [a]	Frequency/cm^{-1}	HR Factor [a]	Frequency/cm^{-1}	HR Factor [b]
1118	0.0349	1096	0.0130	1046	0.0750
1198	0.0263	1120	0.0196	1249	0.0591
1229	0.0874	1203	0.0755	1301	0.0400
1296	0.0199	1225	0.0278	1316	0.0162
1495	0.2029	1447	0.1443	1322	0.1112
1527	0.0367	1447	0.0595	1385	0.0104
				1499	0.0017
				1516	0.0029

[a] Ground and excited states computed with the B3LYP functional. [b] Ground and excited state computed with the CAM-B3LYP functional.

The wavelength dependence of the Raman spectra of **EsQ3** and **EsQ4** (Figure 3.14) is more remarkable due to the concomitant lowering of both the optically allowed SE and forbidden DE state. For **EsQ3** the spectrum measured exciting at 1064 nm can still be considered reasonably far from resonance and is therefore considered for comparison with computed spectra for different geometries (Figure 3.20a).

As for **EsQ2**, the frequency associated with the ECC coordinate (Figures 3.16b, 3.20a) exhibits dominant Raman activity and it downshifts with the increasing diradical character of the predicted geometry. The best agreement is obtained by the Raman spectrum predicted either at the CS-B3LYP or the BS-UCAM-B3LYP geometries. y_0 calculated at these two geometries show comparable values: 0.41 vs 0.50. Additionally, a similar trend in bond length alternation is found for both geometries although the BS-UCAM-B3LYP structure displays a more marked

equalization[88]. The computed dominant activity at 1447 cm^{-1} or 1419 cm^{-1} (due to the ECC mode), for CS-B3LYP or BS-UCAM-B3LYP geometries (Figure 3.20a), is in comparable good agreement with the experimental most intense activity observed at 1425 cm^{-1}. The slight overestimation of frequency at CS-B3LYP and slight underestimation at the BS-UCAM-B3LYP geometry suggest that the correct GS geometry of **EsQ3** may lie in-between the two.
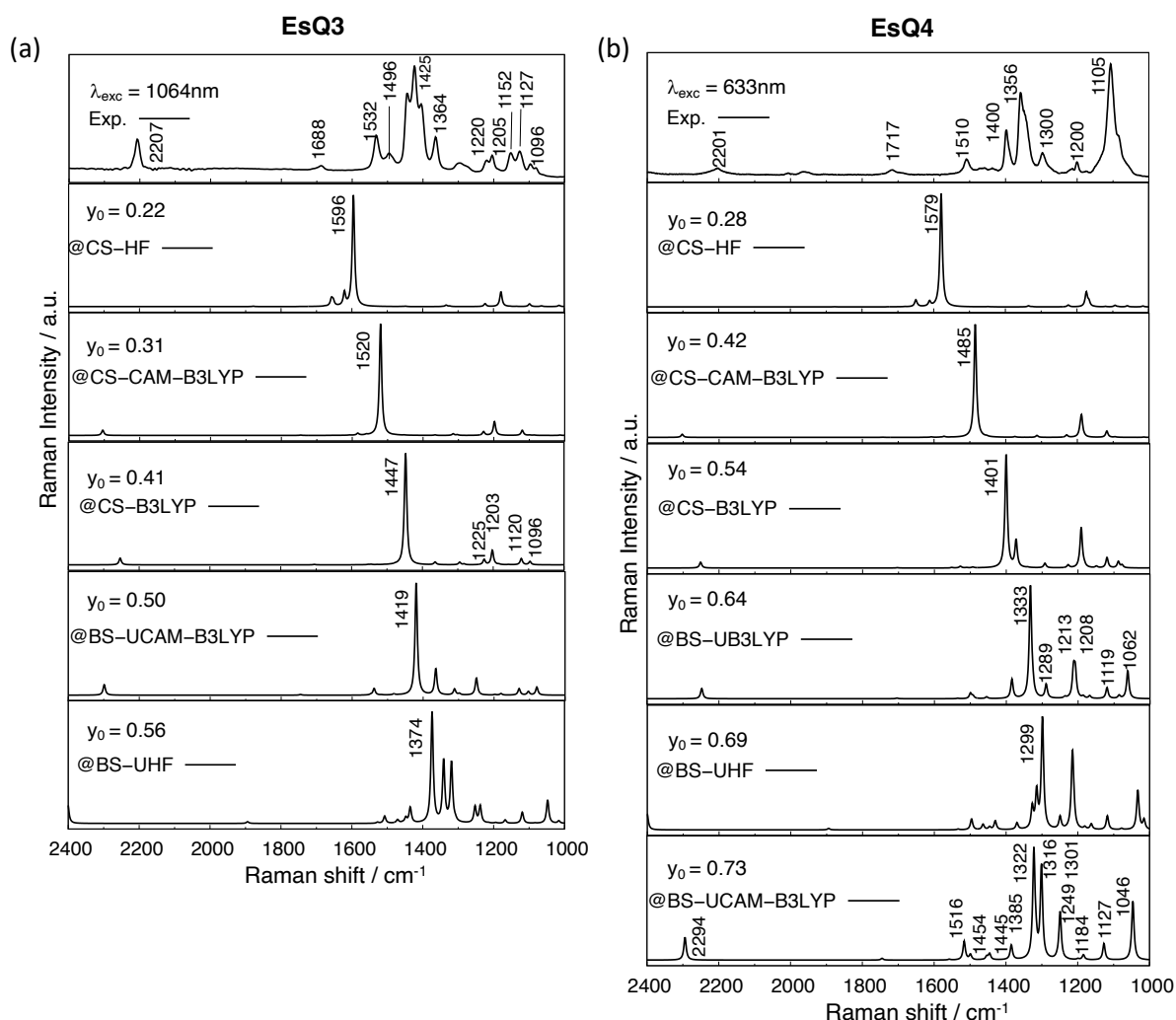
Figure 3.20. Comparison between experimental (top) and computed Raman spectra (B3LYP/6-31G* level of theory) for the library of ground state geometries of (a) **EsQ3** and (b) **EsQ4** characterized by increasing diradical character as indicated in the top left part of each panel. Figure adapted from Ref. [88].

Raman spectrum calculated at the CS-B3LYP geometry is chosen to discuss the resonance effect (Figure 3.21a). Analogously to **EsQ2**, HR parameters computed for the optically active transition of **EsQ3** (Table 3.4) suggest resonance Raman enhancement not only for the mode dominated by the ECC coordinate at 1447 cm^{-1}, but also for vibrations in the 1090–1230 cm^{-1} region (Figure 3.14b), in nice agreement with the intensity increase observed for the Raman spectrum measured exciting in resonance (633 nm) and pre-resonance (532 nm) with the optically active SE state. Additionally, excitation wavelength at 785 nm is in resonance with the DE state, the role of such state in intensity modulations cannot be ruled out as it has been previously reported for other HT induced transitions[174,193]. The out-of-phase adjacent C-C/C=C stretching contribution of some of the low frequency (< 1300 cm^{-1}) active modes is

even more marked for **EsQ3** (Figure 3.22) compared to **EsQ2** and their intensity enhancement, associated to their relevant electron-phonon coupling, is rationalized by the nuclear displacements overlapping with the direction of the ground to excited states geometry change.
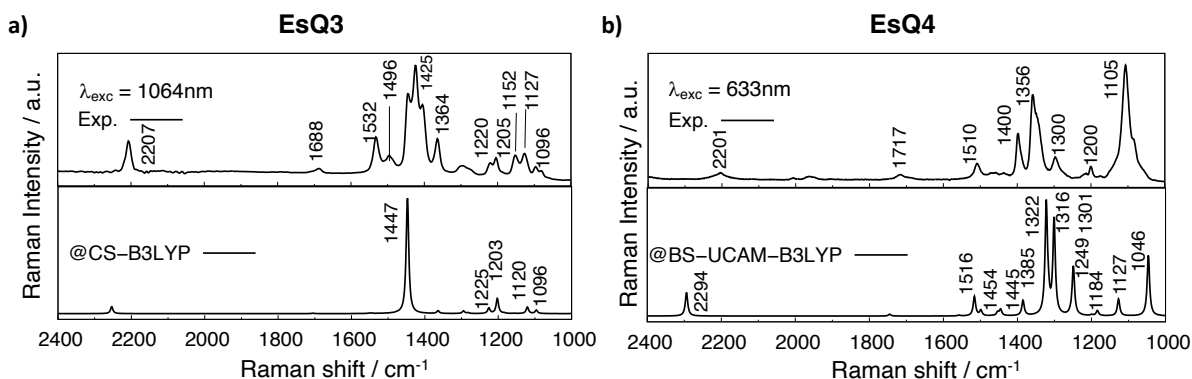
Figure 3.21. Comparison between computed and observed Raman spectra of **EsQ3** (a) and **EsQ4** (b). Figure adapted from Ref. [88].
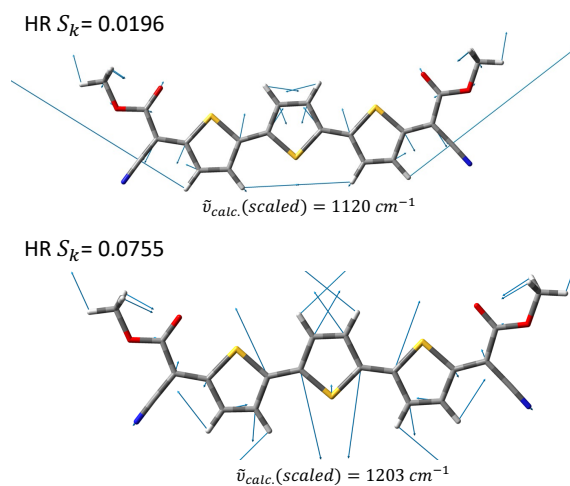
Figure 3.22. Vibrational modes below 1300 cm^{-1} displaying large HR factors and therefore expected to display enhanced Raman activity in resonance with the optically active transition of **EsQ3**. Figure adapted from Ref. [88].

Figure 3.20b shows the comparison between experimental and computed Raman spectra for the set of ground state geometries of **EsQ4.** The 633 nm Raman spectrum is chosen because it is the less affected by resonance effects. The computed spectra show a downshift of the most intense Raman activity with increasing diradical character. A concomitant intensity redistribution on the higher and lower frequency regions with respect to the dominant ECC activity is also observed especially for geometries with larger diradical character. This intensity remodulation finds its closest agreement with the experimental data when the BS-UCAM-B3LYP geometry is employed. Notably, this geometry shows a slight blue-shift of the most intense peak with respect to the corresponding peak calculated at the BS-UHF geometry, which precedes in the scale of diradical character (Figure 3.20b). This blue-shift and increased diradical character can be traced back to the inverted bond length alternation of the BS-UCAM-B3LYP geometry (Figure 3.11) compared to the remaining GS geometries optimized for **EsQ4.** This "inflection point" feature, *i.e.* point after which active Raman frequency upshifts, for more aromatic oligothiophene molecule has already been documented for TCNQ quinoidal thiophene tetramers [131].

Moving to the resonance Raman effects for **EsQ4**, we note that while the Raman activity below 1300 cm^{-1} is modest in **EsQ2**, its intensity contribution increases in **EsQ3**, most likely due to resonance effects as suggested by HR factors and computed low-lying excited states energies. Such low frequency activity becomes dominant in the Raman spectra of **EsQ4** (Figure 3.14c) at all exciting wavelengths. This can be justified by the location of the bright SE and the formally dark DE states (Figure 3.13a, Table 3.3). For this molecule, resonance effects influence the spectra measured with the highest two excitation wavelengths: at 1064 nm resonance with the DE state as suggested by calculations, while at 785 nm with the optically active SE state, as proved by both computed and observed absorption spectra. Further resonance effects with specific vibronic levels of the bright excited state cannot be excluded in the spectra measured at 633 nm and 532 nm, as suggested by the intensity modulation of some bands around 1500 cm^{-1} (Figure 3.14c). Comparison between the 633 nm Raman spectrum and the computed one of **EsQ4** (Figure 3.14c and 3.20b) reveals that the 633 nm spectrum is the less affected by resonance effects and is considered for comparison (Figure 3.21b).

Interestingly, for the longest oligomer of these series, the most intense observed band downshifts at *ca.* 1100 cm^{-1} which corresponds to computed 1046 cm^{-1}. Although this mode is characterized by out-of-phase C-C/C=C stretching contributions (Figure 3.23), it is not dominated by the ECC coordinate which has the largest contribution in the mode corresponding to 1356 cm^{-1} as suggested by *e.g.* computed spectrum (Figure 3.21b). In fact, in the computed spectrum (*i.e.* off-resonance Raman spectrum), the corresponding band peaking at 1322 cm^{-1} exhibits larger Raman activity compared to the one at 1046 cm^{-1} and the normal mode representation shows a clear and larger C-C/C=C out-of-phase stretching (Figure 3.16c). Computed Raman activity for the vibration at 1046 cm^{-1} is, thus, slightly underestimated. However, its stronger observed intensity can be reconciled when resonance effects are taken into account, as indicated by the remarkable HR factor computed for this vibration (Table 3.4), implying an additional intensity contribution *via* resonance with both the optically active SE and the DE state. Finally, we note that HR factors suggest some enhancement also for modes around 1500 cm^{-1}, which may explain the intensity modulation in this region as a function of exciting wavelength.

HR S_k = 0.0750
$\tilde{v}_{calc.}(scaled) = 1046\ cm^{-1}$

HR S_k = 0.0591
$\tilde{v}_{calc.}(scaled) = 1249\ cm^{-1}$
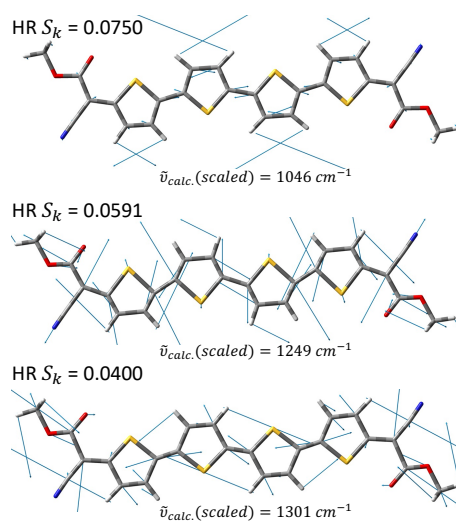
HR S_k = 0.0400
$\tilde{v}_{calc.}(scaled) = 1301\ cm^{-1}$

Figure 3.23. Vibrational modes below 1300 cm^{-1} displaying large HR factors and therefore expected to display enhanced Raman activity in resonance with the optically active transition of **EsQ4**. Figure adapted from Ref. [88].

3.3 Evidence of vibrationally driven spin mobility in a diradical based on azobenzene

Conjugated diradicals are attracting considerable interest thanks to their potential applications not only in optoelectronics but also in spintronics. On the way to uncover the fundamental properties of the spin in the organic matter, an important feature is the description of the connections between structural flexibility of π-conjugated molecules and spin delocalization and dynamics in the flexible backbone. As it has been seen in a previous section, the diradical character is intimately related to the structure assumed by the molecule in its ground state and small structural variations imply different diradical character. Even in a condensed phase such as the solid state, molecular motions (*e.g.,* low frequency vibrations) are always possible and some of them (*i.e.,* the higher-energy ones) can be 'activated' thermally. The molecular geometry, thus, is always changing although slightly. Consequently, also the geometry dependent diradical character for the molecule can be modified. Thermal modulation of the diradical character is interesting and it might be an important venue for the designs of new flexible organic magnetic materials, an aspect that is scarcely explored[194–197]. Herein, thermal dependent features of a conjugated bis(phenyloxy) azobenzene diradical (**CAR,** Figure 3.24a) is presented. More precisely, we describe a dumbbell shape azobenzene diradical and correlate its solid state flexibility with spin relaxation and mobility[89].

With a combined experimental and computational study, we found that heating leads to: i) a modulation of the spin distribution; and ii) a "normal" quinoidal → aromatic transformation at low temperatures driven by the intramolecular rotational vibrations of the azobenzene core and a "reversed" aromatic → quinoidal change at high temperatures activated by the azobenzene's bicycle pedal motion amplified by anisotropic intermolecular interactions. Thermal excitation of these vibrational states modulates the diradical electronic structure and spin distribution.

3.3.1 Experimental characterization of CAR

CAR is formed by an azobenzene core substituted with two phenoxyl groups which, in turn, bear bulky *tert*-butyl groups making the whole molecule dumbbell shaped (see Figure 3.24b). According to ESR and SQUID measurements, **CAR** possesses a **singlet open-shell ground state.**

Several crystal structures of **CAR** were determined at different temperatures, specifically 130 K, 200 K, 250 K, 290 K and 340 K. Main focus, here, is on those obtained at 130 K, 290 K and 340 K. Experimental bond lengths reveal that for the structure obtained at 130 K, there is a significant bond alternation in the two phenoxyl benzenoid rings together with a typical double bond length for bond n.5 (Figure 3.24c, Table 3.5) and a partial N-N single bond character for bond n.10 (Figure 3.24c, Table 3.5). All these features indicate a quinoidal-like structure for **CAR** obtained at 130 K. Hereafter, it will be indicated as **Q**. At 290 K, length of bond n.5 is longer, the bond length alternation inside the azobenzene ring becomes smaller and the N-N bond becomes closer suggesting an aromatic azobenzene. Hereafter, this structure will be indicated as **A**. Finally, bond length changes at 340 K, such as shortening of bond n.5 and

10, suggest a regaining of partial quinoid character for this structure. Hereafter, it will be indicated as **PQ** (*pseudoquinoidal*).
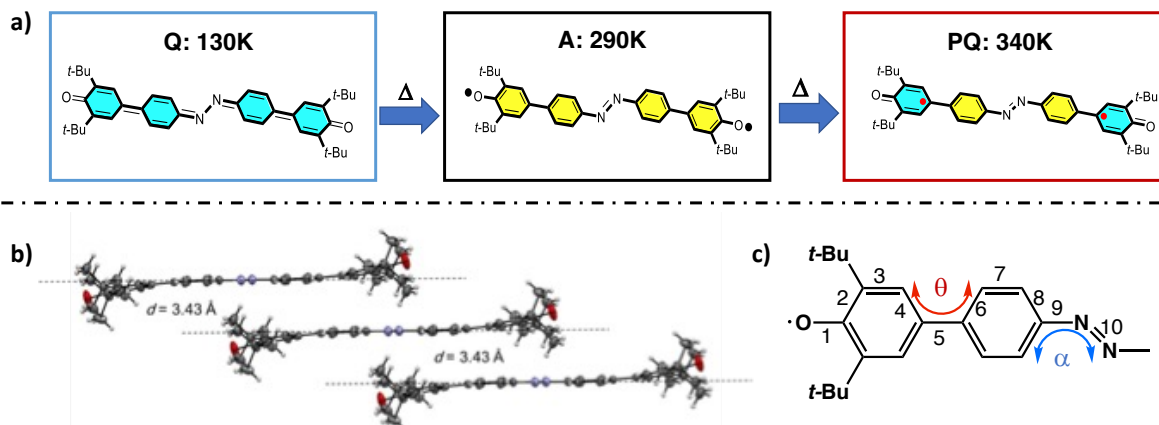
Figure 3.24. Chemical structure of **CAR**. a) Chemical resonance forms for the three structures of **CAR** detected at different temperatures (130 K (**Q**), 290 K (**A**) and 340 K (**PQ**)). b) Side view of the crystal structure of **CAR**. c) Definition of bond lengths and angles studied later to assess the role of low frequency vibrational modes. Figure (b) adapted from Ref. [89].

Table 3.5. Relevant angles and bond lengths of **CAR** measured for the three structures studied here. Experimental XRD measurements accomplished at different temperatures: 130 K, 290 K and 340 K.

Structure ↓	$\alpha(°)$	$\theta(°)$	r_5 (Å)	r_{10}(Å)
Q (130 K)	-0.87	5.78	1.433	1.300
A (290 K)	1.15	8.96	1.478	1.257
PQ (340 K)	0.01	8.36	1.449	1.253

Notably, both α the θ angles measured for the three structures show an increase from **Q** to **A** followed by a decrease to **PQ**. The α angle changes sign passing from **Q** to other two structures suggesting an 'out-of-plane' motion of the azobenzene core with opposite orientations. Indeed, the '*bicycle pedal motion*', a torsional motion associated to the inversion of the NN double bond orientation relative to the lateral benzenes, is well-known in crystals of azobenzene derivatives[198]. This motion is well-known also in carotenoids (*e.g.*, retinal)[199,200] associated with the sequence of double and single bonds of the conjugation path. The increase/decrease of the θ angle, on the other hand, suggest an active role for the twisting of terminal phenoxyl groups with respect to the azobenzene core.

UV-Vis-NIR electronic absorption spectrum of **CAR** was obtained for the crystal at room temperature and revealed the presence of the DE state at 997 nm and a strong and broad absorption peaking at *ca.* 645 nm. Solid-state variable temperature Raman spectra were obtained either including resonance (or pre-resonance) effect (exciting at 633 nm and 785 nm) or out of resonance (exciting at 1064 nm) with the most optically active state. Resonant spectra show temperature dependent nature for specific vibrational frequencies. Furthermore, Raman intensities measured at 340 K are in middle way between those measured at 130 K and 290 K (Figure 3.25). Specifically, in the high frequency region (Figure 3.25b & c, left), intensities of Raman bands in the range of 1600 cm^{-1} and 1560 cm^{-1} are dependent from temperature with

the spectrum measured at 340 K (thus corresponding to **PQ** structure) lying between those obtained at 130 K and 290 K. Whereas, in the low frequency region (Figure 3.25b & c, right), a similar '*middle way nature*' is found for the spectrum obtained at 340 K especially for the band at *ca.* 1130 cm^{-1} .
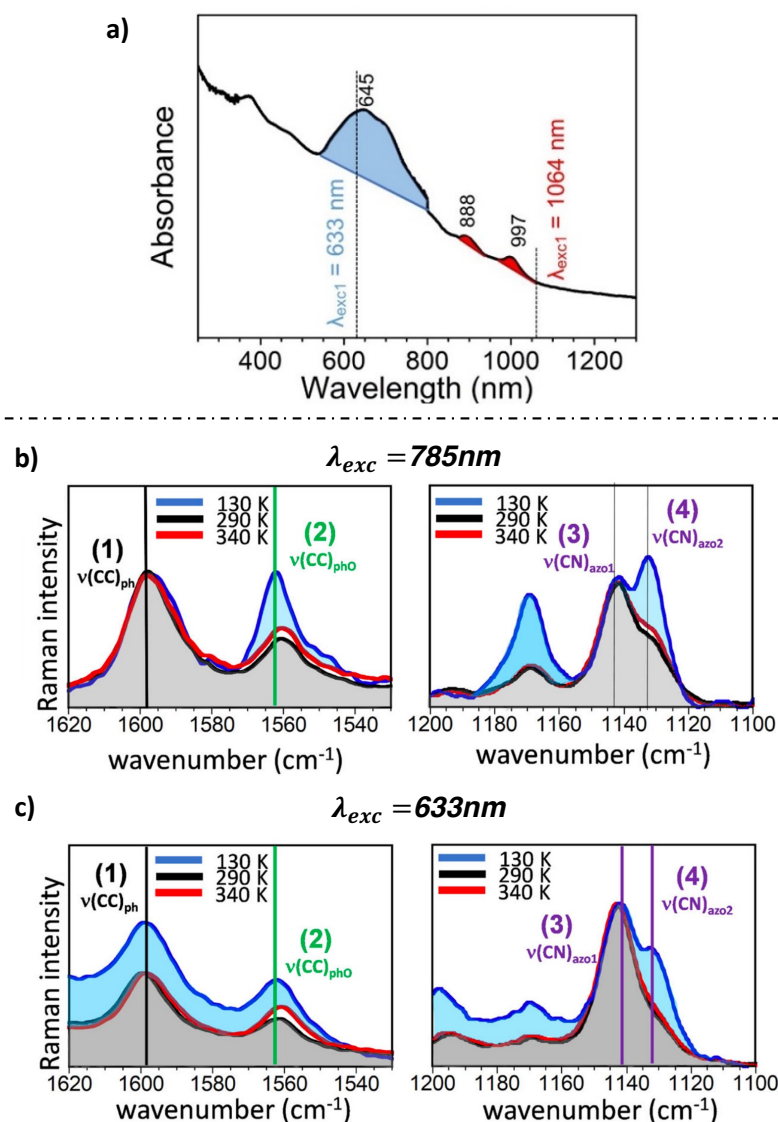
Figure 3.25. Physical characterization for **CAR**. a). Solid state UV-Vis-NIR absorption of CAR. b) Solid-state variable temperature Raman spectra of **CAR** taken by exciting (λ_{exc}) at 785 nm and c) by exciting at 633 nm. Both in resonance (or pre-resonance) with the strongly optical active state in solid state. Figure adapted from Ref. [89].

3.3.2 Computational details

The GS geometries of **CAR** were optimized both at B3LYP and UB3LYP levels leading to CS-B3LYP and BS-UB3LYP geometries, respectively. The 6-31G* basis set was used. It was noticed that CH bond lengths of the crystal structures, compared to equilibrium structures, were unrealistically short. These bond lengths were therefore adjusted, for each crystal structure, with the CLUSTERGEN software[201] and these modified crystal structures were considered for further discussion. The relative energy between the three structures (**Q**, **A** and **PQ**) were evaluated at SF-TDBHHLYP/6-31G* level.

The diradical characters were determined for the optimized geometries (CS & BS) and for the three crystal structures (**Q, A, PQ**) by means of y_0 at PUB3LYP/6-31G* level (hereafter $y_0^{PUB3LYP}$) and N_{FOD} at the default level as mentioned in Section 3.1.5.

The Raman spectrum for each crystal structure was calculated at B3LYP/6-31G* and calculated frequencies were scaled of 0.97. To inspect the normal modes of vibrations that assist the **Q** to **A** and **A** to **PQ** geometry change, we determined the Huang-Rhys factors S_k [191] (Eq. 3.25) by projecting the geometry changes (**A-Q** or **A-PQ**) over the vibrational normal modes of the **A** structure, computed at B3LYP level. In other words, recalling Eq. 3.25 and 3.24, the geometry of A is considered as X_j and those of **Q** and **PQ** as X_i.

To explore the role of the crystal environment, a cluster of **CAR** molecules built up with 19 molecules (*i.e.* one central molecule surrounded by other 18, Figure 3.26) was generated with the CLUSTERGEN software[201]. The potential energy surfaces (PES) along selected nuclear motions were computed at QM/MM level adopting the ONIOM model[202]. In particular, we considered only the nuclear motions of central molecule which was included in the high-level region where quantum-mechanics (QM) calculations at B3LYP/6-31G* level were performed including electronic embedding. Whereas the low-level region (molecular mechanics, MM) including surrounding molecules was modelled by atomic point charges determined by the Qeq approach[203] using the Dreiding force field[204]. Geometries for the surrounding molecules were kept fixed.
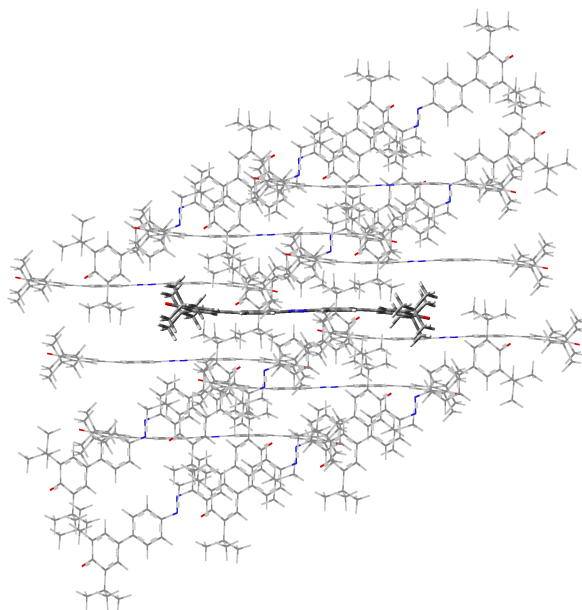
Figure 3.26. Representation of the cluster formed by 19 **CAR** molecules and used for QM/MM calculations to assess the role of crystal environment.

3.3.3 GS geometry, diradical character and computed Raman spectra

SF-TDBHHLYP calculations reveal that, taking as reference the energy computed for **Q**, the **A** structure is more stable by about 1.15 kcal/mol, while the **PQ** structure is computed to be more stable than **A** by about 1.65 kcal/mol.

The CS-B3LYP geometry is similar to the **Q** structure (Figure 3.27) while the BS-UB3LYP geometry resembles more the **A** structure. These conclusions are also supported by diradical

characters either in terms of $y_0^{PUB3LYP}$ or N_{FOD} (Table 3.6) computed for the optimized geometries and for the crystal structures at 130 K, 290 K and 340 K. The trends for the two parameters are similar and indicate a moderate diradical character for **Q**, followed by **PQ** and the largest value is assigned to **A**. Diradical characters calculated for the CS-B3LYP geometry are closer to those of **Q**, while those calculated for the BS-UB3LYP geometry are comparable to those computed for **A**.
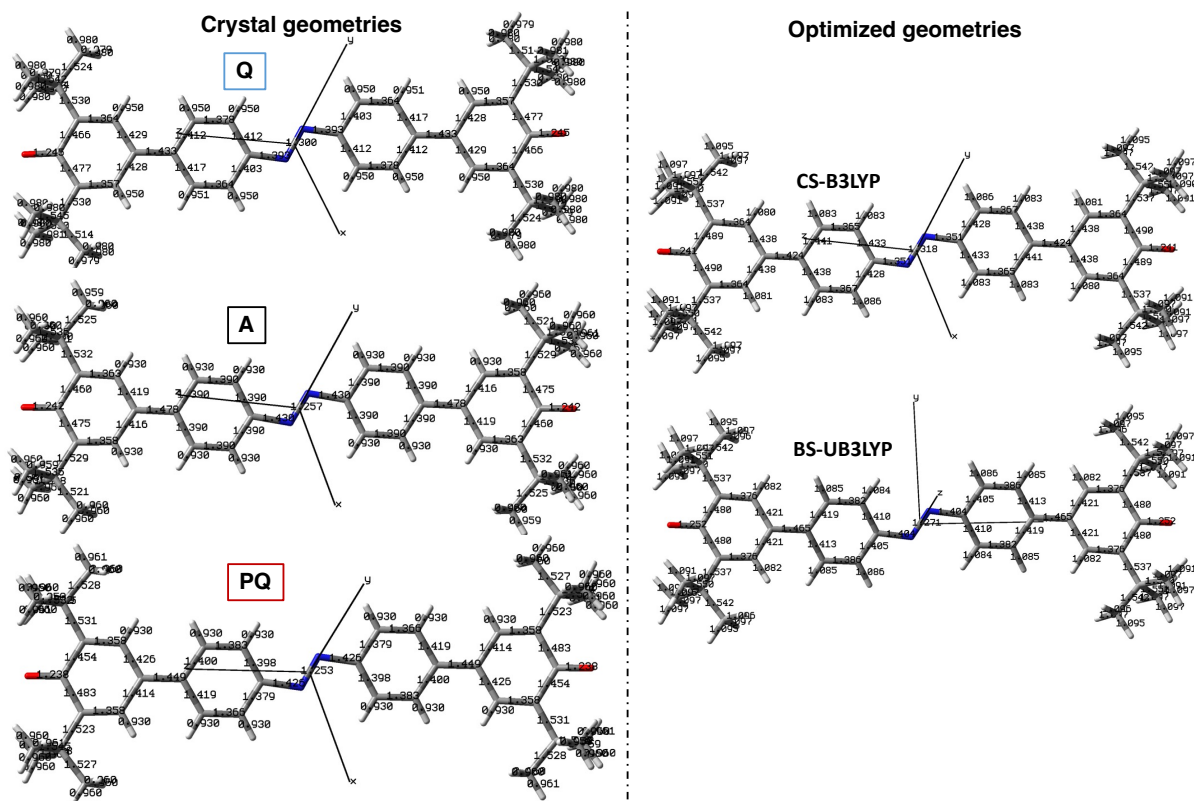
Figure 3.27. Comparison between crystal structures (left) and optimized geometries (right) determined by (U)B3LYP/6-31G* levels.

Table 3.6. Diradical characters for the crystal structures and computed structures of **CAR** evaluated in terms of $y_0^{PUB3LYP}$ and N_{FOD} .

	Diradical character descriptors	
Structure	$y_0^{PUB3LYP}$	N_{FOD}
Q	0.41	2.14
A	0.68	2.28
PQ	0.59	2.22
CS-B3LYP	0.20	2.03
BS-UB3LYP	0.66	2.35

From the comparison between the off-resonance Raman spectra (Figure 3.28) obtained at room temperature and the calculated one for **A** (structure determined at 290 K), a good agreement can be found. Two modes in the low-frequency region (Figure 3.25 b&c) around ~1150 cm^{-1} can be attributed to two vibrations calculated at 1096 cm^{-1} and 986 cm^{-1} (Figure 3.29, frequencies here are referred to the **Q** structure, however it should be mentioned that same normal modes can be found for **A** and **PQ** with similar frequencies). Both normal modes are

characterized mainly by CN bond stretching of the azo group connecting to the benzene rings [*i.e.*, ν(CN)azo]. On the other hand, the two bands in the high frequency region (between 1600 and 1560 cm^{-1}) can be associated to two vibrations calculated at 1601 and 1541 cm^{-1} (Figure 3.29, always considering the **Q** structure). These two vibrations are due to the CC bonds stretching of the azobenzene rings [*i.e.*, ν(CC)ph] and to the CC bonds stretching of the phenoxyl rings [*i.e.,* ν(CC)phO], respectively.
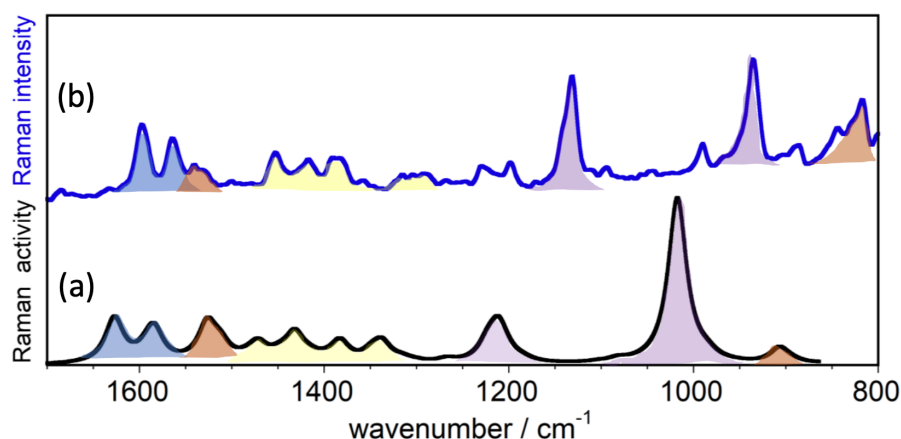
Figure 3.28. Comparison between (a) simulated and (b) experimental solid-state Raman spectra. Theoretical Raman spectrum is calculated at B3LYP/6-31G* level considering the **A** structure. Experimental spectrum is obtained by exciting at 1064 nm (off resonance) at 298 K in solid state. Color codes used in two spectra indicate correlated modes. Figure adapted from Ref. [89].
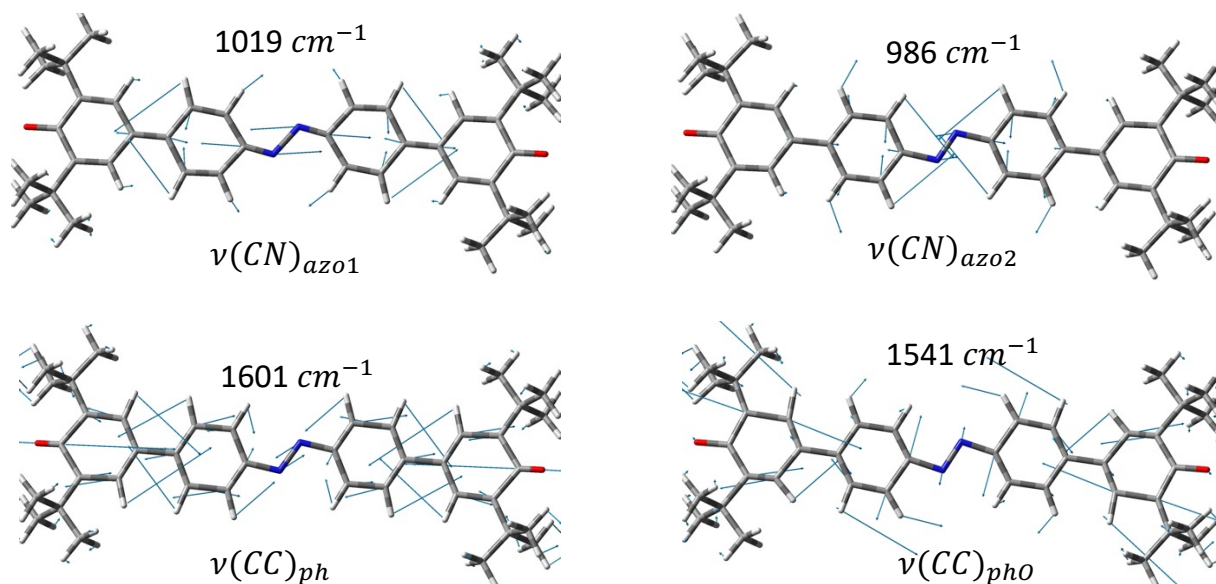
Figure 3.29. Vibrational normal modes associated with (top) two active frequencies in the low-frequency region experimentally determined at *ca.* 1150 cm^{-1} and (bottom) two active frequencies in the high-frequency region experimentally observed between 1600 and 1560 cm^{-1}. Wavenumbers in the figure are calculated at B3LYP/6-31G* level at the crystal structure of **Q** and are scaled of 0.97.

3.3.4 Huang-Rhys parameters

Huang-Rhys parameters associated to high frequency modes both for **Q** to **A** and **A** to **PQ** geometry changes are indicated in Table 3.7 along with graphical representations of the normal mode to which they are associated.

Table 3.7. Computed Huang-Rhys factor (S_k) associated with the high frequency vibrational normal coordinates of **CAR**, for the two geometry changes **Q-A** and **A-PQ**. Calculated S_k values are given in parenthesis for each normal mode. Table adapted from Ref. [89].

Q-A	Graphical representation of the normal coordinate	A-PQ
Frequency[a] / cm^{-1} (Huang-Rhys factor S_k)		Frequency[a] / cm^{-1} (Huang-Rhys factor S_k)
		1688 (0.085)
		1650 (0.064)
1575 (0.065)		1575 (0.062)
1492 (0.058)		
1441 (0.081)		
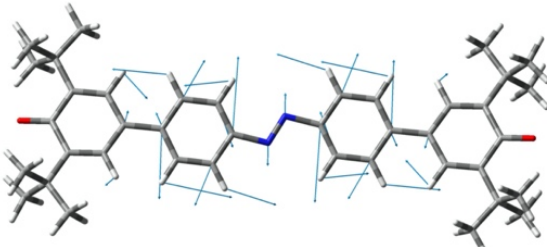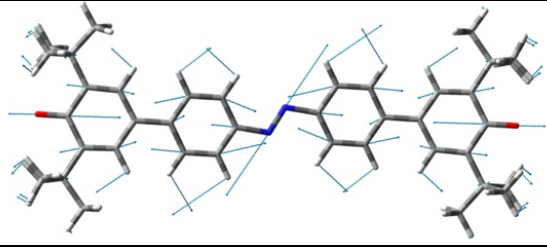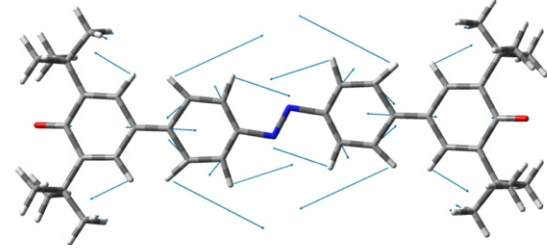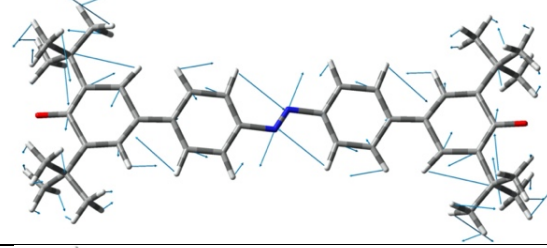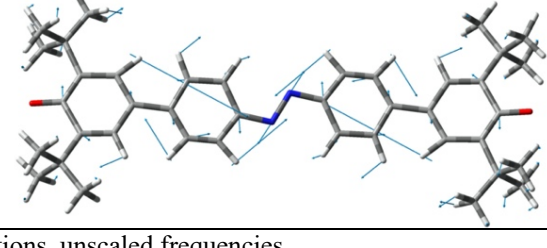
[a]From B3LYP/6-31G* calculations, unscaled frequencies

It can be clearly seen that the **Q** to **A** and **A** to **PQ** geometry changes do not display the same "Huang-Rhys active" modes. Among the five high frequency vibrations shown in Table 3.7, two of them (with frequencies in-between 1400 - 1500 cm^{-1}) are active in assisting only the **Q** to **A** change. This 'transformation', as can be expected from the similarity to CS and BS geometries, respectively, is assisted by specific vibrational normal modes, dominated by the stretching of the conjugated skeleton, a common feature found also in other diradical conjugated

molecules associable with the typical CS to BS change.

Conversely, two different normal modes (with frequency larger than $1600\ cm^{-1}$) are active in assisting only the **A** to **PQ** geometry change. Only the mode with calculated frequency at $1575\ cm^{-1}$ displays similar Huang-Rhys factors for both geometry changes. This implies that, although the diradical character of the **PQ** structure appears to be intermediate between those of the **Q** and **A** structures, the path from **A** to **PQ** cannot be considered as a simple "way back" to the **Q** structure along the same path, but rather as a structural evolution along a pathway which is not the same leading from **Q** to **A**. The two geometry changes are, thus, not sequential along the same 'nuclear coordinate'. Instead, they occur along two different paths that do not necessarily overlap. Therefore, a schematic representation of the geometry changes occurring on **CAR** crystals by increasing the temperature cannot be represented just along one single common nuclear displacement, since it involves a multidimensional space, in which besides different stretching modes, there might be role of torsional motions as suggested by dihedral angle values shown in Table 3.5.

3.3.5 Role of torsional motions

Owing to the distinctive role of torsional motion as suggested by analysis on crystal structures, especially on torsional angles α and θ (Section 3.3.1), the PES of **CAR** is explored along two torsional motions, namely the inter-ring torsion around the CC bonds connecting the azobenzene moiety with the phenoxyl terminal units (Figure 3.30 a&c) and the bicycle pedal motion (Figure 3.31a) involving the two CC bonds adjacent to the central azo group (Figure 3.30 b&d). The three geometries **Q**, **A** and **PQ** were considered inside a cluster as shown in Figure 3.26. In particular, the inter-ring torsion is achieved by varying simultaneously the two θ angles which corresponds to twisting the whole azobenzene moiety inside the crystal cavity with respect to the terminal phenoxyl groups keeping the latter fixed. This is possible in **CAR** crystal without significantly modifying the crystal structure thanks to the dumbbell shape of the molecule (see Figure 3.26). Indeed, free volume (inside the crystal) is left around the conjugated part (nearly planar core). To simplify further discussion, this motion will be indicated as 'azobenzene torsion'. Similarly, also the bicycle pedal motion (Figure 3.31b) can occur by leaving the terminal moieties of the CAR molecule almost fixed.

The QM/MM computed PES along with the two **Q** → **A** and **A** → **PQ** selected torsional paths are shown in Figure 3.30. It is noticed that the computed PESs for both types of torsional motions (twisting of azobenzene and the bicycle pedal motion) are asymmetric (Figure 3.30) even though the molecular structure is nearly planar. The asymmetry is more marked for the azobenzene torsion (Figure 3.30 a&c) compared with the bicycle pedal motion (Figure 3.30 b&d). This asymmetry can be traced back to the interaction with neighbor molecules in the crystal, which are kept fixed while scanning the PES.
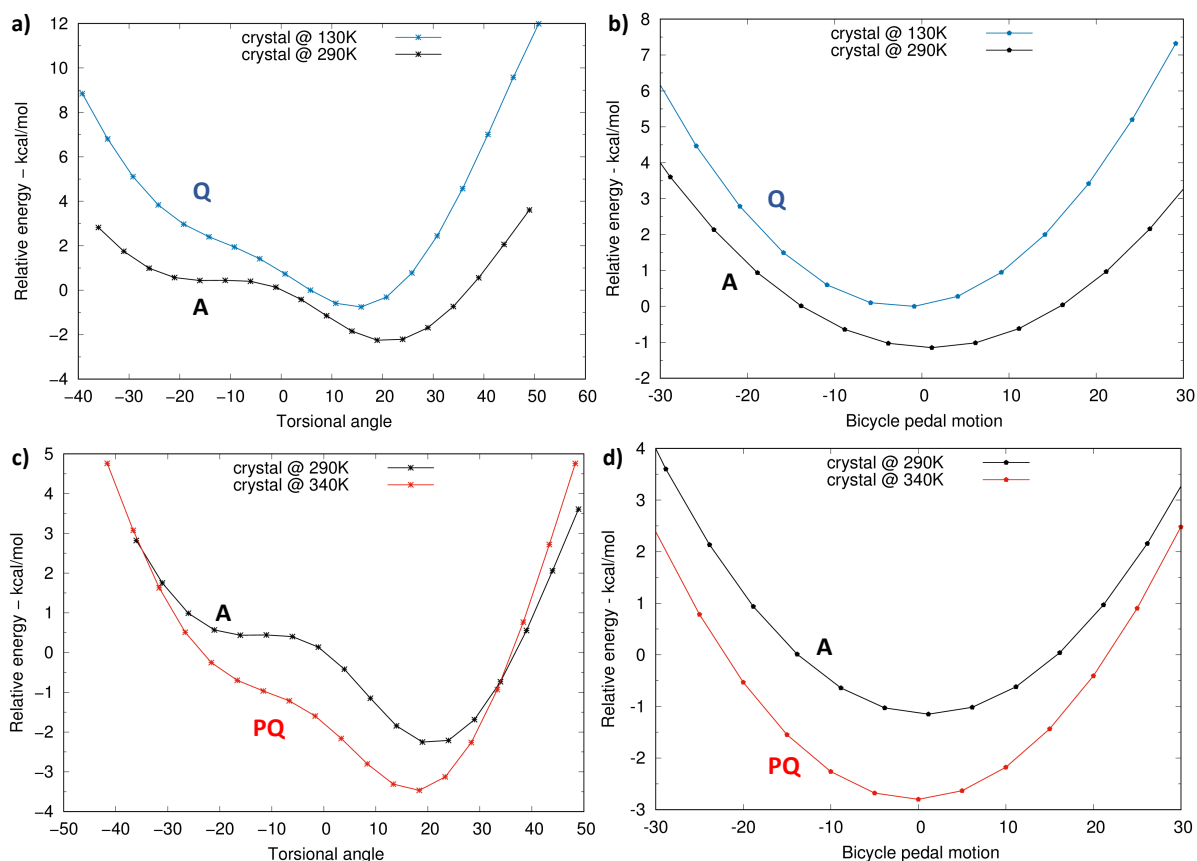
Figure 3.30. Potential energy profiles of the **CAR** molecule inside the crystal structure of **Q** (130 K), **A** (290 K) and **PQ** (340 K) alongside the azobenzene torsion (a&c) and the bicycle pedal motion (b&d). Calculations carried out with the QM/MM ONIOM model on the cluster of **CAR** molecules at B3LYP/6-31G* QM level with electronic embedding for the central molecule. Dreiding force field and charges determined with the Qeq approach are used for the MM part. Figure adapted from Ref. [89].
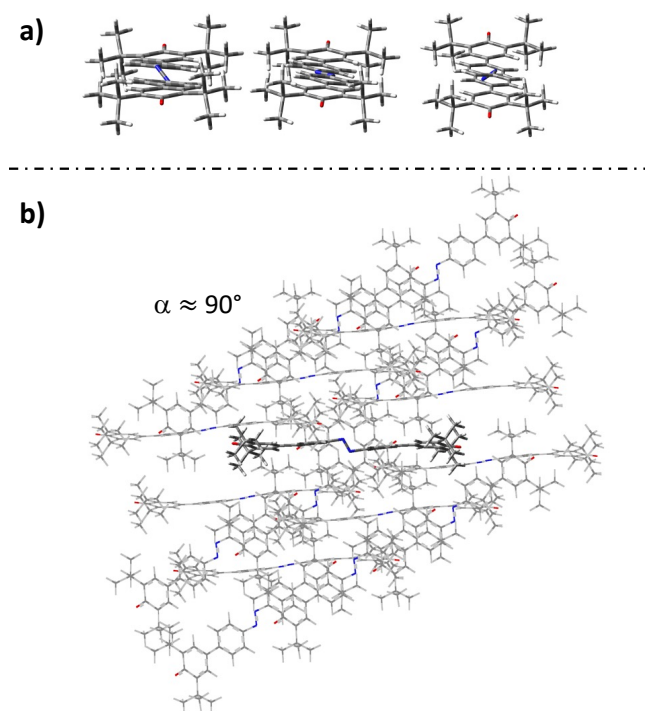
Figure 3.31. Schematic representation of the bicycle pedal motion in a) isolated molecule of **CAR** and b) in the cluster considered for QM/MM calculations. Bicycle pedal motion is considered only on the central molecule. The value of the α angle is indicated. Figure a) adapted from Ref. [89].

The PESs alongside the **Q** → **A** transformation do not intercept each other in the whole range of twisting angle considered (Figure 3.30 a&b). This observation suggests that the **Q** → **A** transformation is progressive and might be driven by entropy effects. The increase of entropy is conducted by thermal excitation/population of low energy torsional modes which is not reflected in the PESs behavior. Thus, at low temperature, heat absorption provokes the preferential excitation of low energy torsional vibrational modes of the "freer" azobenzene moiety driving the π-conjugated structure towards a more aromatic form, or "normal" quinoidal → aromatic transformation.

Differently, the PES along the azobenzene torsion of the **A** → **PQ** transformation (Figure 3.30c) shows a crossing around 30°: **A** is favored for θ larger than 30° and **PQ** form is preferred for θ smaller than 30°. The crossing to the **PQ** structure could be favored and modulated by coupling with the bicycle pedal motion. In fact, by focusing on a trimer of CAR molecule (Figure 3.32) the θ angle is found positive (Figure 3.32a) or negative (Figure 3.32b) only when coupled with a specific orientation of the azo group. This finding suggests a combined role of the azobenzene torsion and the bicycle pedal motion to assist the crossing between PESs and to drive the observed geometry change of **CAR** crystal with increasing temperature. Thus, this aromatic structure steps back to a less-diradical structure thanks to the additional thermal and intermolecularly cooperative population of a molecular bicycle pedal vibrational motion.

Taking into account the distinctive out-of-plane topologies of the twisting and bicycle pedal motions, the two structural transformations can be rationalized:

1. The "normal" **Q** → **A** change is exclusively driven by low energy torsions which always favor the aromatic structures[205];
2. when the higher energy bicycle pedal vibrational states are 'activated' together with the torsional vibrations, the system prefers a less-distorted thermalized molecular structure, **PQ**, with smaller diradical character, outlining a "reversed" quinoidal → aromatic transformation.
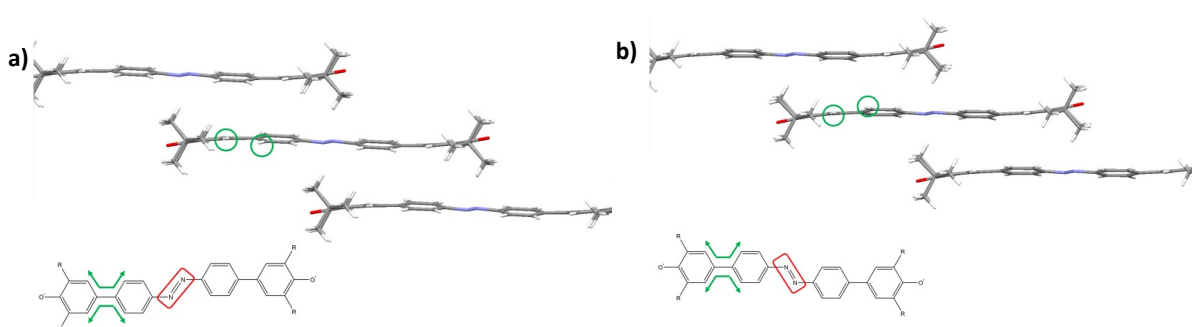
Figure 3.32. Portion of the crystal of **CAR** showing that the positive (a) /negative (b) θ angle (sign determined by the position of the two H atoms circled in green, with respect to the molecular plane) occurs in combination with a specific orientation of the NN azo group, as schematically indicated also on the bottom left part of each figure. Figure adapted from Ref. [89].

3.4 Benchmarking the performance of computational methods to predict the Spectroscopy of Singlet Ground-State Diradicaloids

The discussion on the lowest electronic states of diradicaloids presented in Section 3.1 points to a distinctive character of diradical molecules, that is the presence of a low-lying DE state. The exact energy location of the DE state with respect to the bright SE state, is crucial for the photophysical processes, for linear and non-linear optical (NLO) properties (since the DE state is active in two-photon absorption) as well as for the influence on luminescence efficiency, because of its general dipole-forbidden character.

Because of the large molecular dimension of several recently synthesized diradicaloids, it is desirable to predict their photophysical properties relying on cheaper computational tools. We therefore discuss cost-effective DFT-based computational approaches that can capture, with suitable accuracy, the excitation energies of these low-lying electronic states. Concentrating on these peculiar properties, we have considered a library of conjugated diradicals with the aim of predicting their optical properties and specifically the location of the lowest lying excited states.

For this purpose, we chose a sample of recently synthesized open-shell singlet diradicaloids (Figure 3.33) encompassing Superoctazethrene (SOZ)[206], Superheptazethrene (SHZ)[138], Nonazethrene (NZ)[207], Quarteranthene (QANTHENE)[135], Bisphenalenyl (BISPHE)[134], Diindeno-fused-bischrysene (DFB)[137], Bis-fluoreno-pyrene (FP)[140], Tri-*p*-quinodimethane (TPQ)[133], Thiophene-based Heterophenoquinone (2TIO)[66], Peritetracene (PT)[208], Diindenophenanthrene derivative (DIPh)[209] and some tetracyano oligorylene derivatives with increasing chain length (nR-CN, where n indicates the number of naphthalene units) [150,151]. All these molecules show varying diradical characters. For each of them we determined CS ground state geometries using B3LYP and CAM-B3LYP functionals. The corresponding geometry will be named as CS-B3LYP and CS-CAM-B3LYP or simply CS-CAM. When available, we also determined the BS ground state geometries using the unrestricted version of the two aforementioned functionals. The so-determined geometries are known as BS-B3LYP and BS-CAM-B3LYP (or simply BS-CAM). 6-31G* basis set is considered. Four types of calculations are performed to study their low-lying excited states, namely the bright SE state dominated by H → L excitation and the formally dark DE state. Specifically, TD-B3LYP is adopted only for the SE state; while TD-UB3LYP, SF-TDBHHLYP and DFT/MRCI methods are adopted to study both the SE and DE states. 6-31G* basis set is used if not specified elsewhere. The CS and BS geometries optimized, respectively, at restricted and unrestricted B3LYP level are considered for TD-B3LYP calculations, whereas for TD-UB3LYP and SF-TDBHHLYP calculations only the BS-B3LYP geometry is used. For the nR-CN system, no BS-B3LYP geometry is found, thus TD-UB3LYP and SF calculations were not carried out. DFT/MRCI calculations are applied to all molecules using both the original[107] and the R2018[108] parametrizations.

The B3LYP functional is selected thanks to its general reliable performance for large conjugated systems[210–212] and its general smaller spin contamination compared to hybrid functionals with larger contributions of HF exchange[213] .
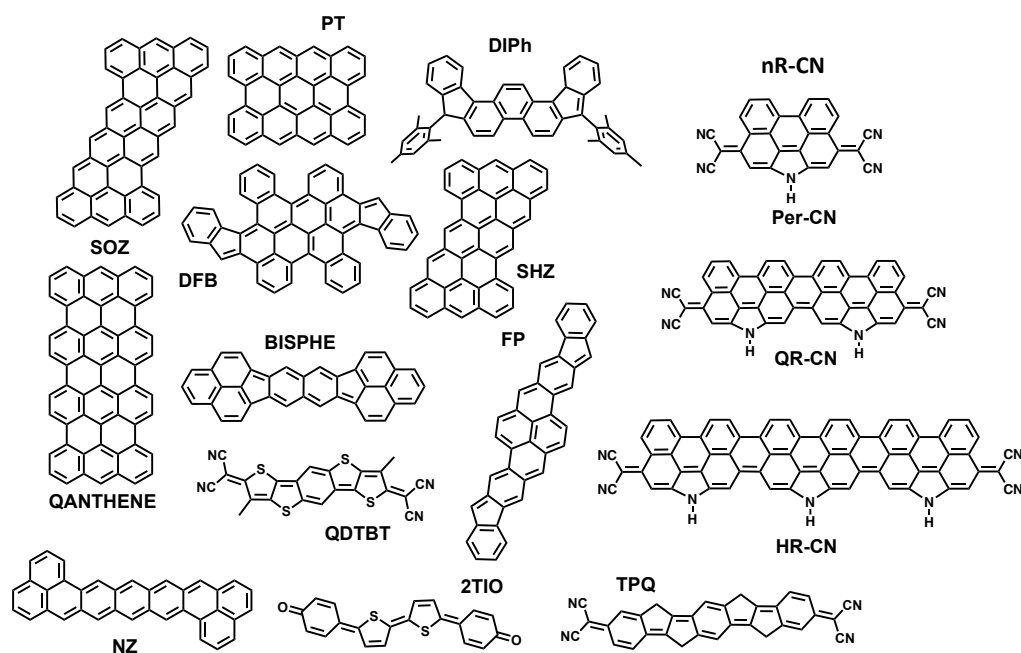
Figure 3.33. Chemical structures of the investigated molecules, all displaying varying diradical character.

Before starting to examine the performance of DFT-based methods, it is important to classify the molecules according to their diradical characters.

3.4.1 Diradical character

The diradical character is evaluated at both CS and BS geometries. The stabilization energies of the BS structures compared to the CS ones are listed in Table 3.8. The BS structures are available for almost all molecules either at UB3LYP and UCAM-B3LYP levels. For a generic molecule, its stabilization energy computed at UCAM-B3LYP is larger than that computed at UB3LYP level. Thus, this study shows that generally, the stabilization energy of the BS structure depends on the functional used and especially, for hybrid functionals, it depends on the amount of the HF exchange included. The larger is the HF exchange amount, the larger is also the corresponding computed stabilization energy.

For each of the so-obtained geometry we calculated Yamaguchi's y_0 parameter at PUHF level. $y_0^{PUB3LYP}$ and y_0^{PUCAM} are also calculated for BS-B3LYP and BS-CAM-B3LYP geometries, respectively. On the other hand, Grimme's N_{FOD} value is calculated only for BS-B3LYP geometries (Table 3.9). As already mentioned in previous work by our group[67,90], it should be stressed that <u>for a single molecule, the y_0 value depends on the level of theory used to determine the ground state geometries and considering the same geometry, y_0 determined at different levels of theory are different</u>.

Taking y_0^{PUHF} as an example, its value depends on the geometry considered. Generally, BS geometries exhibit higher y_0 values compared to the corresponding CS geometries. Secondly, the amount of HF exchange in hybrid functionals influences y_0 values: in CS geometries, a larger contribution of HF exchange determines a smaller y_0; while in BS geometries, the result is the opposite. Conversely, considering the same geometry, *e.g.,* BS-B3LYP, y_0^{PUHF} is greater than $y_0^{PUB3LYP}$. The same conclusion can be made comparing y_0^{PUHF} and y_0^{PUCAM} at BS-CAM

geometries. Thus, from this study an emerging recommendation is to always <u>specify the level of theory/functional used to evaluate y_0</u>. When reporting y_0 values, it is important to refer precisely to the method and geometry employed to calculate the diradical character.

Table 3.8. CS to BS stabilization energies of studied molecules evaluated at B3LYP(UB3LYP)/6-31G* and CAM-B3LYP(UCAM-B3LYP)/6-31G* levels.

	B3LYP	CAM-B3LYP
Molecule	ΔE (kcal/mol)	ΔE (kcal/mol)
2TIO	1.1	7.3
QDTBDT	1.8	10.5
NZ	3.4	-
BISPHE	3.6	15.7
DIPh	3.7	-
DFB	2.9	9.0
FP	3.7	11.5
PT	4.5	-
TPQ	5.2	17.3
SHZ	7.7	20.1
SOZ	10.8	-
QANTHENE	8.8	21.5
Per-CN	0.0	0.04
QR-CN	0.0	1.25
HR-CN	0.0	2.56

While y_0 values are limited to diradical character, the N_{FOD} parameter offers the advantage to take into account, in a single descriptor, also the multi-radical character of the investigated system. Since its introduction in 2015, the N_{FOD} parameter has been widely employed to characterize a variety of open-shell molecules encompassing small molecules, such as boron-dipyrromethene (BODIPY)[214], and very large donor-acceptor semiconducting system with pronounced multi-radical character [215–220]. N_{FOD} measures the so-called 'hot' or correlated electrons: when its value exceeds two, more than two electrons need to be considered for a proper inclusion of correlation effects in the description of both the ground and excited states. Reminding the 2e-2o model for the description of the DE state, we can already say that when N_{FOD} exceeds two, this model is clearly insufficient. For the set of diradicals investigated here (Table 3.9), it can be seen that the N_{FOD} value remains below 2 in most cases suggesting the suitability of the 2e-2o model for the investigation of the DE state. In other cases (*e.g.* DFB, SHZ, SOZ, and QANTHENE), however, it exceeds 2 (Table 3.9) indicating, for these molecules, a multiradical character and the necessity to correlate more than two electrons.

It is now interesting to explore the correlation between the stabilization energy and diradical character. Taking the BS-B3LYP geometry for all molecules as an example we find that the diradical character, either in terms of N_{FOD} or y_0, is larger for molecules displaying larger CS-BS stabilization energy (Figure 3.34). There is also a good correlation between y_0 and N_{FOD}:

molecules with large y_0 values show also very large N_{FOD} numbers.

Table 3.9. Diradical characters of investigated molecules expressed either as y_0 and N_{FOD}. y_0 values are evaluated at PUHF, PUCAM-B3LYP and PUB3LYP levels at CS and BS geometries obtained with B3LYP and CAM-B3LYP functionals. N_{FOD} values are calculated at TPSS/def2-TZVP level with T_{el} = 5000K. The BS-B3LYP geometry is considered here.

Geometry	y_0^{PUHF}				y_0^{PUCAM}	$y_0^{PUB3LYP}$	N_{FOD}
	CS-CAM	CS-B3LYP	BS-B3LYP	BS-CAM	BS-CAM	BS-B3LYP	BS-B3LYP
2TIO	0.46	0.56	0.67	0.74	0.51	0.10	1.60
QDTBDT	0.53	0.60	0.68	0.73	0.53	0.14	1.55
NZ	-	-	-	-	-	0.23	1.80
BISPHE	0.83	0.84	0.85	0.86	0.61	0.26	1.70
DIPh	-	-	-	-		0.28	1.75
DFB	0.65	0.73	0.80	0.81	0.54	0.30	2.26
FP	0.62	0.71	0.80	0.81	0.63	0.34	1.90
PT	-	-	-	-	-	0.36	1.87
TPQ	0.66	0.77	0.86	0.88	0.77	0.42	1.75
SHZ	0.78	0.83	0.87	0.87	0.71	0.52	2.14
SOZ	-	-	-	-	-	0.66	2.58
QANTHENE	0.85	0.89	0.92	0.92	0.84	0.71	2.34
Per-CN	0.35	0.41	-	0.36	0.00	-	-
QR-CN	0.50	0.57	-	0.58	0.09	-	-
HR-CN	0.57	0.65	-	0.68	0.21	-	-
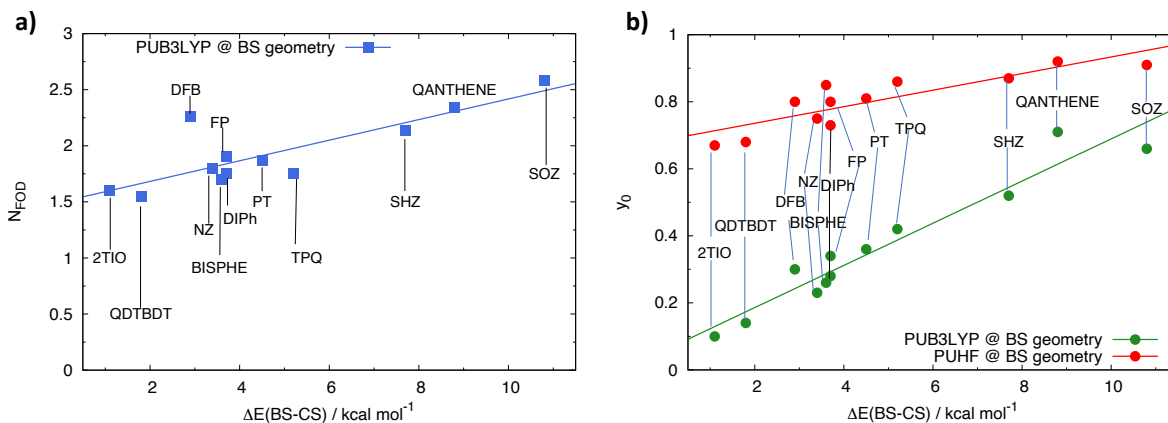
Figure 3.34. Correlation between diradical character descriptors and the CS to BS stabilization energies. (a). N_{FOD} as a function of the stabilization energy for the investigate molecules. (b). y_0 as a function of the stabilization energy. The BS-B3LYP geometry is considered for all molecules. N_{FOD} is calculated at TPSS/def2-TZVP level and y_0 is calculated at PUHF and PUB3LYP level with 6-31G* basis set.

3.4.2 The SE state from DFT-based methods

Computed SE state energies of the selected molecules are collected in Table 3.10. To better appreciate the performance of each method and the relation with the diradical character, the energy differences between the computed and experimental SE energies are plotted as function of N_{FOD} in Figure 3.35 along with the linear fitting. It should be noted that computed data can

be affected by systematic errors since we considered simpler models of the selected molecules (*i.e.* not including substituents) compared to the real system and solvent effect is not considered in these calculations.

Table 3.10. Excitation energy of the bright SE state computed with TD-(U)DFT and DFTMRCI approaches. Computed results are compared with experimental data (where available). All energies are reported in eV.

	DFTMRCI Original	DFTMRCI R2018	TD-UB3LYP	TD-B3LYP	TD-B3LYP	Exp.* (eV)
Geometry			BS B3LYP		CS B3LYP	
2TIO	1.95	1.74	1.81	1.86	1.98	1.88[a]
QDTBDT	1.91	1.64	1.81	1.75	1.89	1.85[b]
NZ	1.84	1.67	-	-	-	1.85[c]
BISPHE	1.66	1.39	1.47	1.35	1.38	1.43[d]
DIPh	1.39	1.32	-	-	-	1.55[e]
DFB	1.19	1.05	1.13	1.01	1.13	1.25[f]
FP	1.62	1.39	1.51	1.32	1.47	1.48[g]
PT	1.55	1.27	-	-	-	1.42[h]
TPQ	1.57	1.41	1.48	1.44	1.59	1.46[i]
SHZ	1.65	1.38	1.49	1.01	1.11	1.50[j]
SOZ	1.40	1.35	-	-	-	1.51[k]
QANTHENE	1.58	1.15	1.28	0.77	0.87	1.35[l]
Per-CN	2.12	2.03	-	-	2.32	1.98[m]
QR-CN	1.49	1.38	-	-	1.64	1.41[n]
HR-CN	1.34	1.13	-	-	1.33	1.27[n]

* Absorption spectra registered: [a]in n-hexane[66]; [b]in CHCl₃ [141]; [c]in CH₂Cl₂ [207]; [d]in CHCl₃ [134]; [e]in CH₂Cl₂ [209]; [f]in CH₂Cl₂ [137]; [g]in CH₂Cl₂ [140]; [h]in CH₂Cl₂ [208]; [i]in CH₂Cl₂ [133]; [j]in CH₂Cl₂ [138]; [k]in CCl₄ [206]; [l]in CH₂Cl₂ [135]; [m]in CHCl₃ [150]; [n]in toluene [151].

Figure 3.35a shows the results from TD-(U)B3LYP calculations. It can be seen that the linear fittings from the two sets of TD-B3LYP results (red and green squares) are very similar suggesting a similar average quality of the method used. With the increase of diradical character (N_{FOD} values) the energy difference between the two sets of data increases. This is an indication of the increased geometry difference between investigated molecules' CS and BS geometries. Furthermore, TD-B3LYP calculations based on CS reference configuration underestimate the excitation energy of the dipole-allowed SE state. This underestimation is larger in molecules showing larger diradical character (N_{FOD} in this case). The increasing diradical character is a sign of larger effects of static correlation in the ground state description. The lack of static correlation in RDFT methods generally leads to the overestimation of the ground state energy. Indeed, larger diradical molecules (higher N_{FOD} values) show stronger deviation from the experimental values (Figure 3.35a) reaching also 0.6 eV in the case of QANTHENE. On the other hand, TD-UB3LYP calculations, that is to say TD calculations based on a BS reference configuration, at BS geometries (purple circles in Figure 3.35a) exhibit minor average deviations from the experimental results. The quality is good for all investigated molecules independently from their N_{FOD} values. In fact, the unrestricted BS reference configuration is

able to recover static correlation effects in the ground state which ultimately leads to a better prediction of the excitation energy. A major drawback of the TD-UB3LYP approach is the spin-contamination as discussed in Sections 3.1.3-3.1.4.

On the other hand, Figure 3.35b shows the same trend of energy difference with the computed energies calculated at DFT/MRCI level with two parametrizations: original and R2018. The performance of the two sets of results is very similar. The original parametrization generally overestimates the excitation energy, while the R2018 parametrization does the opposite. The overall results are independent from the N_{FOD} value. Nonetheless, the R2018 parametrization is recommended because of its spin-independent nature[108].

Comparing Figure 3.35a and 3.35b, we can conclude that excitation energies predicted by TD-UB3LYP approach are averagely closer to the observed values than those obtained with DFT/MRCI method. However, the SE state is generally dominated by the H → L configuration, each of the presented methods are suitable as long as the drawbacks of each method are kept in mind. Specifically, the use of TD-UDFT and DFT/MRCI instead of TD-DFT is compulsory for the prediction of the DE state. In this regard, we have already anticipated the limits of TD-UDFT in Section 3.1.4 by deriving an expression of the DE wavefunction. We will see in the next paragraph from the numerical results that the TD-UDFT approach is suitable to predict the DE state only for large diradical character.
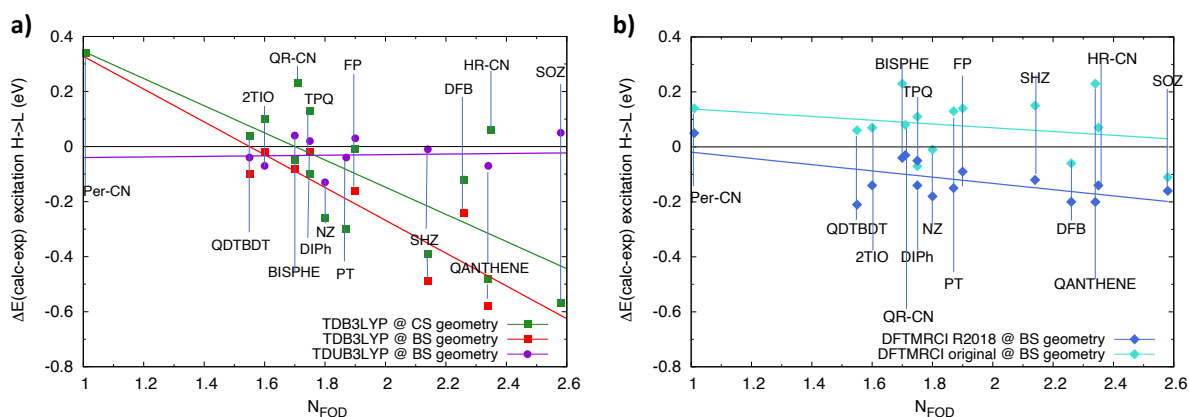
Figure 3.35. Performance of DFT-based methods for the prediction of the SE state for the diradicaloids in Figure 3.33. In y-axis I reported the difference between the computed excitation energies and the experimental ones. In x-axis N_{FOD} values are reported and they act as the identifier of each molecule. a). Excitation energies of the SE state predicted at TD-(U)B3LYP levels. Two geometries are considered here: CS-B3LYP and BS-B3LYP. b). Excitation energies of the SE state predicted at DFT/MRCI level with original (turquoise) and R2018 (blue) parametrizations. Only BS-B3LYP geometries are considered. The lines in the same colors are linear fittings of the computed data to visualize the trends. Vertical bars indicate the compound to which computed data correspond.

3.4.3 The DE state from DFT-based methods

Table 3.11 collects excitation energies of the DE state of diradicals computed at TD-UB3LYP, SF-TDBHHLYP and DFT/MRCI levels of theory. The so-obtained energies are compared with experimentally observed results in Figure 3.36.

The majority of TD-UB3LYP's results (purple circles) is in very good agreement with experiments: most of the computed results are on the bisector or very near to it. Other results, on the contrary, show deviations from experimental data. This behavior can be traced back to

the applicability of the TD-UDFT methods mentioned in Section 3.1.4. First of all, the DE state wavefunction suffers from the triplet component, which accounts for spin contamination. The contribution of singlet and triplet components depends on the BS orbital rotation angle θ (Figure 3.8): when θ is in-between 22.5° and 45°, the singlet component dominates in the DE wavefunction. Furthermore, when BS orbitals are well-localized, which can be achieved when θ is large, the BS reference configuration can recover *via* localization, the static correlation that is missing in the CS reference configuration. The DE state, thus, can be more appropriately and almost correctly described as combination of singly excited configurations: $A^2 + B^2$. In our case, θ values are large enough such that the singlet component is always dominating for the investigated diradicals (see Figure 3.37). Indeed, the S^2 value associated to the DE state remains always acceptably close to the value for a pure singlet spin state, which implies a moderate triplet spin contamination. However, the triplet component is still important when θ is near to 25° as for *e.g.* 2TIO and QDTBDT. On the other hand, for large θ value, diradical character is also very large (Figure 3.9, Eq. 3.18). In this case, there might be a role of multiradical character which can be monitored by considering the N_{FOD} value. When N_{FOD} exceeds two, it means that more than two electrons need to be correlated. This might be the case for some of the investigated molecules such as QANTHENE and SOZ. Summarizing the TD-UDFT method: it can be applied to describe the DE state when the 2e-2o model is valid to a good extent. When N_{FOD} is larger than two, one should be more cautious in considering the suitability of the TD-UDFT method.

Table 3.11. Excitation energy of the dark DE state computed with TD-UB3LYP, SF-TDBHHLYP and DFT/MRCI approaches. Computed results are compared with experimental data (where available). All energies are reported in eV.

Molecule	DFT/MRCI original	DFT/MRCI R2018	TD-UB3LYP	SF-TDBHHLYP	Exp.
2TIO	1.37	1.54	0.98	1.35	1.68[a]
QDTBDT	1.59	1.72	1.07	1.56	1.57[b]
NZ	1.38	1.43	1.22	1.16	1.39[c]
BISPHE	1.58	1.68	1.03	1.57	1.54[d]
DIPh	1.33	1.50	1.21	1.23	1.18[e]
DFB	0.98	1.03	0.91	0.88	0.92[f]
FP	1.22	1.23	1.13	0.93	1.13[g]
PT	1.36	1.48	1.13	1.56	1.23[h]
TPQ	1.31	1.28	1.16	1.01	1.13[i]
SHZ	1.50	1.38	1.32	1.12	1.19[j]
SOZ	1.34	1.14	1.41	0.79	1.07[k]
QANTHENE	1.47	1.26	1.17	0.94	1.08[l]
Per-CN	2.05	2.23	-	-	2.06[m]
QR-CN	1.25	1.37	-	-	1.23[n]
HR-CN	0.97	1.08	-	-	1.12[o]

* Absorption spectra registered: [a]in n-hexane[66]; [b]in CHCl₃ [141]; [c]in CH_2Cl_2 [207]; [d]in CHCl₃ [134]; [e]in CH_2Cl_2 [209]; [f]in CH_2Cl_2 [137]; [g]in CH_2Cl_2 [140]; [h]in CH_2Cl_2 [208]; [i]in CH_2Cl_2 [133]; [j]in CH_2Cl_2 [138]; [k]in CCl₄ [206]; [l]in CH_2Cl_2 [135]; [m] two-photon absorption spectrum in THF [150]; [n]spectrum measured at low temperature from prof. J. Casado's personal communications on unpublished results; [n]in toluene [151].
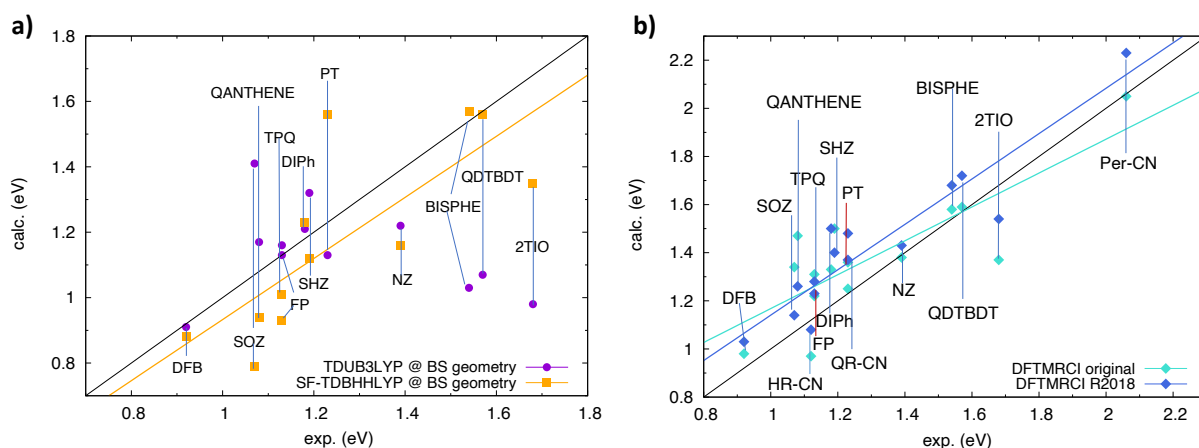
Figure 3.36. DFT-based methods computed DE state energies versus experimental results. a). Excitation energies of the DE state are calculated at TD-UB3LYP and SF-TDBHHLYP levels. b). DE state predicted at DFT/MRCI level with original (turquoise) and R2018 (blue) parametrizations. The lines in the same colors are linear fittings of the computed data to visualize the trends. Vertical bars indicate the compound to which computed data correspond.
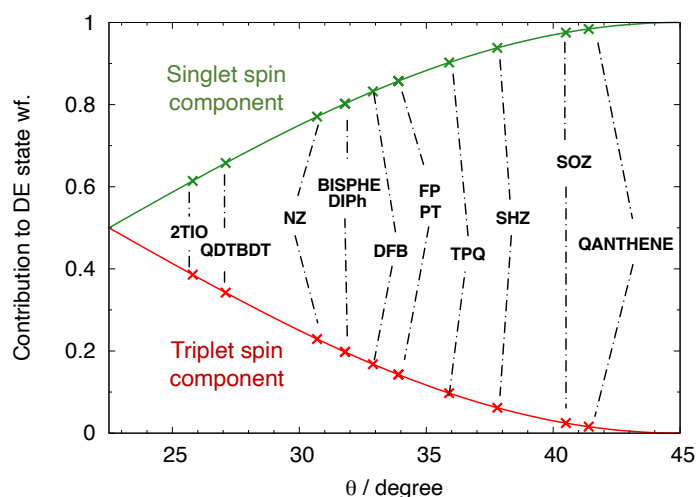
Figure 3.37. Contributions of the singlet and triplet components to the DE state described at TD-UDFT level according to Eq. 3.15 as function of θ for investigated diradicals. Figure adapted from Ref. [91].

In addition, TD-UDFT shows one intrinsic limitation, that is to say the same contribution of the ground $|H_{CS}\overline{H}_{CS}\rangle$ and $|L_{CS}\overline{L}_{CS}\rangle$ doubly excited configurations as already mentioned in Section 3.1.4. This restriction may not be optimal and may lead to inconsistencies for systems displaying marked but not perfect diradical character. In summary, TD-UB3LYP may provide a good estimate of the energy location of the DE state for large diradical with modest multiradical character, as shown by the linear fitting in Figure 3.38.

On the contrary, the SF-TDDFT method is not formally limited by the diradical character of the system investigated. Its quality can be appreciated from orange squares and the linear fitting in Figure 3.36a. The trend of the linear fitting goes almost parallel with the experimental results (black bisector) showing an average similar accuracy for the set of investigated diradicals. The excitation energies of the DE state are generally underestimated by SF-TDBHHLYP calculations.

Compared to TD-UDFT method, the SF approach shows some advantages. The most important one is the suitability to describe systems also displaying some degree of multiradical character because double excitations are not limited to the 2e-2o space. However, the principal

drawback of this approach is the spin contamination. The source of this contamination is not the triplet component typical of TD-UDFT approach. The origin of spin contamination is rather the **spin incompleteness**: only excitations formed within the 2e-2o space is spin complete, other excited configurations formed in a larger space, by spin-flipping, will miss their spin complements leading to a spin-contaminated solution [106]. In this regard, recent implementations of the **spin-adapted (sa) SF** approach[221] can overcome this limit.

Figure 3.36b shows the comparison between the DFT/MRCI computed excitation energies and the experimental results. Turquoise diamonds represent data from the original parametrization, whereas results from the new R2018 parametrization are shown in blue. The original parametrization generally overestimates the DE state. Only two exceptions, where energies are underestimated, are observed. Its overall trend is acceptable for the set of molecules investigated since most of the computed results are very near to the bisector. The linear fitting (turquoise line in Figure 3.36b) is not parallel to the bisector probably due to some large overestimations (*e.g.* QANTHENE and SOZ) and large underestimation (*e.g.* 2TIO).

On the other hand, the linear fitting of data computed with R2018 parametrization is more parallel to the bisector and it is just a little bit above the latter. The parallel trend shows a similar performance for all investigated molecules, with a systematic tendence to overestimate the DE states' excitation energies. Comparing these two sets of data, R2018 parametrization provides better results: DE state energies calculated with this parametrization are more similar to the experimental ones. Additionally, similarly to SF-TDDFT, also DFT/MRCI is formally independent from diradical character. It can be concluded that, compared to the original parametrization, R2018 is more suitable to predict the location of the DE state for molecules with diradical and multiradical characters.
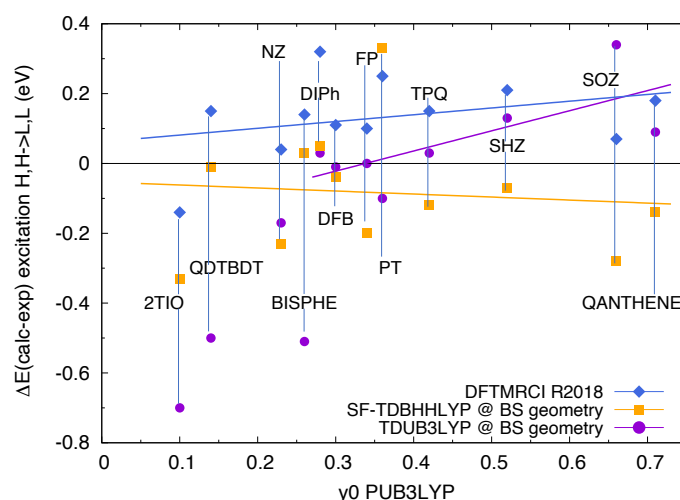
Figure 3.38. Energy difference between the computed DE state excitation energies and experimental results as function of $y_0^{PUB3LYP}$ for the investigated diradicals.

Figure 3.38 encloses the comparison between the three methods proposed for the prediction of the DE state. Differences between the calculated DE state energies and the experimentally observed ones are plotted as function of diradical character, here represented by $y_0^{PUB3LYP}$. All these data are linearly fitted. It is clear that TD-UB3LYP's results (violet circles) are influenced by diradical character: when diradical character is large enough (roughly $y_0^{PUB3LYP} > 0.3$) its

quality is satisfactory. On the contrary, results from SF-TDBHHLYP and DFT/MRCI are, indeed, independent from the amount of diradical character. SF method systematically underestimates the excitation energy of the DE state for diradical molecules, while, for DFT/MRCI method, a systematic overestimation of the DE state energy is observed.

3.5 Emission from the formally dark DE state of a Thiele derivative

In order to employ a conjugated molecule in a real optoelectronic device, for instance in OLED, two major problems need to be solved: molecular stability and luminescence. On one hand, the stability problem can be overcome by different synthetic strategies including cross-conjugation. On the other hand, there are few examples and very little information regarding diradicaloids' luminescence property. This may limit their application in devices which requires light emission such as OLED. Nonetheless, the Thiele's Hydrocarbon (TH, Figure 3.39)[222], a singlet diradicaloid characterized by *p*-QDM core, was described to be fluorescent in solution but its fluorescence is oxygen and light sensitive[223]. From the viewpoint of organic synthesis, perchlorination is an economic and efficient strategy to stabilize triaryl radicals (PTM) and TH-derived diradicals [224,225]. Indeed, chlorine atoms exert a shielding effect on the odd electron localized on the *ipso*-C[226]. Unfortunately, perchlorination leads to the decrease of fluorescence quantum yield in PTM (comparing with its unperchlorinated *partner* TTM) [227,228] and the loss of fluorescence in TH derivatives [225,229].
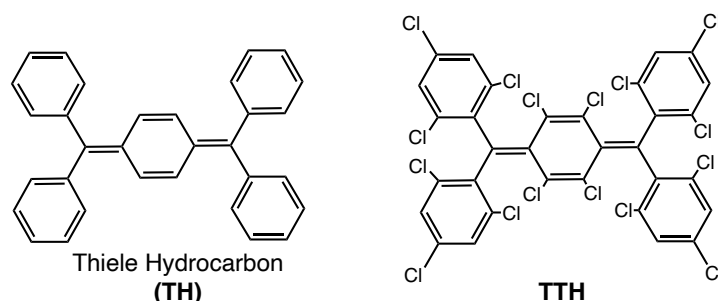
Figure 3.39. Chemical structures of Thiele Hydrocarbon (TH, left) and TTH (right), molecule studied in this work.

Following these guidelines, our collaborators from the University of Bari synthesized a TTM-like Thiele Hydrocarbon (TTH, Figure 3.39). The newly synthesized compound shows extraordinary stability with respect to air and light and exhibit an intense deep-red fluorescence with high quantum yield in solution (around 0.75). While the absorption maxima show no difference in different solvents, the molecule exhibits an intense solvatochromic emission with a large Stokes shift of ca. 0.66 eV in the most polar solvent considered (THF).

Generally, to observe a solvatochromic emission, the responsible excited state should bear a charge-separation (dipole moment) remarkably different with respect to the ground electronic state[230]. Since TTH is not polar, the only possibility would be to have an excited state with charge-transfer (CT) character. However, because the molecule is symmetric, it is difficult to justify a neat charge transfer from one side to the other of the molecule, upon excitation.

Quantum-chemical calculations aiming at providing new insights about the physical nature

of its emitting state, were thus performed.

3.5.1 Computational details

The GS equilibrium structure of TTH was obtained at B3LYP and M06-2X levels together with the inclusion of dispersion-like intramolecular noncovalent interactions: D3BJ correction term was used for B3LYP and D3 for M06-2X[231,232]. Def2-SVP[233] basis set was used. y_0 value was calculated at PUHF/6-31G** level based on the computed equilibrium structures. Additionally, the GS geometry was obtained also at *state-specific* CASSCF (6,6)/def2-SVP level.

For the study of excited states, TD-M06-2X/def2-SVP +D3 level was used to simulate the electronic absorption spectrum of TTH. The SE state geometry was then optimized at the same level of theory. To determine the energy location of the DE state, DFT/MRCI calculations[108] with the new R2018 parametrization were carried out. Geometry of the DE state was optimized at *state-specific* CASSCF (6,6) level using the def2-SVP basis set. The resolution of identity approximation and the related basis sets for both Coulomb and HF exchange integrals (RI-JK)[234] were used. Furthermore, excitation energies at SE and DE geometries were determined with CASSCF (6,6) level followed by NEVPT2[112,114] and CASPT2[110,111] corrections to include dynamical correlation. Four roots were calculated for the state averaged modelling of the singlet excited states.

3.5.2 The ground state of TTH

There are no open-shell structures found at the two levels of theory that we used. Only the CS structure is considered for the following considerations. y_0 determined at B3LYP and M06-2X geometries show comparable values (respectively 0.32 and 0.44) suggesting a small-medium diradical character for TTH.
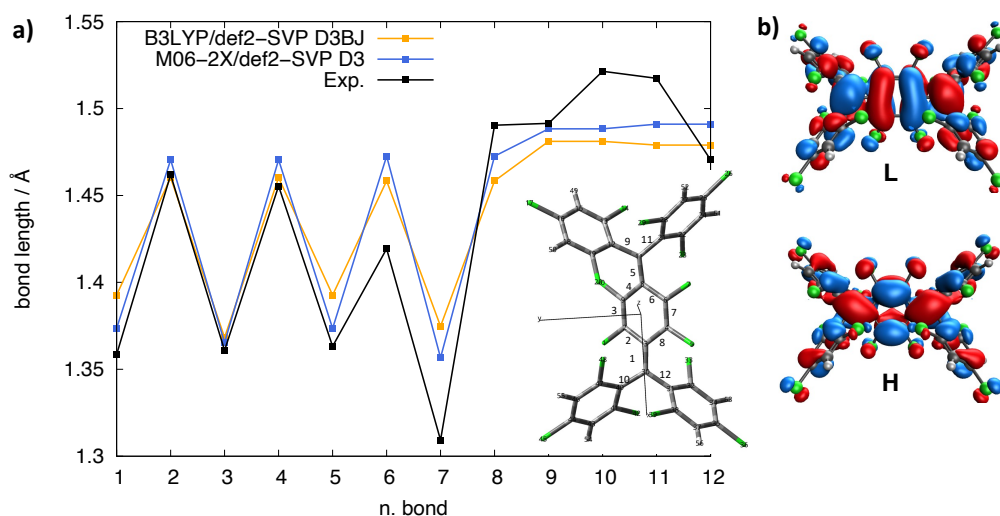
Figure 3.40. a). Computed equilibrium bond lengths (Å) of the *p*-QDM core of TTH in its ground electronic state computed at B3LYP/def2-SVP+D3BJ (orange) and M06-2X/def2-SVP+D3 (blue) levels. Bond lengths of the SCXRD structure are shown in black. The bond numbering is shown inside the plot. b). Shapes of frontier molecular orbitals of TTH.

61
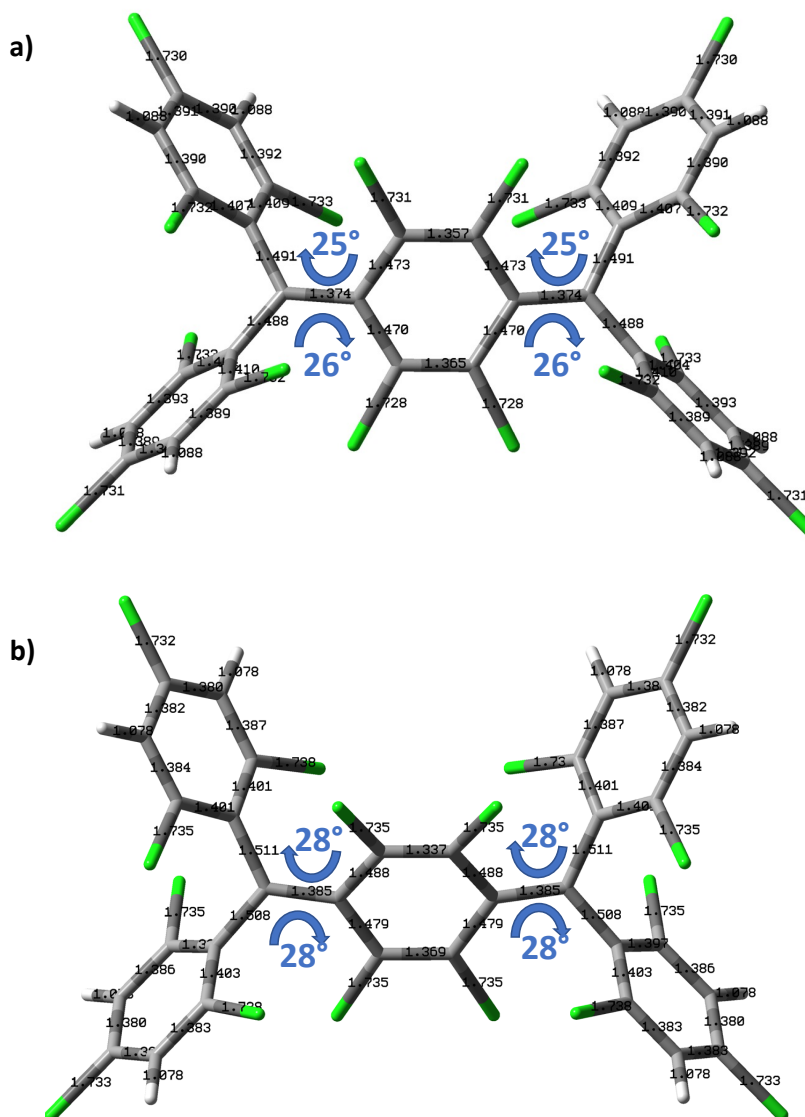
Figure 3.41. Computed bond lengths (Å) of the ground state of TTH at (a) M06-2X/def2-SVP +D3 level and (b) CASSCF (6,6)/def2-SVP level.

Computed bond lengths at B3LYP/def2-SVP+D3BJ and M06-2X/def2-SVP+D3 levels are compared with the experimental ones, determined with *Single Crystal X-ray Diffraction* (SCXRD) technique (Figure 3.40). Both functionals predict similar bond lengths in good agreement with the quinoidal structure reported by SCXRD (Figure 3.40a). The quinoidal nature of the GS can be appreciated also from the shape of the frontier molecular orbitals (Figure 3.40b): the H orbital shows electron density in bonds 1, 3, 5 and 7 (for bond number see Figure 3.40a). Considering the similarity of the two structures determined at DFT level and the average better performance of M06-2X for bonds out of the *p*-QDM core (bonds from 9 to 12), as well as the similarity of M06-2X structure compared to the CASSCF one (Figure 3.41), the M06-2X geometry is considered for further consideration.

TTH is not planar: the central *p*-QDM core is twisted with respect to the terminal groups. The twisting angles are detected to be 37, 29, 26 and 30° according to SCXRD, in good agreement with calculations: 25 and 26° at M06-2X/def2-SVP+D3 level and 28° at CASSCF (6,6)/def2-SVP level.

3.5.3 Excited states of TTH

The computed absorption spectrum of TTH is compared with the experimental absorption spectrum in Figure 3.42. The two major bands experimentally observed are reproduced by calculations. The lowest energy absorption band is assigned to the SE state since its wavefunction is dominated by the H→L excitation. The TD-M06-2X computed excitation energy is overestimated, a typical feature of the functional employed.

Usually, the fastest photophysical process, after absorption, is the vibrational relaxation to the excited state minimum[235] (in this case the SE state). The SE state geometry is optimized at TD-M06-2X level and the optimized structure is shown in Figure 3.43. The SE geometry shows elongated exocyclic CC bonds (bonds 1 and 5) with respect to the corresponding ones in the GS: they become 1.442 Å compared to 1.385 Å in the GS suggesting a diradicaloid structure (see also the nature of the LUMO orbital in Figure 3.40b). The central benzene core becomes more planar and more twisted with respect to terminal groups: the twisting angle increases to 47° for all four angles considered suggesting an even more symmetrized structure for the SE state. Due to this symmetric structure, the solvent-dependent emission cannot be originated from the SE state.
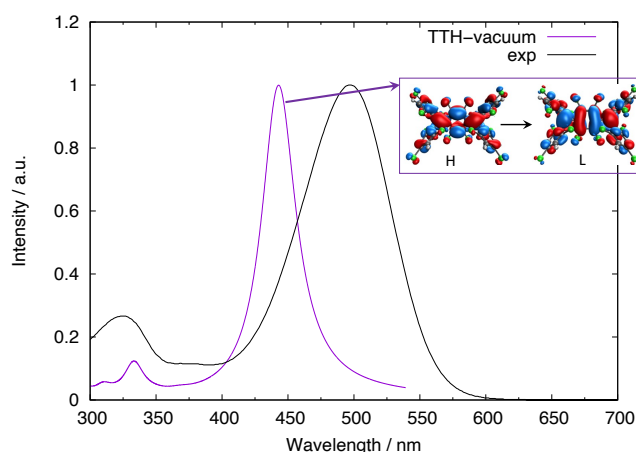
Figure 3.42. Comparison between experimental (black) and TD-M06-2X/def2-SVP +D3 (purple) computed absorption spectrum of TTH.

On the other hand, the H/L gap is drastically reduced at the SE geometry. It becomes 2.60 eV compared to 4.36 eV calculated at the GS geometry suggesting an energy decrease of the doubly excited configuration and consequently of the DE state.

What about the DE state, then? Can it be responsible for the observed emission? To determine the role of the DE state, its energy location was determined firstly with the DFT/MRCI method at the GS and SE optimized geometries (Table 3.12). Both calculations show the DE state to be above the SE state. Both states decrease at the equilibrium geometry of the SE state. The decrease of the DE state is however steeper, leading to a smaller gap between the two excited states (0.50 eV at the GS geometry and 0.30 eV at the SE geometry). In the meanwhile, the weight of the doubly excited configuration, either in the GS wavefunction or in the DE wavefunction, increases (Table 3.12) largely. All these data are consistent with the decrease of the H/L gap.
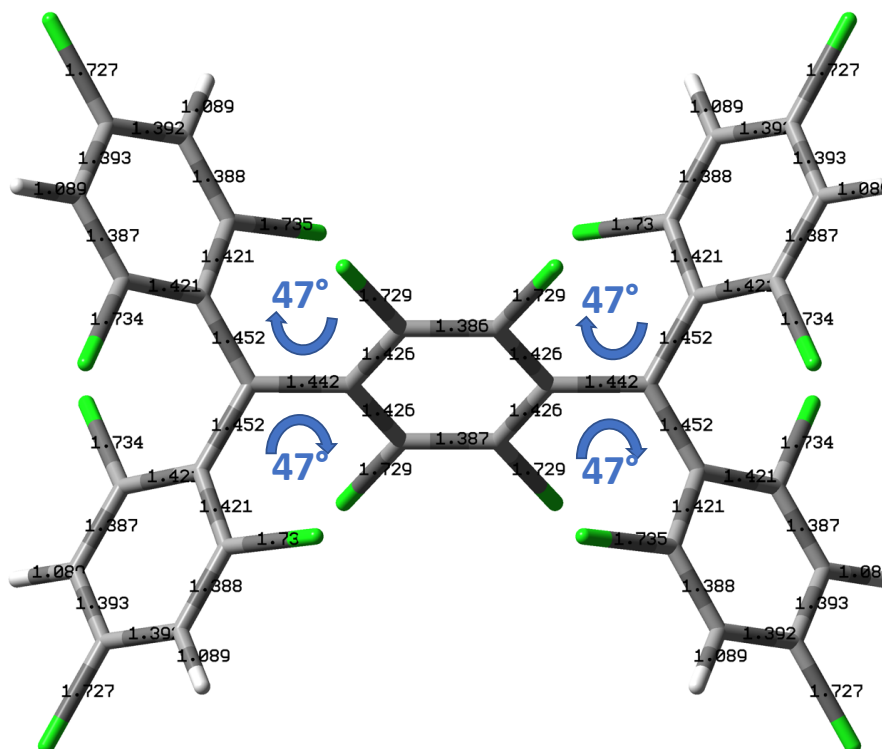
Figure 3.43. Computed bond lengths (Å) at the optimized geometry of the SE state (dominated by the H → L excitation) of TTH, from TD-M06-2X/def2-SVP +D3 calculations**.**

Table 3.12. Excitation energies of the SE and DE states computed with DFT/MRCI at the geometries of the GS and bright SE excited states of TTH. The contribution of the doubly excited configuration $c_{HH \to LL}$ to the wavefunction of GS and DE states is listed in the last column.

Electronic state	Excitation energy (eV)	Excitation energy (nm)	$c_{HH \to LL}$
At the **GS** equilibrium geometry			
GS	---	---	0.12
SE	2.70	459	---
DE	3.20	388	0.29
At the **SE** state equilibrium geometry			
GS	---	---	0.30
SE	1.82	681	---
DE	2.12	585	0.60

Following the results of DFT/MRCI that point to a DE state very close to the SE state, we carried out CASSCF calculations. Since CASSCF only includes static correlation effects, the energies of the excited states were then corrected with NEVPT2 and CASPT2 calculations. There is a noticeable difference between the excited states patterns predicted by TD-DFT and CASSCF/NEVPT2 methods (Figure 3.44) at the SE state equilibrium. While the former is unable to predict the DE state, location of the DE state predicted by CASSCF/NEVPT2 is close to that of the SE state. NEVPT2 predicts the DE state to be slightly above the SE state. On the contrary, according to CASPT2 calculation, the DE state is the lowest singlet excited state. This difference can be traced back to the different Hamiltonians and perturbers used by these two perturbative methods as mentioned in Section 2.5. Nevertheless, the important outcome is that both predict the SE state to be very close to the DE state.

Owing to the vicinity of the DE state and the increasing weight of the doubly excited configuration both in the GS and DE states, we also determined the geometry of the latter, that

was optimized at CASSCF (6,6)/def2-SVP level (Figure 3.45). The optimized geometry of the DE state displays remarkably elongated exocyclic CC bonds: they become 1.471 Å compared to 1.442 Å of the SE state and 1.385 Å of the GS. The dihedral angle between the core and terminal groups increases to ca. 50°. Both two geometry changes (twisting angle and bond length) suggest a small barrier for twisting around the exocyclic CC bond.

Figure 3.44. Comparison between low-lying excited states of TTH predicted at the equilibrium structure of the SE state at TD-M06-2X/def2-SVP, CASSCF (6,6)/NEVPT2 and CASSCF (6,6)/CASPT2 levels. The thick green line is the DE state strongly affected by electron correlation. Molecular orbitals involved in the excitations are depicted inside squares which color code reminds the state to which the excitations belong to.

Figure 3.45. Computed bond lengths (Å) at the optimized geometry of the DE state (dominated by the H,H → L,L excitation) of TTH, from CASSCF (6,6)/def2-SVP calculations.

This distinctive character of the DE geometry, in which the excitation drives a dramatic geometry change (elongation) to the exocyclic CC bonds, reminds a very well-known investigated system: ethylene in the context of sudden polarization. Thus, we explored

65

computationally whether a mechanism similar to sudden polarization might explain the observed luminescence of TTH. It should be noted that following the twisting around the exocyclic CC bond along the DE state is not an easy task: a multireference method (*e.g.*, CASSCF/NEVPT2) is required and TTH is not a small molecule. For this reason, we carried out an investigation on a smaller *p*-QDM derivative, whose emission has also been documented.

Before discussing these computational results I recall in the following subsection, the theoretical interpretation of the sudden polarization[84,236–239] observed in 90°-twisted ethylene.

3.5.3.1 Sudden polarization in twisted ethylene

Sudden polarization (SP) is one of the manifestations of electron transfer in the electronically excited states of molecules. Such effect has been proposed for twisted ethylene. Ethylene is the analogue of H_2 in the Hückel model. Pathway along the twisting around the double bond corresponds, in a way, to the dissociation of H_2, mentioned in Section 3.1.2. Indeed, both can be seen as the evolution to a decoupled system starting from the strongly coupled situation. Also ethylene can be described within the 2e-2o model if the Hückel approximation is considered. Analogously, ignoring the triplet state, the wavefunction of the three singlet states can be written as:

$$\Psi_{GS} = \lambda \pi_+^2 - \sqrt{1 - \lambda^2}\pi_-^2$$

$$\Psi_{SE} = \pi_+ \pi_-$$

$$\Psi_{DE} = \sqrt{1 - \lambda^2}\pi_-^2 + \lambda \pi_+^2$$

(3.26)

with π_+ and π_- indicating HOMO and LUMO, respectively. According to the discussion in Section 3.1.2, the GS is mainly ***covalent + (ionic)*** as shown by Salem and co-workers [84], while the SE and DE states are the two zwitterionic states. More specifically SE is fully zwitterionic while the second term in the DE wavefunction accounts for a covalent contribution (see Section 3.1.2).
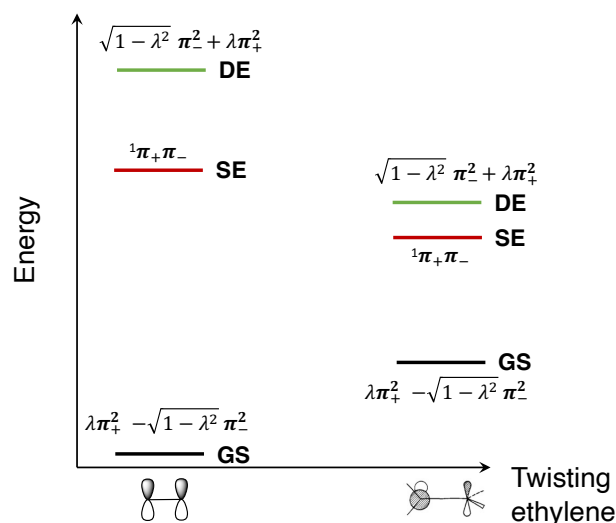

Figure 3.46. Schematic representation of the three singlet states of ethylene along the twisting coordinate.

A schematic representation of the position of these three states along the twisting coordinate

is shown in Figure 3.46. At 0° of twisting, the three states, especially the two excited states are well separated. When the twisting angle reaches 90°, both the DE and SE states' energies drop drastically approaching one another. The DE and SE states in twisted ethylene can be written as the negative and positive combinations of the two charge-transfer structures shown in Figure 3.47a. These linear combinations generate charge-resonances known as V (or Z_1) and Z (or Z_2) states[237–239], respectively.
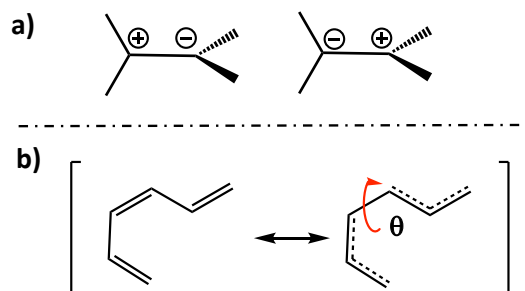
Figure 3.47. a) Two zwitterionic structures of ethylene when it is 90° twisted. b) *s-cis,s-trans* diallyl (1,3,5-hexatriene) studied in the work of Bonačić-Koutecký[237]. The twisting angle θ is indicated with the red arrow.

Any perturbation should allow a mixture of these two charge-resonance states so that each of them can become highly polar through increased participation of one ionic structure.

Bonačić-Koutecký and co-workers explored systems in which the diradical is slightly asymmetrical, since such asymmetry may induce charge separation. They calculated the charge distribution in the Z_1 state in *s-cis,s-trans* diallyl (1,3,5-hexatriene) as a function of the twisting angle θ (Figure 3.47b). They noticed that the charge separation for the related diallyl system peaks sharply when θ is in-between 89° and 91° with the maximum falling at 90° (see also Figure 2 of Ref. [237]). Out of this region, the charge separation drops to practically zero. Such sharp change in charge separation is at the origin of the term **Sudden Polarization**. The results of these calculations were in good agreement with what proposed by Wulfman and Kumei in 1971 for the two lowest excited singlet states of 90° twisted olefins[240].

In summary, sudden polarization is caused by mixing between the two zwitterionic singlet excited states, SE and DE (or Z_1, Z_2).

To correctly take into account the effect of sudden polarization, a multiconfigurational/multireference method which includes at least the doubly excited configuration is required [239].

3.5.4 The role of twisting

To assess the role of twisting around the exocyclic CC bonds, the fully-fluorinated tetracyano-quinodimethane **F4TCNQ** (Figure 3.48a) is chosen as model system. **F4TCNQ** features a similar *p*-QDM core substituted with halogens. Similarly to TTH, also in this molecule the DE state is among the lowest-lying ones. The luminescence of **F4TCNQ** is less efficient than that of TTH, but both show solvatochromism[241]. However, this solvent-dependent emission has been tentatively assigned to an *Internal Charge Transfer* (ICT) state [241] without any attempt to rationalize such assignment.

The optimized geometry of the DE state (Figure 3.48b), determined at CASSCF (6,6)/def2-

SVP level, shows a comparably elongated CC bond as in the case of TTH: 1.458 Å for **F4TCNQ** vs 1.471 Å. The optimized structure displays the terminal groups symmetrically twisted with respect to the central ring, just as TTH (Figure 3.48c, center). This structure will be name as *DE twisted sym*. Based on the DE optimized structure, two other geometries are generated, namely the *planar* one (0° twisting of the central core, Figure 3.48c, left) and the asymmetrically twisted one (*DE twisted asym,* Figure 3.48c, right) obtained by rotating only around one exocyclic CC bond. Energies of the GS and DE states are evaluated with CASSCF/NEVPT2 both in vacuo and in DMSO (a polar solvent).

Calculations show that due to the rotation around the exocyclic CC bond, the energy of the GS drastically increases as a consequence of deviation from its equilibrium structure. On the other hand, the energy of the DE state barely changes. In the meantime, *DE twisted asym* shows a non-negligible dipole moment (μ = 0.42 Debye) as a result of a mechanism that can be associated to sudden polarization[236,239,242] driven by the mixing of the DE and SE states. Furthermore, due to the dipole moment, the DE state is further stabilized (Figure 3.48c) in *DE twisted asym*. At the same time, twisting and SE/DE mixing, confer an increased transition dipole moment favoring radiative decay and accounting for the observed solvatochromic fluorescence. On the contrary, the ground state is remarkably destabilized for increasing torsional angles, thereby red-shifting the emission and increasing the Stokes shift.
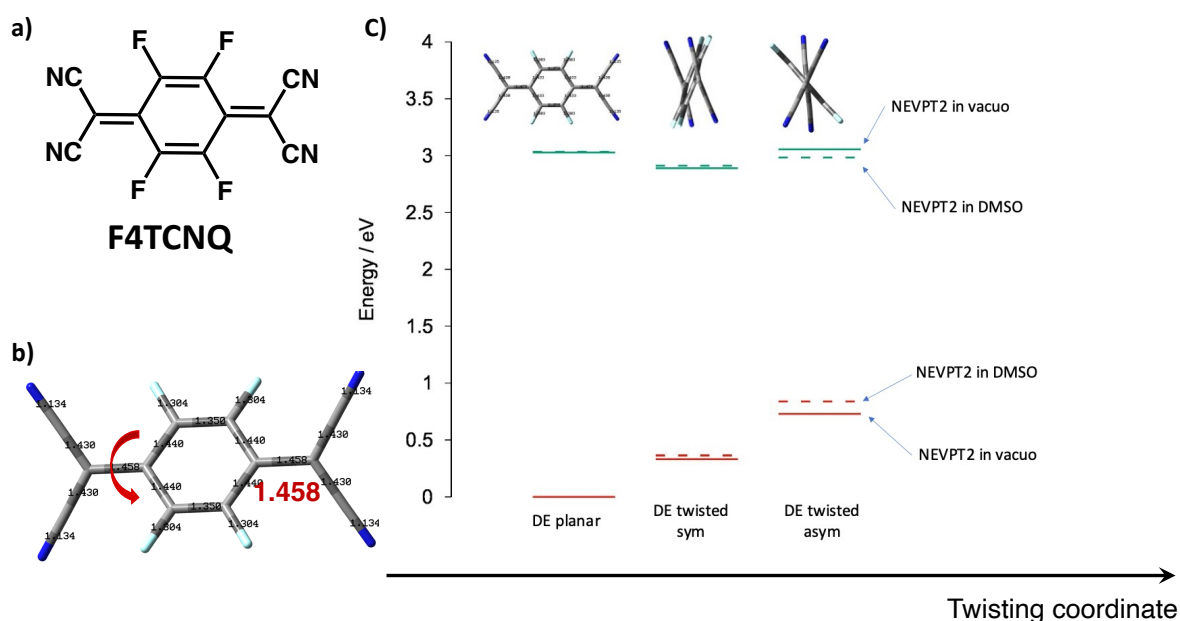
Figure 3.48. a). Chemical structure of the fully-fluorinated tetracyano-quinodimethane **F4TCNQ.** b) Optimized geometry for the DE state of **F4TCNQ** from *state-specific* CASSCF (6,6) calculation. Number in the figure indicates the bond length of the exocyclic CC bond. c). Effect of twisting in the DE excited state (green lines) of **F4TCNQ.** The three structures of the DE state differ by the torsional angle around exocyclic CC bonds. The ground state energy is indicated by red lines. From CASSCF (6,6)/NEVPT2 calculations in vacuo (solid lines) and in DMSO (dashed lines).

Applying these findings to TTH, it can be inferred that, after relaxation to the SE state *via* planarization of the *p*-QDM core, a fast *internal conversion* occurs. The lower lying DE state is populated. Its long exocyclic CC bond length, as well as its proximity to the SE state, assist the intramolecular torsion leading to a charge separated asymmetrically-twisted DE state whose stabilization will be preferential in polar solvents. Thus, a mechanism similar to sudden

polarization[236,239,242] of olefins occurs and explains the observed solvent dependent emission of TTH. At the same time, the GS is destabilized justifying the observed large Stokes shift.

3.6 Conclusions

In this Chapter the electronic structure, diradical character and its influence on optical properties of several different conjugated diradicaloids have been computationally investigated. The aim was generally two-fold. On one side, the ambition was to reproduce and predict properties in agreement with experimental data. At the same time the emphasis was on determining computational protocols suitable to capture the distinctive features (diradical character, aromatic vs quinoidal structures, correct sequence of low-lying excited states, *etc.*) of these promising molecular building blocks for functional materials.

Such dual objective was pursued for a series of quinoidal oligothiophenes. First, we explored to what extent the single reference description provided by RDFT/UDFT approaches may depend on the chosen functional and when the non-negligible contribution of static electron correlation becomes critical for the prediction of Raman activities. In this context we showed that the CS-B3LYP geometry and the associated Raman intensities were reliable for small to medium length conjugation. For the longer **EsQ4** oligomer, the BS-UCAM-B3LYP geometry was of superior quality compared to other ground state structures, as demonstrated by the good agreement of predicted vs experimental Raman spectrum. The second objective was the assessment of resonance enhancement effects. In this regard the study revealed an increasing Raman activity of low frequency vibrations associated with CC stretching modes that were further enhanced by resonance with both the optically active and the DE state, thereby demonstrating the additional potential of Raman spectroscopy in revealing signatures of the elusive double-exciton state that distinctively characterizes conjugated diradicals.

An important feature for π-conjugated diradicals is the description of the connections between structural flexibility and spin delocalization and dynamics in the flexible backbone. In this regard we investigated the "normal" and "reversed" quinoidal → aromatic transformations in a π-conjugated molecule, a dumbbell shape azobenzene derivative, featuring varying diradical character as a function of the temperature in the solid phase, accompanied by the modulation of the spin density distribution and we showed that such spin dynamics is induced by different torsional mobilities activated by temperature.

Conjugated diradicals are characterized by distinctive photophysical properties. In this regard we carried out a benchmark of the performance of several cost-effective computational approaches for the optical properties of conjugated diradicals and we demonstrated that the correct excitation energy of DE state could be captured by suitably choosing among TD-UDFT, SF-TDDFT and DFT/MRCI methods that can be considered acceptable alternatives to expensive high level multi-reference approaches. The relevant outcome of this systematic investigation is therefore the evidence that a careful choice of the appropriate DFT-based computational approach can provide reliable information on the low-lying excited states of diradicaloids with varying diradical characters and large molecular dimension, including the energy location of an uncommon low-lying excited state like the DE state.

Finally, the uncommon luminescence properties of TTH, a small *p*-QDM derivative, was interpreted with the help of correlated multi-reference quantum-chemical calculations, which indicated that the low-lying DE ionic "dark" state, typically found at low excitation energies in diradicaloids, was responsible for light emission. In TTH, such zwitterionic state became the lowest energy excited state and acquired dipole moment and intensity *via* twisting around the elongated exocyclic CC bonds in the excited *p*-QDM core, with a mechanism involving mixing with the nearby SE state, similar to sudden polarization occurring in olefins.

Chapter 4: Charge transport in conjugated molecular materials

In this chapter I move to studies aimed at understanding the condensed phase properties of molecular materials. Specifically, here I focused on the charge transport properties. In this context, the combination of intra-molecular parameters (reorganization energy) and intermolecular electronic couplings governs the efficiency of charge transfer.

Section 4.1 contains an introduction to the methods employed to evaluate the required intra- and intermolecular parameters and the protocol employed to propagate the charge carrier through the molecular materials.

In section 4.2, the reorganization energies are evaluated for a series of conjugated diradicals[69]. One particular feature of diradicaloids is the potential ambipolar charge transport. This is a property generally desired for organic materials employed in all optoelectronic devices and is especially required for applications in OFET. In fact, OFETs are characterized by unipolar transport, namely in the transporting layers only one type of conduction channel (p-type for holes or n-type for electrons) is favored. There have been some examples of OFET devices built up with diradicaloid molecules showing similar hole and electron mobilities[68,128,179,243–245]. Structure-property relationships between diradical character and ambipolar charge transport efficiency, however, have not been derived so far. In this study we rationalized this relationship by disclosing how the intra-molecular reorganization energies are influenced by the diradical character [69].

Other than the intrinsic properties of isolated molecules, also the intermolecular organization (*e.g.,* crystal packing) plays a fundamental role by controlling electronic interactions. Section 4.3 is thus focused on the study of two Naphthodithiophene Diimide (NDTI) derivatives featuring different fluoroalkylated substitution[92]. In particular, I analyze

the charge transport pathways and model charge mobility with the non-adiabatic hopping mechanism using the Marcus-Levich-Jortner (MLJ) rate constant formulation and Kinetic Monte Carlo (KMC) simulations. In addition, the role of thermally induced transfer integral fluctuations is investigated, and electron–phonon couplings are computed to identify the intermolecular modes that can influence charge transport efficiency.

4.1 Computational approaches for Charge Transport

There are two well-known charge transport mechanisms: "band-like" and "hopping". In the band-like" model, the wavefunction is fully delocalized (crystal orbital or bands) and the mobility is high due to the almost barrierless type of transfer. However, an increasing temperature excites low frequency lattice vibrations that break the translational order, causing a localization of the charge wavefunction and hence at higher temperature, a more suitable model is the "hopping". In this situation, charges are localized on molecular units and their motions are characterized by a series of incoherent jumps (*hopping*) between molecular units forming the condensed phase (*e.g.,* crystal). The latter mechanism is generally verified in organic crystal materials at room temperature.

Due to the *localization* nature of the hopping transport, it is possible to consider a limited number of molecules, generally a dimer (the simplest model system for charge transport) is sufficient. Within this simple framework, the charge transfer can be interpreted as a simple redox reaction between a pair of molecules (A and B):

$$A^+B \; \rightleftharpoons \; AB^+ \tag{4.1}$$

where the positively charged molecule A^+ receives an electron from B leading to the formation of AB^+. Such reaction can also be seen as a hole transfer from A^+ to B. In a condensed phase formed by the same molecules (A = B), Eq. 4.1 becomes a self-exchange reaction.

The charge-transfer rate constant (k_{et}) can be described by **Marcus's Law** [246–248]:

$$k_{et} = \frac{2\pi}{\hbar} V_{RP}^2 \frac{1}{\sqrt{4\pi\lambda k_B T}} e^{-\frac{(\Delta G^\circ + \lambda)^2}{4\lambda k_B T}} \tag{4.2}$$

V_{RP}^2 is the electronic coupling between reactant and product; ΔG° is the variation of Gibbs free energy occurred during the reaction (considering Eq. 4.1, it is calculated as $G(AB^+) - G(A^+B)$); k_B is the Boltzmann constant; T is the temperature; λ is known as **reorganization energy** and it is defined as "energy of product at the reactant's geometry".

λ is built up by two contributions: λ_i, known as "intramolecular reorganization energy" and λ_o the "*out-sphere*" reorganization energy.

$$\lambda = \lambda_i + \lambda_o \tag{4.3}$$

λ_i is mainly dominated by geometry change related to charge transfer process, whereas λ_o accounts for long-range interactions due to *e.g.* solvent. In a solid crystal, the contribution of λ_o is very small compared to that of λ_i. To a first approximation, the role of λ_o can be neglected.

Furthermore, considering a self-exchange reaction, $\Delta G°$ is zero since products (*e.g.* AA^+) and reactants (*e.g.* A^+A) are the same. In the absence of external stimuli, *e.g.* electrical field, the Marcus's Law can be simplified into:

$$k_{et} = \frac{2\pi}{\hbar} V^2 \frac{1}{\sqrt{4\pi\lambda_i k_B T}} e^{-\frac{(\lambda_i)^2}{4\lambda_i k_B T}}$$

(4.4)

Subscript *RP* in V^2 is also ignored because of the self-exchange reaction considered: R=P.

It can be already seen that, only V^2 and λ_i are relevant for the final value of k_{et} since others are constants. It should also be noticed that smaller λ_i and larger V^2 favor the charge transfer process since larger k_{et} is guaranteed.

In the following, approaches used to calculate the intramolecular reorganization energies and electronic couplings will be introduced. The section ends with an introduction to Kinetic Monte Carlo (KMC) simulations that were used to model the percolation of charge carriers through the molecular material. All these simulations were carried out with the *in-house* protocol "Pandora" that was previously developed in the group and includes scripts and software to combine quantum-chemical calculations with KMC simulations of charge mobility. This *in-house* approach also allows the simulation of thermally induced dynamical effects by combining molecular dynamics and quantum-chemical calculations[249–251].

4.1.1 The Adiabatic Potential method

The intramolecular reorganization energy can be calculated with the Adiabatic Potential method (AP) which consists in two-point determinations from each potential energy surface (PES) [15,18,19] of the neutral and charged states (see Figure 4.1).
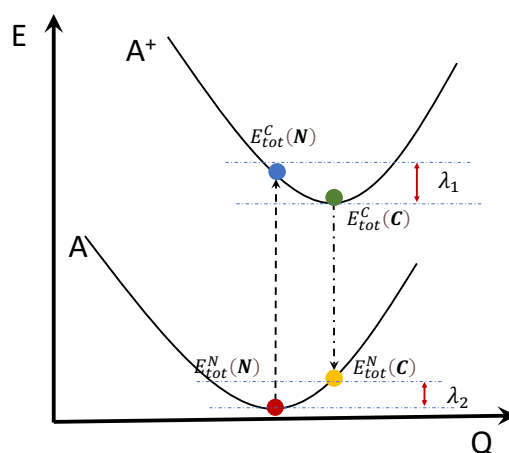
Figure 4.1. Schematic representation for the Adiabatic Potential method. Dashed arrows indicate a generic charge and discharge process.

According to the AP method, λ_i can be calculated as[15]:

$$\lambda_i = [E_{tot}^C(N) + E_{tot}^N(C)] - [E_{tot}^C(C) + E_{tot}^N(N)]$$

(4.5)

where C and N at apices indicate the charged and neutral states, respectively, while **N** and **C** in parenthesis indicate neutral and charged geometries, respectively. $E_{tot}^C(\mathbf{N})$ is thus the energy of the charged system at neutral geometry and it corresponds to the blue point in Figure 4.1; $E_{tot}^N(\mathbf{C})$ is the energy of the neutral state at the charged geometry (yellow point in Figure 4.1); $E_{tot}^C(\mathbf{C})$ corresponds to the green point in Figure 4.1 and is the energy of the charged system at its optimized geometry; finally $E_{tot}^N(\mathbf{N})$ is the energy of the neutral system at the neutral geometry (red point in Figure 4.1).

Gathering energies by geometries, Eq. 4.5 can be rearranged as:

$$\lambda_i = [E_{tot}^C(\mathbf{N}) - E_{tot}^N(\mathbf{N})] + [E_{tot}^N(\mathbf{C}) - E_{tot}^C(\mathbf{C})] \tag{4.6}$$

λ_i, thus, bears two contributions: one from the neutral PES determined arbitrarily as λ_2 according to Figure 4.1 and the other from the charged PES defined as λ_1 in Figure 4.1.

$$\lambda_i = \lambda_1 + \lambda_2 \tag{4.7}$$

While the dominant configurations for charged states, anion and cation, are unique (Figure 4.2) and can be generalized for almost all types of molecules, the dominant configuration for diradicaloids can be either CS type or open-shell (BS in Figure 4.2, Section 3.1.3). Generally, the open-shell configuration is more suitable for diradicaloids since, very often, a BS solution can be found. Therefore, when considering the neutral states for diradicaloids, both the CS and BS geometries need to be taken into account.
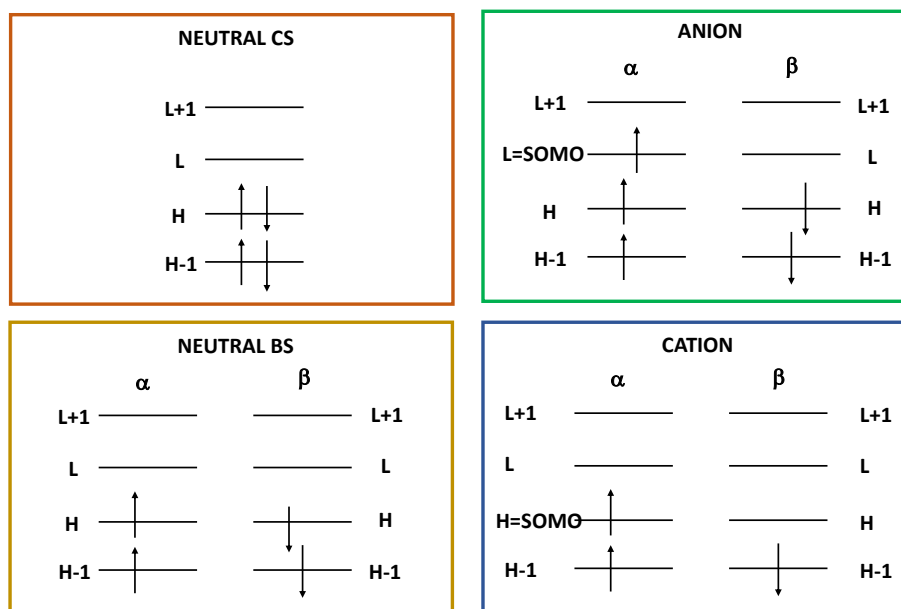
Figure 4.2. Schematic representation of configurations dominating the neutral (left) states and charged (right, anion and cation) states. The neutral BS configuration is dominant in diradicaloids with large diradical character.

4.1.2 Marcus-Levich Jortner rate constant formulation

Because the quantum nature of the most active modes governing local electron-phonon coupling could not be negligible, the simple Marcus's equation is not sufficient. The more suitable formulation of the transfer rate constants (k_{eT}) associated with each hopping event

need to include quantum corrections and it is provided by the Marcus-Levich-Jortner (MLJ) equation[252]:

$$k_{eT} = \frac{2\pi}{\hbar} V_{ij}{}^2 \frac{1}{\sqrt{4\pi\lambda_{o+classic}k_BT}} \sum_{v=0}^{\infty} \left[\exp\left(-S_{eff}\right) \frac{S_{eff}^v}{v!} exp\left(-\frac{(\Delta G^0 + \lambda_{o+classic} + v\hbar\omega_{eff})^2}{4\lambda_{o+classic}k_BT} \right) \right] \quad (4.8)$$

In the MLJ formulation of k_{eT} , the quantum description of the non-classical degrees of freedom was represented by a single effective mode of frequency ω_{eff} and the associated HR factor S_{eff}.

A general assumption introduced in Ref. [249–251] and in Ref. [253,254] is to consider only high frequency modes in the calculation of the effective frequency: ω_{eff} is determined summing over all vibrational frequencies above 200 cm^{-1}. Vibrations with frequencies lower than 200 cm^{-1} are neglected because: 1) they can be described to a good approximation with classical terms at room temperature; and 2) they are susceptible to anharmonicity.

$$\omega_{eff} = \frac{\sum_{m(\omega_m>200cm^{-1})} \omega_m S_m}{\sum_{n(\omega_n>200cm^{-1})} S_n} \quad (4.9)$$

The associated S_{eff} can be determined as:

$$S_{eff} = \frac{\lambda_i}{\hbar\omega_{eff}} \quad (4.10)$$

where λ_i is the total intramolecular reorganization energy and it is determined from the set of computed HR factors (S_m, Section 3.2.2.1).

$$\lambda_i = \sum_{m(\omega_m>200cm^{-1})} (\hbar\omega_m S_m) = \sum_{m(\omega_m>200cm^{-1})} (\lambda_i^m) \quad (4.11)$$

Note that the sum runs over all λ_i^m contributions including also those corresponding to vibrational modes (m) with frequencies below 200 cm^{-1}. Their contributions are included by means of S_m . The exceeding classical contributions were summed to the out-sphere reorganization energy λ_o, and the total contribution reads as $\lambda_{o+classic}$ in Eq. 4.8. The out-sphere contribution was assumed to be 0.01 eV.

ΔG^0 associated to a self-exchange reaction (*e.g.* Eq. 4.1) in the presence of electric field is $\Delta G^0 = -e\mathbf{F} \cdot \mathbf{d}$, where $\mathbf{F}$ is the electric field vector and $\mathbf{d}$ the distance vector between the centers of mass of the molecules composing the dimer.

4.1.3 Intermolecular electronic coupling

The fragment orbital (FO) method is one of the prominent methods used to treat electronic coupling. This approach is based on the construction of charge localized diabatic states from non-interacting fragment densities[255]. The fragment densities correspond to donor ($\mathbf{D^+}$) and acceptor ($\mathbf{A}$) of the charge transfer process. Considering the self-exchange analogue of Eq. 4.1

and a dimer formed only by A molecules, **D⁺** and **A** correspond respectively to A^+A and AA^+. A general electronic coupling element for the charge transport can be written as:

$$V = \langle \Psi^{A^+A} | \hat{H} | \Psi^{AA^+} \rangle \tag{4.12}$$

In the FO framework, both Ψ^{A^+A} and Ψ^{AA^+} are built up with Kohn-Sham determinants of the isolated fragment (*i.e.,* molecular orbitals ϕ) of the charged and neutral molecules. Note that A^+ and A differ only by one electron. It can be shown that, by applying the Slater-Condon rules, only one MO counts for each wavefunction in Eq 4.12[255]. This reduces the calculation of electronic coupling elements to an integral between Kohn-Sham orbitals:

$$V_{ij} = \langle \phi_i | \hat{H} | \phi_j \rangle \tag{4.13}$$

with ϕ_i and ϕ_j indicating HOMOs (for p-type semiconductors) or LUMOs (for n-type semiconductors) of the monomers forming the dimer.

The protocol used to determine electronic coupling follows previous studies [256–259]. It is based on the determination of the matrix $\boldsymbol{H}_{\text{MOB}}$ in the monomer orbital basis (MOB), whose off-diagonal elements are the non-orthogonalized electronic couplings:

$$\boldsymbol{H}_{MOB} = \boldsymbol{C}^t_{MON\_AOB} \boldsymbol{S}_{MON\_AOB} \boldsymbol{C}_{DIM\_AOB} \varepsilon_{DIM} \boldsymbol{C}^t_{DIM\_AOB} \boldsymbol{S}_{MON\_AOB} \boldsymbol{C}_{MON\_AOB} \tag{4.14}$$

ε_{DIM} is the diagonal matrix of the eigenvalues associated to the MO of the dimer, $\boldsymbol{C}_{DIM\_AOB}$ is the matrix of the eigenvectors of the dimer in the atomic orbital basis (AOB), $\boldsymbol{S}_{MON\_AOB}$ is the overlap matrix of the monomers in the AOB, and $\boldsymbol{C}_{MON\_AOB}$ is the monomer-localized orbitals matrix. $\boldsymbol{C}_{MON\_AOB}$ is, therefore, a block diagonal matrix containing the MO coefficients in the AOB from each monomer, with the off-block diagonals set to zero and the superscript t indicating the transpose.

The computed couplings can be transformed in an orthogonalized basis by performing a Löwdin orthogonalization[260]:

$$\boldsymbol{H}^{\perp}_{MOB} = \boldsymbol{S}^{-\frac{1}{2}}_{DIM\_MOB} \boldsymbol{H}_{MOB} \boldsymbol{S}^{-\frac{1}{2}}_{DIM\_MOB} \tag{4.15}$$

where $\boldsymbol{S}_{DIM\_MOB}$ is the overlap matrix between monomer orbitals, which is obtained from the MO coefficients of the monomer orbitals and the overlap of the atomic orbitals in the dimer configuration $\boldsymbol{S}_{DIM\_MOB}$:

$$\boldsymbol{S}_{DIM\_MOB} = \boldsymbol{C}^t_{MON\_AOB} \boldsymbol{S}_{DIM\_AOB} \boldsymbol{C}_{MON\_AOB} \tag{4.16}$$

For a dimer, this was conducted on the 2×2 $\boldsymbol{H}_{MOB}$ matrix including the HOMO (or LUMO) orbitals of the two monomers[20,261].

The electronic couplings presented throughout this work are calculated at B3LYP/6-31G* level of theory.

4.1.4 Kinetic Monte Carlo simulations

The appropriate values of k_{eT} can be included in a KMC simulation to propagate the charge through the condensed phase and ultimately predict charge mobilities. The charge transfer, within the hopping model, can be seen as a stochastic process. Thus, in a KMC simulation, a single charge carrier is left to move through the crystal by hopping events occurring in a dimer. The probability associated with a hopping event involving charge transfer from site i to site j (P_j), is determined by rate constant:

$$P_j = \frac{k_j}{\sum_n k_n} = \frac{k_j}{k_{TOT}} \tag{4.17}$$

n runs over all possible paths for a charge localized on a given molecular unit in the crystal.

The time associated with a single hopping event is given by $-\ln X / k_{TOT}$, where X is a random number uniformly distributed between 0 and 1. The distance associated with the hopping is measured between the centers of mass of the molecules involved in the charge transfer process. In the framework of hopping, these molecules are usually near neighbours. Each trajectory is advanced by choosing a random number r uniformly distributed between 0 and 1 selecting the j-th neighbour such that $\sum_n^{j-1} P_n < r \le \sum_n^j P_n$.

From the set of KMC simulations[262–268] the diffusion coefficient D (Eq. 4.18) can be computed and ultimately leads to the determination of the zero field (Brownian) charge mobilities.

Generally, an approximately linear dependence of the mean square displacement (MSD) $\langle [r(t) - r(0)] \rangle^2$ as a function of time t can be obtained by averaging over the subsets of 1000 KMC trajectories. The diffusion coefficient D can be obtained from the fitted linear dependence of MSD by employing Einstein's equation:

$$D = \lim_{t \to \infty} (MSD/6t) \tag{4.18}$$

The charge mobility can then be calculated using Einstein-Smoluchowski's equation:

$$\mu = \frac{eD}{k_B T} \tag{4.19}$$

In the presence of an electric field, the time-of-flight (TOF) charge mobilities are obtained with the following relation by applying an electric field F of magnitude 10^5 V/cm:

$$\mu = \frac{d_f}{\tau F} \tag{4.20}$$

d_f is the distance travelled by the charge along the F direction and τ is the time required to travel the distance d_f, which is assumed to be 50 μm. The mobility, then, needs to be averaged over a numbers of trajectories (100 is chosen for the study of NDTI, Section 4.3)

## 4.2 Ambipolar charge transport in Difluorenoheteroles

Charge transport in organic semiconductors is a typical molecular material property that depends on intra-molecular and inter-molecular parameters. Inter-molecular effects in the organic semiconducting layer (electronic couplings, V), metal-organic (orbital energy alignment with the electrodes' Fermi energy level, E_{OM-F}) and semiconductor-dielectric interfaces are optimized by material processing. Thus, part of the effort of pre-designing new molecular candidates is focused on enhancing intramolecular properties, such as the intramolecular reorganization energy, λ_i.

Here, we investigate a number of conjugated diradicals exploring the hypothesis that medium diradical character imparts a degree of electron confinement (*i.e.*, electron unpairing) that gives rise to small structural changes and reduced (and similar) reorganization energies for holes and electrons.

The four newly synthesized benzoquinoidal polycyclic conjugated molecules investigated in this work are shown in Figure 4.3. They are built up by two fluorenes (thus **DF**, Figure 4.3a) fused through a bridging five-membered ring featuring heteroatom. The chemical structures of the four compounds differ only by the heterocyclic five-membered ring which encompasses furan (**DFFU**), thiophene (**DFTh**), thiophene dioxide (**DFThSO₂**) and pyrrole (**DFPy**).

Experimental characterizations such as SQUID, Cyclic-Voltammogram (CV), NICS, transient absorption spectra, *etc*. revealed that the four molecules exhibit typical features of open-shell singlet diradicals such as the double and reversible redox potentials, the presence of the dark DE state[69].

OFET devices featuring the four compounds as charge transporting layer were fabricated. Interestingly, the electrical behaviors of these OFETs exhibit 'valley' structure, typical of ambipolar semiconductors[269] (*e.g.* see Figure 5 of Ref. [69]). In the valley region, a balanced p-n transport is suggested by the similar values of hole and electron transport voltage. Furthermore, mobility measurements show comparable values for both hole and electron transport ($\mu_h = 10^{-3}\ cm^2 V^{-1} s^{-1}$ and $\mu_e = 10^{-4}\ cm^2 V^{-1} s^{-1}$).
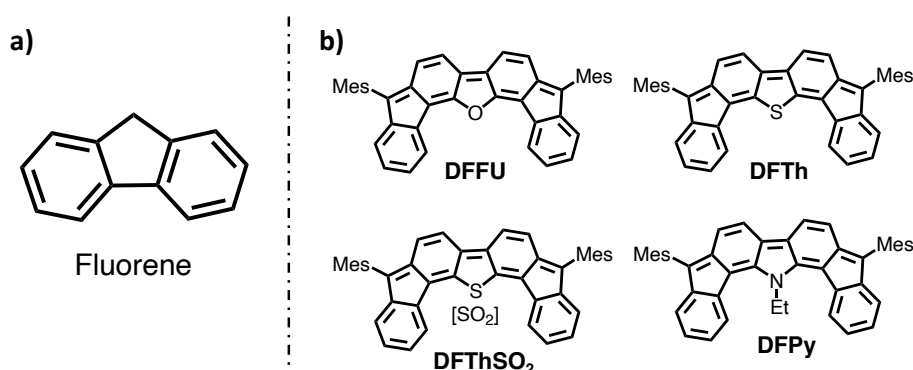
Figure 4.3. Chemical structures of a) fluorene and b) the four difluorenoheterole compounds studied in this part of work.

As outlined in Section 4.1, the simulation of charge mobilities is based on the evaluation of intra- and inter-molecular parameters (reorganization energies λ_i, reciprocal molecular orientation and magnitude of electronic couplings V) that enter the definition of charge transfer

rate constants. In turn, these can be used to determine the percolation of charge carriers in the material, *via* KMC simulations. The objective of this work, however, is not to reproduce experimental charge mobilities but to elaborate structure-property relationships by focusing essentially on the role of intra-molecular factors. Nevertheless, for one of the compounds investigated, also electronic couplings were determined. These, together with the λ_i are sufficient to get insight on charge transport efficiency because of their combined effect on charge transfer rate constants. Indeed, it should be noted that inspection of the Marcus equation (Eq. 4.4) suggests that large λ_i are detrimental for charge transport and large V's favor charge mobilities[19].

4.2.1 Computational details

We performed gas-phase quantum-chemical calculations in order to investigate electronic structures of the four difluorenoheteroles shown in Figure 4.3. Geometry optimization and frequency analysis for **DFFu**, **DFTh** and **DFPy** in the neutral singlet states were performed at the B3LYP/6-311G* level. Diradical characters were evaluated in terms of y_0 at PUHF/6-311G* level[156], hereafter denoted as y_0^{PUHF}.

The intramolecular reorganization energy λ_i was computed with the Adiabatic Potential (AP) method according to Section 4.1.1[15,18,19]. Both the closed-shell (CS) and open-shell (OS) broken-symmetry (BS) neutral ground state geometries were determined for all difluoreno-heteroles at B3LYP and UB3LYP levels of theory, respectively, using the 6-311G* basis set. Geometries of the charged states (anion and cation) were calculated at UB3LYP/6-311G* level of theory.

The electronic couplings (Section 4.1.3) for **DFFu** were also calculated using B3LYP/6-31G* level of theory at the crystal geometry using the *in-house* developed package "Pandora" (see Section 4.1).

4.2.2 Diradical character, electronic coupling and molecular orbital energies

The four molecules in Figure 4.3b are characterized by medium diradical character. The calculated y_0^{PUHF} increases from **DFPy** (0.541) to **DFThSO₂** (0.591) passing through **DFFu** (0.555) and **DFTh** (0.570).

The redox properties of these compounds display a general increase of the first oxidation potential and a decrease of the first reduction potential from **DFPy** to **DFThSO₂**, almost in line with the increase of diradical character. Accurate computational predictions of redox potentials would require comparison of energies for both the starting molecule and its reduced/oxidized forms. However, we can qualitatively use Koopmans' theorem[270] to correlate the redox potentials of the four difluorenoheteroles with computed HOMO and LUMO energies. The comparison is shown in Figure 4.4 and a general good agreement is found with experimental results.

The organic semiconductor material is taken in its crystalline form, and the possible dimers are identified by evaluating the distances between the centers of mass of the molecules surrounding a central reference molecule in the crystal. Among these dimers, those

corresponding to the nearest neighbor of the reference molecule are selected as shown in Figure 4.5 and their electronic couplings (V) are evaluated. Considering the black molecule as reference (Figure 4.5), three charge transport channels can be individuated: charges can move from the black molecule to red (yellow or green) molecules (Figure 4.5). Hereafter these channels will be simply indicated by their color.
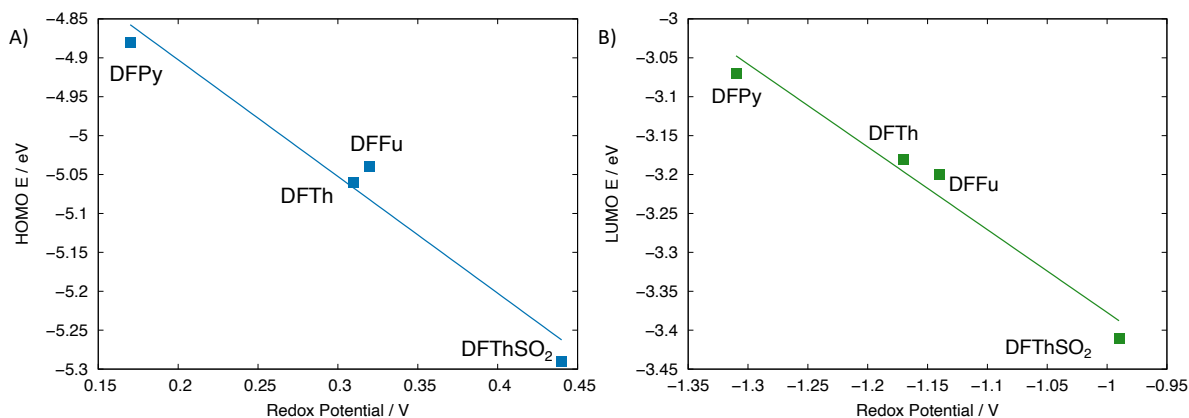
Figure 4.4. Correlation between experimental redox potentials and computed MO energies of the four molecules. A) Correlation between the first oxidation potential and the HOMO energies; B) Correlation between the first reduction potential and the LUMO energies. MO energies calculated at UB3LYP/6-311G* level of theory. Figure adapted from Ref. [69].

color	distance (Å)	V_{hole}(meV)	$V_{electron}$(meV)
green (**1**)	8.05	39	29
yellow (**2**)	8.90	41	30
red (**3**)	10.93	17	3
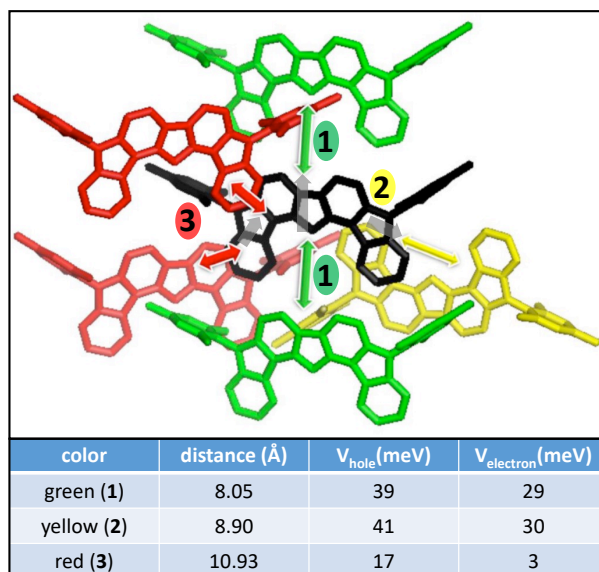
Figure 4.5. Selected cluster from the X-ray structure of **DFFu** where electronic couplings, V, at the B3LYP/6-31G* level are calculated. Dimers are formed between the black central molecule and the red, green and yellow neighbors, denoted by arrows. Figure adapted from Ref. [69].

For each of these paths, V for both electron and hole transport are calculated. The results are shown in Figure 4.5. V calculated for the yellow and green channels display very large values suggesting a favored transport through these two channels. The larger V value is due to more efficient orbital overlap and shorter intermolecular distances (Figure 4.5).

Interestingly, comparing V for hole (V_{hole}) and for electron transport ($V_{electron}$), their values are rather similar for each of the channel considered. This finding supports the similar transport mobilities for the two types of charge carriers with a slight preference for hole conduction, such

as observed experimentally. However, the role of reorganization energies must also be considered for a final assessment of charge transport efficiency.

4.2.3 Intramolecular reorganization energy

Intramolecular reorganization energies have been obtained for radical cations and radical anions in Table 4.1 considering both the CS and BS geometries for the neutral state.

Considering λ_i calculated using the BS geometry for the neutral system, it can be seen that these values are on average around 0.1 eV in magnitude which are rather small among organic semiconductors. Additionally, these values are comparable to the case of pentacene, one of the best p-type semiconductor, for hole transport (0.098 eV at B3LYP/6-31G* level[271]). Interestingly, λ_i values are of the same magnitude for holes and electrons. Hole transport is slightly favored also in this case owing to smaller λ_i (hole).

Table 4.1. Computed intramolecular reorganization energies (RB3LYP/6-31G* and UB3LYP/6-311G* level, in eV) using as reference the closed-shell (CS) or the open-shell (BS) structures of the neutral species. Diradical character in terms of y_0^{PUHF} are also indicated and they are calculated at the minimum BS geometries. Table adapted from Ref. [69].

| Geometry Neu.→ | y_0^{PUHF} | CS-B3LYP | | BS-BL3YP | |
Molecule↓		λ_i(hole)	λ_i (electron)	λ_i(hole)	λ_i (electron)
DFPy	0.541	0.210	0.216	0.104	0.114
DFFU	0.555	0.212	0.222	0.101	0.113
DFTh	0.570	0.190	0.237	0.093	0.136
DFThSO₂	0.591	0.258	0.209	0.123	0.102

Taken together, similar values of electronic couplings (Figure 4.5) and of intramolecular reorganization energies (Table 4.1) suggest similar transfer rate constant for both types of charge carriers considered, in line with the measurement of similar mobilities in both regimes of conduction of the OFET devices. Ambipolar charge transport, in this case, is fueled by the small reorganization energies combined with favorable level alignment and V values that are in line with those of best p-type/n-type organic semiconductors and compatible with mobilities (close to ca. 1 $cm^2 V^{-1} s^{-1}$) for perfect crystalline materials[251].

Comparing λ_i calculated for the CS structures of the four molecules with those obtained for the BS structures (Table 4.1), a two-fold increase of these reorganization energies is predicted for the former. This finding gives a key insight revealing the preferential conditions for charge transport in the diradical structure compared with the closed-shell one. The diradical (BS) form produces a situation of non-bonding frontier unpaired electrons. On one hand, the removal of an electron from the molecule does not largely affect the remaining molecular structure. On the other hand, the addition of an electron will bring about an amount of electronic repulsion but much smaller compared with the situation of full pairing in the closed-shell form. As a result, the structural variations upon charging positively or negatively the diradical are expected to be modest.

Inspection of the computed bond lengths of **DFFU** (Figure 4.6) shows, indeed, that the BS structure of neutral system (red line in Figure 4.6) is more similar to the geometry of the charged

species justifying its reduced reorganization energies. The same effect is also observed in other three molecules[69]. Such reduced geometry difference between neutral and charged species can be rationalized also with simple considerations on electronic structure. The BS frontier molecular orbitals, indeed, can be expressed as the linear combination of HOMO and LUMO CS orbitals (Section 3.1.3, Eq. 3.10), see Figure 4.7 for the example of **DFFU**. The open-shell form of a diradical molecule, compared to the quinoidal closed-shell, is expected to be more similar to that of a HOMO → LUMO (or HOMO,HOMO → LUMO,LUMO) excitation (in which a hole is created in the HOMO and an electron is added to the LUMO). On the other hand, a similar geometry change is expected for the cation (in which a hole in the HOMO is created) or for the anion (where an electron is added to the LUMO). Such simple electronic structure considerations give the vision of the diradical as a structure in which pseudo-hole (partial de-occupation of the HOMO) and pseudo-electron (partial occupation of the LUMO) coexist, a perspective that intuitively explains the reduced reorganization energies for diradicals either for hole and electron transport.
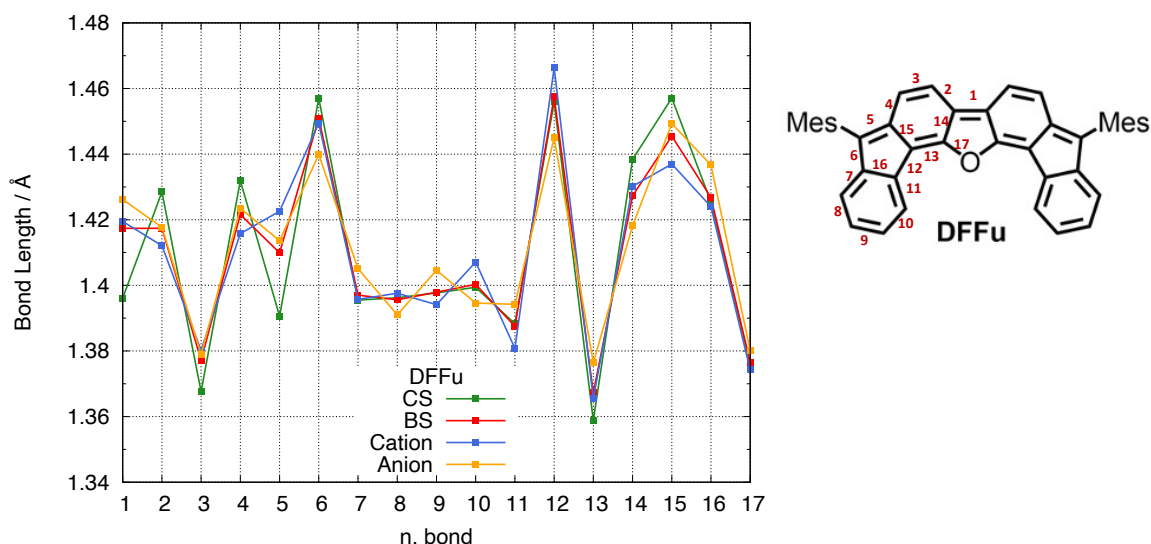
Figure 4.6. Bond lengths of **DFFU** calculated at CS (green), BS (red), cation (blue) and anion (orange) geometries. Top right: the definition of chosen bonds. The CS geometry is calculated with B3LYP functional, while other geometries are obtained with UB3LYP functional. The 6-311G* basis set is used. Figure adapted from Ref. [69].
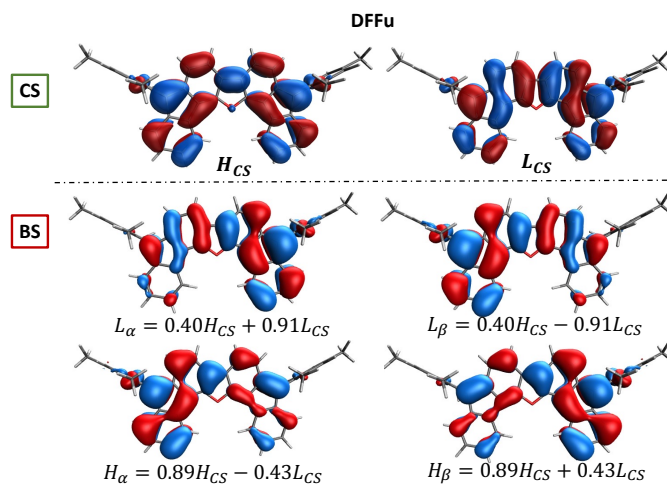

Figure 4.7. HOMO and LUMO of **DFFU** obtained for (top) CS (B3LYP/6-311G* level) and (bottom) BS structures (UB3LYP/6-311G*). BS orbitals are expressed as linear combination of CS orbitals.

4.2.4 Correlation between diradical character and intramolecular reorganization energy

To assess the relationship between diradical character and the ambipolar charge transport property, we extended our investigation including another family of fluorene derivatives (Figure 4.8). These are based on coupling of fluorene and indenofluorene[272] motifs with benzothiophene (BT) or with simple benzene terminal substituents. Additionally, for the BT terminated family, both the anti (A-) and syn (S-) isomers are considered[123,273]. Overall, these molecules are fluorenofluorene[274] (**FF**), diindenoanthracene[275] (**DIAn**), indacenodibenzothiophene (**IDBT**) along with its longer derivatives such as indenoindenodibenzothiophene (**IIDBT**)[123,273] and benzothiophene diindenoanthracene (**BT-DIAn**)[126]. Furthermore, some molecules in Figure 3.33 are also included for this discussion and they are: **2TIO**, **QDTBDT**, **BISPHE**, **TPQ** and **NZ**.

Notably, OFET devices featuring **DIAn**[276], **QDTBDT**[141] and the smaller congener of **BISPHE**[243] as charge transport layers, display balanced hole and electron mobilities.
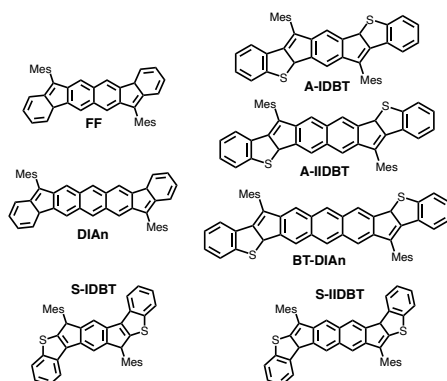
Figure 4.8. Chemical structures for additional diradical molecules for which the intramolecular reorganization energies for cation and anion are evaluated.

Geometry optimizations are determined as outlined in Section 4.2.1. For all geometry optimizations B3LYP functional is used along with 6-311G* basis set except for **2TIO**, **QDTBDT**, **BISPHE**, **TPQ** and **NZ** where the 6-31G* basis set is used. All molecules investigated show a more stable BS geometry except for the two smallest molecules with BT-termination, namely **A-IDBT** and **S-IDBT**. y_0^{PUHF} is employed as diradical character descriptor and the most stable geometry are considered for all molecules (*i.e.,* CS-B3LYP for **A-IDBT** and **S-IDBT**; BS-UB3LYP for all others).

The impact of diradical character can be assessed by comparing the computed λ_i either assuming the CS structure of the neutral species (namely, disregarding the contribution of diradical character), or employing the BS structure (including the contribution of the diradical character) to obtain λ_i. Calculated λ_i for cations and anions are collected in Table 4.2 considering both CS and BS geometries, when possible, for the neutral systems. Comparing λ_i calculated either for CS or for BS structures, a general decrease of λ_i calculated for BS structures is observed. However, some exceptions are observed, for instance λ_i (electron) for **A-IIDBT** and **BT-DIAn** display smaller values for CS structures. This can be traced back to the nature of the frontier molecular orbitals in cationic and anionic systems, which share very similar shapes with HOMO and LUMO of the CS neutral system, respectively (see Figure 4.2).

In fact, taking **A-IIDBT** as an example (Figure 4.9), its HOMO (corresponding to SOMO of the cation) and LUMO (*i.e.* SOMO of the anion) have rather different nature, with the latter showing non-bonding character. As a result, geometry change upon formation of the anion from the CS neutral structure is very small. On the other hand, due to the mixing between H_{CS} and L_{CS} (Eq. 3.10), the BS LUMOs acquire some bonding character from H_{CS} giving rise to the anomalous increase of λ_i (electron). This demonstrates that beside the magnitude of diradical character, also the nature of the SOMO for the conducting species (anion and cation) controls the magnitude of intra-molecular charge transport parameters.

Table 4.2. Computed intramolecular reorganization energies (RB3LYP/6- 31G* and UB3LYP/6-311G* level, in eV) using as reference the closed- shell (CS) or the open-shell (BS) structures of the neutral species. Diradical character in terms of y_0^{PUHF} are also indicated and they are calculated at the minimum (CS or BS) geometries.

Geometry Neu.→	y_0^{PUHF}	CS-B3LYP		BS-BL3YP	
Molecule↓		λ_i(hole)	λ_i (electron)	λ_i(hole)	λ_i (electron)
A-IDBT	0.407	0.204	0.131	-	-
A-IIDBT	0.641	0.219	0.086	0.148	0.100
BT-DIAn	0.774	0.177	0.082	0.090	0.131
FF	0.523	0.227	0.219	0.147	0.158
DIAn	0.681	0.189	0.169	0.069	0.104
S-IDBT	0.432	0.285	0.197	-	-
S-IIDBT	0.691	0.194	0.088	0.126	0.078
2TIO	0.665	0.113	0.313	0.055	0.090
QDTBDT	0.679	0.066	0.234	0.052	0.072
NZ	0.754	0.115	0.121	0.032	0.037
TPQ	0.855	0.047	0.217	0.075	0.031
BISPHE	0.863	0.076	0.022	0.013	0.037
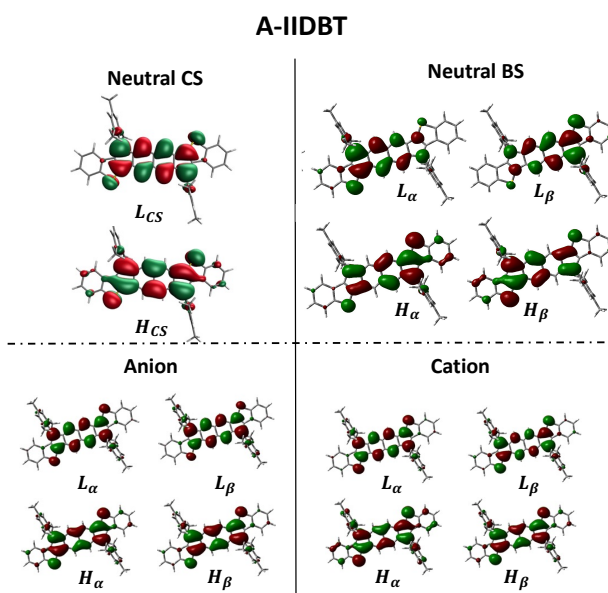
A-IIDBT

Figure 4.9. HOMO and LUMO of **A-IIDBT** calculated for the neutral CS (top left), BS (top right), anion (bottom left) and cation (bottom right) systems. B3LYP/6-311G* is adopted for the CS calculation while UB3LYP/6-311G* level of theory is used to determine the charged systems.

Finally, the relationship between the intramolecular reorganization energy (λ_i) and the diradical character (y_0^{PUHF}) is shown in Figure 4.10. A general good linear relationship is observed, namely: the larger is y_0^{PUHF} the smaller are λ_i both for holes (cations) and electrons (anions).

It can be concluded that larger diradical character favors smaller intramolecular reorganization energy both for cations and anions, which, in principle may ultimately favor a better hole and electron transport. However, one has to remember, that the validity of the nonadiabatic hopping model depends on the relative magnitude of the electronic coupling V and the reorganization energy parameter λ, with V required to be considerably smaller than λ[14,19]. On the other hand, larger diradical character is also associated to strong confinement which restricts charge internal delocalization and might be detrimental for charge transport.
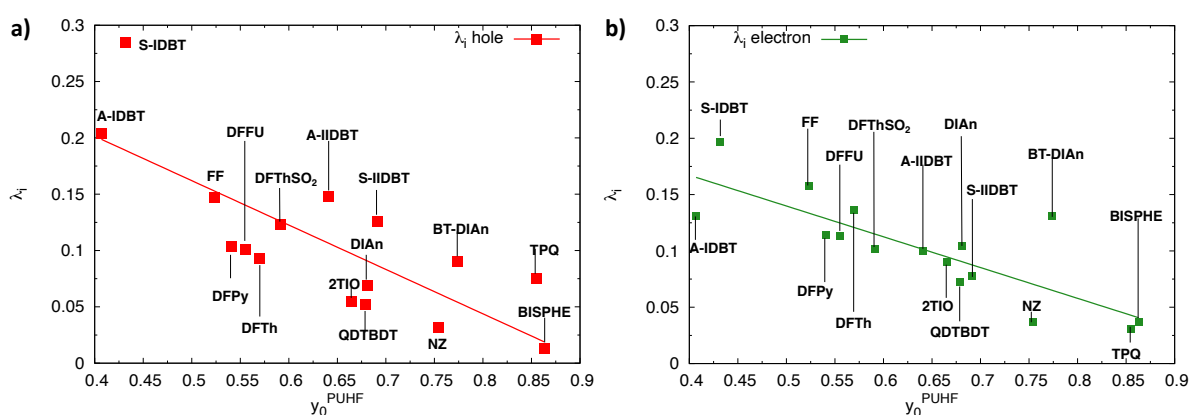
Figure 4.10. Relationship between y_0^{PUHF} and the intramolecular reorganization energy (λ_i) for a) cations (hole) and b) anions (electron) for the set of molecules shown in Figure 4.8, Figure 4.3 and some of molecules from Figure 3.33. Neutral and charged geometries are mainly obtained at UB3LYP level with 6-311G* basis set. For **A-IDBT** and **S-IDBT**, neutral geometries considered here are obtained with B3LYP functional; for molecules from Figure 3.33, their geometries are obtained with UB3LYP/6-31G*.

4.3 Impact of fluoroalkylation on the charge transport of two NDTI derivatives

Naphthodithiophene diimides are well-known n-type semiconductors[277–281]. In this study, two recently synthesized fluoroalkyl-modified NDTI were considered (see Figure 4.11). One derivative features fluoroalkyl substituents in the α position of the terminal thiophenes, while the other features fluoroalkyl substituents on the N position and are hereafter labeled as **α-NDTI** and **N-NDTI**, respectively. The introduction of fluorinated substituents is known to improve the device stability under ambient conditions, but it also impacts the molecular packing arrangements, thereby leading to different device performances. Indeed, single-crystal OFETs of both fluoroalkyl-modified NDTI showed good electron transport properties, with **α-NDTI** displaying an averagely lower electron mobility compared to that of **N-NDTI** (0.037 cm^2 V^{-1} s^{-1} vs 1.27 cm^2 V^{-1} s^{-1}). The highest value of electron mobility found for **α-NDTI** is 0.065 cm^2 V^{-1} s^{-1}, again much lower than that of **N-NDTI** which scores 1.59 cm^2 V^{-1} s^{-1} [282].
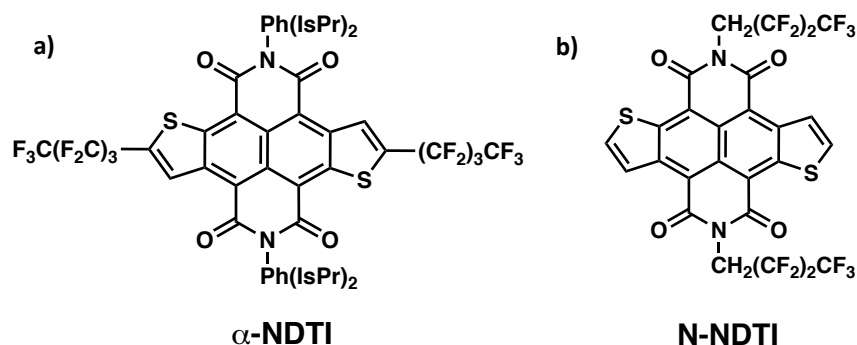
Figure 4.11. Structural formula of the two fluoroalkylated NDTI derivatives considered in this work: (a) **α-NDTI** (b) **N-NDTI**. Figure adapted from Ref. [92].

To model the charge transport properties of the two NDTI derivatives, the non-adiabatic hopping approach (Section 4.1) was applied encompassing evaluation of the electronic couplings and reorganization energies, followed by charge transfer rate constants according to the MLJ formalism[283]. Electronic couplings are calculated at B3LYP/6-31G* level considering the crystal structure, while reorganization energies are evaluated based on optimized neutral and anionic geometries at B3LYP and UB3LYP/6-31G* levels, respectively.

Charge transfer rate constants are then injected in KMC simulations to model the charge percolations and mobilities. This approach has already been adopted to rationalize the trends in n-type charge transport of various fluorinated and chlorinated PDI derivatives[249,250], as well as the anisotropy of charge transport in fluoroalkylated NDIs [251].

Dynamic disorder effects have been shown to influence the charge mobilities of organic semiconductors by inducing large fluctuations in the transfer integrals driven by slow intermolecular modes[14,284–288]. In this work, the intra- and intermolecular parameters governing charge transport for the two NDTI derivatives are evaluated and the eventual role of dynamical disorder effects in affecting the charge mobility is also considered.

4.3.1 Crystal structure and electronic coupling along charge transfer pathways

There are two possible orientations of thiophene rings inside the crystal of both **α-** and **N-NDTI** leaving the rest of the molecule identical. The dominant orientation is labeled are *ANTI-1*, and the other is known as *ANTI-2* (Figure 4.12). Both were considered in the calculation of electronic couplings and charge mobilities. To evaluate the effect of different thiophene orientations in the same solid phase, a crystal containing a mixture of the two orientations was also considered for **N-NDTI** (labelled as *mix*) in the original paper[92]. Since the latter crystal displays intermediate mobility values, it will not be discussed here.

After single-molecule geometry optimization, the two **N-NDTI** structures converged, as expected, to the same equilibrium geometry. In contrast, two slightly different optimized structures of **α-NDTI** *ANTI-1* and **α-NDTI** *ANTI-2* were obtained owing to different conformers of the fluoroalkyl chains.

α-NDTI *ANTI-1*	**α-NDTI** *ANTI-2*	**N-NDTI** *ANTI-1*	**N-NDTI** *ANTI-2*
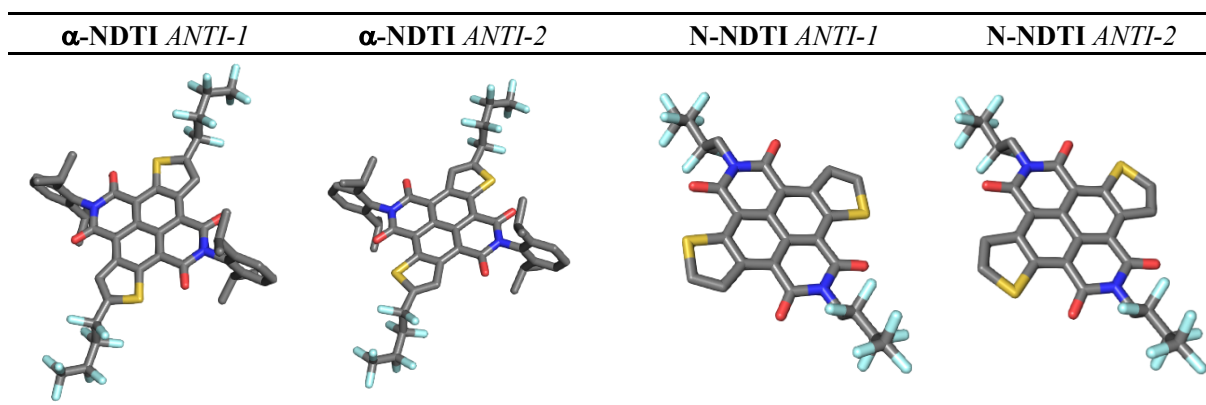
Figure 4.12. The two structures of **α-NDTI** and **N-NDTI** characterized by a different orientation of thiophene groups. Figure adapted from Ref. [92].

α-NDTI and **N-NDTI** show very different charge percolation pathways (Figure 4.13). While for the latter, three pathways with significant electronic coupling have been individuated, for the former, only the P1 pathway (Figure 4.13) carries a significant electronic coupling and its value is reported in Table 4.3. All others display negligible values. This is related to the solid phase packing, which in turn is influenced by the combined effect of N and α substituents favoring a one-dimensional (1D) columnar arrangement for **α-NDTI** (see Figure 4.13a for instance). Only the P1 path displays smaller intermolecular distance leading to an efficient overlap between LUMO orbitals[92]. Overall, for **α-NDTI** the electronic couplings associated with path P1 range between 36–40 meV (for *ANTI-1* and *ANTI-2,* respectively) (see Table 4.3).

On the other hand, **N-NDTI** crystal displays a different packing. Due to reduced number of substituents, the **N-NDTI** crystal features a better columnar π-stacking resulting in smaller intermolecular distances. The three main paths are shown in Figure 4.13 and the associated electronic couplings are in Table 4.3. The P1 path defines a columnar percolation channel along the *c* axis, with a coupling of 35 meV for *ANTI-1* and 50 meV for *ANTI-2*. Path P2 follows the direction of the *b* axis and shows larger distance along with reduced coupling (10 meV for *ANTI-1* and 8 meV for *ANTI-2*). Finally, path P3 defines a zig-zag percolation across two different columns of π-stacked molecules with a minor coupling of 2 meV (1 meV), and it would contribute to seldom jumps to adjacent columns.

(a) **(b)**
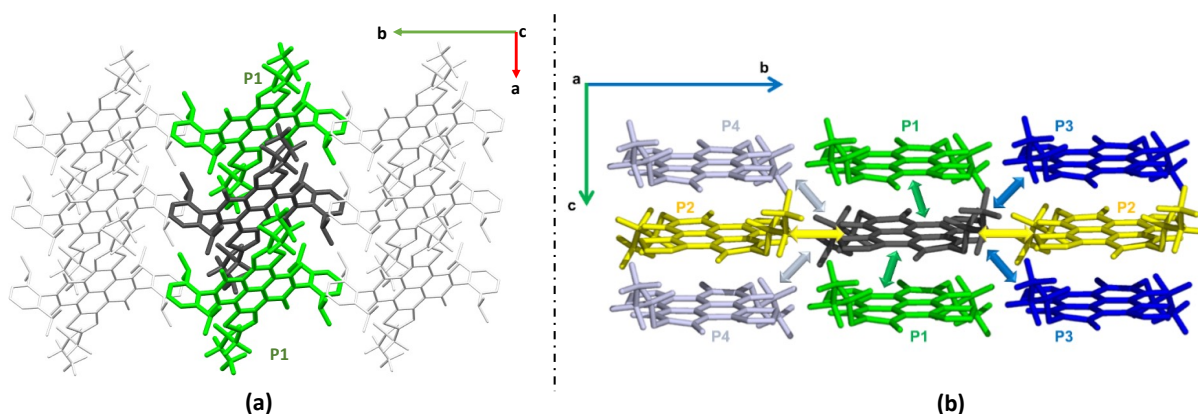
Figure 4.13. The most relevant charge transport path (starting from the central dark gray to the lateral green molecules) shown within a portion of (a) **α-NDTI** and (b) **N-NDTI** crystal. Only P1 is individuated for **α-NDTI** and the view is along the *c* axis. For **N-NDTI** four paths have been drawn: P1 (green), P2 (yellow), P3 (blue), and P4 (light gray). The view is along the *a* axis. Figures adapted from Ref. [92].

Table 4.3. Charge hopping paths (Pn) relevant for charge transport and the intermolecular distances for each dimer, inter-planar distances, and electronic couplings V_{ij} (B3LYP/6-31G*) between the LUMO orbitals and Marcus–Levich–Jortner (MLJ) rate constants k_{eT} computed for two crystalline structures *ANTI-1* and *ANTI-2* of **α-NDTI** and **N-NDTI**. Table adapted from Ref. [92].

Dimer or Charge Transfer Path	Molecules Forming the Dimer	Intermolecular Distance (Å)	Interplanar Distance (Å)	V_{ij} (LUMO) (meV)	k_{eT} [a] (s⁻¹)
		α-NDTI			
P1	*ANTI-1*	6.654	3.646	36	$5.62 \cdot 10^{12}$
	ANTI-2	6.654	3.646	40	$6.88 \cdot 10^{12}$
		N-NDTI			
P1	*ANTI-1*	4.197	3.623	35	$6.87 \cdot 10^{12}$
	ANTI-2	4.197	3.623	50	$1.36 \cdot 10^{13}$
P2	*ANTI-1*	11.002	0.144	10	$5.26 \cdot 10^{11}$
	ANTI-2	11.002	0.144	8	$3.05 \cdot 10^{11}$
P3	*ANTI-1*	11.238	3.467	2	$2.59 \cdot 10^{10}$
	ANTI-2	11.238	3.467	1	$5.12 \cdot 10^{9}$
P4	*ANTI-1*	12.290	3.033	0	$4.40 \cdot 10^{8}$
	ANTI-2	12.290	3.033	0	$1.56 \cdot 10^{8}$

[a] From Eq. 4.8, without applied electric field.

To summarize, fluoroalkyl substitution strongly impacts the solid state organization of the two NDTI derivatives. Through the analysis of charge transfer pathways and the value of electronic coupling, a 1D charge percolation is favored in **α-NDTI** and a more isotropic charge transfer network is expected for **N-NDTI**. However, charge transfer rate constants (Eq. 4.8) depend also on reorganization energies as will be discussed in the next section.

4.3.2 Reorganization energies and Huang-Rhys factors

The intramolecular reorganization energies are computed either with AP method (Section 4.1.1) and from the computed Huang–Rhys (HR) factors S_m (Section 4.1.2).

Figure 4.14 shows the individual components λ_i^m (*i.e.* the reorganization due to vibrational mode *m*) to the total reorganization energy. A larger contribution from vibrations above 1200 cm⁻¹ is observed suggesting that the harmonic approximation is acceptable. Most of these vibrations are associated with C-C bond stretching of the conjugated molecular core, where the largest geometry change occurs. Furthermore, active frequencies (larger λ_i^m values) are very similar for the neutral and charged species.

Notably, inspection on the computed HR factor S_m (see Figure 4.15) shows that a large number of low-frequency intramolecular vibrations, mostly associated with the flexible substituents, displayed unexpectedly large S_m values that are very likely to be overestimated as a result of the anharmonic character of low-frequency vibrations.
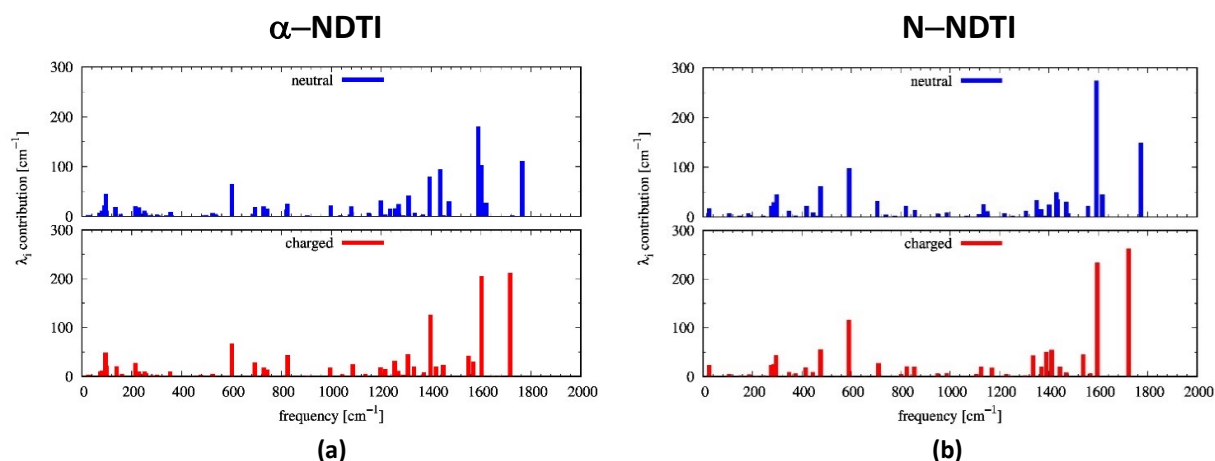
Figure 4.14. The vibrational frequency contributions (from HR factors, B3LYP/6-31G* level of theory) to the computed intramolecular reorganization energies λ_i (for n-type charge transport) of (a) **α-NDTI** and (b) **N-NDTI**. Each graph shows the contribution from neutral species in the top part (blue bars) and from the negatively charged species in the bottom part (red bars). Figures adapted from Ref. [92].
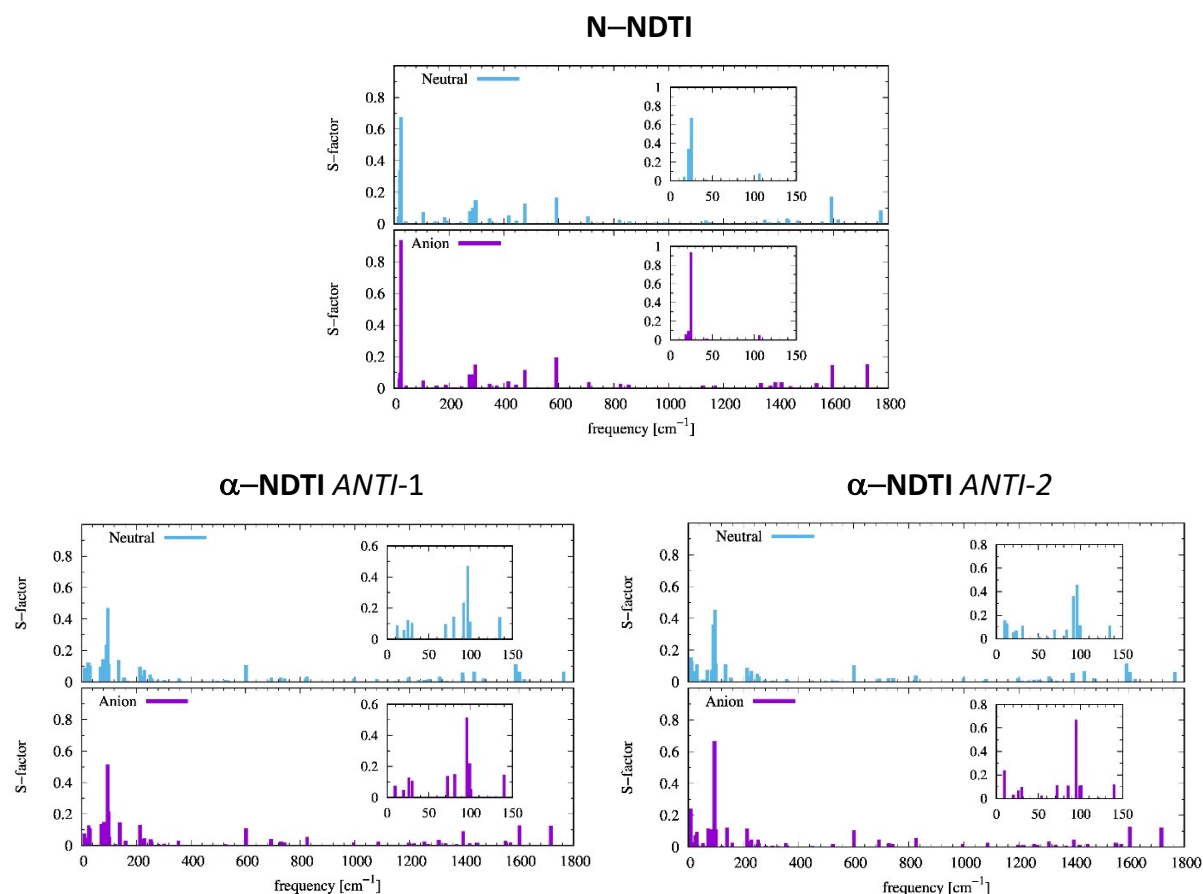
Figure 4.15. HR factors S_m (B3LYP/6-31G*) associated with the vibrational modes m of neutral and charged species of (top) **N-NDTI** and (bottom) two conformers of **α-NDTI**. (top) The graph inside shows that largest HR factor is computed for a vibrational frequency below 50 cm^{-1}. (bottom) For both conformers, the graphs inside show that the largest HR factor is computed for a vibrational frequency below 100 cm^{-1}. Figures adapted from Ref. [92].

Since vibrational frequencies below 200 cm^{-1} can be considered as classical degrees of freedom at room temperature, their contributions can be excluded for the evaluation of charge transfer rate constants with the MLJ equation (Eq. 4.8). Effective parameters included in the

MLJ formulation were determined by retaining only vibrations above 200 cm^{-1} and their values can be found in Table 4.4.

Table 4.4. Intramolecular reorganization energy λ_i, effective frequency ω_{eff}, and effective HR factor S_{eff}, with contributions from intramolecular classical vibrations $\lambda_{classic}$ and from the outer sphere λ_o to $\lambda_{o+classic}$ in Eq. 4.8 for **α-NDTI** and **N-NDTI**. Table adapted from Ref. [92].

|	λ_i [a] (eV)	ω_{eff} [a] (cm^{-1})	S_{eff} [a]	$\lambda_{classic}$ [b] (eV)	λ_o [c] (eV)
α-NDTI *ANTI-1*	0.286	920	2.51	0.032	0.01
α-NDTI *ANTI-2*	0.286	925	2.49	0.033	0.01
N-NDTI [d]	0.294	849	2.79	0.011	0.01

[a] Computed by excluding vibrations with frequencies lower than 200 cm^{-1}. [b] Contribution due to intramolecular vibrations lower than 200 cm^{-1}. [c] Value chosen according to Ref. [289]. [d] Only one value was reported in this case, since both *ANTI-1* and *ANTI-2* structures converged to the same single-molecule equilibrium geometry.

Finally, we note that the magnitudes of the computed reorganization energies are much larger than the computed electronic couplings (never exceeding 50 meV), implying a substantial reliability of the non-adiabatic hopping mechanism ($\lambda_i \gg V_{ij}$)[14,290].

4.3.3 Charge transfer rate constant and KMC simulations

The MLJ rate constants k_{eT}, computed without considering an applied electric field, for the selected charge transfer paths are collected in Table 4.3. The computed values for path P1 of both NDTI derivatives are large ($10^{12} - 10^{13}$ s^{-1}) and similar, as was expected from the λ_i and V_{ij} values. Starting from k_{eT}, the KMC (Brownian) trajectories are generated and collected in Figures 4.16 and 4.17.

Figure 4.16 confirms the 1D charge transport of **α-NDTI**, as expected from the computed V_{ij} value and as previously documented for other NDTI derivatives[291]. Similarly, the columnar charge transport resulted in a remarkable anisotropy of the computed TOF charge mobilities as depicted in Figure 4.18a.
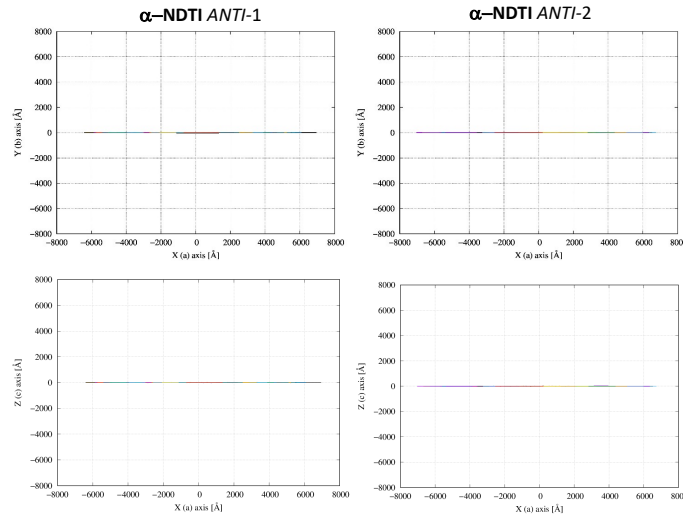
Figure 4.16. KMC brownian trajectories of the charge carrier computed for **α-NDTI** *ANTI*-1 and *ANTI*-2 and projected on (top) the X,Y plane (*a,b* crystallographic plane) and (bottom) the X,Z plane (*a,c* crystallographic plane). For both crystal structures the charge transport is 1D along the *a* axis. Figures adapted from Ref. [92].
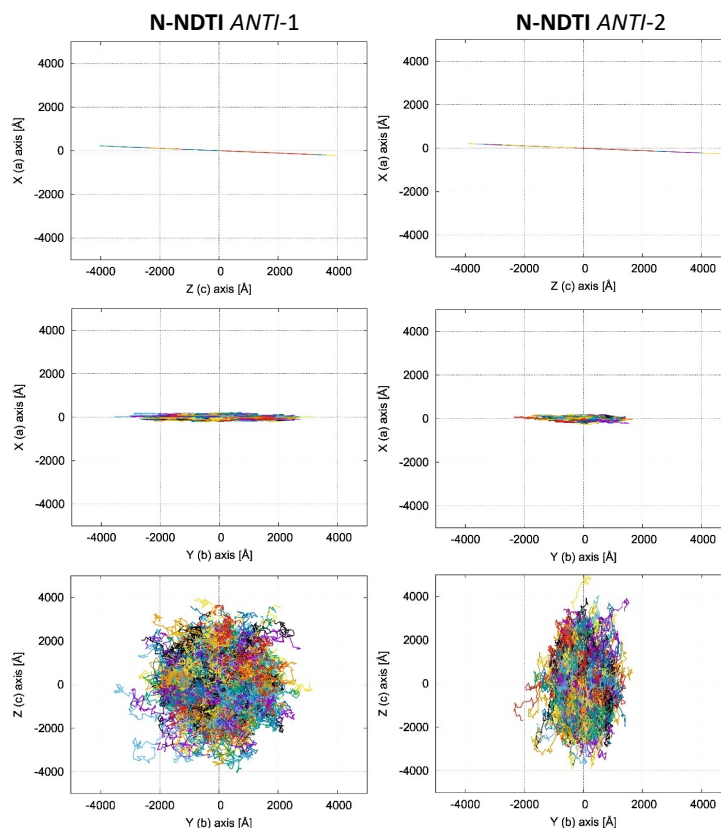
Figure 4.17. Plot of KMC trajectories (each trajectory with a different color) of the charge carrier computed for **N-NDTI** *ANTI-1* and *ANTI-2* and projected on: (top) the X,Z plane (*a,c* crystallographic plane), (middle) the X,Y plane (*a,b* crystallographic plane) and (bottom) Y,Z axis (*b,c* crystallographic plane. For both crystal structures the charge transport is bidimensional in the *b,c* plane. Figures adapted from Ref. [92].

The KMC trajectories in Figure 4.17 show that the charge transport in **N-NDTI** is essentially bidimensional and parallel to the *b,c* crystallographic plane as a result of non-negligible V_{ij} values for paths P1, P2, and P3 (Figure 4.13b). The *b,c* plane almost coincides with the Y,Z Cartesian plane (Figure 4.17, bottom), on which the trajectories' projections are therefore the largest. The charge transport trajectories of **N-NDTI** *ANTI-1* and *ANTI-2* show similar displacements along Z (almost coincident with *c*). For *ANTI-1*, the extension of the charge displacement in the two directions (Y,Z) is quite similar (see *e.g.* Figure 4.17 bottom left), although the P1 rate constant (along $c \approx$ Z) is larger than that of P2 (along $b =$ Y) (Table 4.3). However, since the intermolecular distance for path P2 is larger than that of P1, the charge hopping through P2 needs to cover a larger distance along *b* (Y) with respect to that covered through P1 along *c* ($\approx$ Z). This interplay between rate constants and intermolecular distances leads to a modest anisotropy overall in the *b,c* (or Y,Z) plane for **N-NDTI** *ANTI-1* and a more pronounced one for *ANTI-2*. For the latter, indeed, the rate constant for jump P1 largely dominates over that of P2. Similar differences can be seen from the computed anisotropies of the TOF charge mobilities (Figure 4.18b): *ANTI-1* (purple in Figure 4.18b) shows slightly lower mobilities than *ANTI-2* (green).
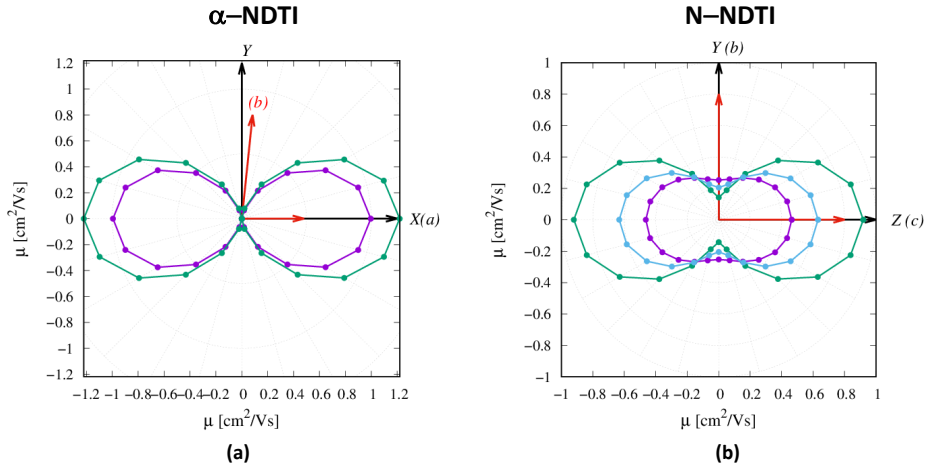
Figure 4.18. Anisotropy of charge transport from TOF KMC simulations for (a) **α-NDTI** and (b) **N-NDTI**. Purple represents *ANTI-1*, green represents *ANTI-2*, and cyan represents the *mix* structure which is not considered here. Figure adapted from Ref. [92].

Table 4.5. Computed Brownian (zero field) and TOF mobilities for **α-NDTI** and **N-NDTI**. Table adapted from Ref. [92].

	Zero Field (Brownian)	TOF	TOF	*Exp*
	μ $(cm^2V^{-1}s^{-1})$	μ_{max} $(cm^2V^{-1}s^{-1})$	μ_{min} $(cm^2V^{-1}s^{-1})$	μ [a] $(cm^2V^{-1}s^{-1})$
α-NDTI *ANTI-1*	0.32	1.00 [b]	$3 \cdot 10^{-6}$ [b]	0.037
α-NDTI *ANTI-2*	0.39	1.23 [b]	$2 \cdot 10^{-6}$ [b]	
N-NDTI *ANTI-1*	0.24	0.46 [c]	0.25 [c]	1.27
N-NDTI *ANTI-2*	0.34	0.92 [c]	0.14 [c]	

[a] Average experimental (Exp) mobilities from Ref. [282]. [b] TOF mobilities computed in the X,Y($\approx a,b$ crystallographic) plane. [c] TOF mobilities computed in the Z,Y ($\approx b,c$ crystallographc) plane.

Overall, the computed charge mobilities from the zero field (Brownian) and TOF KMC simulations (Table 4.5) indicate a similar charge transport efficiency for both NDTI derivatives, with computed values to the order of 1 $cm^2V^{-1}s^{-1}$. Such similar computed mobilities, however, are in contrast with experimental observation of a superior charge transport efficiency for **N-NDTI** vs. **α-NDTI**.

One suggestion can be given inspecting the crystal structures of both NDTI derivatives in OFET. The X-ray diffraction (XRD) measurements of **α-NDTI** single crystal showed that the *a,b* plane was parallel to the OFET substrate. Measured mobility was, thus, averaged in the *a,b* plane. From our calculations, only along the *a*-axis direction the mobility is large. In other directions, namely in the *a,b* plane, which is parallel to the OFET substrate and in the direction perpendicular to it, the mobility reduces to almost zero (compare $\mu_{max} \approx 1$ $cm^2V^{-1}s^{-1}$ and $\mu_{min} \approx 10^{-6}$ $cm^2V^{-1}s^{-1}$ in Table 4.5). On the other hand, XRD measurements of the **N-NDTI** single crystal displayed the *a*-axis standing on the substrate, while the *b,c* plane was arranged parallel to the substrate. The KMC simulations show a similar charge transport efficiency in every direction of the *b,c* plane (*i.e.*, the substrate plane) of **N-NDTI**, and therefore, a favourable mobility is always expected in this case.

A second, minor discrepancy between the computed and observed results concerns the slight underestimation of the computed TOF mobility of **N-NDTI** (largest value of which is 0.92 $cm^2V^{-1}s^{-1}$) compared to the highest experimental mobility (1.56 $cm^2V^{-1}s^{-1}$)[282]. This is unusual

since predicted mobilities are generally overestimated due to the ideal conditions underlying the models used. Several computational and experimental reasons may account for this discrepancy. For instance, although the conditions for the non-adiabatic hopping were satisfied (for both NDTI derivatives), other factors could have limited the quantitative agreement of the computed charge mobilities, among them being the fact that MLJ formulation relies on a single effective parameter and that our KMC simulations did not include the effects of carrier-carrier interactions, a factor that may be relevant for high charge densities[92],.

Overall, the above considerations may explain the differences between the observed and computed mobilities. Aside from these factors, dynamic disorder may also play a role in affecting the final computed charge mobility, as is discussed in the next section.

4.2.4 Influence of dynamic disorder

A general consensus on charge transport in organic semiconductors is that dynamic disorder is one of the crucial parameters. Generally, thermally induced fluctuations of transfer integrals limit charge transport[284,287,292], but for percolation channels characterized by small electronic couplings, they have been shown to open new hopping pathways, thereby increasing the mobility[250,262,293–295]. In recent works, it has been reported that the strength of the dynamic disorder is highly correlated with the gradient of the electronic couplings[292,296] with respect to the phonon modes, a parameter also known as the **non-local electron–phonon coupling** (or Peierls coupling) [14,286].

Recently, dynamic disorder in PDI and NDI derivatives has been investigated[249–251] by running molecular dynamics (MD) simulations followed by quantum-chemical evaluation of V_{ij}. The analysis of fluctuations *via* a Fourier transform of the autocorrelation function of V_{ij}[297] revealed that long and short molecular axis sliding motions were responsible for the transfer integral fluctuations and, interestingly, they were demonstrated to *activate* (*i.e.,* a phonon-assisted mechanism) additional charge transport channels in a PDI derivative[250].

Seeking possible evidence of phonon-assisted charge transport, a similar strategy is applied to investigate the role of thermally induced disorder in **N-NDTI**. Firstly, the two charge pathways displaying limited efficiency (*i.e.,* low V_{ij}), namely P2 and P3 (Table 4.3), were considered since they are more promising for phonon-assisted charge transport activation. However, the thermal fluctuations were negligible for both paths. Therefore, also path P1, the one with large electronic coupling, was included. It should be noted that for large electronic coupling, the dynamic disorder effects may only be detrimental to charge transport, ultimately lowering the mobility.

The computed fluctuations of the P1 transfer integrals is shown in Figure 4.19 (top). The standard deviation (σ) is only 11 meV, about one third of the average electronic coupling ($\langle V_{ij} \rangle$ = 35 meV; see Table 4.3). The most active phonon frequencies in determining the P1 transfer integral fluctuations, are shown in Figure 4.19 (bottom). Low-frequency intermolecular phonons (below 50 cm^{-1}) corresponding to sliding modes[250,298–300] are dominant. However, because the strength of the non-local electron-phonon coupling is related to σ[263,286], its modest value suggests only minor effects of the sliding modes on the **N-NDTI** charge mobility. Similarly, it can be argued that the sliding phonon modes would also be the primary lattice

vibrations determining the P1 transfer integral fluctuations in **α-NDTI**.
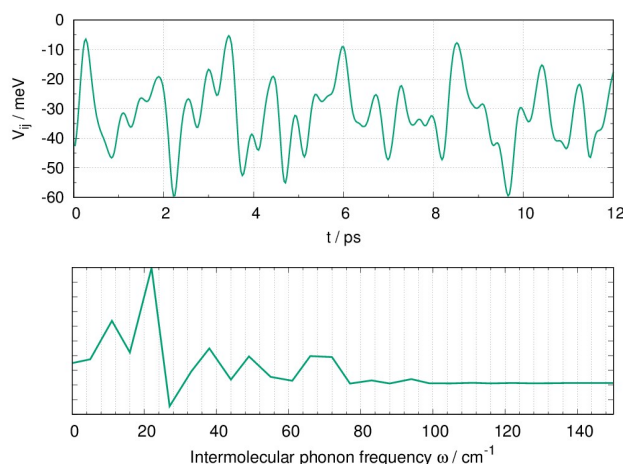
Figure 4.19. Dynamic disorder effects on the crystal of **N-NDTI** from MD simulations, showing (top) the fluctuations of transfer integrals V_{ij} for the P1 charge transfer path, computed from snapshots of MD at 300 K and (bottom) a Fourier transform of the autocorrelation function of the transfer integrals, showing the activity of low-frequency intermolecular phonons. Figures adapted from Ref. [92].
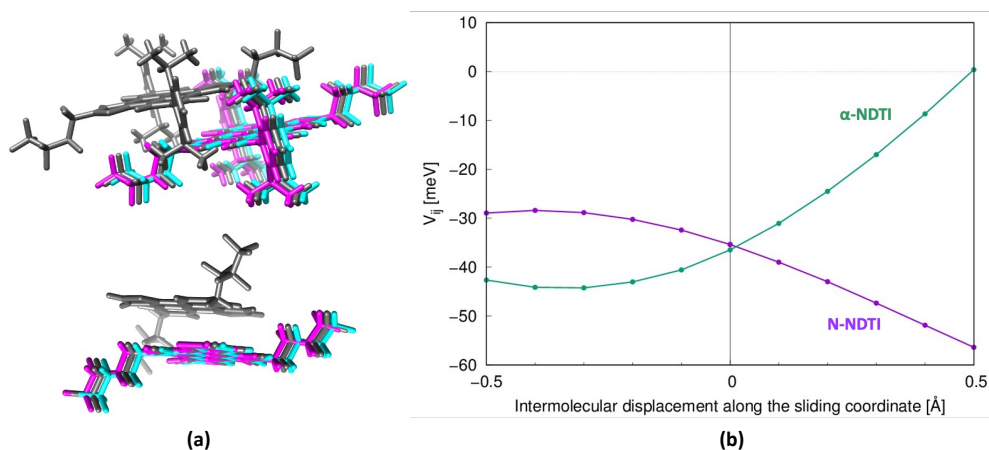
Figure 4.20. (a) Intermolecular sliding motion considered for (top) **α-NDTI** and (bottom) **N-NDTI**. Gray molecules represent the crystal structure of the P1 dimer. Cyan and magenta represent displaced molecules along the sliding coordinates. (b) Electronic coupling dependence on the sliding coordinates (**α-NDTI** in green and **N-NDTI** in purple). Figures adapted from Ref. [92].

Since electronic coupling fluctuations along P1 are expected to depress charge mobility (owing to large V_{ij} value), it is interesting to compare **α-NDTI** and **N-NDTI**, seeking evidence for an additional mechanism accounting for the lower experimental mobility of the former. To this end, the modulations of the P1 electronic couplings were computed along the sliding coordinates represented in Figure 4.20a. The computed coupling dependences are collected in Figure 4.20b. The absolute value of the numerically estimated derivative (associated to the non-local electron–phonon coupling) is 48 meV/Å for **α-NDTI** and 33 meV/Å for **N-NDTI**. The larger electron–phonon coupling for **α-NDTI** may therefore have contributed to reducing its charge transport efficiency, as was similarly shown in a recent work on alkylated DNTT[298], where a similar sliding mode was identified as a *killer* phonon.

Although a more detailed assessment of the entire spectrum of non-local electron–phonon

couplings should be carried out for a conclusive response, the preliminary results of such a higher dependency of **α-NDTI** on thermal fluctuations than **N-NDTI** may further justify its lower observed charge mobility (Table 4.5).

4.4 Conclusions

In this Chapter, I have collected the results of investigations on the charge transport properties of a few organic semiconductors.

In the first study, the molecular units are conjugated diradicals. Thus, quantum chemical calculations were carried out to rationalize the connections between diradical character and ambipolar charge transport. The objective was to characterize the investigated diradicals according to one of the parameters influencing charge transport, namely the reorganization energy λ_i. The novelty of this work is the elucidation of the connection between moderate/medium diradical character and ambipolar charge transport. This connection is set out by means of the pivotal role of the small reorganization energies produced by such medium y_0 values. In addition, these values are similar for holes and electrons supporting equivalent p- and n-type transport.

In the second study I went deep into the role of intermolecular organization in the solid phase. Disregarding the role of impurities, contact resistance limitations and other experimental factors, the lower mobility of **α-NDTI** was rationalized by considering the striking difference in the charge mobility anisotropy. While **N-NDTI** displayed sizable charge mobilities in every direction parallel to the substrate, **α-NDTI** exhibited a prominent anisotropic character with mobility that reduced to zero in some directions parallel to the substrate. I also compared the role of dynamic disorder on the most effective charge transport path (P1) of both derivatives. Although limited to transfer integral fluctuations induced by an intermolecular sliding mode, the computed electron–phonon couplings confirmed a more detrimental effect for **α-NDTI** compared to **N-NDTI**.

Chapter 5: Exciton states in molecular aggregates

5.1 General overview on exciton states in molecular aggregates

Exciton states are referred to excited states in condensed phases which, in the context of this dissertation correspond to molecular materials or molecular aggregates. The exciton states of interest are among the low-lying ones since they determine the photophysical properties of the material. Theory on molecular excitons has been widely developed starting from the two pioneering figures, Kasha [301,302] and Davydov[303]. These works are based on rather simple models which consider the exciton states as a combination of localized excitations on the same monomer. CT type excitons (*i.e.,* charge-transfer excitations from one molecule to the nearby one) are assumed to be very high in energy. Therefore, CT exciton states do not perturb the wavefunction (*i.e.,* nature) of low-lying exciton states of the aggregate. Based on these assumptions, Kasha interpreted the optical responses of a dimer along the longitudinal shift (*i.e.,* along a sliding motion). With the application of a simple transition dipole moment interaction scheme, he provided a simple interpretation of the photophysical properties of aggregates by referring to the orientation of transition dipole moments. The two limiting cases are known as H-aggregate when the two transition dipole moments are parallel; while when these two vectors are in-line, such that the two monomers are stacked head-to-tail, a J-aggregate is formed. However, it has been shown lately that CT excitons do play an important role in modulating the photophysical property of the dimer also at short sliding distance[21,304].

From a standard quantum-chemical (QC) calculation on the aggregate, adiabatic exciton states are obtained and they are expressed as linear combinations of delocalized excitations (*De*) built from delocalized molecular orbitals (DMOs). The contributions of CT and localized excitations in the exciton states are not straightforwardly given and they need to be extracted with some post-processing tools. To give some examples: the TheoDORE program of

Plasser[305], Edmiston-Ruedenberg localization method[306] and Boys localization method[307]. The latter two are included in Q-Chem package of programs.

Parallelly, in the lab where I have carried out my PhD studies, a diabatization protocol has been developed based on QC calculations at TD-DFT level. TD-DFT is a cost-effective approach for the evaluation of exciton states of molecular aggregates and has been shown to provide reliable results when coupled to a suitable choice of the exchange–correlation functional. I have contributed to some parts of this protocol during my PhD.

In addition, motivated by the need of cost-effective approaches to provide results of quality comparable to full-aggregate calculation, we proposed a model Hamiltonian (**mH**) built on the basis of QC calculations carried out only on the dimers composing the aggregate.

Both approaches show very good performance on the low-lying exciton states of different aggregates.

In this Chapter, I will start with a brief summary on Kasha's exciton model followed by a more detailed introduction to J- and H-aggregates. The *in-house* developed diabatization procedure and the strategy to build a **mH** will be introduced in the following sections.

The diabatization protocol has been applied to disentangle the nature of exciton states in Perylene-bis(dicarboximide) (PDI) dimers [93,94] and in small oligoacene dimers[95]. These two applications will be introduced in Sections 5.5 and 5.6, respectively. The application of the **mH** to determine excitation energies and exciton states characters of trimers and tetramers of PDI[93] will be shown in Section 5.7.

5.2 Kasha's exciton model

The simplest model to discuss intermolecular interactions is a dimer, *i.e.,* an aggregate formed only by two monomers (Figure 5.1a).

Kasha's exciton model[301] is a state interaction theory. It assumes that intermolecular electron overlap is small and the molecular units preserve their individuality in the aggregate. In this way, the molecular exciton model satisfies the requirement of a perturbation theory. The solution for the aggregate (its energies and wavefunctions), thus, can be found in terms of the wavefunction of the electronic states of the components.

Considering a dimer formed by molecule *a* and *b* as shown in figure below:
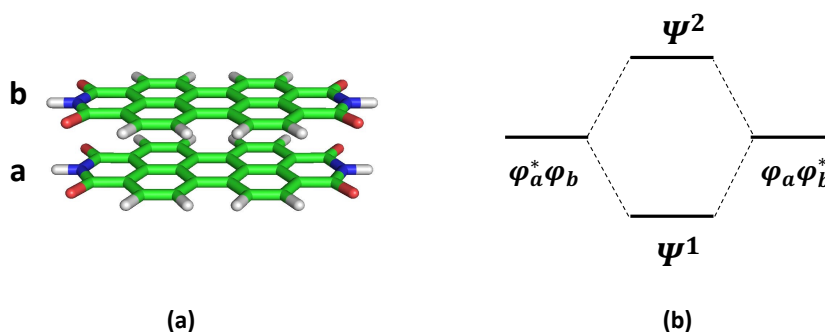
Figure 5.1. (a) A general dimer system formed with two monomers *a* and *b*. (b) Schematic representation of the excitonic interaction between the electronic wavefunctions of the individual components of a dimer.

The ground state wavefunction Ψ_G is defined as:

$$\Psi_G = \psi_a \psi_b \tag{5.1}$$

where ψ_a is the ground state wavefunction of molecule a and ψ_b is that of molecule b. The Hamiltonian operator for the dimer is given as:

$$\hat{H} = \hat{H}_a + \hat{H}_b + \hat{V} \tag{5.2}$$

where $\hat{H}_a$ and $\hat{H}_b$ are the Hamiltonian operators respectively for monomer a and b. $\hat{V}$ is the coulombic potential term that describes the intermolecular perturbation. The ground state energy is then given by:

$$E_G = \langle \psi_a \psi_b | \hat{H} | \psi_a \psi_b \rangle = E_a + E_b + \langle \psi_a \psi_b | \hat{V} | \psi_a \psi_b \rangle \tag{5.3}$$

The first two terms are simply monomers' ground state energies, while the third term represents the Van der Waals interaction energy between the two molecules.

Similarly, the excited states of the dimer could be written as $\psi_a^* \psi_b$ (with the excitation localized on a monomer) or as $\psi_a \psi_b^*$ (where the excitation is localized on monomer b). If the two monomers are isolated, these two localized excited states are exactly degenerate and independent one from the other since a and b are perfectly identical (see Figure 5.1b). However, even though very weak, the interaction between the monomeric units of the dimer is enough to cause the loss of the degeneration. The two states are split and the correct wavefunctions for the dimer's exciton states are, thus, the linear combinations of these two localized excitations.

$$\Psi^{1,2} = c_1 \psi_a^* \psi_b \pm c_2 \psi_a \psi_b^* \tag{5.4}$$

The eigenvalues of the dimer's exciton states can be obtained through the diagonalization of the 2×2 matrix representing the Hamiltonian in the basis of the localized excitations ($\psi_a^* \psi_b$ and $\psi_a \psi_b^*$):

$$\begin{vmatrix} H_{aa} - E & H_{ab} \\ H_{ba} & H_{bb} - E \end{vmatrix} = 0 \tag{5.5}$$

with

$$H_{aa} = H_{bb} = \langle \psi_a^* \psi_b | \hat{H} | \psi_a^* \psi_b \rangle$$

$$H_{ab} = H_{ba} = \langle \psi_a^* \psi_b | \hat{H} | \psi_a \psi_b^* \rangle \tag{5.6}$$

Resolution of Eq. 5.5 leads to two eigenvalues associated with the two normalized exciton states. In particular, energies are:

$$E^1 = H_{aa} - H_{ab} \text{ with } \Psi^1 = \frac{1}{\sqrt{2}} (\psi_a^* \psi_b - \psi_a \psi_b^*)$$

$$E^2 = H_{aa} + H_{ab} \text{ with } \Psi^2 = \frac{1}{\sqrt{2}} (\psi_a^* \psi_b + \psi_a \psi_b^*) \tag{5.7}$$

Substituting Eq. 5.6 into Eq. 5.7, we get

$$E^1 = E_a^* + E_b + \langle \psi_a^* \psi_b | \hat{V} | \psi_a^* \psi_b \rangle - \langle \psi_a^* \psi_b | \hat{V} | \psi_a \psi_b^* \rangle$$

$$E^2 = E_a^* + E_b + \langle \psi_a^* \psi_b | \hat{V} | \psi_a^* \psi_b \rangle + \langle \psi_a^* \psi_b | \hat{V} | \psi_a \psi_b^* \rangle \qquad (5.8)$$

The third terms in Eq. 5.8 are similar to the last term in Eq. 5.3 and represent the *Van der Waals* interaction between an excited molecule (*a**) and the molecule at ground state (*b*). The last terms in Eq. 5.8 are known as **exciton interaction** or *exciton splitting term*[301] (V_{exc} or ε). The separation between the two exciton states is defined by $2V_{exc}$ as result from the subtraction between E^2 and E^1. This splitting in exciton states is known as "*Davydov splitting*".

To sum up, interaction between two excitations localized on the two monomers forming the dimer ($\psi_a^* \psi_b$ and $\psi_a \psi_b^*$) leads to the generation of two delocalized states (Ψ^1 and Ψ^2) whose energies are respectively lower and higher than the original localized excited states.

5.2.1 Optical properties in Kasha's exciton model: J- and H- aggregate

Within the framework of Kasha's exciton model, the transition dipole moments of the two exciton states of the dimer are given by the linear combination of two transition moments related to the localized excitations: μ_a (excitation localized on *a*) and μ_b (related to excitation localized on *b*).

$$\mu^{1,2} = \frac{1}{\sqrt{2}} (\mu_a \pm \mu_b) \qquad (5.9)$$

The electron transition intensity (or probability) is generally proportional to the square modulus of $\mu^{1,2}$. The latter can be calculated, in Kasha's model, adopting a *quasi-classical vector model* [301] which allows the consideration of the angle formed between the two vectors (μ_a and μ_b), *i.e.* the transition dipole moments of the two monomers. Kasha delineated two situations in which the two transition dipoles are **parallel** (Figure 5.2 left) or **in-line** (Figure 5.2 right).
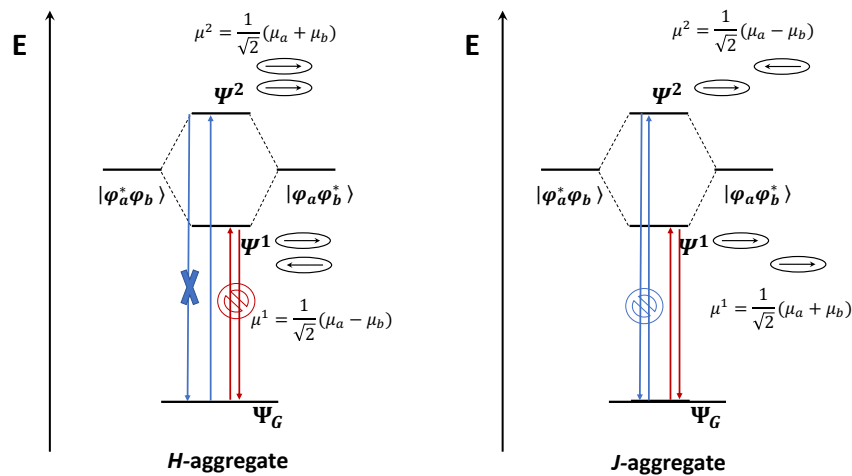
Figure 5.2. Diagram with the exciton states of the dimer in comparison with that of the monomer in the case of parallel and in-line dipoles. The arrows next to the label of the exciton state indicate the orientation of the transition dipoles of the monomers. The transition dipole moments for the dimeric states are also given. Red arrows indicate red-shifted emission and absorption, while blue arrows show blue-shifted absorption and emission.

The ovals in Figure 5.2 represent the molecular profile and the arrows inside indicate the direction of the molecular transition dipole moments.

Kasha showed that when the two transition dipoles are **parallelly aligned**, the *in-phase* (↑↑) situation corresponds to an electronically less stable state with respect to the *out of phase* (↑↓) one owing to a repulsive interaction. The two situations correspond respectively to Ψ^2 and Ψ^1 states. The dimer's transition moment is given by the vector sum of the individual transition dipoles as shown in figure. Transitions from Ψ_G to Ψ^1 (the lowest exciton state) is forbidden because of its null transition dipole moment; whereas transition to Ψ^2 is allowed since μ^2 is different from zero. A *blue shift* with respect to the monomeric absorption, is observed for the dimer's absorption. Moreover, being the lowest energy excited state spectroscopically forbidden, the aggregate cannot show fluorescence. Aggregates showing these spectroscopic characteristics are known as **H aggregate**.

On the other hand, when the two transition dipoles are in-line, the *in-phase* (→→) situation is more stabilized as result of electrostatic attraction and it corresponds to Ψ^1. Consequently, the *out-of-phase* situation (→←) is associated to the higher lying Ψ^2. The net transition dipole moments show that Ψ^1 (*i.e.,* the lowest exciton state) is optically allowed. Therefore, a strong *red shift* in absorption, with respect to monomer's absorption, can be observed in this case and a red-shifted fluorescence can also be noticed. This type of aggregate is known to be **J aggregate.**

5.2.2 Beyond the Kasha model

Kasha's model is rather simple and intuitive. However, it is limited to consider only interactions between excitations localized on the two monomers (*i.e.,* $\psi_a^* \psi_b$ and $\psi_a \psi_b^*$). From a configuration point of view, these two excitations can be represented as shown in the following figure, where excitations are generated promoting one electron from an occupied MO of the monomer (*e.g.,* h_a) to the unoccupied MO of the same monomer (*e.g.,* l_a). This kind of excitations will be called as *localized excitation* (LE)[21,308] in this work.
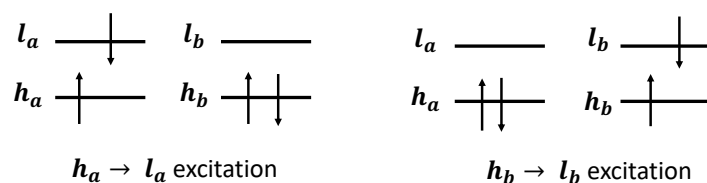
Figure 5.3. Schematic representation of the localized excitations of a dimer. Only HOMO and LUMO orbitals for each monomer have been considered.

The consideration of interactions only between LEs is correct only when the two monomers are far enough to ignore short-range interactions. However, this is not the case of π-stacked aggregate such as those formed by conjugated molecules. The typical intermolecular distance is around 3.4 Å (*i.e.* the sum of the Van der Waals radii of two sp^2 carbons) which allows significant wavefunction overlap and the emergence of short-range interactions [21]. The shorter intermolecular distance also allows *charge transfer excitations* (CT) [21,308] which consist in

transferring an electron from the occupied MO of one monomer (*e.g.* h_a) to the unoccupied MO of the other monomer (*e.g.* l_b), as shown in figure below:
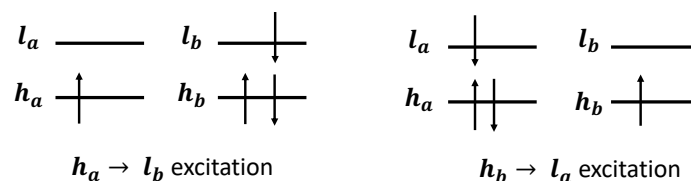
Figure 5.4. Schematic representation of the charge transfer excitations of a dimer. Only HOMO and LUMO orbitals for each monomer have been considered.

At this shorter distance, the energies of CT states can be comparable to those of LEs. Therefore, CT states can interact either with other CTs or with LEs contributing to change the photophysical properties of the aggregate. In Spano's model [21], in fact, CT excitations are shown to have an important contribution to the formation of J-aggregate in perylene dimer at short sliding distances. This phenomenon is known as *CT-mediated J aggregation*[21]. Additionally, CT states have been identified as possible mediators in singlet fission [23–29] and have a crucial role in exciton-dissociation, charge-separation and charge-recombination processes in organic photovoltaics[33,34].

In summary, for a comprehensive understanding of the exciton states in molecular aggregates, the role of CT excitations and especially the interaction between CT/CT and CT/LEs need to be considered. These CT excitations, on the other hand, are automatically included in QC calculations carried out on molecular aggregates.

5.3 The diabatization procedure

A convenient way to analyze the exciton wavefunction character is to express the adiabatic states on a basis of diabatic states. The most natural choice of diabatic states is to consider excitations within monomers forming the aggregate[56,57,59,60,304], which in turn can be either LE and CT introduced in the previous section. These diabatic states emerge respectively from intramolecular and intermolecular excitations involving monomer localized molecular orbitals (LMOs).

When undergoing the character analysis of exciton states obtained from QC calculations, the dimension of the adiabatic/diabatic basis of states to be included in the analysis need to be defined and it is directly related to the number of the selected active orbital space (AOS) from which electron excitations are generated. A common assumption is the minimal orbital space (MIOS) built up from the minimal number of monomer orbitals necessary for the correct description of low-lying excited states of the monomer. MIOS can include only H and L of each monomer[56,59,304,308,309] when the lowest excited state of the monomer is dipole allowed and well described by the H→L excitation, *e.g.* as in PDI. Alternatively, MIOS can range from H−1 to L+1 as in naphthalene and anthracene, where the two low-lying excited states are L_a and L_b following Platt's notation[310]. The latter excited state is dominated by the combination of $H - 1 \to L$ and $H \to L+1$ excitations which implies the inclusion of H−1 and L+1.

In the framework of TD-DFT calculations, the exciton wavefunction is described by single

excitations. Restricting the attention to the MIOS, the number of single excitations of a given spin multiplicity, for an aggregate of n molecules, is n^2, implying that only the computed adiabatic exciton states whose wavefunction is dominated by some of the n^2 excitations, are considered for character analysis and diabatization. Accordingly, n^2 is the dimension of the Hamiltonian's matrix representation in the adiabatic H_{adia} and in the diabatic H_{dia} state basis. The diabatic LE basis of the aggregate encompasses n LE states, localized on each molecular unit, and $n^2 - n$ CT states involving two different monomers.

In the following, the diabatization approach within the MIOS is introduced step by step and the workflow is also shown in Figure 5.5.

In the first step of the character analysis, the **DMOs** are expressed **as linear combinations of the LMOs** by the application of a projection operator, following the procedure outlined in previous works:[259,311]

$$|\psi_{MON\_i}\rangle\langle\psi_{MON\_i}|\psi_{AGGR\_j}\rangle = C_{i,j}^{AGGR\_MOB}|\psi_{MON\_i}\rangle \qquad (5.10)$$

where $|\psi_{MON\_i}\rangle$ are the monomers' MOs in the atomic orbital basis (AOB) and $|\psi_{AGGR\_j}\rangle$ are the aggregate MOs in the AOB. In matrix formulation, $|\psi_{MON\_i}\rangle$ build up the column vectors of the C_{MON_AOB} matrix which is, therefore, a block diagonal matrix containing the MOs coefficients in the AOB from each monomer. The off-diagonal blocks are simply set to zero. Similarly, $|\psi_{AGGR\_j}\rangle$ form the column vectors of the C_{AGGR_AOB} matrix.

The linear combinations of DMOs in LMOs are defined by the $C_{i,j}^{AGGR\_MOB}$ coefficients in the monomer orbital basis (MOB) which, for a given aggregate orbital j, constitute the columns of the C_{AGGR_MOB} matrix and are obtained as:

$$C_{AGGR\_MOB} = C_{MON\_AOB}^t \cdot S_{MON\_AOB} \cdot C_{AGGR\_AOB} \qquad (5.11)$$

S_{MON_AOB} is the overlap matrix of the monomers in the AOB and the superscript t indicates the transpose.

Monomer orbitals belonging to two different molecules are not orthogonal to each other. Therefore, aggregate's orbitals, $C_{AGGR\_MOB}^L$, expressed in terms of orthogonalized monomer orbitals are obtained as:

$$C_{AGGR\_MOB}^L = S_{AGGR\_MOB}^{-\frac{1}{2}} \cdot C_{AGGR\_MOB} \qquad (5.12)$$

where superscript L indicates Löwdin's orthogonalization[260], and the overlap matrix $S_{AGGR\_MOB} = C_{MON\_AOB}^t \cdot S_{AGGR\_AOB} \cdot C_{MON\_AOB}$ is obtained from the coefficients of monomer's orbitals C_{MON_AOB} and the overlap of the atomic orbitals in the aggregate configuration S_{AGGR_AOB}.

The initial dimension of $C_{AGGR\_MOB}^L$ matrix corresponds to the full dimension of the MOB. However, since the occupied DMOs involved in low-lying exciton states are mainly determined by the occupied and unoccupied LMOs belonging to the MIOS, only the submatrices $MIOS\_O_{AGGR\_MOB}^L$ (for occupied MOs) and $MIOS\_U_{AGGR\_MOB}^L$ (for unoccupied MOs) are extracted from $C_{AGGR\_MOB}^L$, which are then Löwdin orthogonalized and used in the subsequent

steps.

With the DMOs expressed as linear combinations of LMOs belonging to the MIOS, a generic *De* $(i \rightarrow j)$ (where i and j are DMOs) can be readily expanded in terms of excitation $(k \rightarrow l)$ involving only LMOs. The expansion coefficients form the columns of the unitary matrix $\boldsymbol{U_{De \rightarrow dia}}$ given by

$$U_{k\rightarrow l,i\rightarrow j}^{De\rightarrow LE} = MIOS\_O_{k,i}^{AGGR\_MOB,L} \cdot MIOS\_U_{l,j}^{AGGR\_MOB,L} \tag{5.13}$$

The subset of the $\boldsymbol{n^2}$ exciton states originated from the MIOS are then selected out from the full set of computed eigenstates, Gram-Schmidt orthogonalized[312] and used to form the columns of the $\boldsymbol{B_{De}^{adia}}$ matrix.

Exciton states are then readily expressed in the diabatic basis through the unitary transformation as $\boldsymbol{B_{\text{dia}}^{adia}} = \boldsymbol{U_{De\rightarrow dia}} \cdot \boldsymbol{B_{De}^{adia}}$. The adiabatic exciton state wavefunction as linear combination of diabatic states are shown in the following:

$$\Psi_{dia}^{adiab} = \sum_{i=1}^{n^2} a_i^{dia} \, \varphi_i^{dia} \tag{5.14}$$

The exciton states characters (*e.g.,* CT) are obtained by summing up the contributions (a_i^{dia}) corresponding to *e.g.,* CT states.

The $\boldsymbol{n^2}$ eigenvalues, namely excitation energies of the selected $\boldsymbol{n^2}$ exciton states, form the diagonal $\boldsymbol{H_{adia}}$ matrix, from which the Hamiltonian in the diabatic LE/CT basis, $\boldsymbol{H_{dia}}$, can be obtained as [55,57,59,313]:

$$\boldsymbol{H_{dia}} = \boldsymbol{B_{dia}^{adia}} \cdot \boldsymbol{H_{adia}} \cdot \boldsymbol{B_{dia}^{adia}}^{t} \tag{5.15}$$

Finally, $\boldsymbol{H_{dia}}$ can be rotated in the symmetry-adapted (SA) diabatic basis giving rise to $\boldsymbol{H_{dia}^{SA}}$. Frenkel (FE) and charge resonance (CR) diabatic states can be obtained from the $\pm$ combinations of LEs and CTs, respectively. The off-diagonal elements of $\boldsymbol{H_{dia}^{SA}}$ are the interactions between the CR and FE states that ultimately govern the modulation of adiabatic exciton state energies. These interaction energies have been shown to correspond to $\pm$ combinations of electron (D_e) and hole (D_h) transfer integrals [56,60,93,304].

```
┌─────────────────────┐    ┌──────────────────────────────────────────────────────┐
│ QC exciton state    │    │ DMOs as linear combinations of LMOs                    │
│ calculations on the │    │                                                        │
│ aggregate           │    │ C_AGGR_MOB = C^t_MON_AOB · S_MON_AOB · C_AGGR_AOB       │
│                     │    │                                                        │
│                     │    │ C^L_AGGR_MOB = S^(-1/2)_AGGR_MOB · C_AGGR_MOB           │
└─────────────────────┘    └──────────────────────────────────────────────────────┘

┌─────────────────────┐    ┌──────────────────────────────────────────────────────┐
│ Selection of        │    │ De s as linear combinations of LEs within the MIOS     │
│ adiabatic states    │    │ Construction of U_De→dia                               │
│ within the MIOS     │    │                                                        │
│ B^adia_De           │    │                                                        │
└─────────────────────┘    └──────────────────────────────────────────────────────┘

                           ┌──────────────────────────────────┐    ┌──────────────┐
                           │ Adiabatic states as linear       │    │ CT/FE        │
                           │ combinations of LEs – diabatic   │    │ character    │
                           │ states                           │    │ analysis     │
                           │ B^adia_dia = U_De→dia · B^adia_De │    └──────────────┘
                           └──────────────────────────────────┘

                           ┌──────────────────────────────────┐
                           │ Hamiltonian in the diabatic basis│
                           │ H_dia = B^adia_dia · H_adia · B^adia_dia^t │
                           └──────────────────────────────────┘
```

$$C_{AGGR\_MOB} = C^t_{MON\_AOB} \cdot S_{MON\_AOB} \cdot C_{AGGR\_AOB}$$

$$C^L_{AGGR\_MOB} = S^{-\frac{1}{2}}_{AGGR\_MOB} \cdot C_{AGGR\_MOB}$$

$$B^{adia}_{dia} = U_{De \to dia} \cdot B^{adia}_{De}$$

$$H_{dia} = B^{adia}_{dia} \cdot H_{adia} \cdot B^{adia^t}_{dia}$$

Figure 5.5. Workflow for exciton state character analysis and diabatization. Reprinted from: S. Canola, *et al., J. Chem. Phys.* **2021**, 154, 1–37, with the permission of AIP Publishing.

5.3.1 H_{dia} in different MIOS

The dimension of H_{dia} depends on the dimension of diabatic basis, which is ultimately related to the number of MOs included in the MIOS. In this work, two dimensions of MIOS will be presented. These are two MOs per monomer in the case of PDI[93,94] and four MOs per monomer in the case of naphthalene and anthracene dimers[95]. In the first case, H_{dia} is a 4×4 matrix, while the H_{dia} dimension for the latter is 16× 16. It is worth to discuss the structures of the two diabatic Hamiltonians.

When the MIOS includes only two orbitals per monomer, that is to say only H and L, the only type of monomeric excitation, either LE or CT, is H→L.The corresponding H_{dia} has the following form, where the superscript *n* stands for a specific type of excitation, which in this case is H→L.

Table 5.1. Matrix elements of H_{dia} between diabatic states of the same type ($LE^{(n)}, CT^{(n)}$). Adapted from Ref. [95].

H_{dia}	$LE_A^{(n)}$	$LE_B^{(n)}$	$CT_{AB}^{(n)}$	$CT_{BA}^{(n)}$
$LE_A^{(n)}$	$E_{LE}^{(n)}$	$V_e^{(n)}$	$D_e^{(n)}$	$D_h^{(n)}$
$LE_B^{(n)}$	$V_e^{(n)}$	$E_{LE}^{(n)}$	$D_h^{(n)}$	$D_e^{(n)}$
$CT_{AB}^{(n)}$	$D_e^{(n)}$	$D_h^{(n)}$	$E_{CT}^{(n)}$	$W^{(n)}$
$CT_{BA}^{(n)}$	$D_h^{(n)}$	$D_e^{(n)}$	$W^{(n)}$	$E_{CT}^{(n)}$

On the other hand, when MIOS encompasses four MOs per monomer, there are four different types of diabatic states depending on the LMOs involved in the excitation and they

are distinguished by a different superscript (Eq. 5.16). Considering the dimer, the diabatic basis are:

$$LE_A^{(1)} = |1_A\rangle = (H-1)_A \rightarrow (L+1)_A$$
$$LE_B^{(1)} = |1_B\rangle = (H-1)_B \rightarrow (L+1)_B$$
$$CT_{AB}^{(1)} = |1_{AB}\rangle = (H-1)_A \rightarrow (L+1)_B$$
$$CT_{BA}^{(1)} = |1_{BA}\rangle = (H-1)_B \rightarrow (L+1)_A$$

$$LE_A^{(2)} = |2_A\rangle = (H-1)_A \rightarrow (L)_A$$
$$LE_B^{(2)} = |2_B\rangle = (H-1)_B \rightarrow (L)_B$$
$$CT_{AB}^{(2)} = |2_{AB}\rangle = (H-1)_A \rightarrow (L)_B$$
$$CT_{BA}^{(2)} = |2_{BA}\rangle = (H-1)_B \rightarrow (L)_A$$

(5.16)

$$LE_A^{(3)} = |3_A\rangle = (H)_A \rightarrow (L)_A$$
$$LE_B^{(3)} = |3_B\rangle = (H)_B \rightarrow (L)_B$$
$$CT_{AB}^{(3)} = |3_{AB}\rangle = (H)_A \rightarrow (L)_B$$
$$CT_{BA}^{(3)} = |3_{BA}\rangle = (H)_B \rightarrow (L)_A$$

$$LE_A^{(4)} = |4_A\rangle = (H)_A \rightarrow (L+1)_A$$
$$LE_B^{(4)} = |4_B\rangle = (H)_B \rightarrow (L+1)_B$$
$$CT_{AB}^{(4)} = |4_{AB}\rangle = (H)_A \rightarrow (L+1)_B$$
$$CT_{BA}^{(4)} = |4_{BA}\rangle = (H)_B \rightarrow (L+1)_A$$

As a result, the 16x16 $\boldsymbol{H}_{dia}$ matrix includes not only interactions between diabatic states of the same type ($LE_A^{(n)}, LE_B^{(n)}, CT_{AB}^{(n)}, CT_{BA}^{(n)}$ and the 4x4 $\boldsymbol{H}_{dia}$ in Table 5.1) such as excitonic interactions $V_e^{(n)}$ and super-exchange interactions[314] $D_{e/h}^{(n)}$, but also interactions between diabatic states of different type ($LE/CT^{(n)}, LE/CT^{(p)}$), hereafter labelled with two superscript numbers, *e.g.,* $V_e^{(n,p)}$ (Table 5.2). In addition, intramolecular interactions between diabatic states localized on the same monomer ($LE_A^{(n)}, LE_A^{(p)}$) are also uncovered by the diabatization procedure ($H^{(n,p)}$ in Table 5.2).

Table 5.2. Matrix elements of $\boldsymbol{H}_{dia}$ between diabatic states of different types ($LE^{(n)}, CT^{(n)}$ and $LE^{(p)}, CT^{(p)}$). The additional superscript $-p/-n$ for super-exchange interactions denotes the type of LE diabatic state. Adapted from Ref. [95].

| $\boldsymbol{H}_{dia}$	$LE_A^{(p)}$	$LE_B^{(p)}$	$CT_{AB}^{(p)}$	$CT_{BA}^{(p)}$
$LE_A^{(n)}$	$H^{(n,p)}$	$V_e^{(n,p)}$	$D_e^{(n,p)-n}$	$D_h^{(n,p)-n}$
$LE_B^{(n)}$	$V_e^{(n,p)}$	$H^{(n,p)}$	$D_h^{(n,p)-n}$	$D_e^{(n,p)-n}$
$CT_{AB}^{(n)}$	$D_e^{(n,p)-p}$	$D_h^{(n,p)-p}$	$H_{CT}^{(n,p)}$	$W^{(n,p)}$
$CT_{BA}^{(n)}$	$D_h^{(n,p)-p}$	$D_e^{(n,p)-p}$	$W^{(n,p)}$	$H_{CT}^{(n,p)}$

5.4 Construction of the model Hamiltonian (*mH*)

The diabatization procedure requires QC calculations on the exciton states of an aggregate, which may become computationally demanding as the dimension of the aggregate increases (*e.g.,* trimer, tetramer, *etc.*). A more cost-effective approach such as a model Hamiltonian may be preferred in this regard.

Within a dimer model, the connection between the elements of H_{dia} and the matrix elements of a frontier-orbitals configuration interaction singles was derived[75,304] according to Slater–Condon (SC) rules[315]. This connection allowed to rationalize the magnitude of the elements of H_{dia} by considering the integrals that define each matrix element.

Based on this relation, we proposed the construction of a **dimer-based** model Hamiltonian *mH*[93] based on the TD-DFT derived H_{dia} matrix elements as described previously.

In our dimer-based *mH* approach, an aggregate larger than dimer can be partitioned in composing dimers, each dimer is characterized by different interplanar distances (labelled as D1, D2 and D3, *etc.*) as shown in Figure 5.6. Each element of *mH* can be related to one of the elements of the H_{dia} of the corresponding dimer. Indeed, also for the larger aggregates, its H_{dia} matrix elements are integral whose expressions can be inferred from SC rules[315], with a straightforward generalization of the strategy employed in previous work[75,304] to identify the elements for a dimer.
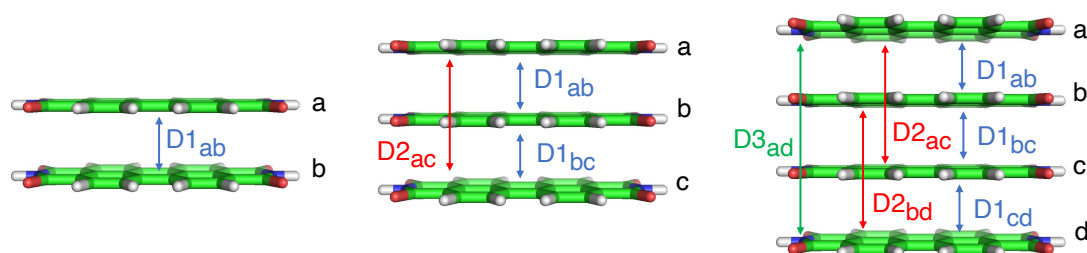
Figure 5.6. Scheme for the construction of the simplified *mH* for dimer, trimer and tetramer. Reprinted from: S. Canola, *et al., J. Chem. Phys.* **2021**, 154, 1–37, with the permission of AIP Publishing.

Thus, for instance, to describe the trimer in Figure 5.6, formed by the three monomers *a*, *b*, *c*, two types of dimers need to be considered: D1 with the two monomers at short distance and D2 whose intermolecular distance is twice as big as that of D1. The diabatic basis is formed by three LE excitations (a^*bc, ab^*c, abc^*) and six CT excitations (a^+b^-c, a^-b^+c, ab^+c^-, ab^-c^+, a^+bc^-, a^-bc^+), four of which labelled as CT1 (corresponding to short-distance dimers D1) and the last two labelled as CT2 (corresponding to the large-distance dimer D2). The resulting *mH* matrix is shown in Table 5.3, whose elements are labelled according to their counterpart taken from H_{dia} of the composing dimers and the superscript (1) and (2) refer to dimer D1 and D2, respectively. Some of the *mH* matrix elements of the trimer (and similarly those of larger aggregates) do not correspond to any elements in D1 or D2's H_{dia}. These elements, according to SC rules, correspond to integrals that contain differential overlaps and are therefore expected to be very small. For this reason, they are approximated to zero in Table 5.3.

Exciton states energies and characters are obtained from the diagonalization of *mH*.

Table 5.3. Matrix elements of mH for a trimer. The color code refers to the two different types of dimers D1 and D2 (see Figure 5.6) used to decompose the trimer aggregate and to establish the connection between matrix elements of the trimer and those of the H_{dia} of the composing dimers. Reprinted from: S. Canola, *et al., J. Chem. Phys.* **2021**, 154, 1–37, with the permission of AIP Publishing

mH	a^*bc	ab^*c	abc^*	a^+b^-c	a^-b^+c	ab^+c^-	ab^-c^+	a^+bc^-	a^-bc^+
a^*bc	E_{FE}	$Ve^{(1)}$	$Ve^{(2)}$	$De^{(1)}$	$Dh^{(1)}$	0	0	$De^{(2)}$	$Dh^{(2)}$
ab^*c	$Ve^{(1)}$	E_{FE}	$Ve^{(1)}$	$Dh^{(1)}$	$De^{(1)}$	$De^{(1)}$	$Dh^{(1)}$	0	0
abc^*	$Ve^{(2)}$	$Ve^{(1)}$	E_{FE}	0	0	$Dh^{(1)}$	$De^{(1)}$	$Dh^{(2)}$	$De^{(2)}$
a^+b^-c	$De^{(1)}$	$Dh^{(1)}$	0	$E_{CT}^{(1)}$	$W^{(1)}$	0	$Dh^{(2)}$	$De^{(1)}$	0
a^-b^+c	$Dh^{(1)}$	$De^{(1)}$	0	$W^{(1)}$	$E_{CT}^{(1)}$	$De^{(2)}$	0	0	$Dh^{(1)}$
ab^+c^-	0	$De^{(1)}$	$Dh^{(1)}$	0	$De^{(2)}$	$E_{CT}^{(1)}$	$W^{(1)}$	$Dh^{(1)}$	0
ab^-c^+	0	$Dh^{(1)}$	$De^{(1)}$	$Dh^{(2)}$	0	$W^{(1)}$	$E_{CT}^{(1)}$	0	$De^{(1)}$
a^+bc^-	$De^{(2)}$	0	$Dh^{(2)}$	$De^{(1)}$	0	$Dh^{(1)}$	0	$E_{CT}^{(2)}$	$W^{(2)}$
a^-bc^+	$Dh^{(2)}$	0	$De^{(2)}$	0	$Dh^{(1)}$	0	$De^{(1)}$	$W^{(2)}$	$E_{CT}^{(2)}$

Overall, mH represents an approximation of H_{dia} obtained from full-aggregate QC calculations discussed in the previous section. It is expected to provide a cheaper alternative for the analysis on aggregates' energy profiles, character of exciton states and other exciton state properties such as the interchange from H- to J- spectroscopic features.

5.5 Exciton state characters in PDI dimers from H_{dia}

Perylene-bis(dicarboximide) (PDI) and its derivatives have attracted great interest as chromophores for energy and charge-transport studies, thanks to their propensity to self-organize into ordered assemblies, both in solution and in the solid state via π−π-stacking interactions [35,316,317]. Thanks to its distinctive solid-state packing feature and the nature of its lowest-lying singlet excited state (strongly dominated by H→ L excitation), PDI dimers can be considered also as ideal model systems for the study of the effects of intermolecular coupling on exciton states. Indeed, several computational investigations on PDI aggregates have been focused on the prediction of exciton states with different QC approaches, including configuration interaction truncated to single excitations (CIS), TD-DFT [5,19,22,39–41,45], and highly accurate levels of theory [320–322].

So far, many studies have focused on the modelling and analysis of singlet exciton states of PDI [52,58,60,318,319,323–327], much less attention has been given to triplet excitons and only few investigations have been reported [60,328,329]. However, in recent years, triplet excitons have shown to cover a relevant role in photoinduced processes such as in the nonradiative-charge recombination observed in various polymer-blend films in organic photovoltaic devices[330].

The relationship between structural arrangement and the correlated exciton state character

is important both for singlet and triplet excitons. Here, we investigate the modulation of singlet and triplet exciton state energies and characters in PDI dimers along the longitudinal translation coordinate z as shown in Figure 5.7. The analysis on exciton states is carried out with the diabatization procedure described in Section 5.3.

The symmetry point group of the PDI aggregate considered in this work is C_{2h} (Figure 5.7). As a result, the most relevant $\pi\pi^*$ exciton states, along with the FE and CR diabatic states, all belong to A_g and B_u symmetry representations. Symmetry can be exploited to easily identify H- and J- aggregation types, since only B_u exciton states are accessible as dipole-allowed transitions.
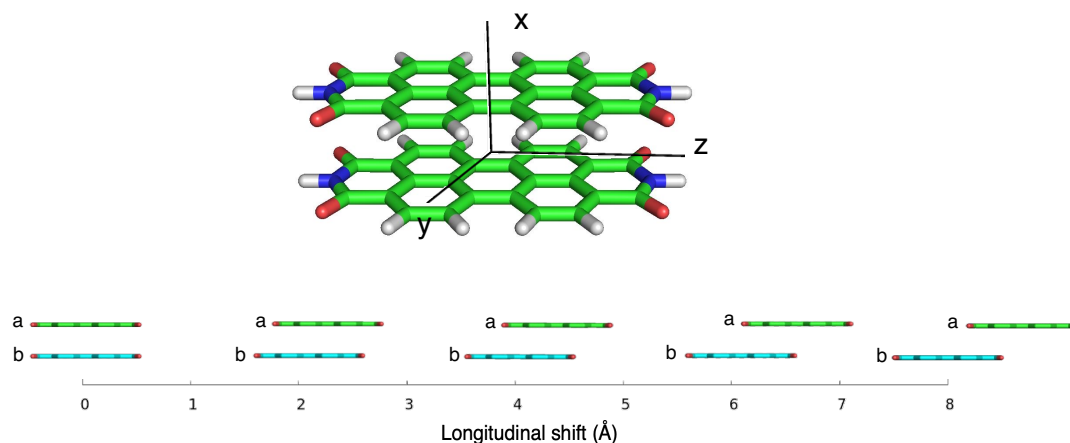
Figure 5.7. PDI dimer considered in this work. (top): PDI dimer at the eclipsed configuration; (bottom): Schematic representation of the translation along z.

5.5.1 Computational details

The PDI monomer structure was the same used in previous investigations on PDI aggregates, optimized at the BLYP-D/TZV(P) level of theory[331]. The interplanar distance was set to 3.4 Å. The exciton states were computed for the eclipsed aggregates and for displacements of 0.5 Å up to 8.0 Å, along the longitudinal translation coordinate (z) (see Figure 5.7).

Excitation energies for low-lying singlet exciton states were determined with TD-DFT and TDA-DFT calculations using the ωB97X-D functional and the 6-31G* basis set. The ωB97X-D functional was chosen owing to its reliable description of charge transfer states as reported in previous investigations of the PDI dimer[52]. On the contrary, triplet exciton states are calculated only at TDA-ωB97X-D/6-31G* level because TD-DFT predicted wavefunctions show a large contribution of de-excitations.

5.5.2 Modulation of singlet exciton state energy profiles and characters in PDI dimers

Previous investigations of excitation energy profiles and CT character in PDI dimers for interchromophore longitudinal shifts have shown that computed exciton states are generally strong mixtures of the two types of diabatic states. The weight of LE and CT characters, however, strongly depends on the energy difference between FE and CR diabatic states, and on their couplings [52,93,304]. This is the reason why the CT character of the lowest singlet exciton

state is critically dependent on the chosen functional.
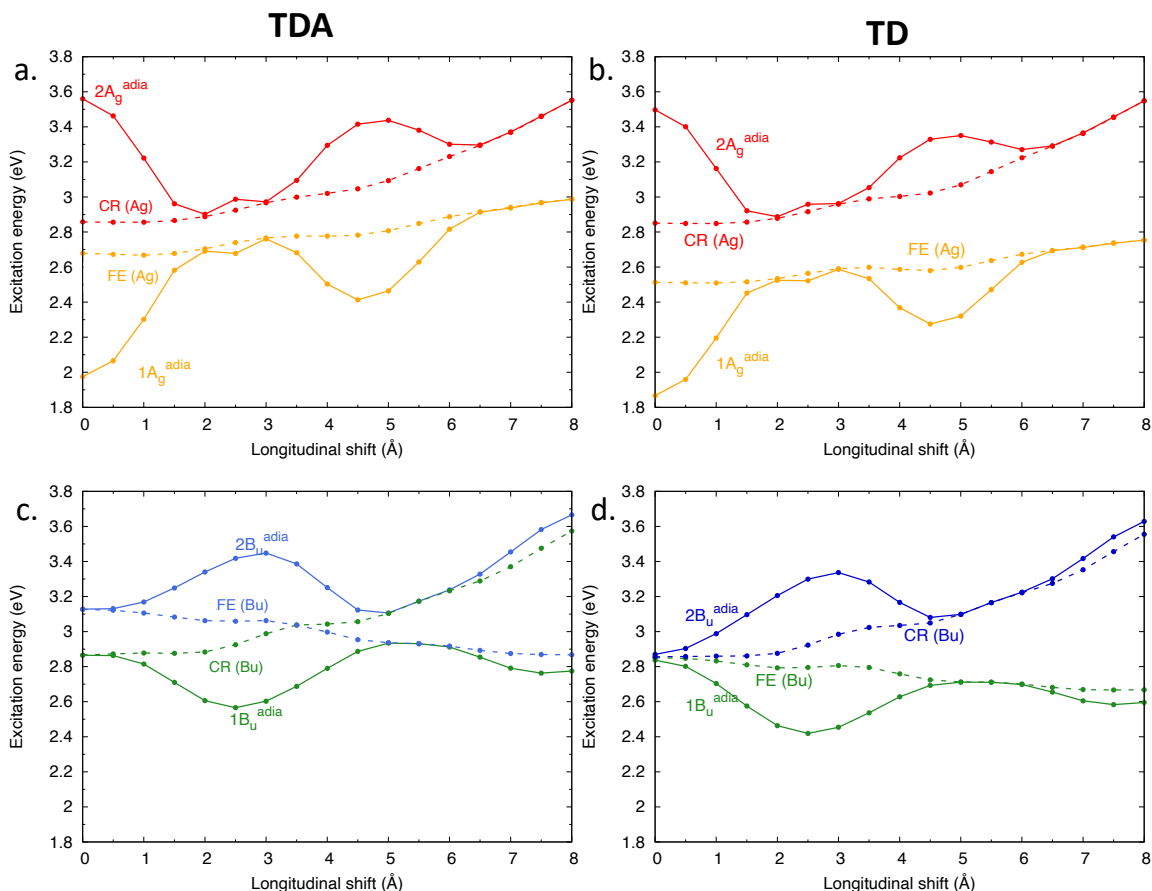
Figure 5.8. Excitation energy profiles of the PDI dimer from (left, a & c) TDA-ωB97X-D/6-31G* and (right, b & d) TD-ωB97X-D/6-31G* calculations. (a & b) Adiabatic (adia, solid) singlet exciton states of A_g symmetry and the corresponding symmetry adapted diabatic FE and CR states (dashed); (c & d) Adiabatic (adia, solid) singlet exciton states of B_u symmetry and the corresponding symmetry adapted diabatic FE and CR states (dashed). Figure adapted from Ref. [94].

Figure 5.8 reports the adiabatic (solid lines) and diabatic (dashed) energy profiles of the four exciton states from the TD- and TDA-ωB97X-D/6-31G* calculations. The energy profiles of the four adiabatic states (solid lines), from the two levels of theory, are quite similar and both set of calculations show an oscillating trend. This trend can be readily rationalized by the oscillating trend of the interactions between CR and FE diabatic states, which can be obtained from $\boldsymbol{H}_{dia}^{SA}$ [93]. More precisely, these interactions are proportional to the + and – combinations of the D_e and D_h elements (Table 5.1, Figure 5.9a), whose dependence on the longitudinal translation is also oscillating. The negative combination of D_e and D_h determines the energy profile of A_g exciton state, while the energy profile of B_u state is related to the positive combination of D_e and D_h . The oscillating trend of $D_e + D_h$ and $D_e - D_h$ interaction terms give rise to the energy separation for B_u and A_g states, respectively, causing, ultimately, the interchange between B_u and A_g states along the longitudinal shift. Therefore, for the two lowest lying exciton states, when $D_e + D_h$ shows a maximum, this interaction will push the adiabatic $1B_u$ state below the $1A_g$ state (see Figure 5.9b) leading to the well-known switch from H- to J-aggregate for the dimer[21]. Interestingly, the appearance of the CT-mediated J-type aggregation occurs also at small longitudinal displacement, a range where Kasha's theory only predicts H-

type aggregation. Therefore, CR states create an effective short-range exciton coupling that can induce unconventional J-type spectroscopic features [21,22,93,304,311,316,318,332,333].
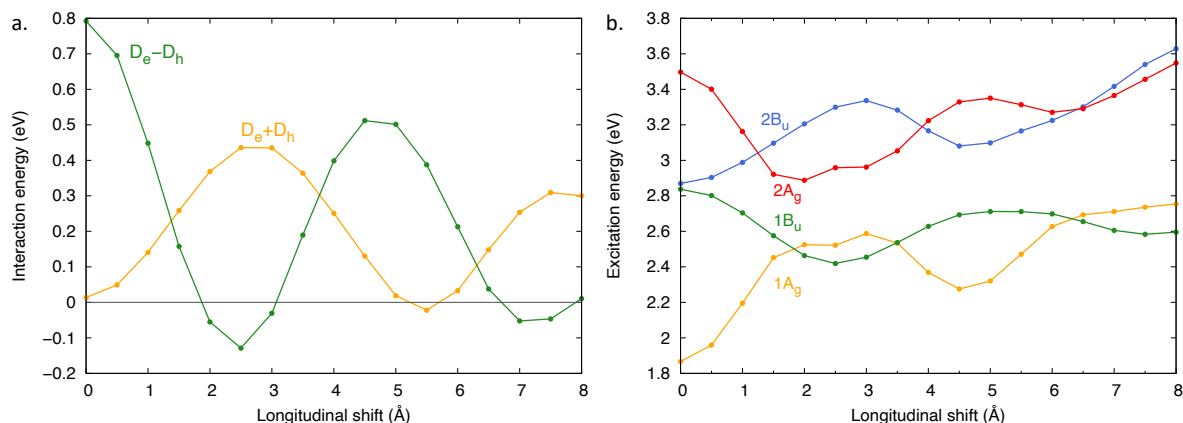

Figure 5.9. (a)Magnitude and modulation along the longitudinal translation coordinate, of the De ± Dh terms, proportional to the interaction between CR/FE symmetry-adapted diabatic states of the dimer. (b) Adiabatic excitation energy profiles of the PDI dimer calculated at TD- ωB97X-D/6-31G* level. The De + Dh term (orange in (a)) regulates the oscillation of the B_u states (green in (b)): when there is a large interaction, the B_u states are more separated. Reprinted from: S. Canola, *et al., J. Chem. Phys.* **2021**, 154, 1–37, with the permission of AIP Publishing.

Additionally, also the oscillating trend of CT character (Figure 5.10) is related to the interaction between SA diabatic states. To be more precise, in this case, the energy location of CR and FE diabatic states is very important. Figure 5.8 also shows the energy profile of FE and CR diabatic states. For the A_g state, the trends are very similar comparing TDA and TD-DFT results: only a slight underestimation of the FE state is observed from TD-DFT calculations. For B_u state, a crossing between FE and CR states is only obtained from TDA-ωB97X-D/6-31G* calculations (Figure 5.8c, d). This has a consequence on the CT character of the four exciton states (Figure 5.10) as detailed in the following.

The profile of CT character of A_g exciton states are quite similar along the longitudinal shift, only a slight underestimation for the $1A_g$ state and overestimation of $2A_g$ from TD-ωB97X-D/6-31G* results are observed. This is in line with their similar SA diabatic energy profiles (FE/CR) shown in Figure 5.8a, b and a lower FE state predicted by TD-DFT calculations. The CT character profile of B_u exciton states show considerable difference: the CT character of the lowest B_u exciton state (at the eclipsed geometry and for small displacements, Figure 5.10a) is greater than 50% similar to previously reported results from CIS calculations[304]. On the contrary, the CT character profile determined from TD-DFT calculations show that the amount of CT character is always lower than 50% for the lowest B_u and A_g states. This latter result is in good agreement with experimental data and with previously reported results from high-level QC calculations[52,304]. The amount of CT character is determined by the energy location of the FE state, always below the CR state in TD-DFT calculations, in agreement with the results of reference high-level calculations and in contrast with the results of other long-range corrected functionals or CIS[52,304]. Obviously, slightly larger intermonomer separations will reduce the contrasting results between TD and TDA-ωB97X-D/6-31G* calculations, which, however, illustrate the crucial role determined by the energy difference between the CR and FE states.

We also compared the CT character deduced from our diabatization procedure with the results of TheoDORE [305]. Exciton states computed with TDA-DFT level of theory are chosen. The comparison shows an excellent agreement for all the four low-lying states investigated (Figure 5.10a).
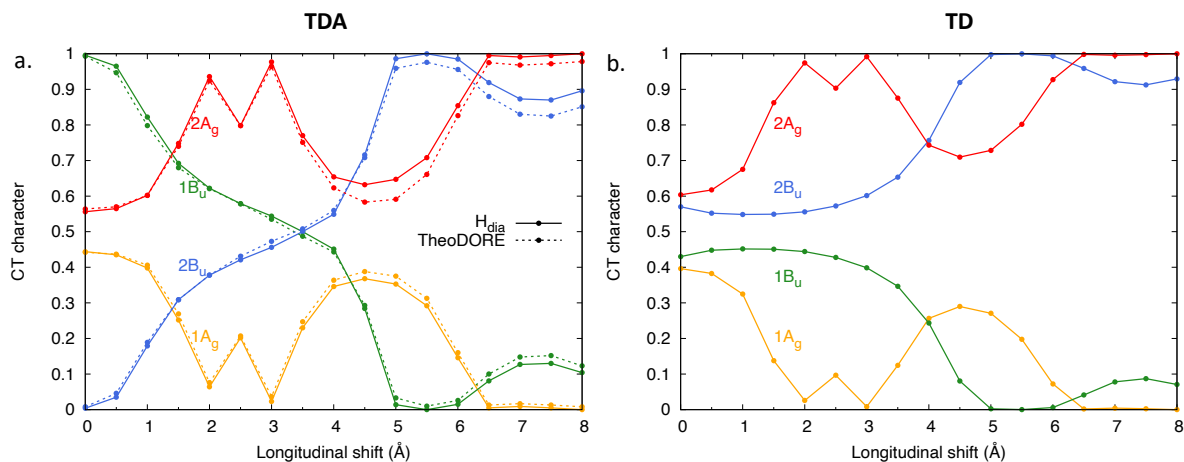

Figure 5.10. a) CT character of adiabatic singlet exciton states of PDI dimer from TDA-ωB97X-D/6-31G* calculations. CT characters are determined with two different approaches: (solid) using ***H**dia* and (dashed) using TheoDORE analysis tool[305]. Figure (a) adapted from Ref. [94]. b) CT character of adiabatic singlet exciton states of PDI dimer from TD-ωB97X-D/6-31G* calculations. Figure (b) reprinted from: S. Canola, *et al.*, *J. Chem. Phys.* **2021**, 154, 1–37, with the permission of AIP Publishing.

5.5.3 Modulation of triplet exciton state energy profiles and characters in PDI dimers

The oscillating trend in adiabatic energy profiles (Figure 5.11a) is very similar to that of the singlet exciton states (Figure 5.8). Analogously, also in this case, the exciton states' behaviour can be easily rationalized by the oscillating trend of the interactions between the CR and FE states (Figure 5.11b), which are of the same magnitude as those computed for singlet exciton states. In analogy with singlet excitons, these interactions determine not only the CT character of the adiabatic triplet exciton states (Figure 5.11c), but also the symmetry of the lowest energy state (Figure 5.11a), with an interchange of A_g and B_u along the longitudinal translation coordinate. This phenomenon is well-known in singlet exciton states of PDI (see previous section) where the interchange between A_g and B_u states along the longitudinal translation is due to short-range exciton coupling induced by CR diabatic states.

Notably, here we show that the same mechanism is active also in the triplet exciton manifold, albeit with less effective CR/FE mixing. Indeed, as previously reported [60], one of the most relevant differences between singlet and triplet exciton states is the larger energy difference between FE and CR states, which triggers a modest CR/FE mixing. This can be appreciated in Figure 5.11c, showing that the largest CT contribution for the lowest triplet exciton state does not exceed 20%. At the same time, Figure 5.12 compares the results of CR/FE interactions for singlet and triplet A_g exciton states of the PDI dimer. The important role of the increased energy difference between FE and CR states is clear. Although the CR/FE mixing is very small in triplet states, it is sufficient to modulate the triplet exciton energies and to lead the observed alternation between B_u and A_g states as it did for singlet exciton states. More

111

specifically, the oscillation of the CR/FE interaction (see the $D_e \pm D_h$ profiles shown in Figure 5.11b) determines an interchange of the lowest A_g and B_u exciton states for longitudinal shifts in the range of *ca.* 2 – 3 Å, where the interaction between A_g symmetry FE and CR states is almost negligible. At the same time, the interaction between the FE and CR B_u states is maximum and pushes the adiabatic $1B_u$ state energetically below $1A_g$ (see Figure 5.11a), thereby switching the aggregate character from H- to J-type.
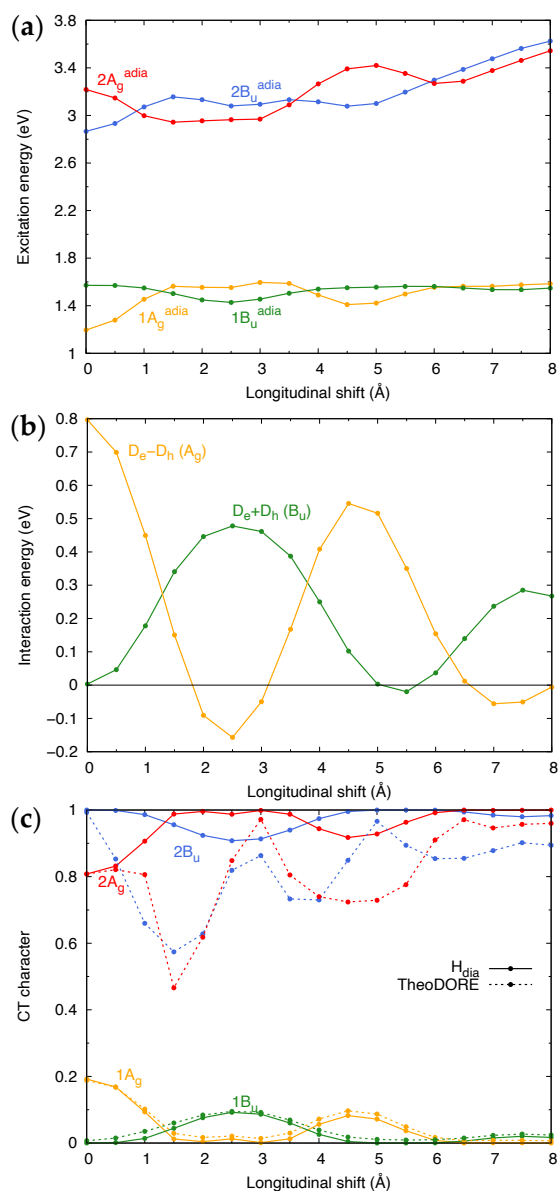
Figure 5.11. Analysis of triplet exciton states of the PDI dimer (TDA-ωB97X-D/6-31G*). (a) Computed adiabatic excitation energy profiles. (b) Magnitude and modulation along the longitudinal translation coordinate of the $D_e \pm D_h$ terms and the interaction between CR/FE states of the dimer. (c) Comparison between the CT character determined with $\boldsymbol{H_{dia}}$ and with TheoDORE [305] for the selected triplet exciton states of PDI dimer. Reprinted from Ref. [94].

These results suggest that radiative and nonradiative decays from the lowest triplet exciton states of molecular aggregates, intimately related to the nature and symmetry of the lowest energy state, may be modulated by the intermolecular organization, a concept that could be exploited for systems displaying dimerization-induced triplet state populations [334].
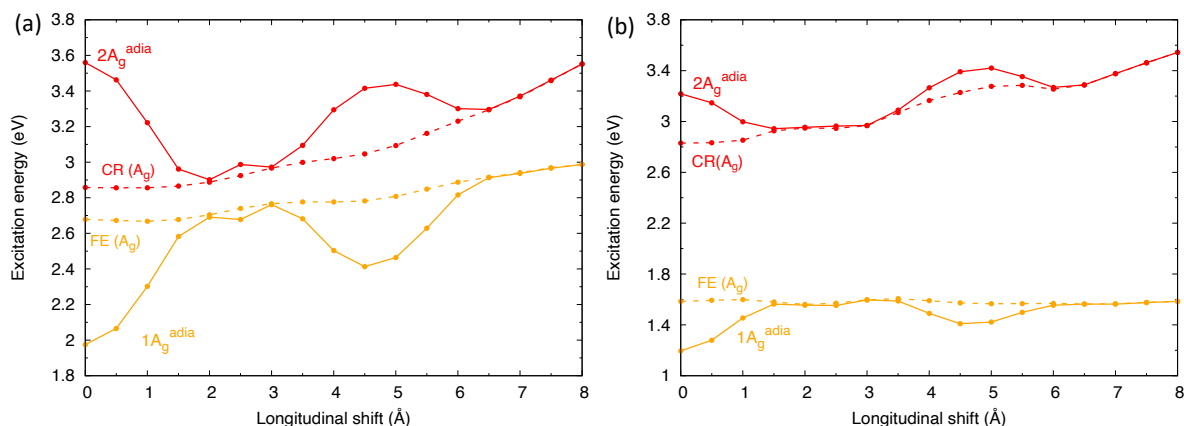
Figure 5.12. Energy profiles (TDA-ωB97X-D/6-31G∗) of (solid) A_g adiabatic exciton states and (dashed) A_g FE and CR states for the PDI dimer along the longitudinal translation coordinate: (a) singlet exciton states; (b) triplet exciton states. The computed exciton energy profiles result from the interactions between CR and FE states of the same symmetry. When the interactions (Figure 5.11b) are strong, the exciton-state energies deviate from FE and CR energies. The interaction is less effective for triplet states due to the larger energy difference between FE and CR states. Reprinted from Ref. [94].

Finally, we compare the CT character analysis obtained from our protocol (solid lines in Figure 5.11c) with the results from TheoDORE (dashed lines in Figure 5.11c). The agreement is very good for the two lowest triplet exciton states, while remarkable differences appear for two high-lying states. The reason is that for several intermolecular configurations the selected $\pi\pi^*$ triplet exciton states (whose wavefunction is dominated by excitations within the selected $\pi\pi^*$ orbital space) are spread over more than one TDA-DFT-computed exciton state. Consequently, TheoDORE analysis picks up only the CT contribution corresponding to the fraction of the selected $\pi\pi^*$ exciton state. In contrast, with $\boldsymbol{H_{dia}}$ the selected $\pi\pi^*$ exciton states are projected out of the entire space of computed exciton states and renormalized.

Interestingly, triplet exciton states (belonging to the selected orbital space) appear to mix more strongly than singlet states with other exciton states of the dimer, as suggested by wavefunction analysis and by the fragmentation of the CT contributions in TheoDORE analysis. Such fragmentation contrasts with the almost perfect match discussed for singlet excitons of the PDI dimer (Figure 5.10a) and suggests that diabatization procedures are likely to be more problematic when triplet exciton states need to be analyzed.

5.6 Exciton state characters in small oligoacene dimers from H_{dia}

Since a long time, oligoacenes have attracted great interest of chemists and physicists for their applications as energy and charge transport materials for low cost, flexible, large-scale optoelectronic devices [335,336]. Understanding the character of their electronic excitations is of prior importance for real applications since the properties of these devices are generally governed by the nature of their low-lying exciton states [2,21,43–45,317,337–339,22,35,37–42].

Additionally, from a computational point of view, oligoacene dimers are another perfect model system for the investigation of triplet-triplet and singlet-singlet interactions between π-conjugated molecules and how these interactions are modulated by different intermolecular organizations. It is known that the lowest singlet excited state of small oligoacenes (*i.e.*

naphthalene and anthracene) changes from L_b (dominated by the combination of $H - 1 \to L$ and $H \to L + 1$ excitations) to L_a (dominated by $H \to L$ excitation)[109,340–342]. This implies a larger orbital space for the diabatization procedure: at least four MOs per monomer need to be included for the correct description of low-lying exciton states.

In the present work, we seek to provide a better understanding of the photophysical properties of two oligoacene aggregates, naphthalene and anthracene, and employ the same diabatization procedure to characterize singlet and triplet exciton states in terms of LE and CT contributions. Seeking a comparison with our previous study carried out on PDI dimers, also for oligoacene dimers we focused on the longitudinal translation coordinate (Figure 5.13) keeping in mind though, that most of oligoacene crystals exhibit a *"herringbone"* arrangement in contrast to PDI.
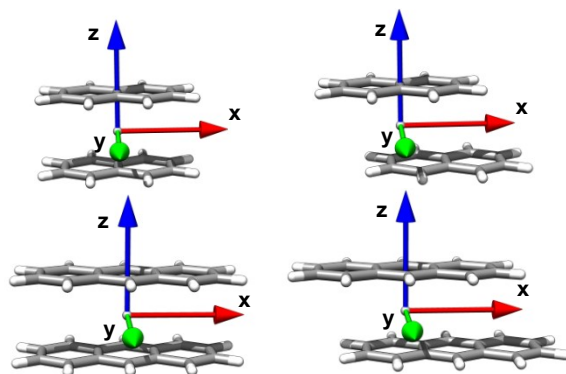
Figure 5.13. The oligoacene dimers considered in this work. Singlet and triplet exciton states have been determined at the eclipsed configuration and along the interchromophore longitudinal (x axis) translation coordinate. Figure reprinted from Ref. [95].

5.6.1 Computational details

The ground state monomer structures of naphthalene and anthracene were optimized at ωB97X-D/6-31G* level of theory. The interplanar distance of different monomers was set to 3.4 Å, as used in PDI dimers (Section 5.5). Exciton states were computed for the eclipsed aggregates and for displacements of 0.5 Å up to 8.0 Å, along the longitudinal translation coordinate (x) (Figure 5.13). Excitation energies, either for the monomer's excited states or for exciton states, were determined with TDA-DFT calculations[343], using the ωB97X-D functional[344] and the 6-31G* basis set.

5.6.2 Orbital space and diabatic states for the diabatization

The most relevant frontier MOs of naphthalene and anthracene are shown in Figure 5.14. The lowest singlet and triplet excited states for the isolated monomer are collected in Tables 5.4 and 5.5. L_a, L_b, B_a, B_b in parenthesis is Platt's notation[310] for the lowest lying singlet and triplet states of oligoacenes. The ωB97X-D functional correctly predicts the S_1 state of naphthalene to be the L_b state, while in the case of anthracene the lowest state is L_a. Computed excitation energies are generally overestimated, as is typical of the long-range corrected functional employed and of the TDA[345,346].

Notably, in-between the four L_a, L_b, B_a, B_b excited states, there are states originated from

excitations also involving H–2 and L+2 orbitals. However, these states are relatively high in energy and their omission will not affect the analysis of intermolecular interactions leading to the lowest exciton states of the two oligoacenes. Accordingly, the orbital space selected in the following analysis of exciton states includes two unoccupied and two occupied MOs for each monomer and, consequently, four occupied and four unoccupied orbitals for their dimers, thus, sixteen exciton states need to be considered for the diabatization procedure.
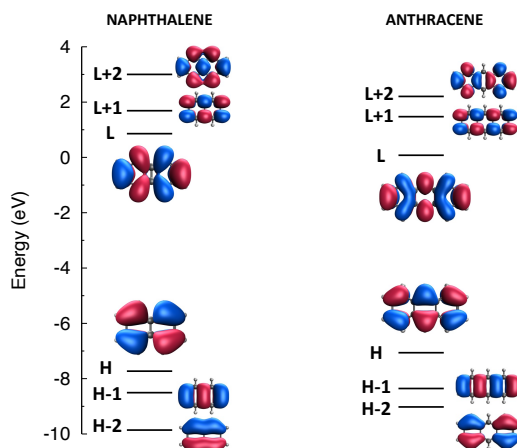
Figure 5.14. Frontier molecular orbital levels and shapes of (left) naphthalene and (right) anthracene, from ωB97X-D/6-31G* calculations (HOMO and LUMO abbreviated as H and L). Figure reprinted from Ref. [95].

The symmetry point group of an oligoacene aggregate, when intermolecular displacements along the longitudinal translation coordinate are considered (Figure 5.13) is C_{2h}. As a result, the most relevant $\pi\pi^*$ exciton states along with FE and CR diabatic states, all belong to A_g, A_u, B_g and B_u symmetry representations. In the following Figures, each symmetry will be distinguished by a specific color code used throughout this work: yellow for A_g, orange for A_u, blue for B_g and green for B_u.
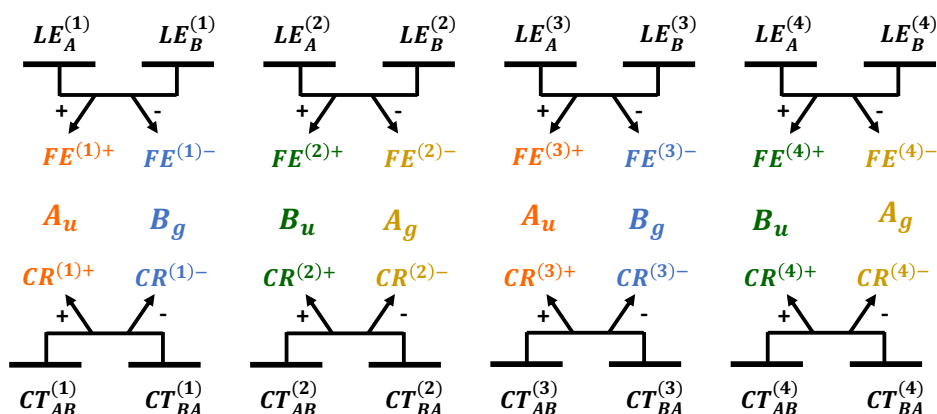
Figure 5.15. Definition of SA diabatic states (FE, CR, each symmetry with a specific color code used throughout this work: yellow for A_g, orange for A_u, blue for B_g and green for B_u) defined as linear combinations of diabatic states (black, LE, CT) and employed to analyze the nature and the effect of interactions on the adiabatic exciton states of oligoacene dimers. Figure reprinted from Ref. [95].

The SA diabatic states are then obtained as linear combinations of LE and CT states as shown in Figure 5.15. The definition of localized LE and CT configurations can be found in

Section 5.3.1 and the corresponding diabatic matrices $\boldsymbol{H}_{dia}^{SA}$ can be found in the supporting information of Ref. [95].

In the following sections we analyze the TDA computed singlet and triplet exciton states of oligoacene dimers to determine their character (CT/LE) and disentangle the role of interactions between diabatic states along the longitudinal translation coordinate.

Table 5.4. Singlet excited states of Naphthalene and Anthracene monomers. TDA-ωB97X-D /6-31G* calculations. Excited states according to Platt's notation[310] are in bracket. The states out of the chosen monomeric orbital space are in bold type. Table reprinted from Ref. [95].

State	Sym.	Energy (eV)	λ (nm)	Osc.strength	Wavefunction	
Naphthalene						
S1 (L_b)	B2U	4.80	259	0.0002	0.49	H → L+1
					0.50	H−1 → L
S2 (L_a)	B1U	5.08	244	0.0914	0.65	H → L
S3	**B3G**	**6.65**	**186**	**0**	**0.53**	**H → L+2**
					−0.47	**H−2 → L**
S4	**AG**	**6.71**	**185**	**0**	**0.47**	**H−1 → L+2**
					0.47	**H−2 → L**
S5 (B_b)	B2U	6.85	181	1.9677	0.49	H → L+1
					−0.48	H−1 → L
S6 (B_a)	B1U	6.99	177	0.3628	0.63	H−1 → L+1
Anthracene						
S1 (L_a)	B1U	3.99	311	0.1304	0.68	H → L
S2 (L_b)	B2U	4.22	294	0.0017	0.50	H−1 → L
					0.48	H → L+1
S3	**B3G**	**5.56**	**223**	**0**	**0.68**	**H−2 → L**
S4	**B3G**	**5.68**	**218**	**0**	**0.68**	**H → L+2**
S5	**AG**	**6.00**	**207**	**0**	**0.44**	**H−2 → L+1**
					0.40	H−1 → L+2
S6 (B_b)	B2U	6.03	206	3.0937	0.50	H → L+1
					−0.47	H−1 → L
S7	**B1U**	**6.32**	**196**	**0**	**0.54**	**H → L+3**
					−0.46	**H−3 → L**
S8	**B3U**	**6.60**	**188**	**0**	**0.68**	**H−5 → L**
S9 (B_a)	B1U	6.63	187	0.2023	0.63	H-1 → L+1

Table 5.5. Triplet excited states of Naphthalene and Anthracene monomers. TDA-ωB97X-D /6-31G* calculations. Excited states according to Platt's notation[310] are in bracket. The states out of the chosen monomeric orbital space are in bold type. Table reprinted from Ref. [95].

State	Sym.	Energy (eV)	λ (nm)	Wavefunction	
Naphthalene					
T1 (L_a)	B1U	3.21	386	0.67	H → L
T2 (L_b)	B2U	4.28	290	0.55	H-1 → L
				-0.42	H → L+1
T3	**B3G**	**4.57**	**272**	**0.50**	**H-2 → L**
				0.48	**H → L+2**
T4 (B_b)	B2U	4.57	271	0.55	H → L+1
				0.43	H-1 → L
T5 (B_a)	B1U	4.77	260	0.68	H-1 → L+1
Anthracene					
State	Sym.	Energy (eV)	l (nm)	Wavefunction	
T1 (L_a)	B1U	2.29	542	0.68	H → L
T2	**B3G**	**3.66**	**339**	**0.50**	**H-2 → L**
				0.45	**H → L+2**
T3 (L_b)	B2U	3.83	324	0.61	H-1 → L
				-0.32	H → L+1
T4 (B_b)	B2U	4.05	306	0.61	H → L+1
				0.32	H-1 → L
					H-1 → L+1
T5	**B1U**	**4.49**	**276**	**0.44**	**H-3 → L**
				0.43	**H → L+3**
				- 0.32	**H-2 → L+2**
T6 (B_a)	B1U	4.83	257	0.67	H-1 → L+1

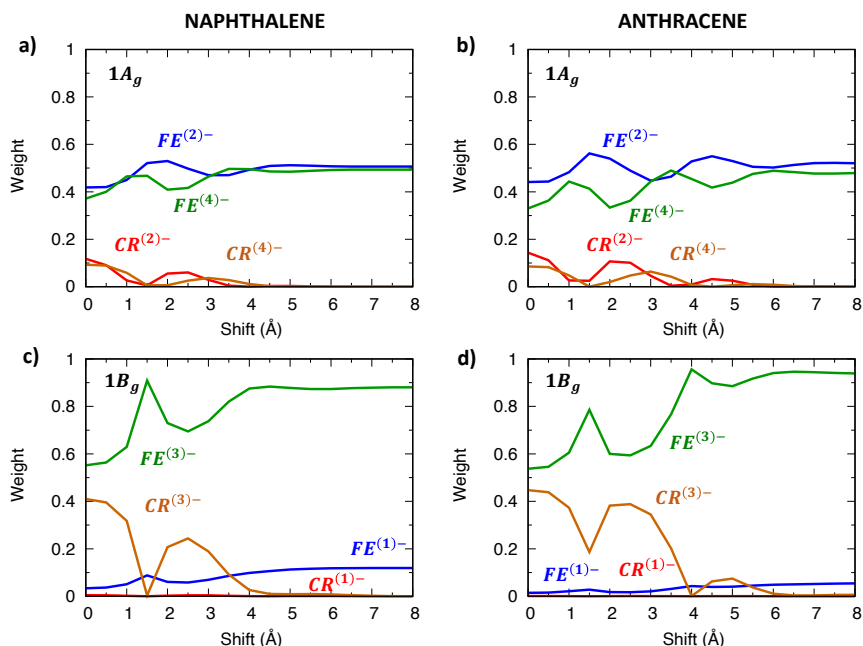### 5.6.3 Singlet exciton states of Naphthalene and Anthracene dimers

The TDA computed excitation energy profiles of the singlet exciton states of naphthalene and anthracene dimers are collected in Figure 5.16. We note that L_a (B_{1u} symmetry) states of the isolated molecules originate two LE states in the dimer, belonging to A_u and B_g symmetries of the C_{2h} point group, while L_b (of B_{2u} symmetry) monomer excited states originate two LE states in the dimer belonging to A_g and B_u symmetries. Because the lowest excited states of naphthalene and anthracene are, respectively, L_b and L_a, one might expect the lowest exciton state with different nature and symmetry for the two aggregates. In contrast, both naphthalene and anthracene dimers show that, for small displacements from the eclipsed geometry, the lowest exciton state belongs to B_g symmetry, which is therefore originated from the L_a (B_{1u}) monomer state for both dimers. This result is expected for anthracene while it implies an inversion of the L_b/L_a states for naphthalene, when moving from the monomer to the aggregate. Such an inversion has been documented in previous studies at the equilibrium intermolecular distance of the singlet state excimer[347,348], though the interplanar distance is

considerably shorter than 3.4 Å considered here. Interestingly, the stabilization of the lowest B_g state leading to the formation of the naphthalene excimer is predicted by our TDA-ωB97X-D calculations even at such large intermolecular distances.

Although the $1B_g$ exciton state of the oligoacene dimers is derived from the L_a state and therefore owns a considerable LE contribution, the CT contribution to its wavefunction is not negligible: more that 40% CT contribution (Figure 5.16c,d) is detected at the eclipsed geometry. This is true not only for the $1B_g$ state, but also for other low-lying exciton states, with the CT contribution slightly increasing from naphthalene to anthracene dimers. Such a mixed character can be appreciated by graphically representing the wavefunction of the two lowest exciton states ($1B_g$ and $1A_g$) in terms of their SA diabatic states. The contributions of CR states (red and brown lines in Figure 5.17) emerge clearly not only for the eclipsed dimer configuration, but up to *ca.* 4 Å longitudinal displacements, even though the weight of FE states (green and blue lines) is dominant.
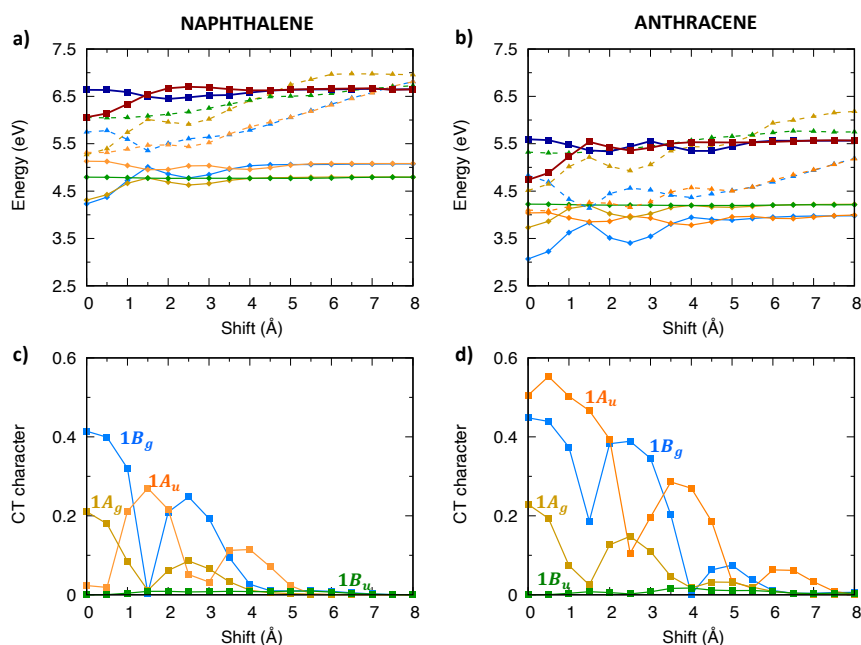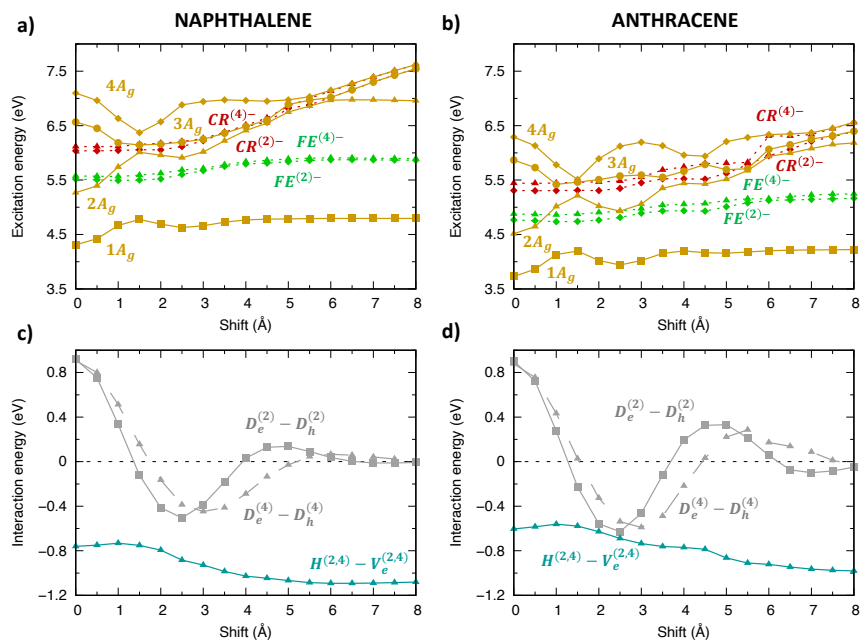

Figure 5.16. Lowest energy singlet exciton states of (left) naphthalene and (right) anthracene: (a, b) adiabatic excitation energy profiles of the low-lying exciton states depicted with different color codes for different symmetries: yellow for A_g, orange for A_u, blue for B_g and green for B_u. The lowest energy exciton states not included in the diabatization procedure are also shown (dark blue, B_g symmetry, dark red, A_u symmetry), (c, d) CT character of the lowest four exciton states. Figure reprinted from Ref. [95].

Figure 5.17. Wavefunction composition of the adiabatic lowest exciton states of (left) naphthalene and (right) anthracene in terms of the SA diabatic states defined in Figure 5.15. (a, b) $1A_g$ state and (c, d) $1B_g$ state. Red and brown lines represent the contributions to the total wavefunction of CT states, while green and blue lines represent the weight of LE states. Figure reprinted from Ref. [95].

As shown in previous investigations[60,93,94,304], the modulation of adiabatic energy profiles along the longitudinal translation coordinate can be rationalized in terms of inter-state interactions between SA diabatic states. The different effects of inter-state and intermolecular interactions can be appreciated by comparing SA diabatic and the resulting adiabatic energy profiles. Here, we focus on the lowest two exciton states at the eclipsed geometry, namely A_g (Figure 5.18) and B_g (Figure 5.19) states. In both cases, the adiabatic exciton energy profiles result from the combination of the interaction between FE and CR SA diabatic states (grey lines in panels (c,d)). This interaction is maximum at the eclipsed geometry and oscillates along the translation. The interaction between the two FE SA diabatic states (dark-turquoise lines in panels (c,d)) changes less dramatically along the translational coordinate. Such an interaction is larger for A_g symmetry states and more effective because of the *quasi* degeneracy of $FE^{(2)-}$ and $FE^{(4)-}$ energy profiles, while it is far less effective for B_g states owing to the large energy difference between $FE^{(1)-}$ and $FE^{(3)-}$ states. This explains the remarkable energy lowering of the $1A_g$ adiabatic exciton state (yellow squares in Figure 5.18(a,b)) compared to the SA diabatic states (green) for all translational displacements, which is not observed for B_g states except for specific displacement ranges corresponding to large FE/CR interactions.

Figure 5.18. Analysis of the excitation energy profiles of singlet exciton states (A_g symmetry) for (left) naphthalene and (right) anthracene dimer (TDA-ωB97X-D/6-31G*) in terms of SA diabatic states (green for FE states, red for CR states) and their interactions. (a, b) Computed adiabatic and SA diabatic excitation energy profiles. (c, d) Magnitude and modulation along the longitudinal translation coordinate of the (grey) $D_e^{(2)} - D_h^{(2)}$, $D_e^{(4)} - D_h^{(4)}$ interactions, coupling FE and CR states, and of the (dark-turquoise) $H^{(2,4)} - V_e^{(2,4)}$ interactions mixing $FE^{(2)}$ and $FE^{(4)}$ states. Details on SA diabatic Hamiltonian can be found in the supporting information of Ref. [95]. Figure reprinted from Ref. [95].
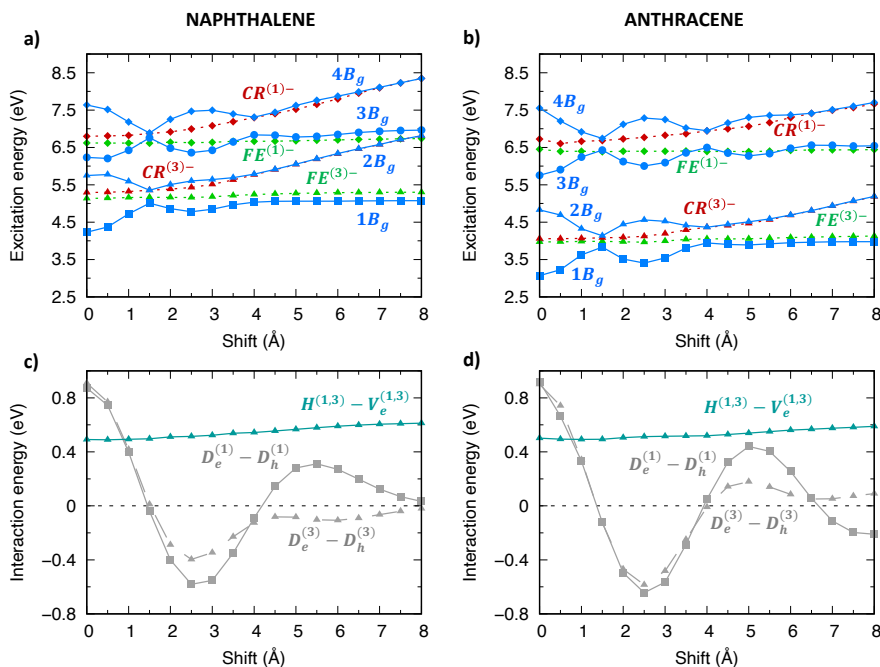
Figure 5.19. Analysis of the excitation energy profiles of singlet exciton states (B_g symmetry) for (left) naphthalene and (right) anthracene dimer (TDA-ωB97X-D/6-31G*) in terms of SA diabatic states (green for FE states, red for CR states) and their interactions. (top) Computed adiabatic and SA diabatic excitation energy profiles. (bottom) Magnitude and modulation along the longitudinal translation coordinate of the (grey) $D_e^{(1)} - D_h^{(1)}$, $D_e^{(3)} - D_h^{(3)}$ interactions, coupling FE and CR states, and of the (dark-turquoise) $H^{(1,3)} - V_e^{(1,3)}$ interactions mixing $FE^{(1)}$ and $FE^{(3)}$ states. Details on SA diabatic Hamiltonian can be found in the supporting information of Ref. [95]. Figure reprinted from Ref. [95].
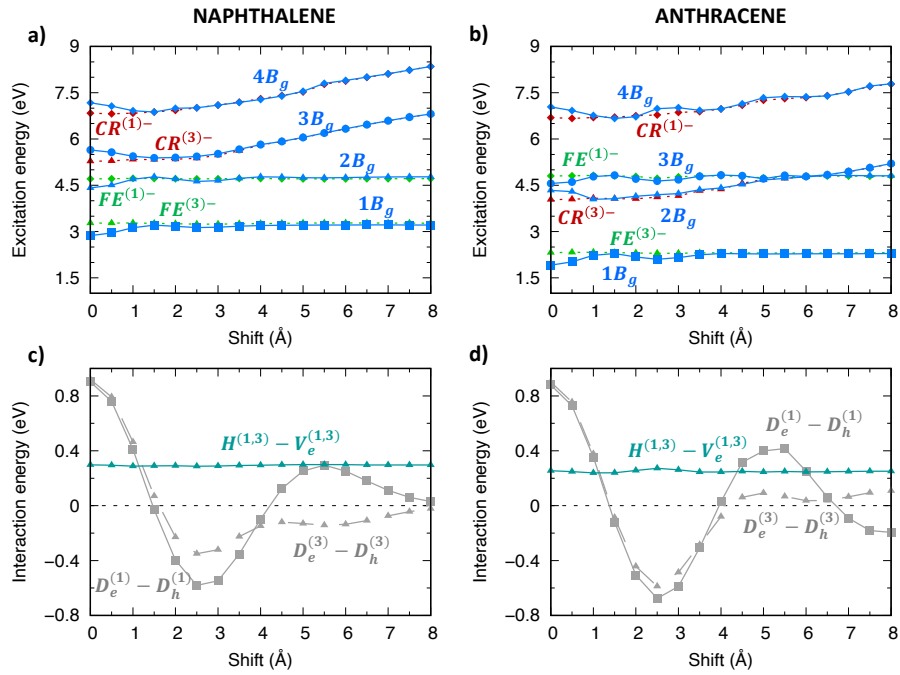
5.6.4 Triplet exciton states of Naphthalene and Anthracene dimers

Figure 5.20 collects the excitation energy profiles of triplet excitons of oligoacene dimers. In contrast with singlet excitons, we note that the lowest two triplet exciton states belong to B_g and A_u symmetries, while the lowest A_g exciton state is found at much higher energy. Similar to singlet excitons, a few low-lying states (dark-blue/dark-red in Figure 5.20) were not included in the diabatization procedure, since their influence is negligible due to their different orbital nature and energy separation from the lowest exciton states. The CT character analysis (Figure 5.20c,d) demonstrates that either the $1B_g$ and $1A_g$ states have a mixed CT/LE character with a slightly higher CT contribution observed for the longer acene dimer.
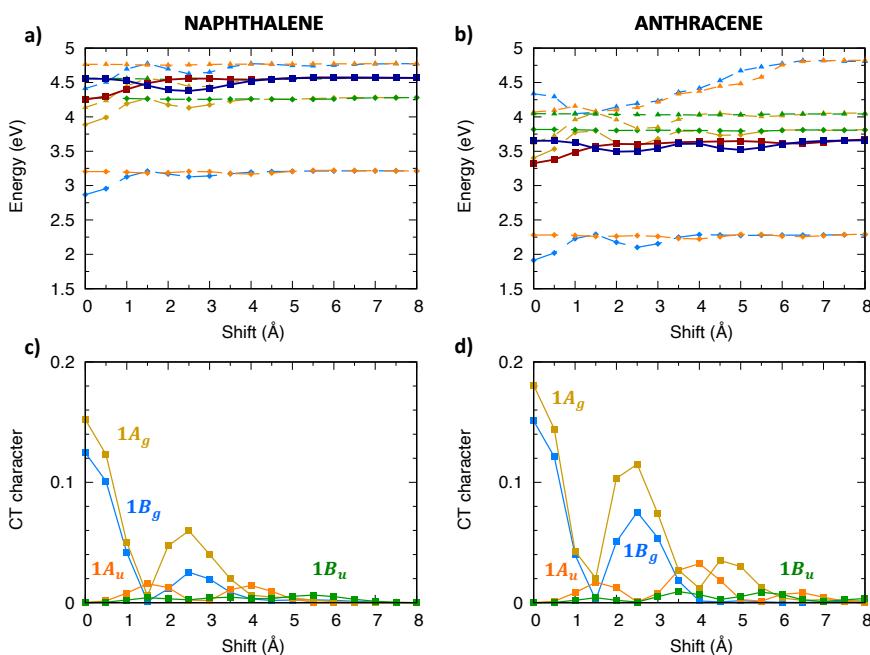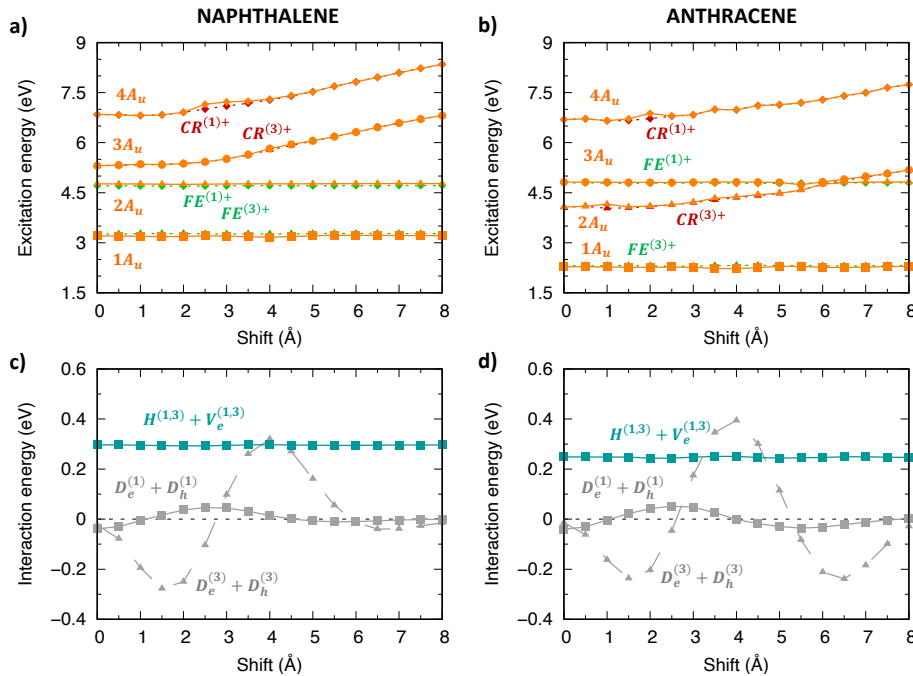

Figure 5.20. Lowest energy triplet exciton states of (left) naphthalene and (right) anthracene): (a,b) adiabatic excitation energy profiles of the low-lying exciton states depicted with different color codes for different symmetries: yellow for A_g, orange for A_u, blue for B_g and green for B_u. The lowest energy exciton states not included in the diabatization procedure are also shown (dark blue, B_g symmetry, dark red, A_u symmetry); (c, d) CT character of the lowest four exciton states. Figure reprinted from Ref. [95].

The significant CT contribution to $1B_g$ and $1A_g$ states contrasts with the almost negligible contribution to $1B_u$ and $1A_u$ states. Such differences can be rationalized by comparing, for instance, the SA diabatic energy profiles (B_g and A_u symmetry) with FE and CR character (green and red curves, respectively, in Figures 5.21 and 5.22) and their inter-state interactions, depicted in the bottom part of the above figures. The FE/CR energy differences are very similar for the two sets of SA diabatic states, but their couplings (grey lines) are much larger for the B_g states. Specifically, the largest interaction amounts to more than 0.8 eV for B_g and it does not exceed 0.3 eV for A_u states. As a result, $1B_g$ adiabatic states display a non-negligible CT character for small longitudinal displacements, while $1A_u$ states do not.

Figure 5.21. Analysis of the excitation energy profiles of triplet exciton states (B_g symmetry) for (left) naphthalene and (right) anthracene dimer (TDA-ωB97X-D/6-31G*) in terms of SA diabatic states (green for FE states, red for CR states) and their interactions. (a, b) Computed adiabatic and SA diabatic excitation energy profiles. (c, d) Magnitude and modulation along the longitudinal translation coordinate of the (grey) $D_e^{(1)} - D_h^{(1)}$, $D_e^{(3)} - D_h^{(3)}$ interactions, coupling FE and CR states, and of the (dark-turquoise) $H^{(1,3)} - V_e^{(1,3)}$ interactions mixing $FE^{(1)}$ and $FE^{(3)}$ states. Figure reprinted from Ref. [95].


Figure 5.22. Analysis of the excitation energy profiles of triplet exciton states (A_u symmetry) for (left) naphthalene and (right) anthracene dimer (TDA-ωB97X-D/6-31G*) in terms of SA diabatic states (green for FE states, red for CR states) and their interactions. (a, b) Computed adiabatic and SA diabatic excitation energy profiles. (c, d) Magnitude and modulation along the longitudinal translation coordinate of the (grey) $D_e^{(1)} + D_h^{(1)}$, $D_e^{(3)} + D_h^{(3)}$ interactions, coupling FE and CR states, and of the (dark-turquoise) $H^{(1,3)} + V_e^{(1,3)}$ interactions mixing $FE^{(1)}$ and $FE^{(3)}$ states. Figure reprinted from Ref. [95].

The analysis of interactions between SA diabatic states uncovers also specific differences between singlet and triplet excitons. One distinctive element, as we have outlined in a previous section on PDI dimers and documented in literature [60,94], is the larger energy separation between CR and FE triplet diabatic states compared to singlet states, which separation accounts for the reduced effect of super-exchange interactions and leads to a less marked CT character of lowest-lying triplet exciton states. An additional distinction can be appreciated in the case of oligoacenes and concerns the couplings between SA diabatic states of FE type (dark-turquoise lines in Figures 5.18, 5.19 for singlet and Figures 5.21, 5.22 for triplet excitons). These range from *ca.* 0.45 eV to 0.8 eV for singlet SA states of A_g/B_g symmetry while they do not exceed 0.35 eV for the triplet SA states of any symmetry. As a result, the adiabatic triplet exciton states of all symmetry species almost overlap with the SA diabatic states for large portions of the energy profiles, in contrast with those of singlet spin multiplicity discussed in the previous section. These interactions result from the combination of an intramolecular contribution (top part of Figures 5.23, 5.24) with the intermolecular exciton coupling (bottom part of Figures 5.23, 5.24), both of which are much larger for singlet states.
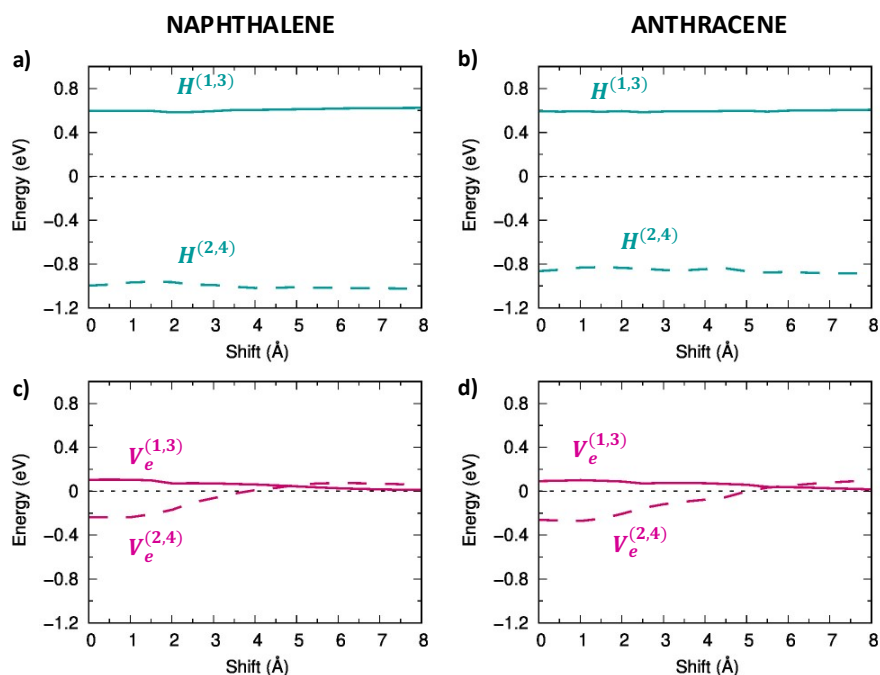
Figure 5.23. Energy profiles of interactions between LE diabatic **singlet** states of different type (see also Table 5.2), along the longitudinal shift. (Top) Intramolecular interactions between LE diabatic states of (a) naphthalene and (b) anthracene dimers; (Bottom) Intermolecular interactions between LE diabatic states of different type of naphthalene (c) and anthracene (d). Figure reprinted from Ref. [95].
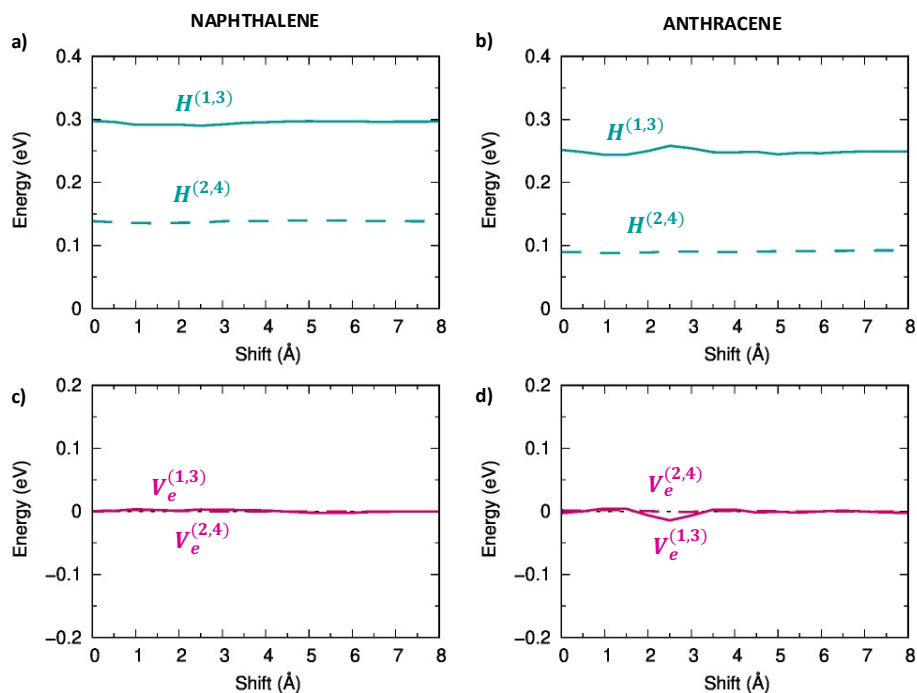
Figure 5.24. Energy profiles of interactions between LE diabatic **triplet** states of different type (see also Table 5.2), along the longitudinal shift. (Top) Intramolecular interactions between LE diabatic states of (a) naphthalene and (b) anthracene dimers; (Bottom) Intermolecular interactions between LE diabatic states of different type of naphthalene (c) and anthracene (d). Figure reprinted from Ref. [95].

5.6.5 CT Character of singlet and triplet exciton states of oligoacenes.

The CT character analysis obtained from the above discussed diabatization procedure (Figures 5.16(c,d) and 5.20(c,d)) can be compared with the results of other analysis tools. To visualize the nature of the lowest singlet and triplet exciton states, for the eclipsed configurations of the two oligoacene dimers, we carried out a fragment-based analysis via electron–hole correlation plots, using TheoDORE [305] (Figure 5.25). The two selected fragments correspond to the two molecules forming the dimer. Exciton states are identified by the non-vanishing elements of the 2×2 matrix (the Ω-matrix[305]) represented by different levels of grey. Locally excited contributions appear in Figure 5.25 off-diagonally (going from lower left to upper right), while CT contributions appear on the main diagonal. In agreement with the character analysis shown in Figures 5.16(c,d) and 5.20(c,d), also Figure 5.25 shows that for the eclipsed configuration, the character of the lowest singlet and triplet exciton states is mixed LE/CT as indicated by the light-grey squares in the electron-hole correlation plot. As discussed in previous sections, the CT contribution is larger for singlet exciton states than for triplet exciton states: main diagonal squares for the singlet excitons are dark grey while those of triplet exciton states are light grey. This is a result of the larger energy separation between CR and FE diabatic triplet states. Overall, both approaches provide the same results, regarding the CT contributions, for the lowest triplet and singlet exciton states. Our diabatization analysis also provides detailed information on relevant intermolecular and inter-state interactions.
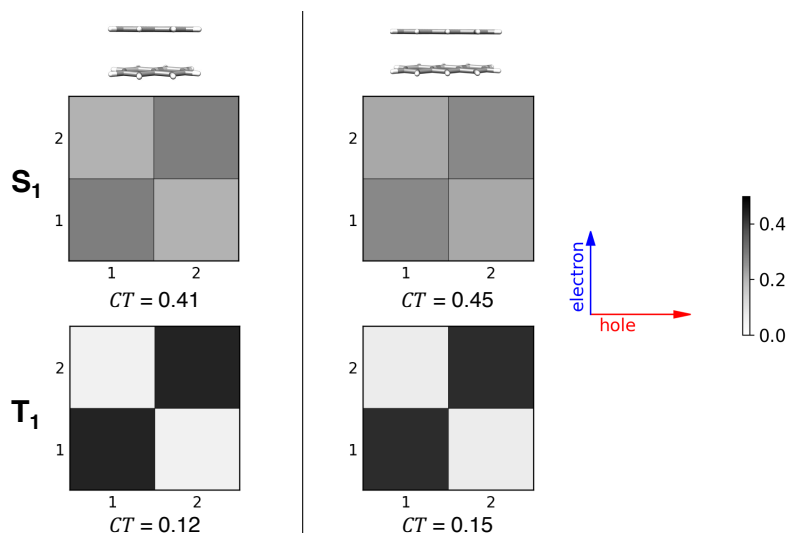
Figure 5.25. Lowest energy singlet and triplet exciton-state analysis via electron-hole correlation plots[305] for (left) naphthalene and (right) anthracene dimers in their eclipsed configuration. The grey scale used is shown on the right panel. From TDA-ωB97X-D/6-31G* calculations. The magnitude of the CT contribution is shown on the bottom part of each panel. Figure reprinted from Ref. [95].

5.6.6 Absorption spectrum and H-/J- character switch along the longitudinal translation coordinate

In previous sections we focused the attention on low-lying exciton states of the oligoacene dimers. Since the absorption spectrum of oligoacenes is dominated by the transition to the higher energy B_{2u} state (the B_b state in Platt's notation), it is interesting to discuss the evolution (along the displacement coordinate) of the dipole allowed exciton state originated from the B_b state and how its excitation energy modulation influences the appearance of the absorption spectrum. The computed absorption spectrum for increasingly large translational displacements (Figure 5.26) shows that the intense absorption occurs at higher energies than the isolated molecule (black bar in Figure 5.26), suggesting an H-type aggregation for small displacements from the eclipsed configurations. For larger displacements, the most intense absorption band moves abruptly to lower excitation energies (J-type) after a narrow intermediate region in which two bands of similar intensity appear. The evolution of the excitation energy of such strongly allowed exciton state is shown in black in Figure 5.27. This state corresponds to the $4B_u$ state for both naphthalene and anthracene at the eclipsed geometry and for displacements up to 4 or 5 Å, then it switches to the $2B_u$ state. Such a switch is associated with a sudden change in the exciton state character, acquiring a dominant CT contribution for larger displacements (Figure 5.28), suggesting that the H- to J- type transition along the longitudinal displacement is assisted not only by the sign change of the exciton interaction but also by the interaction between FE and CR states.

Finally, for large displacements (8 Å) the strongest absorption peak has moved back almost toward the isolated molecule value, although not completely owing to some still non-negligible exciton interactions. Indeed the $V_e^{(2)}$ and $V_e^{(4)}$ couplings (Figure 5.29, Table 5.1) are still not vanishing at such distance, in contrast with the $V_e^{(1)}$ and $V_e^{(3)}$ interactions that have already become negligible.
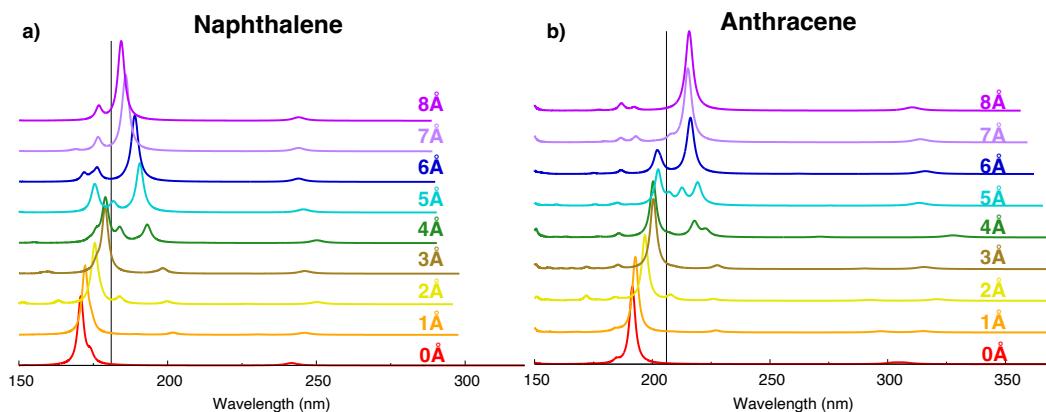
Figure 5.26. Comparison between vertical absorption spectra predicted for (a) naphthalene and (b) anthracene dimer, from TDA-ωB97X-D/6-31G* calculations. Modulation along the longitudinal shift from 0 Å to 8 Å. Different colors are used to plot spectra computed for different displacements. Black bar: absorption peak of the B_b state of the monomer, calculated at TDA-ωB97X-D/6-31G* level. Figure reprinted from Ref. [95].
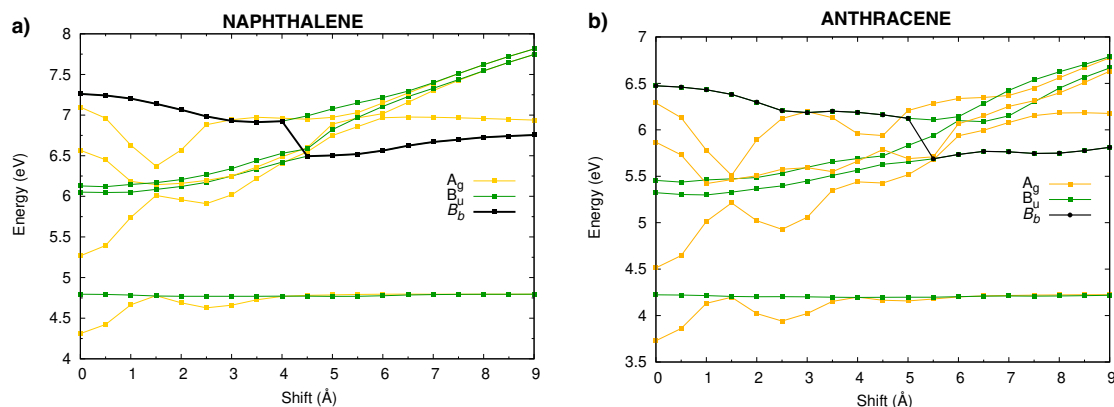
Figure 5.27. Singlet adiabatic exciton states of A_g (yellow) and B_u (green) symmetry of (a) naphthalene and (b) anthracene. The evolution of the strongly allowed exciton state (state that bears a parentage with monomers' B_b state) is shown in black. TDA-ωB97X-D/6-31G* calculations. Figure reprinted from Ref. [95].
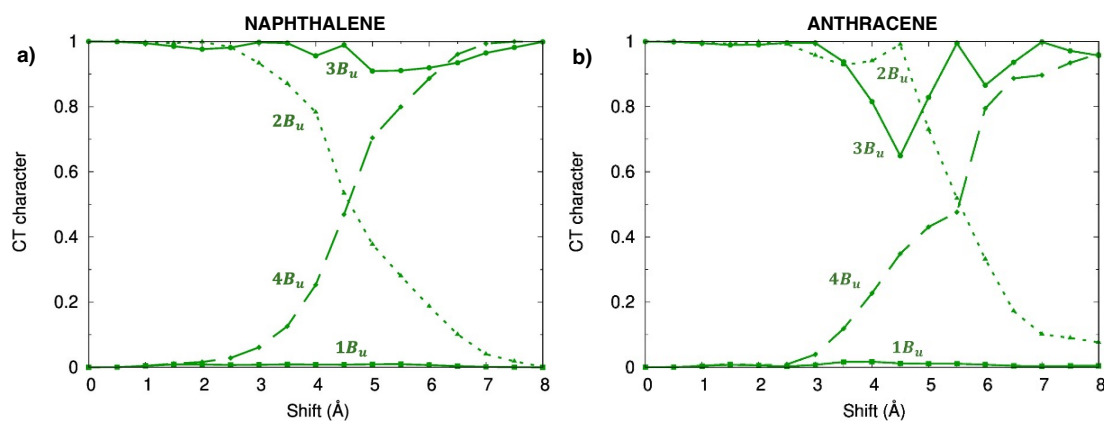
Figure 5.28. CT characters of the singlet adiabatic exciton states of B_u symmetry along the longitudinal translation coordinate for (a) naphthalene and (b) anthracene. Figure reprinted from Ref. [95].
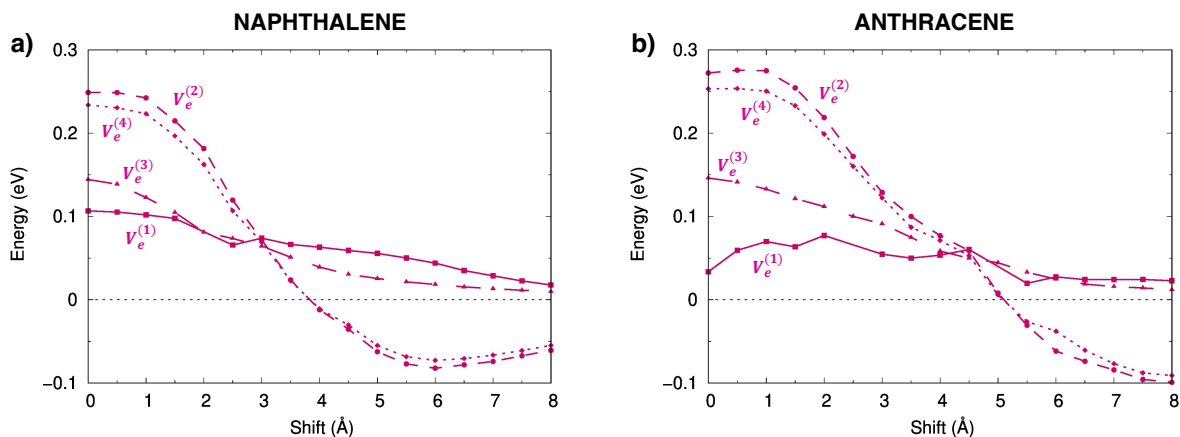
Figure 5.29. Energy profiles of the excitonic interactions between singlet diabatic states of the same type of (a) naphthalene and (b) anthracene. Figure reprinted from Ref. [95].

5.7 Exciton states of PDI's trimers and tetramers from *mH* analysis

Trimers and tetramers of PDI are chosen as model systems to build the *mH* and to determine adiabatic exciton states and CT character from its diagonalization. Notably, because the objective here is to test the reliability of the protocol chosen to build the *mH*, the resulting exciton states were checked against those produced by TD-DFT calculations carried out on the full aggregate. The eclipsed configuration of both can be seen from Figure 5.6. The interplanar distances between D1, D2, and D3 are respectively 3.4 Å, 6.8 Å and 10.2 Å.

As presented in Section 5.4, the construction of *mH* relies on H_{dia} matrix elements of the component dimers. So, beside the dimer with monomers at 3.4 Å distance, exciton states of the dimers with interplanar distances of 6.8 Å and 10.2 Å also need to be calculated and diabatized along the longitudinal shift. The exciton states of dimers at 6.8 Å and 10.2 Å distances, along the longitudinal displacement, are calculated with TD-ωB97X-D/6-31G*. The resulting exciton states are then diabatized with the diabatization procedure described in Section 5.3.

Overall, in order to assess the performance of the *mH* , two sets of results are compared for the PDI trimer and tetramer: 1) exciton states determined with TD-ωB97X-D/6-31G* calculations carried out on the **<u>full aggregate</u>**, whose adiabatic states originated from the MIOS were subject to the diabatization procedure described in Section 5.3 to obtain the H_{dia} matrix and the CT/LE character of each state; 2) exciton states and CT/LE character determined from diagonalization of the **<u>mH</u>** matrix, built on the basis of TD-ωB97X-D/6-31G* calculations carried out on the dimers composing the aggregate.

5.7.1 Exciton states energy profiles of trimers and tetramers of PDI

The excitation energy profiles of the adiabatic states, obtained from the two approaches (see Figure 5.30a,b) are very similar, an indication that the *mH* approach reproduces well the excitation energies of full-aggregate calculations.

We note that, compared to the dimer, the lowest energy exciton state of the trimer is always $1B_u$ and therefore implies a symmetry allowed transition for all longitudinal shifts. However, the computed transition dipole moment of the $1B_u$ state of the trimer (see Figure

5.30c) switches from very low values typical of an H-aggregate (in the interval 0.0 Å - 1.5 Å and 4.0 Å - 6.0 Å) to larger values typical of J-aggregates (in the interval 2.0 Å -3.5 Å and 6.5 Å to 8.0 Å). The oscillation of the transition dipole moment of the $1B_u$ state determines an interchange of H- and J- spectroscopic features, which is very similar to the well-established predictions for a PDI dimer[21,22,304,311,316,318,332,333].
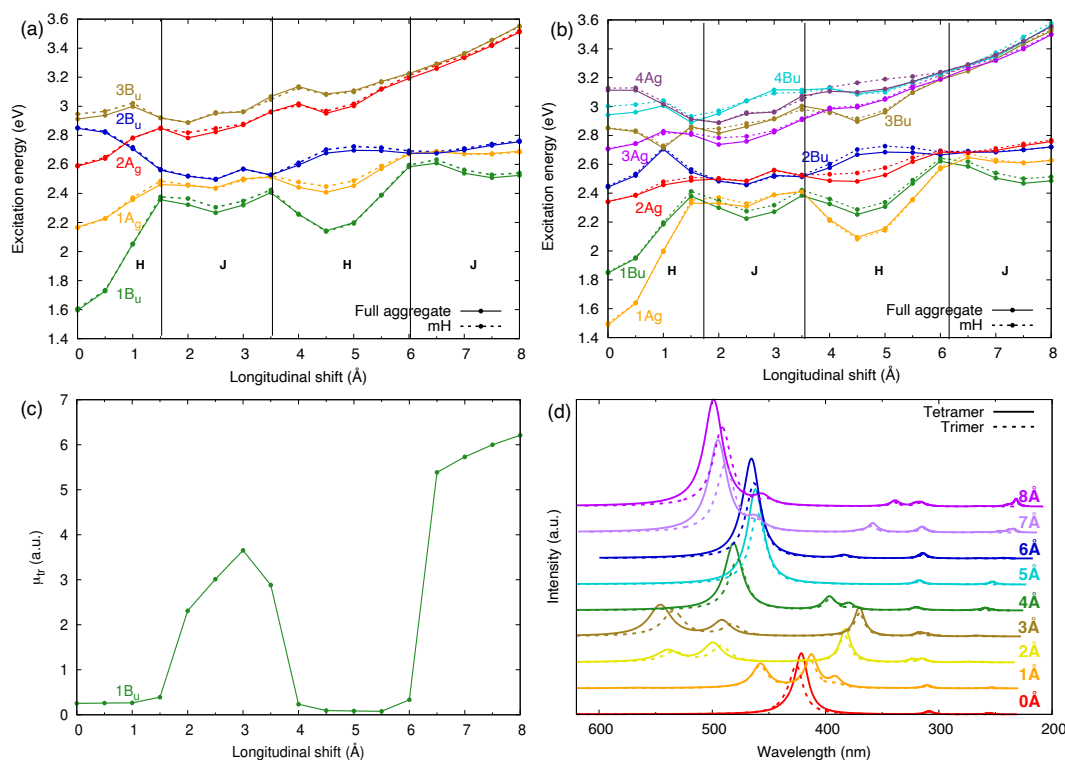
Figure 5.30. Low-lying exciton states of (a) the PDI trimer and (b) the tetramer from full-aggregate calculations (solid) and from diagonalization of the dimer-based **mH** (dashed). (c) Transition dipole moment of the lowest energy exciton state of the trimer, from TD-ωB97X-D/6-31G* calculations. (d) Comparison between vertical absorption spectra predicted for the trimer (dashed) and for the tetramer (solid). Different colours are used to distinguish the spectra computed for different displacements. Reprinted from: S. Canola, *et al., J. Chem. Phys.* **2021**, 154, 1–37, with the permission of AIP Publishing.
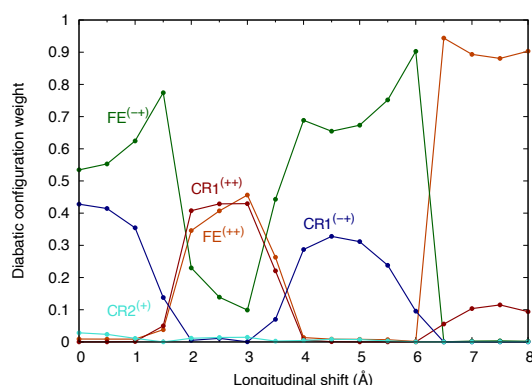
 Figure 5.31. The wavefunction composition of the adiabatic lowest exciton state ($1B_u$) of the PDI trimer in terms of the symmetry-adapted diabatic states defined in Ref. [93]. Reprinted from: S. Canola, *et al., J. Chem. Phys.* **2021**, 154, 1–37, with the permission of AIP Publishing.

Interestingly, by expressing the wavefunction in terms of SA diabatic states as shown in Figure 5.31, it emerges that a CR diabatic state (arising from the ++ combination of two CT configurations of B_u symmetry) contributes significantly to the wavefunction of the $1B_u$

exciton state of the trimer in the interval 2.0 Å - 3.5 Å, where also a FE diabatic state (from the ++ combination of two LE configurations of B_u symmetry) contributes with the same weight and confers optical activity to the exciton state. Therefore, also in PDI trimer, the appearance of J-aggregate at short longitudinal displacement is CT-mediated, as it has been found in the dimer[21,93,304].

For the tetramer the situation is much closer to the dimer, as the lowest energy exciton state (Figure 5.30b) switches from A_g to B_u and drives an interchange of H-/J-/H-/J-aggregate character as in the dimer.

In summary, both trimer and tetramer display the typical switch to J-aggregation for small longitudinal shifts followed by further H-/J- interchanges and, accordingly, they display a very similar modulation of computed vertical absorption spectra along the longitudinal translation (Figure 5.30d).

5.7.2 CT character profiles in PDI trimers and tetramers

Figure 5.32 compares the CT character determined by the two approaches, for the nine and sixteen adiabatic states resulting by excitations within the MIOS for the trimer and tetramer, respectively. The differences are slightly more significant compared to those observed in the energy profiles, but do not affect substantially the character of a given exciton state, whose dominant CT character remains the same for both approaches.
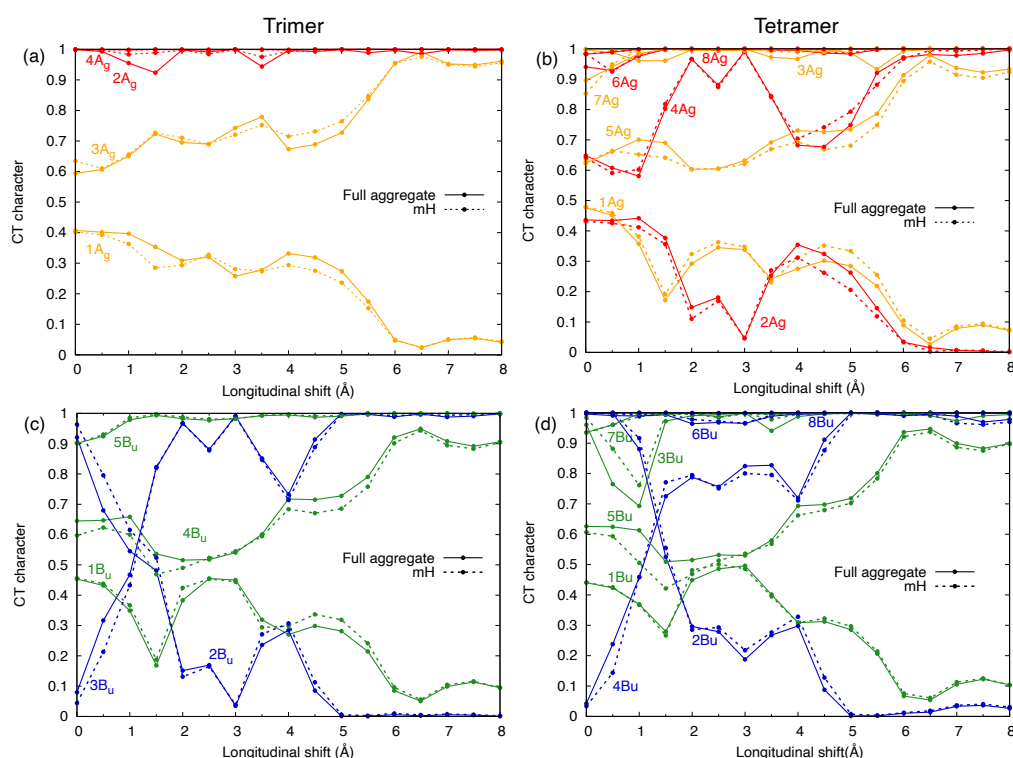
Figure 5.32. Modulation of the CT character of the exciton states of PDI trimers and tetramers, as a function of the longitudinal displacement. The A_g exciton states are shown in panel (a) for trimer and (b) for tetramer. The B_u exciton states are shown in panel (c) for trimer and (d) for tetramer. Solid lines: CT character determined from the diabatization of exciton states from TD-ωB97X-D/6-31G* calculations on the full-aggregate. Dashed lines: CT character resulting from diagonalization of the **mH**. Reprinted from: S. Canola, *et al., J. Chem. Phys.* **2021**, 154, 1–37, with the permission of AIP Publishing.

Considering the eclipsed configuration for both aggregates, a similar character description, from either the full-aggregate calculation or from diagonalization of *mH*, is clearly seen in Figure 5.33. A very similar character description is also found in other geometrical configurations[93].
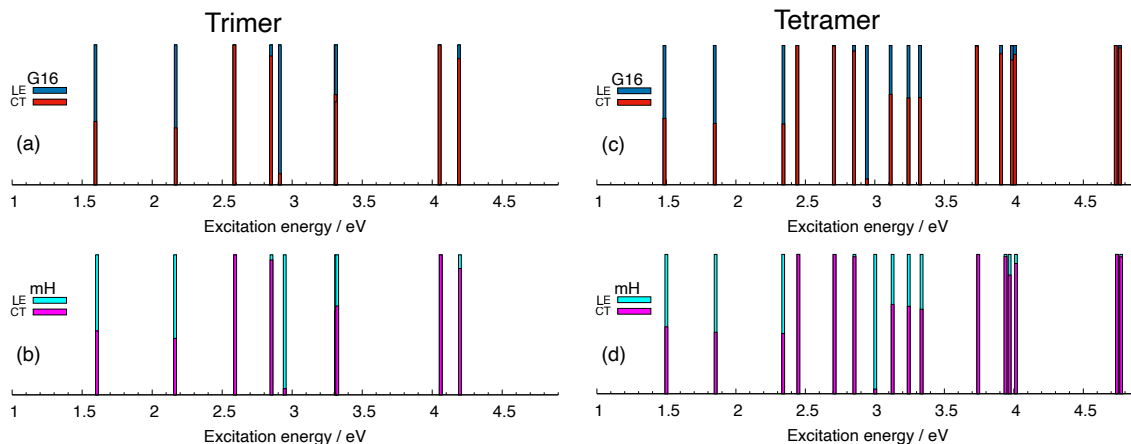

Figure 5.33. The CT/LE character of exciton states: results for (left) PDI trimer and (right) PDI tetramer: (a, c) from full-aggregate (G16 label) TD-ωB97X-D/6-31G* calculations and (b, d) from *mH*. The longitudinal displacement is 0.0 Å. Reprinted from: S. Canola, *et al., J. Chem. Phys.* **2021**, 154, 1–37, with the permission of AIP Publishing.

5.7.3 Assessment of the mH approach

The profiles of the diagonal and some of the off-diagonal matrix elements of the trimer from H_{dia} and *mH* (Table 5.3), collected in Figure 5.34, allow to critically assess the performance of the more approximated *mH*.

Firstly, H_{dia} and *mH* differ from the diabatic energy profiles of the three E_{FE} terms (which correspond to E_{LE} in H_{dia}, Table 5.1). In *mH* they are chosen to be identical to those computed for the dimer D1 according to the definition in Table 5.3. In contrast, two slightly different energy profiles are extracted from H_{dia}, one corresponds to the energy of the LE diabatic states centered on monomer *b*, labelled FE_b and the other corresponds to the two degenerate LE diabatic states centered on the terminal monomers *a* and *c* (labelled FE_a and FE_c). While the latter are very similar to the E_{FE} term extracted from D1 calculations, the former is slightly lower, as a result of different chemical environment of terminal and central monomers, a distinction that is missing for the construction of *mH*. Similarly, only one energy profile for CT diabatic states involving D1 (monomers 3.4 Å apart, CT1) or D2 (monomers 6.4 Å apart, CT2) is used to build *mH*, whereas two slightly different energy profiles for CT diabatic states are extracted from the H_{dia} matrix. It should be noted that the additional differences between the CT energy profiles obtained from H_{dia} and *mH* in the regions 1–2 Å and 4–5 Å are likely to be due to the additional adiabatic states generated by full-aggregate TD-DFT calculations which are not included in the MIOS.
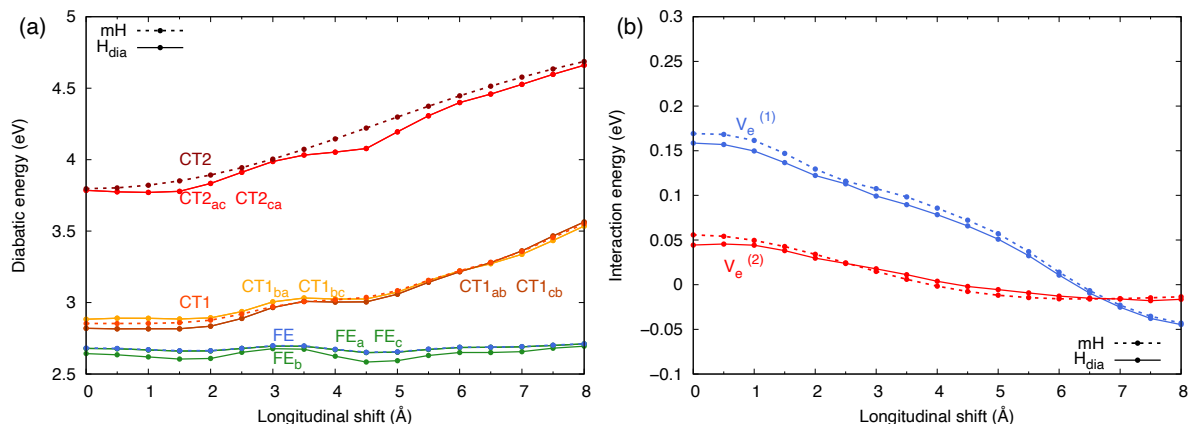
Figure 5.34. (a) Comparison between LE (FE label)/CT diabatic state energy profiles for PDI trimers from (solid) H_{dia} and (dashed) mH. The energies of the three LE (FE label) and the four CT diabatic states, extracted from H_{dia}, are not identical and are identified by a subscript letter indicating the monomer (or pair of monomers for CT) to which they correspond. (b) Comparison between diabatic state interactions ($V_e^{(1)}$ and $V_e^{(2)}$ elements, see Table 5.3) from (dashed) mH and (solid) the corresponding elements extracted from H_{dia}. Reprinted from: S. Canola, *et al., J. Chem. Phys.* **2021**, 154, 1–37, with the permission of AIP Publishing.
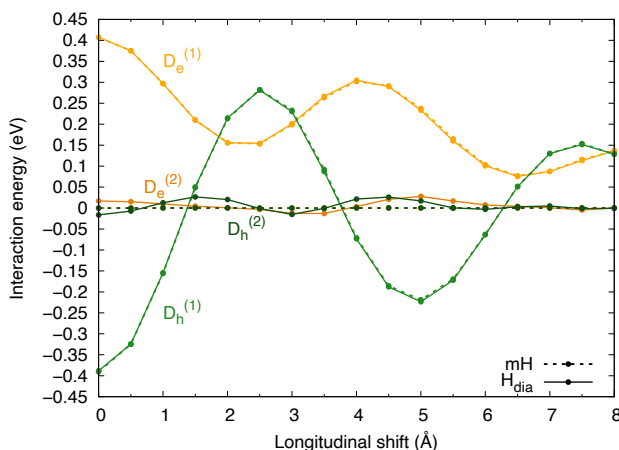
Figure 5.35. PDI trimer: comparison between diabatic state interactions ($D_{e/h}^{(1)}$ and $D_{e/h}^{(2)}$ elements (Table 5.3) from (solid) H_{dia} and (dashed) mH. Reprinted from: S. Canola, *et al., J. Chem. Phys.* **2021**, 154, 1–37, with the permission of AIP Publishing.

Concerning off-diagonal matrix elements, in Figure 5.34b we compare $V_e^{(1)}$ and $V_e^{(2)}$ interactions extracted from the *mH* matrices (Table 5.3) with the corresponding elements in the H_{dia} matrices, while in Figure 5.35 the comparison for $D_e^{(1,2)}/D_h^{(1,2)}$ elements is shown. The differences between full-aggregate calculations and *mH* are acceptably small either for $V_e^{(1,2)}$ and for $D_e^{(1,2)}/D_h^{(1,2)}$ elements. The largest discrepancy is observed for the matrix elements identified as $D_e^{(2)}/D_h^{(2)}$ in *mH* (Table 5.3). They are underestimated compared to the corresponding elements extracted from H_{dia}. Interestingly, for PDI trimer the inclusion of the molecule in-between the two distant monomers (in full-aggregate calculations) does not screen these "long-range" interaction terms, which are larger than those introduced in the construction of *mH,* possibly as a result of indirect interactions mediated by the central molecule which is missing in the *mH* approach.

These differences, in all cases, are not large but, together with other similar approximations in the off-diagonal elements of *mH*, account for the small discrepancies above discussed, some

of which could be corrected by building the elements of mH from non-symmetric dimer calculations or taking advantage of solvent effects[325,349] to simulate the embedding of internal monomers.

Finally, we note that $V_e^{(2)}$ term, accounting for interactions between two LE diabatic states that are not near-neighbors, are not negligible suggesting that for the aggregates investigated in this work, the approximation of interaction terms limited to near neighbors would not be appropriate.

5.8 Conclusions

In this chapter, we investigated the role of intermolecular interactions in determining the nature of exciton states. The latter strongly influence the optoelectronic properties and the outcome of photoinduced processes in molecular materials. To disentangle the nature of exciton states, we proposed two approaches: 1) to use a diabatization protocol and build the H_{dia} matrix and 2) the dimer based mH, the latter being a cost-effective alternative for larger aggregates.

These two approaches were tested considering two well-known molecular systems, namely, PDI and small oligoacenes (naphthalene and anthracene). In particular, we investigated the nature of singlet and triplet exciton states in homo-dimers of PDI, naphthalene and anthracene along the intermolecular longitudinal translation coordinate with H_{dia}. The modulation of exciton states' nature of larger aggregates of PDI (trimer and tetramer) along the longitudinal displacement was evaluated also with the mH.

The study on dimers showed that either singlet or triplet exciton-state energies could be rationalized in terms of the interactions between CR and FE symmetry adapted diabatic states. Such CR/FE interactions, although less effective for triplet excitons, led to a mixed LE/CT character of the low-lying singlet and triplet exciton states. Additionally they were found to be responsible for the CT-mediated J-aggregation mechanism occurred for small longitudinal displacements in PDI and in the two oligoacene dimers, similarly to the already observed mechanism in singlet exciton states of perylene dimer [21]. The role of CR states, thus, must be carefully considered as a factor influencing the processes following singlet and triplet exciton generation.

Concerning the analysis from the dimer-based mH, we showed that both adiabatic excitation energy and the CT character of each eigenstate (obtained from the diagonalization of mH) were in very good agreement with results from the full-aggregate calculations. Nevertheless, the less expensive mH approach showed some limited deviations due to the approximations used to define the mH matrix elements. The dimer-based mH could be considered a suitable alternative for the study of large chromophore aggregates since it provides results comparable to full-aggregate calculations at a fraction of the cost. At the same time, it provides a simple rationalization of the CT contribution to the photophysical character of the aggregate.

In addition, along the longitudinal translation coordinate, either H_{dia} and mH predicted an interchange of the H-/J- spectroscopic character for trimer and tetramer in agreement with the well-established interchange determined for dimers of PDI. The CT-mediated J aggregation in

trimers was rationalized in terms of symmetry adapted CR and FE diabatic states.

We believe that this study provides useful insights on the magnitude of intermolecular interactions occurring in molecular materials and determining the nature of exciton states of both singlet and triplet spin multiplicity, paving the way to future investigations on more complex aggregates and intermolecular organizations.

Chapter 6: Conclusions

The purpose of this dissertation was to investigate deeply, through theoretical models and computational studies, the structure-property relationships governing electronic, optical and charge transport properties of organic molecular materials. In particular, the main focus was on the interplay of intra-molecular properties and inter-molecular interactions governing the condensed phase of organic molecular materials. Through this dissertation, my main objective was to better understand the constituent properties of the investigated systems in order to rationalize experimental data and improve the design of new organic functional materials. Because of the combined effect of individual molecular properties and inter-molecular organization, I pursued three major areas of investigation which can be summarized by three keywords: **diradicaloids**, **charge transport** and **exciton states.** These keywords characterize three tasks featuring different complexity in terms of computational approaches: the first keyword refers to individual molecules with unusual electronic structures (open-shell) and promising applications, the second refers to a process in organic molecular materials where intra- and inter- molecular factors contribute generally on equal footing and finally the latter keyword refers, in the context of this dissertation, to the need to disentangle the character of electronic excitations in molecular aggregates and their dependence on inter-molecular organization, as a first step toward understanding photoinduced processes in molecular materials. To this end, in my work I was seeking optimized procedures based on state-of-the-art quantum-chemical methods to characterize the emerging class of conjugated diradicaloids. Moreover, *in-house* developed protocols were used and in part developed, to uncover the effects of condensed-phase organization on charge transport processes and exciton states of molecular materials.

In Chapter 3, the diradical character and its influence on optical properties of several different conjugated diradicaloids, promising molecular materials for optoelectronic applications, were computationally investigated. This part of my work was fostered also by collaborations with experimental groups and therefore one objective was to provide results in agreement with experimental data. At the same time, this study was also aimed at establishing suitable computational protocols to capture the distinctive features of ground and excited

electronic states (diradical character, aromatic vs quinoidal structures, correct sequence of low-lying excited states, *etc.*) of these promising molecules for which electron correlation plays a remarkable role.

One example is represented by quinoidal oligothiophenes for which I explored the applicability of DFT/UDFT to predict molecular structures and their effect on computed Raman activities. In this context I showed that a long-range corrected functional is more appropriate to correctly capture the molecular structure in case of large diradical character. This study further revealed that the Raman activity associated with CC stretching modes of low frequency is enhanced by resonance with both the optically active SE and the dark DE state.

The role of vibrations was essential to explain the "normal" quinoidal → aromatic and "reversed" aromatic → quinoidal transformations in a dumbell shape π-conjugated azobenzene derivative, featuring varying diradical character as a function of the temperature in the solid phase, accompanied by the modulation of the spin density distribution. My computational investigation supported such spin dynamics and indicated that it was induced by different low-frequency torsional mobilities activated by increasing temperature.

Another contribution of my work concerned the optical properties of diradicaloids which are unusual and generally high-level computational models are required to describe their low-lying excitations. In this regard I performed a benchmark study on a library of such molecules with the aim of recommending cost-effective methods able to correctly describe their low-lying excited states. This systematic investigation proved that a careful choice of the appropriate DFT-based computational approach can provide reliable excitation energy predictions for diradicaloids with varying diradical characters and large molecular dimension, including the energy location of an uncommon low-lying excited state like the DE state.

My last investigation on individual molecular species with promising optoelectronic properties concerns the uncommon luminescence of a Thiele derivative. In this case I showed that a mixing of the SE and DE states explains the appearance of a charge separated excited state accounting for the experimentally observed solvatochromic behavior.

In Chapter 4 I focused on the task of charge transport processes and this required to move to models taking into account the combination of intra-molecular parameters (reorganization energy), intermolecular electronic couplings and in some cases simulations ultimately used to propagate the charge carrier through the molecular material.

The first system I considered was a class of diradicaloid molecules and I showed that there is a connection between diradical character and ambipolar charge transport. The charge transport efficiencies were assessed by focusing essentially on intramolecular reorganization energies λ_i, which were shown to be generally inversely proportional to the diradical character. Thus, molecules showing medium diradical character were shown to exhibit also small reorganization energies, very similar for holes and electrons suggesting an equivalent p- and n-type transport.

Another objective of this task was instead to compare the effect of chemical substituents (thus molecular structure) on crystal packing and ultimately on charge mobility. In this context I demonstrated that the anisotropic / isotropic charge mobilities in **α-NDTI** and **N-NDTI** are related to their different crystal arrangements. Additionally, the role of dynamic disorder due to an intermolecular sliding mode was inferred by computing electron–phonon couplings and

confirmed a more detrimental effect for **α-NDTI** compared to **N-NDTI**.

Finally, as a third task of my PhD project, I scrutinized in Chapter 5 the role of intermolecular interactions in determining the nature of exciton states. To disentangle the nature of exciton states, I worked on two approaches: the diabatization procedure and the construction of a dimer based ***mH***.

The diabatization procedure was applied to analyse the exciton states of dimers of PDI, naphathalene and anthracene along the intermolecular longitudinal translation coordinate. I showed that either singlet or triplet exciton-state energies can be rationalized in terms of the interactions between CR and FE diabatic states. Such CR/FE interactions, although less effective for triplet excitons, lead to a mixed LE/CT character of the low-lying singlet and triplet exciton states. The role of CR diabatic states was shown to be relevant also at short displacement distance and our analysis supported the CT-mediated J-aggregation mechanism occurring in PDI and in the two oligoacene dimers. Furthermore, the assessment of non-negligible CR contributions not only to singlet but also to triplet states suggested a possible formation of triplet excimers, and demonstrated that these contributions must be carefully considered as a factor influencing the outcome of photoinduced processes in molecular materials. Having shown the capabilities of our diabatization procedures, a second objective was to propose a cost-effective alternative to quantum-chemical calculations of exciton states on large molecular assemblies. In this case a ***mH*** built on the basis of simple dimer calculations was proposed and applied to trimers and tetramers of PDI. The comparison with full aggregate calculations showed indeed that such ***mH*** can be considered as a suitable alternative for the study of large aggregates.

Bibliography

[1]   Y. Zhang, Y. Zheng, H. Zhou, M. S. Miao, F. Wudl, T. Q. Nguyen, *Adv. Mater.* **2015**, *27*, 7412–7419.

[2]   O. Ostroverkhova, *Chem. Rev.* **2016**, *116*, 13279–13412.

[3]   T. Lei, J. Y. Wang, J. Pei, *Chem. Mater.* **2014**, *26*, 594–603.

[4]   M. Chason, P. W. Brazis, J. Zhang, K. Kalyanasundaram, D. R. Gamota, *Proc. IEEE* **2005**, *93*, 1348–1356.

[5]   A. N. Sokolov, C. J. Bettinger, Z. Bao, *Acc. Chem. Res* **2012**, *45*, 361–371.

[6]   S. Lee, H. Kim, Y. Kim, *InfoMat* **2021**, *3*, 61–81.

[7]   A. Salehi, X. Fu, D. H. Shin, F. So, *Adv. Funct. Mater.* **2019**, *29*, DOI 10.1002/adfm.201808803.

[8]   J.-L. Bredas, J. R. Durrant, *Acc. Chem. Res.* **2009**, *42*, 1689–1690.

[9]   L. Duan, A. Uddin, *Adv. Sci.* **2020**, *7*, DOI 10.1002/advs.201903259.

[10]   C. A. Di, F. Zhang, D. Zhu, *Adv. Mater.* **2013**, *25*, 313–330.

[11]   Y. Guo, G. Yu, Y. Liu, *Adv. Mater.* **2010**, *22*, 4427–4447.

[12]   J. M. Verilhac, *EPJ Appl. Phys.* **2013**, *63*, 1–7.

[13]   X. Hu, Y. Dong, F. Huang, X. Gong, Y. Cao, *J. Phys. Chem. C* **2013**, *117*, 6537–6543.

[14]   A. Troisi, *Chem. Soc. Rev.* **2011**, *40*, 2347.

[15]   H. Oberhofer, K. Reuter, J. Blumberger, *Chem. Rev.* **2017**, *117*, 10319–10357.

[16]   S. Ciuchi, S. Fratini, D. Mayou, *Phys. Rev. B* **2011**, *83*, 081202.

[17]   S. Fratini, S. Ciuchi, D. Mayou, G. T. De Laissardière, A. Troisi, *Nat. Mater.* **2017**, *16*, 998–1002.

[18]   J.-L. Brédas, D. Beljonne, V. Coropceanu, J. Cornil, *Chem. Rev.* **2004**, *104*, 4971–5004.

[19]   V. Coropceanu, J. Cornil, D. da Silva Filho, Y. Olivier, R. Silbey, J.-L. Brédas, *Chem. Rev.* **2007**, *107*, 926–952.

[20]   B. Baumeier, J. Kirkpatrick, D. Andrienko, *Phys. Chem. Chem. Phys.* **2010**, *12*, 11103.

[21]   N. J. Hestand, F. C. Spano, *Acc. Chem. Res.* **2017**, *50*, 341–350.

[22]   N. J. Hestand, F. C. Spano, *Chem. Rev.* **2018**, *118*, 7069–7163.

[23]   E. A. Margulies, J. L. Logsdon, C. E. Miller, L. Ma, E. Simonoff, R. M. Young, G. C. Schatz, M. R. Wasielewski, *J. Am. Chem. Soc.* **2017**, *139*, 663–671.

[24]   E. A. Margulies, C. E. Miller, Y. Wu, L. Ma, G. C. Schatz, R. M. Young, M. R. Wasielewski, *Nat. Chem.* **2016**, *8*, 1120–1125.

[25]   R. M. Young, M. R. Wasielewski, *Acc. Chem. Res.* **2020**, *53*, 1957–1968.

[26]   D. Beljonne, H. Yamagata, J. L. Brédas, F. C. Spano, Y. Olivier, *Phys. Rev. Lett.* **2013**, *110*, 226402.

[27]   T. C. Berkelbach, M. S. Hybertsen, D. R. Reichman, *J. Chem. Phys.* **2013**, *138*, 114103.

[28]   T. Zeng, R. Hoffmann, N. Ananth, *J. Am. Chem. Soc.* **2014**, *136*, 5755–5764.

[29]   D. Casanova, *Chem. Rev.* **2018**, *118*, 7164–7207.

[30] A. Diaz-Andres, D. Casanova, *J. Phys. Chem. Lett.* **2021**, *12*, 7400–7408.

[31] A. Krishnan, A. Diaz-Andres, K. P. Sudhakaran, A. T. John, M. Hariharan, D. Casanova, *J. Phys. Org. Chem.* **2022**, 1–9.

[32] A. L. L. East, E. C. Lim, *J. Chem. Phys.* **2000**, *113*, 8981–8994.

[33] G. Han, Y. Yi, *J. Phys. Chem. Lett.* **2019**, *10*, 2911–2918.

[34] V. Coropceanu, X.-K. Chen, T. Wang, Z. Zheng, J.-L. Brédas, *Nat. Rev. Mater.* **2019**, *4*, 689–707.

[35] F. Würthner, C. R. Saha-Möller, B. Fimmel, S. Ogi, P. Leowanawat, D. Schmidt, *Chem. Rev.* **2016**, *116*, 962–1052.

[36] M. Hecht, T. Schlossarek, S. Ghosh, Y. Tsutsui, A. Schmiedel, M. Holzapfel, M. Stolte, C. Lambert, S. Seki, M. Lehmann, F. Würthner, *ACS Appl. Nano Mater.* **2020**, *3*, 10234–10245.

[37] R. Haldar, A. Mazel, R. Joseph, M. Adams, I. A. Howard, B. S. Richards, M. Tsotsalas, E. Redel, S. Diring, F. Odobel, C. Wöll, *Chem. - A Eur. J.* **2017**, *23*, 14316–14322.

[38] F. J. M. Hoeben, P. Jonkheijm, E. W. Meijer, A. P. H. J. Schenning, *Chem. Rev.* **2005**, *105*, 1491–546.

[39] F. Su, G. Chen, P. A. Korevaar, F. Pan, H. Liu, Z. Guo, A. P. H. J. Schenning, H. Zhang, J. Lin, Y. Jiang, *Angew. Chem. Int. Ed. Engl.* **2019**, *58*, 15273–15277.

[40] L. Yang, P. Langer, E. S. Davies, M. Baldoni, K. Wickham, N. A. Besley, E. Besley, N. R. Champness, *Chem. Sci.* **2019**, *10*, 3723–3732.

[41] C. Kaufmann, D. Bialas, M. Stolte, F. Würthner, *J. Am. Chem. Soc.* **2018**, *140*, 9986–9995.

[42] S. Samanta, D. Chaudhuri, *J. Phys. Chem. Lett.* **2017**, *8*, 3427–3432.

[43] Y. Hong, J. Kim, W. Kim, C. Kaufmann, H. Kim, F. Würthner, D. Kim, *J. Am. Chem. Soc.* **2020**, *142*, 7845–7857.

[44] R. Haldar, A. Mazel, M. Krstić, Q. Zhang, M. Jakoby, I. A. Howard, B. S. Richards, N. Jung, D. Jacquemin, S. Diring, W. Wenzel, F. Odobel, C. Wöll, *Nat. Commun.* **2019**, *10*, 2048.

[45] F. C. Spano, *Acc. Chem. Res.* **2010**, *43*, 429–439.

[46] R. E. Cook, B. T. Phelan, R. J. Kamire, M. B. Majewski, R. M. Young, M. R. Wasielewski, *J. Phys. Chem. A* **2017**, *121*, 1607–1615.

[47] A. Schubert, V. Settels, W. Liu, F. Würthner, C. Meier, R. F. Fink, S. Schindlbeck, S. Lochbrunner, B. Engels, V. Engel, *J. Phys. Chem. Lett.* **2013**, *4*, 792–796.

[48] M. Deutsch, S. Wirsing, D. Kaiser, R. F. Fink, P. Tegeder, B. Engels, *J. Chem. Phys.* **2020**, *153*, 224104.

[49] S. A. Mewes, A. Dreuw, *Phys. Chem. Chem. Phys.* **2019**, *21*, 2843–2856.

[50] S. A. Mewes, F. Plasser, A. Krylov, A. Dreuw, *J. Chem. Theory Comput.* **2018**, *14*, 710–725.

[51] S. Jurinovich, L. Cupellini, C. A. Guido, B. Mennucci, *J. Comput. Chem.* **2018**, *39*, 279–286.

[52] C. Walter, V. Krämer, B. Engels, *Int. J. Quantum Chem.* **2017**, *117*, e25337.

[53] D. Accomasso, M. Persico, G. Granucci, *ChemPhotoChem* **2019**, *3*, 933–944.

[54] H. Tamura, *J. Phys. Chem. A* **2016**, *120*, 9341–9347.

[55] W. Liu, B. Lunkenheimer, V. Settels, B. Engels, R. F. Fink, A. Köhn, *J. Chem. Phys.* **2015**, *143*, 084106.

[56] A. Carreras, O. Uranga-Barandiaran, F. Castet, D. Casanova, *J. Chem. Theory Comput.* **2019**, *15*, 2320–2330.

[57] S. Shirai, S. Iwata, T. Tani, S. Inagaki, *J. Phys. Chem. A* **2011**, *115*, 7687–7699.

[58] A. A. M. H. M. Darghouth, G. C. Correa, S. Juillard, M. E. Casida, A. Humeniuk, R. Mitrić, *J. Chem. Phys.* **2018**, *149*, 134111.

[59] D. Casanova, *Int. J. Quantum Chem.* **2015**, *115*, 442–452.

[60] M. Zubiria-Ulacia, J. M. Matxain, D. Casanova, *Phys. Chem. Chem. Phys.* **2020**, *22*, 15908–15918.

[61] Y. Mao, A. Montoya-Castillo, T. E. Markland, *J. Chem. Phys.* **2019**, *151*, 164114.

[62] Y. Mao, A. Montoya-Castillo, T. E. Markland, *J. Chem. Phys.* **2020**, *153*, 244111.

[63] M. Abe, *Chem. Rev.* **2013**, *113*, 7011–7088.

[64] J. Wu, *Diradicaloids*, Jenny Stanford Publishing, New York, **2022**.

[65] X. Hu, W. Wang, D. Wang, Y. Zheng, *J. Mater. Chem. C* **2018**, *6*, 11232–11242.

[66] S. Di Motta, F. Negri, D. Fazzi, C. Castiglioni, E. V. Canesi, *J. Phys. Chem. Lett.* **2010**, *1*, 3334–3339.

[67] S. Canola, J. Casado, F. Negri, *Phys. Chem. Chem. Phys.* **2018**, *20*, 24227–24238.

[68] H. Koike, M. Chikamatsu, R. Azumi, J. Tsutsumi, K. Ogawa, W. Yamane, T. Nishiuchi, T. Kubo, T. Hasegawa, K. Kanai, *Adv. Funct. Mater.* **2016**, *26*, 277–283.

[69] S. Mori, S. Moles Quintero, N. Tabaka, R. Kishi, R. González Núñez, A. Harbuzaru, R. Ponce Ortiz, J. Marín-Beloqui, S. Suzuki, C. Kitamura, C. J. Gómez-García, Y. Dai, F. Negri, M. Nakano, S. Kato, J. Casado, *Angew. Chemie Int. Ed.* **2022**, *61*, DOI 10.1002/anie.202206680.

[70] S. Lukman, J. M. Richter, L. Yang, P. Hu, J. Wu, N. C. Greenham, A. J. Musser, *J. Am. Chem. Soc.* **2017**, *139*, 18376–18385.

[71] J. Messelberger, A. Grünwald, P. Pinter, M. M. Hansmann, D. Munz, *Chem. Sci.* **2018**, *9*, 6107–6117.

[72] T. Minami, S. Ito, M. Nakano, *J. Phys. Chem. Lett.* **2012**, *3*, 2719–2723.

[73] C. K. Yong, A. J. Musser, S. L. Bayliss, S. Lukman, H. Tamura, O. Bubnova, R. K. Hallani, A. Meneau, R. Resel, M. Maruyama, S. Hotta, L. M. Herz, D. Beljonne, J. E. Anthony, J. Clark, H. Sirringhaus, *Nat. Commun.* **2017**, *8*, DOI 10.1038/ncomms15953.

[74] M. Nakano, Excitation Energies and Properties of Open-Shell Singlet Molecules, Springer International Publishing, Cham, **2014**.

[75] M. B. Smith, J. Michl, *Chem. Rev.* **2010**, *110*, 6891–6936.

[76] M. Nakano, *Chem. Rec.* **2017**, *17*, 27–62.

[77] M. Nakano, B. Champagne, *J. Phys. Chem. Lett.* **2015**, *6*, 3236–3256.

[78] J. Camarero, E. Coronado, *J. Mater. Chem.* **2009**, *19*, 1678–1684.

[79] Z. X. X. Chen, Y. Li, F. Huang, *Chem* **2021**, *7*, 288–332.

[80] S. Muhammad, M. Nakano, A. G. Al-Sehemi, Y. Kitagawa, A. Irfan, A. R. Chaudhry, R. Kishi, S. Ito, K. Yoneda, K. Fukuda, *Nanoscale* **2016**, *8*, 17998–18020.

[81] H. Angliker, E. Rommel, J. Wirz, *Chem. Phys. Lett.* **1982**, *87*, 208–212.

[82] J. Michl, V. Bonačić-Koutecký, *Tetrahedron* **1988**, *44*, 7559–7585.

[83] J. P. Malrieu, R. Caballol, C. J. Calzado, C. De Graaf, N. Guihe, C. De Graaf, N. Guihéry, *Chem. Rev.* **2014**, *114*, 429–492.

[84] L. Salem, C. Rowland, **1972**, *11*, 92–111.

[85] B. Vlasta, J. Koutecky, J. Michl, **1987**, *26*, 170–189.

[86] T. Stuyver, B. Chen, T. Zeng, P. Geerlings, F. De Proft, R. Hoffmann, *Chem. Rev.* **2019**, *119*, 11291–11351.

[87] G. David, N. Ferré, G. Trinquier, J.-P. Malrieu, *J. Chem. Phys.* **2020**, *153*, 054120.

[88] Y. Dai, L. Bonometti, J. L. Zafra, K. Takimiya, J. Casado, F. Negri, *Chemistry (Easton).* **2022**, *4*, 329–344.

[89] Y. Shen, G. Xue, Y. Dai, S. M. Quintero, H. Chen, D. Wang, F. Miao, F. Negri, Y. Zheng, J. Casado, *Nat. Commun.* **2021**, *12*, 6262.

[90] F. Negri, S. Canola, Y. Dai, in *Diradicaloids* (Ed.: J. Wu), Jenny Stanford Publishing, New York, **2022**, pp. 145–179.

[91] S. Canola, Y. Dai, F. Negri, *Computation* **2019**, *7*, 1–13.

[92] G. Ricci, S. Canola, Y. Dai, D. Fazzi, F. Negri, *Molecules* **2021**, *26*, DOI 10.3390/molecules26144119.

[93] S. Canola, G. Bagnara, Y. Dai, G. Ricci, A. Calzolari, F. Negri, *J. Chem. Phys.* **2021**, *154*, 1–37.

[94] Y. Dai, M. Zubiria-Ulacia, D. Casanova, F. Negri, *Computation* **2022**, *10*, 18.

[95] Y. Dai, A. Calzolari, M. Zubiria-Ulacia, D. Casanova, F. Negri, *Molecules* **2023**, *28*, DOI 10.3390/molecules28010119.

[96] C. Christopher J., *Essentials of Computational Chemistry*, John Wiley & Sons, Ltd, Chichester, UK, **2004**.

[97] W. Kohn, L. J. Sham, *Phys. Rev.* **1965**, *140*, A1133–A1138.

[98] A. Dreuw, M. Head-Gordon, *Chem. Rev.* **2005**, *105*, 4009–4037.

[99] E. Runge, E. K. U. Gross, *Phys. Rev. Lett.* **1984**, *52*, 997–1000.

[100] M. E. CASIDA, **1995**, 155–192.

[101] S. Hirata, M. Head-Gordon, *Chem. Phys. Lett.* **1999**, *314*, 291–299.

[102] A. I. Krylov, *Chem. Phys. Lett.* **2001**, *350*, 522–530.

[103] A. I. Krylov, *Chem. Phys. Lett.* **2001**, *338*, 375–384.

[104] Y. Shao, M. Head-Gordon, A. I. Krylov, *J. Chem. Phys.* **2003**, *118*, 4807–4818.

[105] Y. A. Bernard, Y. Shao, A. I. Krylov, *J. Chem. Phys.* **2012**, *136*, DOI 10.1063/1.4714499.

[106] Z. Rinkevicius, O. Vahtras, H. Ågren, *J. Chem. Phys.* **2010**, *133*, DOI 10.1063/1.3479401.

[107] S. Grimme, M. Waletzke, *J. Chem. Phys.* **1999**, *111*, 5645–5655.

[108] C. M. Marian, A. Heil, M. Kleinschmidt, *WIREs Comput. Mol. Sci.* **2019**, *9*, 1–31.

[109] C. M. Marian, N. Gilka, *J. Chem. Theory Comput.* **2008**, *4*, 1501–1515.

[110] K. Andersson, P. Å. Malmqvist, B. O. Roos, A. J. Sadlej, K. Wolinski, *J. Phys. Chem.* **1990**, *94*, 5483–5488.

[111] K. Andersson, P. Å. Malmqvist, B. O. Roos, *J. Chem. Phys.* **1992**, *96*, 1218–1226.

[112] C. Angeli, R. Cimiraglia, S. Evangelisti, T. Leininger, J. P. Malrieu, *J. Chem. Phys.* **2001**, *114*, 10252.

[113] C. Angeli, R. Cimiraglia, J. P. Malrieu, *Chem. Phys. Lett.* **2001**, *350*, 297–305.

[114] C. Angeli, R. Cimiraglia, J. P. Malrieu, *J. Chem. Phys.* **2002**, *117*, 9138–9153.

[115] R. Sarkar, P. F. Loos, M. Boggio-Pasqua, D. Jacquemin, *J. Chem. Theory Comput.* **2022**, *18*, 2418–2436.

[116] M. J. Frisch, G. W. Trucks, H. B. Schlegel, G. E. Scuseria, M. A. Robb, J. R. Cheeseman, G. Scalmani, V. Barone, G. A. Petersson, H. Nakatsuji, X. Li, M. Caricato, A. V Marenich, J. Bloino, B. G. Janesko, R. Gomperts, B. Mennucci, H. P. Hratchian, J. . Ortiz, A. F. Izmaylov, J. L. Sonnenberg, D. Williams-Young, F. Ding, F. Lipparini, F. Egidi, J. Goings, B. Peng, A. Petrone, T. Henderson, D. Ranasinghe, V. G. Zakrzewski, J. Gao, N. Rega, G. Zheng, W. Liang, M. Hada, M. Ehara, K. Toyota, R. Fukuda, J. Hasegawa, M. Ishida, T. Nakajima, Y. Honda, O. Kitao, H. Nakai, T. Vreven, K. Throssell, J. A. Montgomery, Jr., J. E. Peralta, F. Ogliaro, M. J. Bearpark, J. J. Heyd, E. N. Brothers, K. N. Kudin, V. N. Staroverov, T. A. Keith, R. Kobayashi, J. Normand, K. Raghavachari, A. P. Rendell, J. C. Burant, S. S. Iyengar, J. Tomasi, M. Cossi, J. M. Millam, M. Klene, C. Adamo, R. Cammi, J. W. Ochterski, R. L. Martin, K. Morokuma, O. Farkas, J. B. Foresman, D. J. Fox, *Gaussian, Inc., Wallingford CT,* **2016**.

[117] F. Neese, Wiley Interdiscip. Rev. Comput. Mol. Sci. **2012**, 2, 73–78.

[118] F. Neese, F. Wennmohs, U. Becker, C. Riplinger, *J. Chem. Phys.* **2020**, *152*, 224108.

[119] M. W. Schmidt, K. K. Baldridge, J. A. Boatz, S. T. Elbert, M. S. Gordon, J. H. Jensen, S. Koseki, N. Matsunaga, K. A. Nguyen, S. Su, T. L. Windus, M. Dupuis, J. A. Montgomery, *J. Comput. Chem.* **1993**, *14*, 1347–1363.

[120] G. P. Moss, P. A. S. Smith, D. Tavernier, *Pure Appl. Chem.* **1995**, *67*, 1307–1375.

[121] S. E. Braslavsky, *Pure Appl. Chem.* **2007**, *79*, 293–465.

[122] E. Clar, in *Mob. Source Emiss. Incl. Policyclic Org. Species*, Springer Netherlands, Dordrecht, **1983**, pp. 49–58.

[123] J. E. Barker, J. J. Dressler, A. Cárdenas Valdivia, R. Kishi, E. T. Strand, L. N. Zakharov, S. N. Macmillan, C. J. Gómez-García, M. Nakano, J. Casado, M. M. Haley, *J. Am. Chem. Soc.* **2020**, *142*, 1548–1555.

[124] C. Zhang, S. Medina Rivero, W. Liu, D. Casanova, X. Zhu, J. Casado, *Angew. Chem. Int. Ed.* **2019**, *58*, 11291–11295.

[125] Z. Sun, J. Wu, *J. Mater. Chem.* **2012**, *22*, 4151–4160.

[126] J. J. Dressler, M. M. Haley, *J. Phys. Org. Chem.* **2020**, *33*, 1–13.

[127] R. Nieman, N. J. Silva, A. J. A. Aquino, M. M. Haley, H. Lischka, *J. Org. Chem.* **2020**, *85*, 3664–3675.

[128] G. E. Rudebusch, J. L. Zafra, K. Jorner, K. Fukuda, J. L. Marshall, I. Arrechea-Marcos, G. L. Espejo, R. Ponce Ortiz, C. J. Gómez-García, L. N. Zakharov, M. Nakano, H. Ottosson, J. Casado, M. M. Haley, *Nat. Chem.* **2016**, *8*, 753–759.

[129] T. Y. Gopalakrishna, W. Zeng, X. Lu, J. Wu, *Chem. Commun.* **2018**, *54*, 2186–2199.

[130] T. Takahashi, K.-I. I. Matsuoka, K. Takimiya, T. Otsubo, Y. Aso, *J. Am. Chem. Soc.* **2005**, *127*, 8928–8929.

[131] R. Ponce Ortiz, J. Casado, S. González Rodríguez, V. Hernández, J. T. López Navarrete,

P. M. Viruela, E. Ortí, K. Takimiya, T. Otsubo, R. P. Ortiz, J. Casado, S. R. González, V. Hernández, J. T. López Navarrete, P. M. Viruela, E. Ortí, K. Takimiya, T. Otsubo, *Chem. - A Eur. J.* **2010**, *16*, 470–484.

[132] D. Fazzi, E. V. Canesi, F. Negri, C. Bertarelli, C. Castiglioni, *ChemPhysChem* **2010**, *11*, 3685–3695.

[133] X. Zhu, H. Tsuji, K. Nakabayashi, S. I. Ohkoshi, E. Nakamura, *J. Am. Chem. Soc.* **2011**, *133*, 16342–16345.

[134] K. Kamada, K. Ohta, A. Shimizu, T. Kubo, R. Kishi, H. Takahashi, E. Botek, B. Champagne, M. Nakano, *J. Phys. Chem. Lett.* **2010**, *1*, 937–940.

[135] A. Konishi, Y. Hirao, K. Matsumoto, H. Kurata, R. Kishi, Y. Shigeta, M. Nakano, K. Tokunaga, K. Kamada, T. Kubo, *J. Am. Chem. Soc.* **2013**, *135*, 1430–1437.

[136] J. Liu, P. Ravat, M. Wagner, M. Baumgarten, X. Feng, K. Müllen, *Angew. Chemie* **2015**, *127*, 12619–12623.

[137] J. Ma, J. Liu, M. Baumgarten, Y. Fu, Y. Z. Tan, K. S. Schellhammer, F. Ortmann, G. Cuniberti, H. Komber, R. Berger, K. Müllen, X. Feng, *Angew. Chem. Int. Ed.* **2017**, *56*, 3280–3284.

[138] W. Zeng, Z. Sun, T. S. Herng, T. P. Gonçalves, T. Y. Gopalakrishna, K. W. Huang, J. Ding, J. Wu, *Angew. Chem. Int. Ed.* **2016**, *55*, 8615–8619.

[139] P. Ravat, T. Šolomek, M. Rickhaus, D. Häussinger, M. Neuburger, M. Baumgarten, M. Juríček, *Angew. Chem. Int. Ed.* **2016**, *55*, 1183–1186.

[140] P. Hu, S. Lee, T. S. Herng, N. Aratani, T. P. Gonçalves, Q. Qi, X. Shi, H. Yamada, K. W. Huang, J. Ding, D. Kim, J. Wu, *J. Am. Chem. Soc.* **2016**, *138*, 1065–1077.

[141] J. Li, X. Qiao, Y. Xiong, H. Li, D. Zhu, *Chem. Mater.* **2014**, *26*, 5782–5788.

[142] D. Xia, A. Keerthi, C. An, M. Baumgarten, *Org. Chem. Front.* **2017**, *4*, 18–21.

[143] Z. Lin, L. Chen, Q. Xu, G. Shao, Z. Zeng, D. Wu, J. Xia, *Org. Lett.* **2020**, *22*, 2553–2558.

[144] W. Zeng, Y. Hong, S. Medina Rivero, J. Kim, J. L. Zafra, H. Phan, T. Y. Gopalakrishna, T. S. Herng, J. Ding, J. Casado, D. Kim, J. Wu, *Chem. - A Eur. J.* **2018**, *24*, 4944–4951.

[145] Y. Tobe, *Top. Curr. Chem.* **2018**, *376*, DOI 10.1007/s41061-018-0189-0.

[146] R. Q. Lu, S. Wu, L. L. Yang, W. Bin Gao, H. Qu, X. Y. Wang, J. B. Chen, C. Tang, H. Y. Shi, X. Y. Cao, *Angew. Chem. Int. Ed.* **2019**, *58*, 7600–7605.

[147] H. Hayashi, J. E. Barker, A. Cárdenas Valdivia, R. Kishi, S. N. Macmillan, C. J. Gómez-García, H. Miyauchi, Y. Nakamura, M. Nakano, S. I. Kato, M. M. Haley, J. Casado, *J. Am. Chem. Soc.* **2020**, *142*, 20444–20455.

[148] W. Zeng, H. Phan, T. S. Herng, T. Y. Gopalakrishna, N. Aratani, Z. Zeng, H. Yamada, J. Ding, J. Wu, *Chem* **2017**, *2*, 81–92.

[149] W. Zeng, Q. Qi, J. Wu, *European J. Org. Chem.* **2018**, *2018*, 7–17.

[150] Z. Zeng, M. Ishida, J. L. Zafra, X. Zhu, Y. M. Sung, N. Bao, R. D. Webster, B. S. Lee, R. W. Li, W. Zeng, Y. Li, C. Chi, J. T. L. Navarrete, J. Ding, J. Casado, D. Kim, J. Wu, *J. Am. Chem. Soc.* **2013**, *135*, 6363–6371.

[151] Z. Zeng, S. Lee, J. L. Zafra, M. Ishida, X. Zhu, Z. Sun, Y. Ni, R. D. Webster, R. W. Li, J. T. López Navarrete, C. Chi, J. Ding, J. Casado, D. Kim, J. Wu, *Angew. Chem. Int. Ed.* **2013**, *52*, 8561–8565.

[152] A. Szabo, N. L. Ostlund, in *Mod. Quantum Chem. Introd. to Adv. Electron. Struct.*

Theory, Dover Publications, Inc., New York, **1996**.

[153] K. Schulten, M. Karplus, *Chem. Phys. Lett.* **1972**, *14*, 305–309.

[154] J. Gu, W. Wu, D. Danovich, R. Hoffmann, Y. Tsuji, S. Shaik, *J. Am. Chem. Soc.* **2017**, *139*, 9302–9316.

[155] R. Einholz, T. Fang, R. Berger, P. Grüninger, A. Früh, T. Chassé, R. F. Fink, H. F. Bettinger, *J. Am. Chem. Soc.* **2017**, *139*, 4435–4442.

[156] K. Yamaguchi, *Chem. Phys. Lett.* **1975**, *33*, 330–335.

[157] S. Grimme, A. Hansen, *Angew. Chem. Int. Ed.* **2015**, *54*, 12308–12313.

[158] C. A. Bauer, A. Hansen, S. Grimme, *Chem. - A Eur. J.* **2017**, *23*, 6150–6164.

[159] R. Ponce Ortiz, J. Casado, V. Hernández, J. T. López Navarrete, E. Ortí, P. M. Viruela, B. Milián, S. Hotta, G. Zotti, S. Zecchin, B. Vercelli, *Adv. Funct. Mater.* **2006**, *16*, 531–536.

[160] J. Casado, L. L. Miller, K. R. Mann, T. M. Pappenfus, H. Higuchi, E. Ortí, B. Milián, R. Pou-Amérigo, V. Hernández, J. T. López Navarrete, *J. Am. Chem. Soc.* **2002**, *124*, 12380–12388.

[161] J. Casado, V. Hernández, J. T. López Navarrete, *Chem. Rec.* **2015**, *15*, 1110–1118.

[162] J. Casado, *Top. Curr. Chem.* **2017**, *375*, 73.

[163] R. Ponce Ortiz, J. Casado, V. Hernández, J. T. López Navarrete, P. M. Viruela, E. Ortí, K. Takimiya, T. Otsubo, *Angew. Chem. Int. Ed.* **2007**, *46*, 9057–9061.

[164] J. Casado, R. Ponce Ortiz, J. T. López Navarrete, *Chem. Soc. Rev.* **2012**, *41*, 5672–5686.

[165] J. Casado, J. T. López Navarrete, *Chem. Rec.* **2011**, *11*, 45–53.

[166] C. Castiglioni, J. T. López Navarrete, G. Zerbi, M. Gussoni, *Solid State Commun.* **1988**, *65*, 625–630.

[167] G. Zerbi, C. Castiglioni, J. T. López Navarrete, T. Bogang, M. Gussoni, *Synth. Met.* **1989**, *28*, D359–D368.

[168] C. Castiglioni, M. Tommasini, G. Zerbi, *Philos. Trans. R. Soc. A Math. Phys. Eng. Sci.* **2004**, *362*, 2425–2459.

[169] F. Negri, M. Z. Zgierski, *J. Chem. Phys.* **1994**, *100*, 2571–2587.

[170] S. Medina Rivero, S. Canola, W. Zeng, F. J. Ramírez, J. L. Zafra, J. Wu, F. Negri, J. Casado, *Phys. Chem. Chem. Phys.* **2019**, *21*, 7281–7287.

[171] R. C. González-Cano, S. Di Motta, X. Zhu, J. T. López Navarrete, H. Tsuji, E. Nakamura, F. Negri, J. Casado, *J. Phys. Chem. C* **2017**, *121*, 23141–23148.

[172] A. C. Albrecht, *J. Chem. Phys.* **1961**, *34*, 1476–1484.

[173] J. Guthmuller, *J. Chem. Phys.* **2016**, *144*, 064106.

[174] J. Guthmuller, *J. Chem. Phys.* **2018**, *148*, 124107.

[175] T. M. Pappenfus, R. J. Chesterfield, C. D. Frisbie, K. R. Mann, J. Casado, J. D. Raff, L. L. Miller, *J. Am. Chem. Soc.* **2002**, *124*, 4184–4185.

[176] D. E. Janzen, M. W. Burand, P. C. Ewbank, T. M. Pappenfus, H. Higuchi, D. A. da Silva Filho, V. G. Young, J.-L. Brédas, K. R. Mann, *J. Am. Chem. Soc.* **2004**, *126*, 15295–15308.

[177] Y. Kunugi, K. Takimiya, Y. Toyoshima, K. Yamashita, Y. Aso, T. Otsubo, *J. Mater. Chem.* **2004**, *14*, 1367.

[178] S. Handa, E. Miyazaki, K. Takimiya, Y. Kunugi, *J. Am. Chem. Soc.* **2007**, *129*, 11684–11685.

[179] J. C. Ribierre, T. Fujihara, S. Watanabe, M. Matsumoto, T. Muto, A. Nakao, T. Aoyama, *Adv. Mater.* **2010**, *22*, 1722–1726.

[180] K. Yamamoto, Y. Ie, M. Nitani, N. Tohnai, F. Kakiuchi, K. Zhang, W. Pisula, K. Asadi, P. W. M. Blom, Y. Aso, *J. Mater. Chem. C* **2018**, *6*, 7493–7500.

[181] K. Yamamoto, S. Kato, H. Zajaczkowska, T. Marszalek, P. W. M. Blom, Y. Ie, *J. Mater. Chem. C* **2020**, *8*, 3580–3588.

[182] S. Moles Quintero, J. L. Zafra, K. Yamamoto, Y. Aso, Y. Ie, J. Casado, *J. Mater. Chem. C* **2021**, *9*, 10727–10740.

[183] Y. Suzuki, E. Miyazaki, K. Takimiya, *J. Am. Chem. Soc.* **2010**, *132*, 10453–10466.

[184] F. Negri, G. Orlandi, in *Theor. Comput. Chem.*, **2005**, pp. 129–169.

[185] F. Negri, E. Di Donato, M. Tommasini, C. Castiglioni, G. Zerbi, K. Müllen, *J. Chem. Phys.* **2004**, *120*, 11889–11900.

[186] C. Castiglioni, C. Mapelli, F. Negri, G. Zerbi, *J. Chem. Phys.* **2001**, *114*, 963–974.

[187] M. Rigolio, C. Castiglioni, G. Zerbi, F. Negri, *J. Mol. Struct.* **2001**, *563–564*, 79–87.

[188] C. Castiglioni, F. Negri, M. Rigolio, G. Zerbi, *J. Chem. Phys.* **2001**, *115*, 3769–3778.

[189] F. Negri, C. Castiglioni, M. Tommasini, G. Zerbi, *J. Phys. Chem. A* **2002**, *106*, 3306–3317.

[190] M. Malagoli, V. Coropceanu, D. A. Da Silva Filho, J. L. Brédas, *J. Chem. Phys.* **2004**, *120*, 7490–7496.

[191] F. Negri, M. Z. Zgierski, *J. Chem. Phys.* **1992**, *97*, 7124–7136.

[192] E. Di Donato, D. Vanzo, M. Semeraro, A. Credi, F. Negri, *J. Phys. Chem. A* **2009**, *113*, 6504–6510.

[193] J. Guthmuller, B. Champagne, *J. Phys. Chem. A* **2008**, *112*, 3215–23.

[194] X. Yin, J. Z. Low, K. J. Fallon, D. W. Paley, L. M. Campos, *Chem. Sci.* **2019**, *10*, 10733–10739.

[195] A. Kawamura, J. Xie, J. N. Boyn, K. A. Jesse, A. J. McNeece, E. A. Hill, K. A. Collins, J. A. Valdez-Moreira, A. S. Filatov, J. W. Kurutz, D. A. Mazziotti, J. S. Anderson, *J. Am. Chem. Soc.* **2020**, *142*, 17670–17680.

[196] R. Zhang, J. P. Peterson, L. J. Fischer, A. Ellern, A. H. Winter, *J. Am. Chem. Soc.* **2018**, *140*, 14308–14313.

[197] Y. Su, X. Wang, L. Wang, Z. Zhang, X. Wang, Y. Song, P. P. Power, *Chem. Sci.* **2016**, *7*, 6514–6518.

[198] J. Harada, K. Ogawa, *Chem. Soc. Rev.* **2009**, *38*, 2244–2252.

[199] W. A, *Nature* **1976**, *260*, 679.

[200] I. Schapiro, O. Weingart, V. Buss, *J. Am. Chem. Soc.* **2009**, *131*, 16–17.

[201] R. Kamiński, K. N. Jarzembska, S. Domagała, *J. Appl. Crystallogr.* **2013**, *46*, 540–543.

[202] S. Dapprich, I. Komáromi, K. S. Byun, K. Morokuma, M. J. Frisch, *J. Mol. Struct. THEOCHEM* **1999**, *461–462*, 1–21.

[203] A. K. Rappé, L. M. Bormann-Rochotte, D. C. Wiser, J. R. Hart, M. A. Pietsch, C. J. Casewit, W. M. Skiff, *Mol. Phys.* **2007**, *105*, 301–324.

[204] S. L. Mayo, B. D. Olafson, W. A. Goddard, *J. Phys. Chem.* **1990**, *94*, 8897–8909.

[205] S. Medina Rivero, P. Mayorga Burrezo, M. E. Sandoval-Salinas, T. Li, F. J. Ramírez, D. Casanova, X. Wang, J. Casado, *ChemPhysChem* **2018**, *19*, 1465–1470.

[206] W. Zeng, T. Y. Gopalakrishna, H. Phan, T. Tanaka, T. S. Herng, J. Ding, A. Osuka, J. Wu, *J. Am. Chem. Soc.* **2018**, *140*, 14054–14058.

[207] R. Huang, H. Phan, T. S. Herng, P. Hu, W. Zeng, S. Q. Dong, S. Das, Y. Shen, J. Ding, D. Casanova, J. Wu, *J. Am. Chem. Soc.* **2016**, *138*, 10323–10330.

[208] Y. Ni, T. Y. Gopalakrishna, H. Phan, T. S. Herng, S. Wu, Y. Han, J. Ding, J. Wu, *Angew. Chem. Int. Ed.* **2018**, *57*, 9697–9701.

[209] M. A. Majewski, P. J. Chmielewski, A. Chien, Y. Hong, T. Lis, M. Witwicki, D. Kim, P. M. Zimmerman, M. Stępień, *Chem. Sci.* **2019**, *10*, 3413–3420.

[210] H. Qian, F. Negri, C. Wang, Z. Wang, *J. Am. Chem. Soc.* **2008**, *130*, 17970–17976.

[211] Y. Li, J. Gao, S. Di Motta, F. Negri, Z. Wang, *J. Am. Chem. Soc.* **2010**, *132*, 4208–4213.

[212] W. Yue, A. Lv, J. Gao, W. Jiang, L. Hao, C. Li, Y. Li, L. E. Polander, S. Barlow, W. Hu, S. Di Motta, F. Negri, S. R. Marder, Z. Wang, *J. Am. Chem. Soc.* **2012**, *134*, 5770–5773.

[213] A. S. Menon, L. Radom, *J. Phys. Chem. A* **2008**, *112*, 13225–13230.

[214] V. Postils, F. Ruipérez, D. Casanova, *J. Chem. Theory Comput.* **2021**, *17*, 5825–5838.

[215] I. Badía-Domínguez, S. Canola, V. Hernández Jolín, J. T. López Navarrete, J. C. Sancho-García, F. Negri, M. C. Ruiz Delgado, *J. Phys. Chem. Lett.* **2022**, *13*, 6003–6010.

[216] A. Omist, G. Ricci, A. Derradji, A. J. Pérez-Jiménez, E. San-Fabián, Y. Olivier, J. C. Sancho-García, *Phys. Chem. Chem. Phys.* **2021**, *23*, 24016–24028.

[217] A. Pérez-Guardiola, M. E. Sandoval-Salinas, D. Casanova, E. San-Fabián, A. J. Pérez-Jiménez, J. C. Sancho-García, *Phys. Chem. Chem. Phys.* **2018**, *20*, 7112–7124.

[218] Z. Chen, W. Li, M. A. Sabuj, Y. Li, W. Zhu, M. Zeng, C. S. Sarap, M. M. Huda, X. Qiao, X. Peng, D. Ma, Y. Ma, N. Rai, F. Huang, *Nat. Commun.* **2021**, *12*, 1–10.

[219] M. E. Sandoval-Salinas, A. Carreras, D. Casanova, *Phys. Chem. Chem. Phys.* **2019**, *21*, 9069–9076.

[220] C.-C. Chen, J.-D. Chai, *Nanomaterials* **2022**, *12*, 3943.

[221] X. Zhang, J. M. Herbert, *J. Chem. Phys.* **2015**, *143*, DOI 10.1063/1.4937571.

[222] J. Thiele, H. Balhorn, *Berichte der Dtsch. Chem. Gesellschaft* **1904**, *37*, 1463–1470.

[223] L. K. Montgomery, J. C. Huffman, E. A. Jurczak, M. P. Grendze, *J. Am. Chem. Soc.* **1986**, *108*, 6004–6011.

[224] M. Ballester, J. Riera, J. Castafier, C. Badía, J. M. Monsó, *J. Am. Chem. Soc.* **1971**, *93*, 2215–2225.

[225] J. Castañer, J. Riera, *J. Org. Chem.* **1991**, *56*, 5445–5448.

[226] I. Ratera, J. Veciana, *Chem. Soc. Rev.* **2012**, *41*, 303–349.

[227] H. Guo, Q. Peng, X. K. Chen, Q. Gu, S. Dong, E. W. Evans, A. J. Gillett, X. Ai, M. Zhang, D. Credgington, V. Coropceanu, R. H. Friend, J. L. Brédas, F. Li, *Nat. Mater.* **2019**, *18*, 977–984.

[228] A. Abdurahman, T. J. H. Hele, Q. Gu, J. Zhang, Q. Peng, M. Zhang, R. H. Friend, F. Li, E. W. Evans, *Nat. Mater.* **2020**, *19*, 1224–1229.

[229] V. M. Domingo, J. Castañer, J. Riera, E. Brillas, E. Molins, B. Martinez, B. Knight, *Chem. Mater.* **1997**, *9*, 1620–1629.

[230] J. R. Lakowicz, *Principles of Fluorescence Spectroscopy*, Springer US, Boston, MA, **2006**.

[231] S. Grimme, J. Antony, S. Ehrlich, H. Krieg, *J. Chem. Phys.* **2010**, *132*, DOI 10.1063/1.3382344.

[232] S. Grimme, S. Ehrlich, L. Goerigk, *J. Comput. Chem.* **2011**, *32*, 1456–1465.

[233] A. Schäfer, H. Horn, R. Ahlrichs, *J. Chem. Phys.* **1998**, *97*, 2571.

[234] F. Weigend, *J. Comput. Chem.* **2008**, *29*, 167–175.

[235] V. Balzani, P. Ceroni, A. Juris, *Photochemistry and Photophysics. Concepts, Research, Applications*, Wiley, Weinheim, Germany, **2014**.

[236] J. Koutecky, V. Bonačič-Koutecký, J. Čížek, D. Döhnert, *Int. J. Quantum Chem.* **1978**, *14*, 357–369.

[237] V. Bonačić-Koutecký, P. Bruckmann, P. Hiberty, J. Koutecký, C. Leforestier, L. Salem, J. Kouteckj, C. Lrforestier, *Angew. Chem. Int. Ed. Engl.* **1975**, *14*, 575–576.

[238] B. R. Brooks, H. F. Henry, *J. Am. Chem. Soc.* **1979**, *101*, 307–311.

[239] M. Filatov, S. Lee, C. H. Choi, *J. Chem. Theory Comput.* **2021**, *17*, 5123–5139.

[240] C. E. Wulfman, S. Kumei, *Science (80-.).* **1971**, *172*, 1061.

[241] Y. Torii, Y. Niioka, K. Syundo, D. Kashiwagi, T. Iimori, *J. Lumin.* **2022**, *241*, 118503.

[242] I. B. Bersuker, *Chem. Rev.* **2021**, *121*, 1463–1512.

[243] M. Chikamatsu, T. Mikami, J. Chisaka, Y. Yoshida, R. Azumi, K. Yase, A. Shimizu, T. Kubo, Y. Morita, K. Nakasuji, *Appl. Phys. Lett.* **2007**, *91*, DOI 10.1063/1.2766696.

[244] T. Jousselin-Oba, M. Mamada, A. Okazawa, J. Marrot, T. Ishida, C. Adachi, A. Yassar, M. Frigoli, *Chem. Sci.* **2020**, *11*, 12194–12205.

[245] R. J. Chesterfield, C. R. Newman, T. M. Pappenfus, P. C. Ewbank, M. H. Haukaas, K. R. Mann, L. L. Miller, C. D. Frisbie, *Adv. Mater.* **2003**, *15*, 1278–1282.

[246] R. A. Marcus, *J. Chem. Phys.* **1957**, *26*, 867–871.

[247] R. A. Marcus, *Angew. Chem. Int. Ed. Engl.* **1993**, *32*, 1111–1121.

[248] R. A. Marcus, N. Sutin, *Biochim. Biophys. Acta - Rev. Bioenerg.* **1985**, *811*, 265–322.

[249] E. Di Donato, R. P. Fornari, S. Di Motta, Y. Li, Z. Wang, F. Negri, *J. Phys. Chem. B* **2010**, *114*, 5327–5334.

[250] S. Di Motta, M. Siracusa, F. Negri, *J. Phys. Chem. C* **2011**, *115*, 20754–20764.

[251] S. Canola, F. Negri, *Phys. Chem. Chem. Phys.* **2014**, *16*, 21550–21558.

[252] P. F. Barbara, T. J. Meyer, M. A. Ratner, *J. Phys. Chem.* **1996**, *100*, 13148–13168.

[253] P. K. Samanta, D. Kim, V. Coropceanu, J. L. Brédas, *J. Am. Chem. Soc.* **2017**, *139*, 4042–4051.

[254] K. Schmidt, S. Brovelli, V. Coropceanu, D. Beljonne, J. Cornil, C. Bazzini, T. Caronna, R. Tubino, F. Meinardi, Z. Shuai, J. L. Brédas, *J. Phys. Chem. A* **2007**, *111*, 10490–10499.

[255] C. Schober, K. Reuter, H. Oberhofer, *J. Chem. Phys.* **2016**, *144*, 054103.

[256] S. Canola, C. Pecoraro, F. Negri, *Chem. Phys.* **2016**, *478*, 130–138.

[257] A. Troisi, G. Orlandi, *Chem. Phys. Lett.* **2001**, *344*, 509–518.

[258] K. Senthilkumar, F. C. Grozema, F. M. Bickelhaupt, L. D. A. Siebbeles, *J. Chem. Phys.* **2003**, *119*, 9809–9817.

[259] J. E. Norton, J.-L. Brédas, *J. Chem. Phys.* **2008**, *128*, 034701.

[260] P. Löwdin, *J. Chem. Phys.* **1950**, *18*, 365–375.

[261] E. F. Valeev, V. Coropceanu, D. da Silva Filho, S. Salman, J.-L. Brédas, *J. Am. Chem. Soc.* **2006**, *128*, 9882–9886.

[262] N. G. Martinelli, Y. Olivier, S. Athanasopoulos, M.-C. Ruiz Delgado, K. R. Pigg, D. da Silva Filho, R. S. Sánchez-Carrera, E. Venuti, R. G. Della Valle, J.-L. Brédas, D. Beljonne, J. Cornil, *ChemPhysChem* **2009**, *10*, 2265–2273.

[263] Z. Shuai, H. Geng, W. Xu, Y. Liao, J.-M. André, *Chem. Soc. Rev.* **2014**, *43*, 2662.

[264] Y. Olivier, V. Lemaur, J. L. Brédas, J. Cornil, *J. Phys. Chem. A* **2006**, *110*, 6356–6364.

[265] M. Schrader, C. Körner, C. Elschner, D. Andrienko, *J. Mater. Chem.* **2012**, *22*, 22258–22264.

[266] B. Baumeier, O. Stenzel, C. Poelking, D. Andrienko, V. Schmidt, *Phys. Rev. B* **2012**, *86*, 184202.

[267] R. A. Marsh, C. Groves, N. C. Greenham, *J. Appl. Phys.* **2007**, *101*, 083509.

[268] B. Baumeier, F. May, C. Lennartz, D. Andrienko, *J. Mater. Chem.* **2012**, *22*, 10971.

[269] T. Higashino, T. Mori, *Phys. Chem. Chem. Phys.* **2022**, *24*, 9770–9806.

[270] T. Koopmans, *Physica* **1934**, *1*, 104–113.

[271] N. E. Gruhn, D. A. Da Silva Filho, T. G. Bill, M. Malagoli, V. Coropceanu, A. Kahn, J. L. Brédas, *J. Am. Chem. Soc.* **2002**, *124*, 7918–7919.

[272] D. T. Chase, B. D. Rose, S. P. McClintock, L. N. Zakharov, M. M. Haley, *Angew. Chem. Int. Ed.* **2011**, *50*, 1127–1130.

[273] J. J. Dressler, M. Teraoka, G. L. Espejo, R. Kishi, S. Takamuku, C. J. Gómez-García, L. N. Zakharov, M. Nakano, J. Casado, M. M. Haley, *Nat. Chem.* **2018**, *10*, 1134–1140.

[274] J. E. Barker, C. K. Frederickson, M. H. Jones, L. N. Zakharov, M. M. Haley, *Org. Lett.* **2017**, *19*, 5312–5315.

[275] J. J. Dressler, A. Cárdenas Valdivia, R. Kishi, G. E. Rudebusch, A. M. Ventura, B. E. Chastain, C. J. Gómez-García, L. N. Zakharov, M. Nakano, J. Casado, M. M. Haley, *Chem* **2020**, *6*, 1353–1368.

[276] G. E. Rudebusch, G. L. Espejo, J. L. Zafra, M. Pena-Alvarez, S. N. Spisak, K. Fukuda, Z. Wei, M. Nakano, M. A. Petrukhina, J. Casado, M. M. Haley, M. Peña-Alvarez, S. N. Spisak, K. Fukuda, Z. Wei, M. Nakano, M. A. Petrukhina, J. Casado, M. M. Haley, *J. Am. Chem. Soc.* **2016**, *138*, 12648–12654.

[277] X. Gao, C. Di, Y. Hu, X. Yang, H. Fan, F. Zhang, Y. Liu, H. Li, D. Zhu, *J. Am. Chem. Soc.* **2010**, *132*, 3697–3699.

[278] M. Nakano, I. Osaka, D. Hashizume, K. Takimiya, *Chem. Mater.* **2015**, *27*, 6418–6425.

[279] K. Takimiya, I. Osaka, *Chem. Rec.* **2015**, *15*, 175–188.

[280] H. Ran, L. Chen, X. Yang, J. Zhang, Z. Zhao, R. Han, X. Duan, J.-Y. Hu, *Dye. Pigment.* **2019**, *169*, 7–14.

[281] H. Ran, X. Duan, R. Zheng, F. Xie, L. Chen, Z. Zhao, R. Han, Z. Lei, J.-Y. Hu, *ACS Appl. Mater. Interfaces* **2020**, *12*, 23225–23235.

[282] W. Fan, C. Liu, Y. Li, Z. Wang, *Chem. Commun.* **2017**, *53*, 188–191.

[283] S. Canola, C. Graham, Á. J. Pérez-Jiménez, J.-C. Sancho-García, F. Negri, *Phys. Chem. Chem. Phys.* **2019**, *21*, 2057–2068.

[284] S. Fratini, D. Mayou, S. Ciuchi, *Adv. Funct. Mater.* **2016**, *26*, 2292–2315.

[285] A. Troisi, *Adv. Mater.* **2007**, *19*, 2000–2004.

[286] V. Coropceanu, R. S. Sánchez-Carrera, P. Paramonov, G. M. Day, J.-L. Brédas, *J. Phys. Chem. C* **2009**, *113*, 4679–4686.

[287] T. F. Harrelson, V. Dantanarayana, X. Xie, C. Koshnick, D. Nai, R. Fair, S. A. Nuñez, A. K. Thomas, T. L. Murrey, M. A. Hickner, J. K. Grey, J. E. Anthony, E. D. Gomez, A. Troisi, R. Faller, A. J. Moulé, *Mater. Horizons* **2019**, *6*, 182–191.

[288] Z. Tu, Y. Yi, V. Coropceanu, J.-L. Brédas, *J. Phys. Chem. C* **2018**, *122*, 44–49.

[289] J. E. Norton, J.-L. Brédas, *J. Am. Chem. Soc.* **2008**, *130*, 12377–12384.

[290] S. Giannini, A. Carof, M. Ellis, H. Yang, O. G. Ziogos, S. Ghosh, J. Blumberger, *Nat. Commun.* **2019**, *10*, 3843.

[291] L.-F. F. Ji, J.-X. X. Fan, S.-F. F. Zhang, A.-M. M. Ren, *Phys. Chem. Chem. Phys.* **2017**, *19*, 13978–13993.

[292] T. Nematiaram, A. Troisi, *Mater. Horizons* **2020**, *7*, 2922–2928.

[293] P. Gosar, I. Vilfan, *Mol. Phys.* **1970**, *18*, 49–61.

[294] R. W. Munn, R. Silbey, *J. Chem. Phys.* **1985**, *83*, 1854–1864.

[295] A. Girlando, L. Grisanti, M. Masino, A. Brillante, R. G. Della Valle, E. Venuti, *J. Chem. Phys.* **2011**, *135*, 084701.

[296] X. Xie, A. Santana-Bonilla, A. Troisi, *J. Chem. Theory Comput.* **2018**, *14*, 3752–3762.

[297] S. S. Skourtis, I. A. Balabin, T. Kawatsu, D. N. Beratan, *Proc. Natl. Acad. Sci.* **2005**, *102*, 3552–3557.

[298] G. Schweicher, G. D'Avino, M. T. Ruggiero, D. J. Harkin, K. Broch, D. Venkateshvaran, G. Liu, A. Richard, C. Ruzié, J. Armstrong, A. R. Kennedy, K. Shankland, K. Takimiya, Y. H. Geerts, J. A. Zeitler, S. Fratini, H. Sirringhaus, *Adv. Mater.* **2019**, *31*, 1902407.

[299] A. Troisi, G. Orlandi, *J. Phys. Chem. A* **2006**, *110*, 4065–4070.

[300] A. Troisi, G. Orlandi, J. E. Anthony, *Chem. Mater.* **2005**, *17*, 5024–5031.

[301] M. Kasha, H. R. Rawls, M. A. El-Bayoumi, *Pure Appl. Chem.* **1965**, *11*, 371–392.

[302] M. Kasha, *Radiat. Res.* **1963**, *20*, 55–70.

[303] A. S. Davydov, *Uspekhi Fiz. Nauk* **1964**, *82*, 393–448.

[304] W. Liu, S. Canola, A. Köhn, B. Engels, F. Negri, R. F. Fink, *J. Comput. Chem.* **2018**, *39*, 1979–1989.

[305] F. Plasser, *J. Chem. Phys.* **2020**, *152*, DOI 10.1063/1.5143076.

[306] C. Edmiston, K. Ruedenberg, *Rev. Mod. Phys.* **1963**, *35*, 457–464.

[307] S. F. Boys, *Rev. Mod. Phys.* **1960**, *32*, 296–299.

[308] C. J. Bardeen, *Annu. Rev. Phys. Chem.* **2014**, *65*, 127–148.

[309] P. Petelenz, *Chem. Phys. Lett.* **1977**, *47*, 603–605.

[310] J. R. Platt, *J. Chem. Phys.* **1949**, *17*, 484–495.

[311] D. Kim, *Bull. Korean Chem. Soc.* **2015**, *36*, 2284–2289.

[312] Å. Björck, *Linear Algebra Appl.* **1994**, *197–198*, 297–316.

[313] M. Nottoli, S. Jurinovich, L. Cupellini, A. T. Gardiner, R. Cogdell, B. Mennucci, *Photosynth. Res.* **2018**, *137*, 215–226.

[314] H. Yamagata, C. M. Pochas, F. C. Spano, *J. Phys. Chem. B* **2012**, *116*, 14494–14503.

[315] A. Szabo, N. Ostlund, Dover Publ. Inc., New York, 1996, 1st ed. **2018**.

[316] A. Oleson, T. Zhu, I. S. Dunn, D. Bialas, Y. Bai, W. Zhang, M. Dai, D. R. Reichman, R. Tempelaar, L. Huang, F. C. Spano, *J. Phys. Chem. C* **2019**, *123*, 20567–20578.

[317] M. Hecht, F. Würthner, *Acc. Chem. Res.* **2021**, *54*, 642–653.

[318] W. Liu, V. Settels, P. H. P. Harbach, A. Dreuw, R. F. Fink, B. Engels, *J. Comput. Chem.* **2011**, *32*, 1971–1981.

[319] V. Settels, W. Liu, J. Pflaum, R. F. Fink, B. Engels, *J. Comput. Chem.* **2012**, *33*, 1544–53.

[320] A. Hellweg, S. A. Grün, C. Hättig, *Phys. Chem. Chem. Phys.* **2008**, *10*, 4119.

[321] N. O. C. Winter, N. K. Graf, S. Leutwyler, C. Hättig, *Phys. Chem. Chem. Phys.* **2013**, *15*, 6623–6630.

[322] A. Dreuw, M. Wormit, *Wiley Interdiscip. Rev. Comput. Mol. Sci.* **2015**, *5*, 82–95.

[323] B. Shi, D. Nachtigallová, A. J. A. Aquino, F. B. C. Machado, H. Lischka, *Phys. Chem. Chem. Phys.* **2019**, *21*, 9077–9088.

[324] H. Fliegl, Z. You, C. Hsu, D. Sundholm, *J. Chinese Chem. Soc.* **2016**, *63*, 20–32.

[325] D. Bellinger, J. Pflaum, C. Brüning, V. Engel, B. Engels, *Phys. Chem. Chem. Phys.* **2017**, *19*, 2434–2448.

[326] B. Engels, V. Engel, *Phys. Chem. Chem. Phys.* **2017**, *19*, 12604–12619.

[327] A. Mukazhanova, W. Malone, H. Negrin-Yuvero, S. Fernandez-Alberti, S. Tretiak, S. Sharifzadeh, *J. Chem. Phys.* **2020**, *153*, 244117.

[328] D. A. Hartzler, L. V. Slipchenko, S. Savikhin, *J. Phys. Chem. A* **2018**, *122*, 6713–6723.

[329] Z.-Q. You, C.-P. Hsu, G. R. Fleming, *J. Chem. Phys.* **2006**, *124*, 044506.

[330] A. J. Gillett, A. Privitera, R. Dilmurat, A. Karki, D. Qian, A. Pershin, G. Londi, W. K. Myers, J. Lee, J. Yuan, S.-J. Ko, M. K. Riede, F. Gao, G. C. Bazan, A. Rao, T.-Q. Nguyen, D. Beljonne, R. H. Friend, *Nature* **2021**, *597*, 666–671.

[331] R. F. Fink, J. Seibt, V. Engel, M. Renz, M. Kaupp, S. Lochbrunner, H. M. Zhao, J. Pfister, F. Würthner, B. Engels, *J. Am. Chem. Soc.* **2008**, *130*, 12858–12859.

[332] N. J. Hestand, R. V. Kazantsev, A. S. Weingarten, L. C. Palmer, S. I. Stupp, F. C. Spano, *J. Am. Chem. Soc.* **2016**, *138*, 11762–11774.

[333] V. Stehr, B. Engels, C. Deibel, R. F. Fink, *J. Chem. Phys.* **2014**, *140*, 024503.

[334] L. A. Galán, J. M. Andrés Castán, C. Dalinot, P. S. Marqués, J. Galiana, P. Blanchard, C. Andraud, E. Dumont, O. Maury, C. Cabanetos, C. Monnereau, T. Le Bahers, *J. Phys. Chem. B* **2021**, *125*, 8572–8580.

[335] N. E. Lee, J. J. Zhou, L. A. Agapito, M. Bernardi, *Phys. Rev. B* **2018**, *97*, 1–8.

[336] A. Mohajeri, M. Farmani, *ACS Appl. Electron. Mater.* **2022**, *4*, 246–258.

[337] Y. Xu, P. Xu, D. Hu, Y. Ma, *Chem. Soc. Rev.* **2021**, DOI 10.1039/D0CS00391C.

[338] P. Yu, Y. Zhen, H. Dong, W. Hu, *Chem* **2019**, *5*, 2814–2853.

[339] C. Kaufmann, W. Kim, A. Nowak-Król, Y. Hong, D. Kim, F. Würthner, *J. Am. Chem. Soc.* **2018**, *140*, 4253–4258.

[340] M. Parac, S. Grimme, *Chem. Phys.* **2003**, *292*, 11–21.

[341] B. M. Wong, T. H. Hsieh, *J. Chem. Theory Comput.* **2010**, *6*, 3704–3712.

[342] F. Bettanin, L. F. A. Ferrão, M. Pinheiro, A. J. A. Aquino, H. Lischka, F. B. C. Machado, D. Nachtigallova, *J. Chem. Theory Comput.* **2017**, *13*, 4297–4306.

[343] S. Hirata, M. Head-Gordon, *Chem. Phys. Lett.* **1999**, *314*, 291–299.

[344] J.-D. Chai, M. Head-Gordon, *Phys. Chem. Chem. Phys.* **2008**, *10*, 6615.

[345] J. Liang, X. Feng, D. Hait, M. Head-Gordon, *J. Chem. Theory Comput.* **2022**, *18*, 3460–3473.

[346] D. Jacquemin, B. Mennucci, C. Adamo, *Phys. Chem. Chem. Phys.* **2011**, *13*, 16987.

[347] P. Bao, C. P. Hettich, Q. Shi, J. Gao, *J. Chem. Theory Comput.* **2021**, *17*, 240–254.

[348] S. Shirai, Y. Kurashige, T. Yanai, *J. Chem. Theory Comput.* **2016**, *12*, 2366–2372.

[349] D. Bellinger, V. Settels, W. Liu, R. F. Fink, B. Engels, *J. Comput. Chem.* **2016**, *37*, 1601–1610.

Acknowledgement